

**Electronic Structure
Of
Crystalline Solids And Finite-Sized Clusters**

**Thesis submitted for the degree of
Doctor of Philosophy (Sc.)
in Physics (Theoretical)**

**by
Swarnakamal Mukherjee
Department of Physics
University of Calcutta
2015**

– To My Parents –

Abstract Of The Thesis

Scientists in this recent time are investing a lot of effort to study the physical and chemical properties of the materials. For advancement of industry, material science engineering has become a hot research topic in both theoretical and experimental fields. The vast variety of structural and physical properties exhibited by materials makes them promising for industrial applications. Material properties like structural, magnetic, optical properties primarily depend on the electrons. Study of electronic structure of materials thus forms an important area in condensed matter science. Advancement in technique like density functional theory (DFT), makes the theoretical study of electronic structure efficient. In this thesis, we will discuss about first principles DFT study of two distinct classes of materials. (i) crystalline transition metal oxide and (ii) materials at nano scale, primarily the clusters.

Crystalline transition metal oxides (TMO) have been in focus because of their tremendous application possibilities in industry. Charge, Spin, orbital ordering, complex phase transition in oxides make them site of many activities. Such classes of oxides have wide ranging applications in device engineering. On the other hand, rich varieties in the electronic properties among the nano-scale materials are noticed mainly because of the finite-size effect. Among different classes of nano scale materials, "clusters", a relatively small structure consisting of a few to few thousands of atoms, are one of the interesting class of nano-material because of their unique behaviour. Clusters have wide ranging applications in biomedical sciences, nano-catalysis. Large surface to volume ratio in clusters introduces many interesting properties. Electrons in such clusters produces discreet energy levels instead of forming continuous band feature. The abrupt change in electronic and structural properties of the nano-clusters compared to bulk materials has drawn the attention of many researchers during decades.

In this thesis, I report first-principle electronic structure results on nano-clusters as well as complex bulk materials such as A site ordered perovskite oxides.

Acknowledgments

In my PhD days at Satyendra Nath Bose National Centre for Basic Sciences, I have been encouraged, supported and inspired by many of my well-wishers. Without their help, it would not be possible for me to complete the PhD work and to submit this thesis. Here, I would like to take this opportunity to express my gratitude to them.

First of all, my sincere respect and deepest gratitude goes to my thesis supervisor, **Prof. Tanusri Saha Dasgupta** who has offered her time, expertise, wisdom, and continuous encouragement in guiding me through the whole research process.

I would like to acknowledge **Prof. Jacques Chakhalian** and his PhD student **Derek Meyers** from University of Arkansas for their helpful discussions and collaboration, which resulted in two of my publications.

I would like to appreciate **Dr. Mukul Kabir** from the Department of Materials Science and Engineering, Massachusetts Institute of Technology, Cambridge, Massachusetts and **Dr. Jaita Paul** from Satyendra Nath Bose National Centre for Basic Sciences for their involvement in the nano-scale projects.

Special thanks go to all my group-mates, especially to **Dr. Soumyajit Sarkar**.

Finally, my warmest thanks and respects must be to my family for their enormous sacrifice for my PhD degree. In this context, the first name that comes into my mind is my father **Mr. Santosh Kumar Mukherjee** and the second name is very obvious my mother **Smt. Geeta Mukherjee**. I feel very lucky because of my parents. A special thanks goes to my brother **Supratik Mukherjee**. From my school days I was inspired by my parents and my well-wishers to study the subject physics. In this context, my special regards go to my school physics teacher **Gurupada Ghosh**, college physics teacher **Dr. Arun Sen** and **Dr. Alope Ghosh**. I wish to express my sincere gratitude and appreciation to **Prof. Arun Kanti Bhattacharya** for his encouraging thoughts on science. During my days at the Burdwan University, his guidance, patience and continuous support always represented him as 'an example to follow'. I am also especially indebted to all the faculties from physics department of Siksha-Bhavana (Visva Bharati).

Swarnakamal Mukherjee

Santiniketan, India

November, 2015

List of Publications

1. Mukul Kabir, **Swarnakamal Mukherjee** and Tanusri Saha-Dasgupta

Substantial reduction of Stone-Wales activation barrier in fullerene

Phys. Rev. B 84, 205404 (2011)

2. Jaita Paul, **Swarnakamal Mukherjee** and Tanusri Saha-Dasgupta

*A first principles density functional investigation of ligand-protected
eight atom gold nanoclusters*

AIP Advances 1, 032150 (2011)

3. **Swarnakamal Mukherjee**, Soumyajit Sarkar, T. Saha-Dasgupta

First-principles study of $\text{CaCu}_3\text{B}_4\text{O}_{12}$ ($B=\text{Co, Rh, Ir}$)

Journal of Materials Science 47, 7660 (2012)

4. D. Meyers, **Swarnakamal Mukherjee**, J.-G. Cheng, S. Middey, J.-S. Zhou, J. B. Goodenough, B. A. Gray, J. W. Freeland, T. Saha-Dasgupta, J. Chakhalian

*Zhang-Rice physics and anomalous copper states in
A-site-ordered perovskites*

Sci. Rep. 3, 1834 (2013)

5. D. Meyers, S. Middey, J.-G. Cheng, **Swarnakamal Mukherjee**, B.A. Gray, Yanwei Cao, J.-S. Zhou, J.B. Goodenough, Yongseong Choi, D. Haskel, J.W. Freeland, T. Saha-Dasgupta, J. Chakhalian

*Competition between heavy fermion and Kondo interaction in
isoelectronic A-site-ordered perovskites*

Nat Commun, 5, 5818 (2014)

Contents

List of Figures	xii
List of Tables	xiv
Chapter 1 Introduction	1
1.1 Nanoclusters	2
1.1.1 Alkali metal clusters	3
1.1.2 Transition metal clusters	3
1.1.3 Boranes clusters	4
1.1.4 Inert gas clusters	5
1.1.5 Superatom	5
1.1.6 C ₆₀	5
1.2 Transition Metal Perovskites	6
1.2.1 AB _{1-x} B' _x O ₃ type perovskite	7
1.2.1.1 AB _{1/3} B' _{2/3} O ₃ type perovskite	7
1.2.1.2 AB _{1/2} B' _{1/2} O ₃ type perovskite	8
1.2.2 A _{1-x} A' _x BO ₃ type perovskite	9
1.2.2.1 A _{1/4} A' _{3/4} BO ₃ type perovskite	12
1.2.2.1.1 Transition metal at both A' - and B-sites : .	13
1.2.2.1.2 Transition metal only at A' -site :	15
1.2.3 Oxygen deficient perovskite	16
1.2.4 Cation deficient perovskite	18
1.3 Overview of Thesis	19
Chapter 2 Methodology	35
2.1 Wave function based approach	36
2.2 Density based approach (Density Functional Theory)	37
2.3 Exchange-correlation functional	40

2.4	Basis set	41
2.4.1	MTO basis set: LMTO, NMTO	41
2.4.2	Pseudopotential Method	47
2.4.3	Augmented Plane Wave + local orbital method	50
2.4.4	Projector Augmented Wave Method	54
2.5	Spin Density Functional Theory	60
2.5.1	Collinear Magnetism	60
2.5.2	Non-collinear Magnetism	61
Chapter 3	Zhang-Rice physics and anomalous copper states in A-site ordered perovskites	68
3.1	Cuprate superconductors and Zhang-Rice physics	68
3.2	Motivation behind the project	71
3.3	Computational Details	72
3.4	Results and Discussions	73
3.4.1	Crystal Structure	73
3.4.2	Electronic Structure	73
3.4.3	Experimental Observation	78
3.5	Conclusion	80
Chapter 4	Competition between heavy fermion and Kondo interaction in isoelectronic A-site-ordered perovskites	84
4.1	Kondo Lattice and Heavy Fermions	84
4.2	Motivation behind the project	86
4.3	computational detail	89
4.4	Results and Discussions	90
4.4.1	Structural details	90
4.4.2	Electronic structure	91
4.4.3	Experimental observation	96
4.5	Unified Picture	98
4.6	Conclusion	99

Chapter 5	A first principles density functional investigation of ligand-protected eight atom gold nanoclusters	106
5.1	Background	106
5.2	Motivation behind the project	108
5.3	Computational Details	108
5.4	Results and Discussions	110
5.4.1	Structural stability of clusters	110
5.4.2	Energetics	112
5.4.3	<i>sd</i> hybridization	113
5.4.4	Density of states	114
5.4.5	HOMO-LUMO charge densities	114
5.4.6	Bonding charge density	116
5.5	Conclusion	118
Chapter 6	Substantial reduction of Stone-Wales activation barrier in fullerene	123
6.1	Stone-Wales transformation	123
6.2	Motivation behind the project	124
6.3	Computational Details	126
6.4	Results and Discussions	129
6.4.1	$C_{60-x}B_x$ ($x = 0, 1, 2$): Structure and Electronic properties	129
6.4.2	Activation barrier: Effect of substitutional B doping	131
6.4.3	Reaction rate and characteristic time scale	135
6.5	Conclusion	136
Chapter 7	Conclusion and scope for future study	141
7.1	Crystalline perovskite	141
7.2	Nanoclusters	142
7.2.1	Gold nanoclusters	143
7.2.2	C_{60}	143
7.3	Future Scope of Work	144

List of Figures

1.1	Structural phase transformation in 3D and 0D systems	4
1.2	Jahn-Teller and Mackay transformation in Fe_{13} cluster.	4
1.3	Structure of C_{60-I_h} and two its molecular subunit corannulene pyracylene	6
1.4	A- and B-site ordered double perovskite	9
1.5	Electronic phase diagram of $La_{1-x}Sr_xMnO_3$, $Pr_{1-x}Sr_xMnO_3$, $Pr_{1-x}Ca_xMnO_3$	10
1.6	Temperature profile of $Pr_{1-x}Ca_xMnO_3$ ($x = 0.3$) crystal	11
1.7	A-site ordered quadruple perovskite	12
1.8	phase diagram for the $Ca_{1-x}La_xCu_3Fe_4O_{12}$	13
1.9	Classification of the half-metallicity	15
1.10	Crystal structure of Hg-1223 ($HgBa_2Ca_2Cu_3O_{8+\delta}$).	17
1.11	Crystal structure of Cu-12($n-1$) homologous series.	17
1.12	Shifted and twinned hexagonal perovskite	18
3.1	Crystal field splitting of Cu : d and O : p states and their covalent bonding	69
3.2	σ and π bonding in CuO_4 sub-unit	69
3.3	Bonding, anti-bonding and non-bonding phases between Cu : $d_{x^2-y^2}$ and O : p	70
3.4	Three band $p-d$ model	70
3.5	Schematic diagram of Zhang-Rice spin singlet state	71
3.6	Structural building blocks of $CaCu_3Cr_4O_{12}$	75
3.7	Spin polarized density of states and band structure for CCCrO and CCCoO	76
3.8	Crystal field splitting of B : d , Cu : d and O : p states	77
3.9	Cu : $d_{x^2-y^2}$ Wannier function plot	77
3.10	XAS measurements on Cu $L_{3-,2-}$ edge for both CCCrO and CCCoO	79
4.1	Quantum criticality in Ce-115 system.	86

4.2	Low temperature Specific heat of $\text{CaCu}_3\text{Ir}_4\text{O}_{12}$	87
4.3	Orbital evolution from $3d$ to nd ($n= 4, 5$) atomic orbital.	88
4.4	Crystal structure of $\text{CaCu}_3\text{B}_4\text{O}_{12}$ ($\text{B}= \text{Co, Rh, Ir}$)	89
4.5	Non-spin polarized density of states of $\text{CaCu}_3\text{B}_4\text{O}_{12}$ ($\text{B}= \text{Co, Rh, Ir}$)	92
4.6	Spin polarized DOS and band structure of $\text{CaCu}_3\text{B}_4\text{O}_{12}$ ($\text{B}= \text{Co, Rh, Ir}$) .	93
4.7	Spin-Orbit coupling in $\text{CaCu}_3\text{B}_4\text{O}_{12}$ ($\text{B}= \text{Rh, Ir}$)	94
4.8	Wannier function plot for Cu: $d_{x^2-y^2}$ - O: p hybridized states	94
4.9	Crystal field splitting of B: d , Cu: d and O: d states	95
4.10	Cu-L edge soft XAS of $\text{CaCu}_3\text{B}_4\text{O}_{12}$ ($\text{B}= \text{Co, Rh, Ir}$)	97
4.11	Doniach phase diagram of Kondo lattice $\text{CaCu}_3\text{B}_4\text{O}_{12}$ ($\text{B}= \text{Co, Rh, Ir}$) . .	99
4.12	Many-body spin singlet state (a) Kondo effect (b) Zhang-Rice state	100
5.1	Relativistic effect on the $6s$ orbital	107
5.2	Structure of $\text{Au}_8(\text{SR})_n$, $\text{R}= \text{CH}_3 - \text{CH}_2\text{H}$	111
5.3	DOS of Au-s complexes	115
5.4	HOMO and LUMO charge density distributions	116
5.5	Charge density difference	117
6.1	Preliminary steps for the Stone-Wales transformation	124
6.2	Stone-Wales mechanism	125
6.3	Schematic diagram of the NEB method	127
6.4	Local pyracyclene region for optimized $\text{C}_{60-x}\text{B}_x$ ($x= 0, 1, 2$) structure . .	130
6.5	Orbital degeneracy in $\text{C}_{60-x}\text{B}_x$ ($x= 0, 1, 2$)	131
6.6	SW barrier height plotted against the angular distortion	133
6.7	Bonding charge densities in $\text{C}_{60-x}\text{B}_x$ ($x= 0, 1, 2$)	134
6.8	Phonon modes in the 14-atom pyracyclene around the rotating dimer . . .	135
6.9	$I_h \rightarrow C_{2v}$ transition rate.	136

List of Tables

1.1	$AB_{1/3}B'_{2/3}O_3$ type perovskite and their tolerance factor	8
1.2	$AB_{1/2}B'_{1/2}O_3$ type perovskite and their tolerance factor	8
1.3	$A_{1-x}A'_xMnO_3$ type perovskite and their tolerance factor	10
1.4	Microwave dielectric properties of cation-deficient perovskites	19
3.1	Wyckoff Positions of Ca, Cu, B (=Cr, Co) and O in $CaCu_3B_4O_{12}$ (B=Cr, Co)	74
3.2	Structural parameters of $CaCu_3B_4O_{12}$ (B=Cr, Co)	74
4.1	Comparison between optimized and experimental structural parameters of $CaCu_3B_4O_{12}$ (B= Co, Rh, Ir).	91
4.2	Comparison between theoretical and experimental spin magnetic moments at B, Cu site in $CaCu_3B_4O_{12}$ (B= Co, Rh, Ir).	97
5.1	Energetics of bare and passivated Au_8	113
5.2	Adiabatic and vertical ionization potential and electron affinity	113
6.1	Energetics of $C_{60-x}B_x$ ($x = 0, 1, 2$) in eV unit	132
6.2	Stone-Wales activation energy barrier for $I_h \rightarrow C_{2v}$ transition	133

Introduction

During past decades, computational material science has emerged as one of the important field of research. Designing new materials with unique properties from the *ab initio* calculations using the electronic structure methods is one of the exciting and interesting areas of theoretical research. Nowadays, with the availability of fast computers and efficient algorithm, *first principles* electronic structure calculation has emerged as an effective tool to design 'novel materials' with novel properties.

In this context, transition metal oxides are one of the most interesting class of crystalline solids, exhibiting wide-ranging varieties in crystal structures and electronic properties. Properties exhibited by the transition metal compounds depend on the quantum cloud of the *d* electrons, bonding nature between transition metal and oxygen. Charge-orbital interplay existing in such compounds results in high T_C superconductivity in layered cuprates, colossal magneto resistance (CMR) in perovskite manganites, coexistence of magnetism and ferroelectricity - termed as multiferroicity, coexistence of magnetism and superconductivity in heavy fermion systems, quantum phase transitions to name a few. Electron-electron correlation has a dominant contribution to the ground state properties of such transition metal compounds. In the limit of strong electron-electron correlation, localized electrons describe the Mott insulating state characterized by the anti-ferromagnetic spin ordering. In addition to the Mott-Hubbard electron-electron correlations, the relativistic effect and the ligand field effect are also important aspects of the transition metal based compounds. The relativistic correction gives rise to the so-called spin-orbit interaction which becomes important for "heavy" transition metal.

Different ligand field makes different d orbitals being responsible for the bonding. Crystal field dominated orbital physics forms an important component for the *first-principle* electronic structure studies.

In addition to the crystalline solids, *first principle* based simulations have been also very successful in describing the electronic structure of materials at nano-meter length scale, an important topic for both science and engineering. Quantum confinement effect plays a crucial role for such low dimensional materials. In this category, nanoclusters are systems of profound research interest since they offer applications in various fields such as nanocatalysis, biomedical sciences and in nanotechnology industry in general. Though several investigations have been conducted to understand the properties of these clusters, several challenges still remain. It is well known that the properties of clusters not only deviate significantly from their bulk behavior but they also exhibit strong dependence on the size and the atomic arrangement of the cluster. This in turn affects the nature of the bonds formed when these clusters interact with other compounds as often is the case when they are used in e.g., catalysis. Detailed understanding of the structural evolution of nanoclusters and their electronic properties is thus extremely important.

In the present thesis we have studied two broad category of materials namely; (1) cluster (2) bulk transition metal perovskite. In the following sections we will discuss these two classes of materials in greater detail.

1.1 Nanoclusters

Nanocluster is a finite sized system containing a few to few thousand atoms. Large surface to volume ratio introduces many anomalous electronic properties of the clusters. Continuous band feature completely fails for materials at nano-scale. In stead, electrons occupy discrete energy levels. Stability of clusters depends on the structure and coupling between of constituting atoms. Some of the prominent cluster types are described below.

1.1.1 Alkali metal clusters

In 1984, Knight and his co-workers [1,2] reported the non-monotonic variation of abundance distribution of sodium (Na) cluster where maxima occurs at cluster sizes $N = 8, 20, 40, 58$ and 92 . Similar types of trend were observed for other alkaline metal clusters, like Li [3], K [4], Rb [5], Cs [5]. In addition to this, ionization potential (IP), energy required for removal of an electron from the cluster, also shows upturn for cluster sizes $N = 8, 20, 40 \dots$ [2,6]. Typical intensity distribution of sodium (Na) clusters can be understood by jellium model where valance electrons are treated as completely free. These sets of cluster sizes where additional stability in the alkaline metal clusters are noticed, are called as "magic numbers". Close shell electronic configuration gives rise to such anomalous stability. Electrons in such magic numbered clusters of alkaline metals occupy discrete energy sub-shells $1s, 1p, 1d, 2s, 1f, 2p, 1g, 2d, 1h, 3s \dots$. Such close shell analysis also suggests that Al_{13}^- ($40 e^-$) [7,8], KAl_{13} , $NaAl_{13}$ ($40 e^-$), AlH_3 [9] are also magic cluster. In general, magic clusters are less reactive and exhibit larger HOMO-LUMO gaps. Noble metal clusters, Cu_n , Ag_n , Au_n also show such shell-effect. Electronic configuration of the noble metal cluster systems is, in general, $(n+1)d^{10}s^1$. So, if we consider 's' electron moves in a spherical symmetrical potential, then jellium model can be applied successfully.

1.1.2 Transition metal clusters

The concept of magic number is not valid for the transition metal clusters. Structural stability of transition metal complexes can be well described by 18-electron rule [10]. In the crystalline phase, transition metal (Fe, Co, Ni...) can transform from *fcc* to *bcc* phase. During this Bain transformation [11], minimum energy path (MEP) passes through a intermediate structure of body center tetragonal symmetry which is formed by simple elongation of the [001] axis perpendicular to [100] and [010] as shown in Fig. 1.1. But, the cluster system of M_{13} ($M = Fe, Co, Ni$) does not show such mechanism. Moreover structural transition in M_{13} can be explained by two other mechanisms, named as Jahn-Teller transformation (JT) and Mackay transformation (MT). JT theorem suggests that the degenerate electronic states in a non-linear system are unstable with respect to a geometrical distortion that lifts the degeneracy. MT explains the switching mechanism

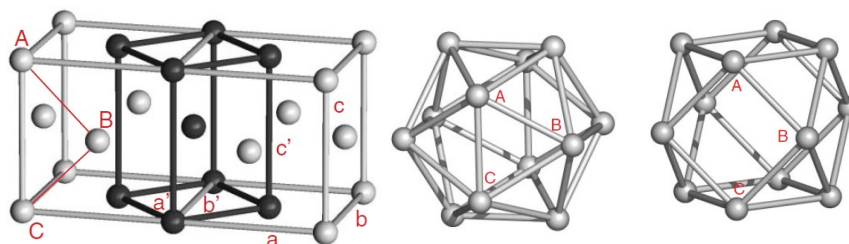


Figure 1.1: Left: the face-centered cubic lattice (grey balls) with the embedded body-centered tetragonal cell formed by Bain transformation (black balls). During the Bain transformation simple elongation of c with respect to a and b takes place. The prime letters correspond to the body center tetragonal structure. Middle and right figure show the structures of icosahedron and cuboctahedron, respectively. Due to the Mackay transformation, \vec{AC} bond elongates resulting in the formation of a square with the two adjacent triangles turning into the same plane. The capital letters represent the same atomic sites in each structure. Adopted from *Phys. Rev. Lett.* **99**, 083402 (2007).

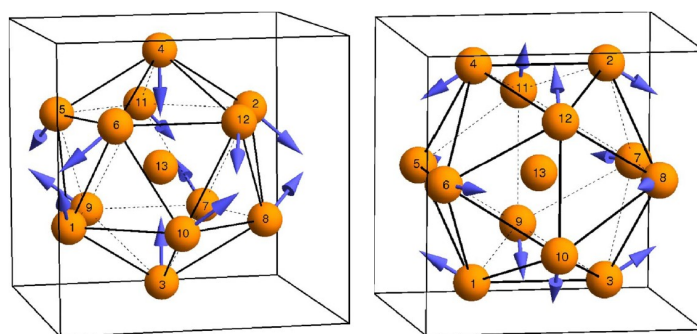


Figure 1.2: Fe_{13} cluster having JT-distortion (left) and MT (right) respectively. Arrows represent the direction of relative movement of atoms with respect to the ideal crystalline positions. Reproduced from [12].

from icosahedron to cuboctahedron geometry of a cluster. JT-distorted cluster is stable for a Fe_{13} cluster resulting icosahedron structure as a ground state (see Fig. 1.2) while MT-distorted structure is stable for cuboctahedron Co_{13} . Both JT and MT geometry become energetically almost degenerate for Ni_{13} [12, 13].

1.1.3 Boranes clusters

Similarly, stability of boranes (boron hydrogen complexes) can not be explained in terms of magic number. In this case Wade-Mingos rule is highly favorable which suggests that stability of boranes require $(n + 1)$ pairs of electrons where the structure is based on n -vertex polyhedron [14, 15]. According to this rule, $[\text{B}_n\text{H}_n]^{2-}$ with $(n + 1)$ skeletal electron-pairs, is called as “closo”, B_nH_{n+4} has $(n + 2)$ skeletal electron-pairs and this structure

is called “nido”. B_nH_{n+6} with $(n + 3)$ skeletal electron-pairs is termed as “arachno” [16]. Al_nH_m cluster complexes also obey the above stated law [17].

1.1.4 Inert gas clusters

Inert gas clusters are also important type of clusters. Stable structure for xenon occurs for cluster size $N = 13, 19, 25, 55, 71, 87, 147$ [18]. On the other hand He cluster shows different behavior than the alkaline metal clusters and inert gas clusters like xenon clusters. Magic numbers for ^4He clusters are $N = 7, 10, 14, 23, 30$, while magic numbers for ^3He switch to different cluster sizes, $N = 7, 10, 14, 30$ [19]. One of the unusual property of the He cluster is the super-fluidity for cluster size $N = 64, 128$ [20].

1.1.5 Superatom

An interesting property of nanoclusters is the formation of *superatom*. A *superatom* is a stable cluster with physical and chemical properties similar to that an isovalent atom. For example, Al_{13}^- shows both electron shell closing and atomic shell closing. Al_{13}^- has 40 (valance) electrons and stabilized in icosahedral symmetry. Al_{13}^- is isovalent to Cl^- . Similar to halide ion, Al_{13}^- is noticed to form ionic bond with the electropositive elements from the periodic table and covalent bond with alkaline groups. In addition to this, Al_{13}^- acts as a superhalogen during the reaction with iodine and hydriodic acid (HI) [25, 26]. Al_{13} shows high electron affinity of 3.57 eV comparable to 3.36 eV for Br and 3.62 eV of Cl [25–28]. Theoretical studies suggest that core of Al_{13} remains almost intact as in Al_{13} while a covalent bond is formed between the aluminum cluster and the iodine atom suggesting analogy to stable halogen dimer anion. Similarly, superatoms like Al_7 exhibit multiple valance state which results many stable molecules, like Al_7C , Al_7O , Al_7S , Al_7I_2 and Al_7^+ [29].

1.1.6 C_{60}

There are 1812 possible C_{60} fullerene structures involving 12 pentagons and 20 hexagonal rings [30–32]. C_{60} structure with I_h symmetry is the most stable. Carbon atoms occupy the 60 vertices of a regular truncated icosahedron. A regular truncated icosahedron has 90

edges of equal lengths, 60 equivalent vertices, 20 hexagonal faces and 12 pentagonal faces. Hexagon-pentagon sharing single bonds are 1.46 Å while double bonds sharing between two hexagons are smaller (1.40 Å). There are 60 single and 30 double bonds in the structure of C_{60-I_h} . Carbon atoms in C_{60-I_h} have no dangling bonds. Curvature in the structure

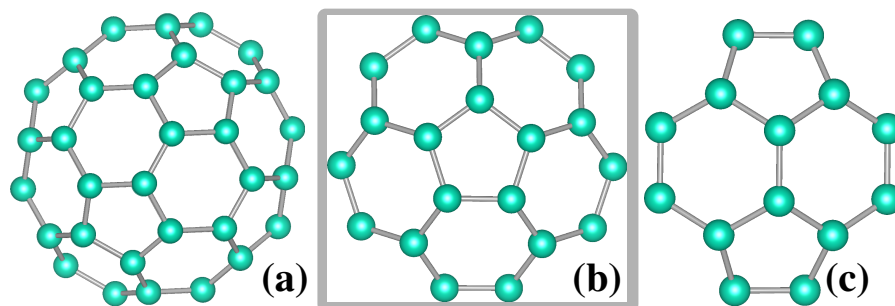


Figure 1.3: Structure of (a) C_{60-I_h} and two its molecular subunit (b) corannulene (c) pyracylene. During fullerene isomerization, hexagon-hexagon sharing bond is rotated at an angle 90° so that pentagons and hexagons change their positions. Such pyracylene rearrangement is termed as stone-Wales transformation [30–32] which leads to the product C_{2v} symmetric structure which includes a pair of adjacent pentagonal carbon rings.

introduces some sp^3 nature in the sp^2 type bonding. Thus, each σ bond bears a small amount of π signature. Each pentagonal ring is surrounded by five hexagonal rings. Due to this isolated pentagonal rule, strain in C_{60-I_h} becomes the minimum. The structure of isolated pentagon and surrounding five hexagonal rings looks like a corannulene molecule ($C_{20}H_{10}$) (see Fig. 1.3) [33]. Another important structural sub-unit of C_{60-I_h} is pyracylene composed of a pair of pentagons and hexagons as shown in Fig. 1.3 [34]. Solid state of C_{60} crystallizes into face-centered-cubic phase with lattice constant of 14.17 Å and density 1.72 gm/cc (1.44×10^{21} C_{60} molecules/cc) [35]. This face-centered-cubic phase of solid C_{60} shows simple-cubic ordering around $T < 249-270$ K [36]. This first order phase transition is modulated by both the temperature and pressure. Similar to C_{60} , boron clusters (B_n , $n = 38, 44, 65, 72, 80, 92, 110$) are also noticed to form hollow cages [37].

1.2 Transition Metal Perovskites

Perovskite has general chemical formula ABO_3 where A site is occupied by a large metal ion like alkaline earth or rare earth. B-site is occupied by smaller cation *ie.* transition metal ion. Such crystal structure is one of the most extensively studied structure in the

material science. Ideal perovskite structure has cubic symmetry, but there exists a number of perovskite compounds with crystal symmetry different from cubic at room temperature which transforms to cubic at higher temperature. This low symmetry and low temperature phase is called as 'hettotype' while high temperature is termed as 'aristotype' [38] structure. Perovskites show a lot of variation in the electronic properties. Such electronic properties can be tuned by creating substitution at A or B site or vacant sites. This can be symbolized as $A_{1-x}A'_xBO_3$, $AB_{1-x}B'_xO_3$, A-site cationic vacancies like $A_x\Box_{1-x}BO_3$.

1.2.1 $AB_{1-x}B'_xO_3$ type perovskite

$Ag(Nb_xTa_{1-x})O_3$ is an example of such class of perovskite compounds which has the ability to split water into hydrogen and oxygen [40, 41]. For different concentration x , $Ag(Nb_xTa_{1-x})O_3$ shows perovskite structure with different symmetry (monoclinic, rhombohedral, orthogonal, tetragonal, cubic). Tetragonal structure is noticed in the sample from 692 K to 777 K beyond which it transforms to cubic symmetry. In the region $0 \leq x \leq 0.9$, coexistence of monoclinic phase and orthorhombic phases are noticed. Ferroelectric or anti-ferroelectric effects appear during the structural transitions of $Ag(Nb_xTa_{1-x})O_3$ [42–49].

Example of ordered perovskites of type $AB_{1-x}B'_xO_3$ are

1. $AB_{1/3}B'_{2/3}O_3$
2. $AB_{1/2}B'_{1/2}O_3$.

1.2.1.1 $AB_{1/3}B'_{2/3}O_3$ type perovskite

$Ba(Zn_{1/3}Ta_{2/3})O_3$ is an example of this class of perovskite oxides where long range ordering between Zn-Ta has been noticed [50]. Experiments also suggest the existence of ordered hexagonal and cubic disordered phase in $Ba(Zn_{1/3}Ta_{2/3})O_3$ [51]. During sample preparation, $Ba(Zn_{1/3}Ta_{2/3})O_3$ crystallizes in an apparently disordered phase and after annealing, structure switches to an ordered hexagonal structure with Zn-Ta-Ta repeat sequences along $\langle 111 \rangle$ direction of the parent cubic cell. This type of B-site cation ordering is called as 1:2 ordering. Similar to $Ba(Zn_{1/3}Ta_{2/3})O_3$, crystal structure of $Ba(Mg_{1/3}Ta_{2/3})O_3$ undergoes a phase transition from disordered cubic perovskite with

$Pm\bar{3}m$ space group to 1:2 ordered (-Mg-Ta-Ta-Mg-Ta-Ta) hexagonal phase with $P\bar{3}m1$ space group resulting from the distortion along $\langle 111 \rangle$ direction of the cubic cell [52, 53]. Such order-disorder transition in $\text{Ba}(\text{Ni}_{1/3}\text{Nb}_{2/3})\text{O}_3$ takes place around 1500 °C [54–57].

Table 1.1: $\text{AB}_{1/3}\text{B}'_{2/3}\text{O}_3$ type perovskite and their tolerance factor (t). From [58].

	A=Ba	A=Ba	A=Ba	A=Ba	A=Ba	A=Ba
$\text{AB}_{1/3}\text{B}'_{2/3}\text{O}_3$	B=Mg	B=Mg	B=Ni	B=Ni	B=Zn	B=Zn
	B'=Nb	B'=Ta	B'=Nb	B'=Ta	B'=Nb	B'=Ta
t	1.033	1.030	1.039	1.036	1.031	1.028

Table 1.1 shows some compounds belong to this class of perovskite with their calculated tolerance factors.

1.2.1.2 $\text{AB}_{1/2}\text{B}'_{1/2}\text{O}_3$ type perovskite

A large number of B-site ordered double perovskites $\text{A}(\text{B}'_{1/2}\text{B}''_{1/2})\text{O}_3$ were reported in 1960's [59–65]. Due to B-site cation ordering, primitive undistorted perovskite cell ABO_3 gets doubled which also result in a change in the space group (see Fig. 1.4). Low temperature phase of $\text{Ba}(\text{Y}_{1/2}\text{Ta}_{1/2})\text{O}_3$ is cubic ($Fm\bar{3}m$) which goes to tetragonal ($I4/m$) at ~ 253 K [61, 66, 67, 69, 71–73]. On the other hand, structure of $\text{Sr}(\text{B}_{1/2}\text{Mo}_{1/2})\text{O}_3$ (B=Cr, Fe, Mn) show cubic symmetry ($Fm\bar{3}m$) while $\text{Sr}(\text{Co}_{1/2}\text{Mo}_{1/2})\text{O}_3$ shows tetragonal ($I4/mmm$) symmetry [74].

Table 1.2 summarizes some examples of such class of perovskite oxides with their tolerance factors.

Table 1.2: $\text{AB}_{1/2}\text{B}'_{1/2}\text{O}_3$ type perovskite and their tolerance factor (t). From [67].

	A=Ba	A=Ba	A=Ba	A=Ba	A=Ba	A=Ba
$\text{AB}_{1/2}\text{B}'_{1/2}\text{O}_3$	B=Nd	B=Gd	B=Y	B=In	B=Nd	B=Ga
	B'=Ta	B'=Ta	B'=Ta	B'=Ta	B'=Nb	B'=Nb
t	0.965	0.975	0.984	1.008	0.965	0.975
Structure (300K)	Tetragonal	Tetragonal	Cubic	Cubic	Tetragonal	Tetragonal
and remarks	$T_c=638.0$ K	$T_c=452.3$ K	$T_c=253.1$ K	—	$T_c=646.2$ K	$T_c=445.9$ K

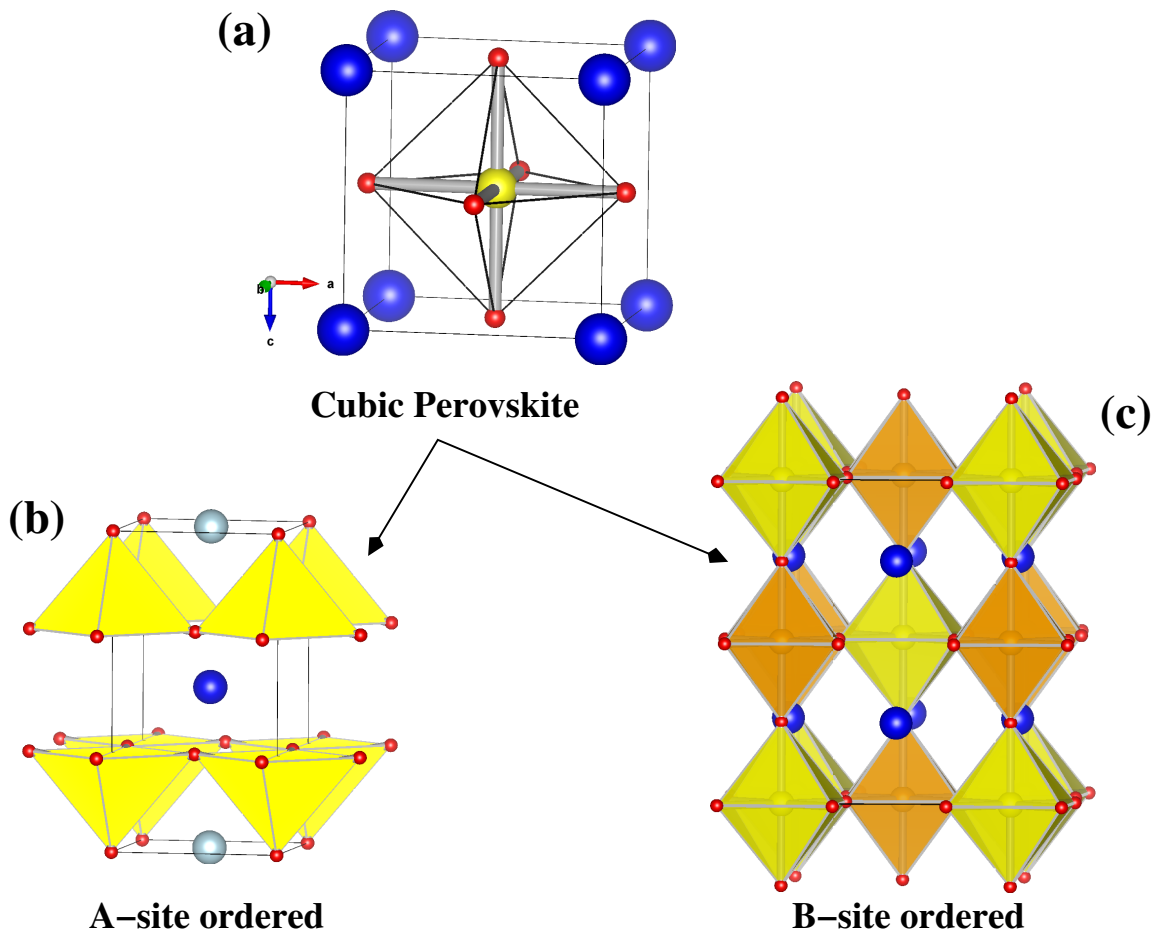


Figure 1.4: Crystal structure of (a) cubic perovskite BaTiO_3 , (b) A-site ordered double perovskite $\text{GdBaCo}_2\text{O}_5$ and (c) B-site ordered double perovskite $\text{Sr}_2\text{FeMoO}_6$. Deep blue stands for cations Ba and Sr. Cobalt sites are shown by yellow colors while Fe/Mo sites are shown by yellow/orange color. Light blue denotes Gd and oxygen ions are shown by red colour.

1.2.2 $\text{A}_{1-x}\text{A}'_x\text{BO}_3$ type perovskite

Colossal magneto-resistance (CMR) is one of the prominent example of this type of perovskite compounds with Mn atom at the B-site. Initially, giant magneto resistance (GMR) was noticed in metallic multilayers of Fe/Cr/Fe [75]. CMR was reported in a class of perovskite compounds $\text{Ln}_{1-x}\text{A}_x\text{MnO}_3$ (Ln = Lanthanide, A = Alkaline earth metal) where magneto-resistive effect was found to be much larger than GMR [76–78]. Most of the CMR oxomanganates are based on anti-ferromagnetic insulator LaMnO_3 . When LaMnO_3 is doped with alkali metal cations, like Ca, Sr, Ba, product $\text{Ln}_{1-x}\text{A}_x\text{MnO}_3$ becomes ferromagnetic metal. Large magneto-resistance (below Curie temperature T_C) is also noticed in $\text{La}_{1-x}\text{Sr}_x\text{MnO}_3$ ($0 \leq x \leq 0.6$), $\text{La}_{1-x}\text{Ca}_x\text{MnO}_3$ ($0.20 \leq x \leq 0.50$), $\text{Pr}_{1-x}\text{Sr}_x\text{MnO}_3$

($x=0.33$) [79–86]. Some of the $A_{1-x}A'_x\text{MnO}_3$ type perovskite structures and their tolerance factors are summarized in table 1.3.

Table 1.3: $A_{1-x}A'_x\text{BO}_3$ type perovskite and their tolerance factor (t). From [87].

$A_{1-x}A'_x\text{MnO}_3$	$\text{Pr}_{0.7}\text{Sr}_{0.3}$	$\text{La}_{0.7}\text{Sr}_{0.3}$	$\text{La}_{0.7}\text{Ca}_{0.3}$	$\text{Pr}_{0.7}\text{Ca}_{0.3}$	$\text{La}_{0.7}\text{Ba}_{0.3}$	$\text{Gd}_{0.7}\text{Ba}_{0.3}$	$\text{Gd}_{0.7}\text{Sr}_{0.3}$
t	0.926	0.936	0.922	0.912	0.953	0.926	0.908
T_c (K)=	260	352	255	-	320	-	-

Thus, in manganese based perovskite oxides hole concentration (x) is an important component for magnetoresistance property. In this context, different hole concentrations (x) show complex electronic structure in a series of compounds $\text{La}_{1-x}\text{Sr}_x\text{MnO}_3$, $\text{Pr}_{1-x}\text{Sr}_x\text{MnO}_3$, $\text{Pr}_{1-x}\text{Ca}_x\text{MnO}_3$ resulting interesting physical properties [88, 89]. Strong

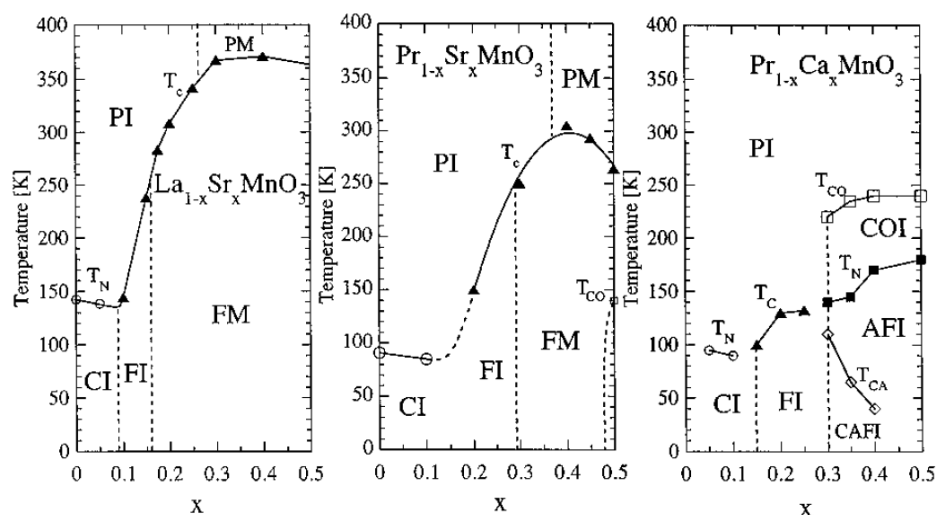


Figure 1.5: The magnetic as well as electronic phase diagrams of $\text{La}_{1-x}\text{Sr}_x\text{MnO}_3$ (left), $\text{Pr}_{1-x}\text{Sr}_x\text{MnO}_3$ (middle) and $\text{Pr}_{1-x}\text{Ca}_x\text{MnO}_3$ (right). The PI, PM, CI, CAFI, COI denote the paramagnetic insulating, paramagnetic metallic, spin-canted insulating, canted anti-ferromagnetic insulating and charge ordered insulating states, respectively. The FI, FM, and AFI denote the ferromagnetic insulating and ferromagnetic metallic, and anti-ferromagnetic insulating states, respectively. Reproduced from [88].

Jahn-Teller distortion present in the parent compound LaMnO_3 results orbital-ordering in the crystallographic ab plane [90]. Such ordered state undergoes an anti-ferromagnetic transition at 120 K. In this spin-ordered state ferromagnetic ab planes are coupled anti-ferromagnetically along crystallographic c axis. As a result of hole doping ordered spins

start canting towards c axis [91, 92]. Such spin-canting is noticed upto $x = 0.15$, while for $x \geq 0.10$ spin-ordered state is completely ferromagnetic as shown in Fig. 1.5 [93, 94]. On the other hand, $\text{Pr}_{1-x}\text{Sr}_x\text{MnO}_3$ is ferromagnetic metal for $x > 0.3$ while at $x \sim 0.5$ transition from this ferromagnetic metallic state to charge-ordered insulating state is noticed for $T < 140$ K (see Fig. 1.5) [95]. This charge-ordering is CE type [91, 96–98]. For $x > 0.52$, A-type anti-ferromagnetic ordering is noticed [99–101]. From Fig. 1.5 it is seen that $\text{Pr}_{1-x}\text{Ca}_x\text{MnO}_3$ ($x = 0.3$) shows such charge-ordered phase at $T < 220$ -240 K. Ferromagnetic state is completely vanished for this compound. Within the charge-ordered

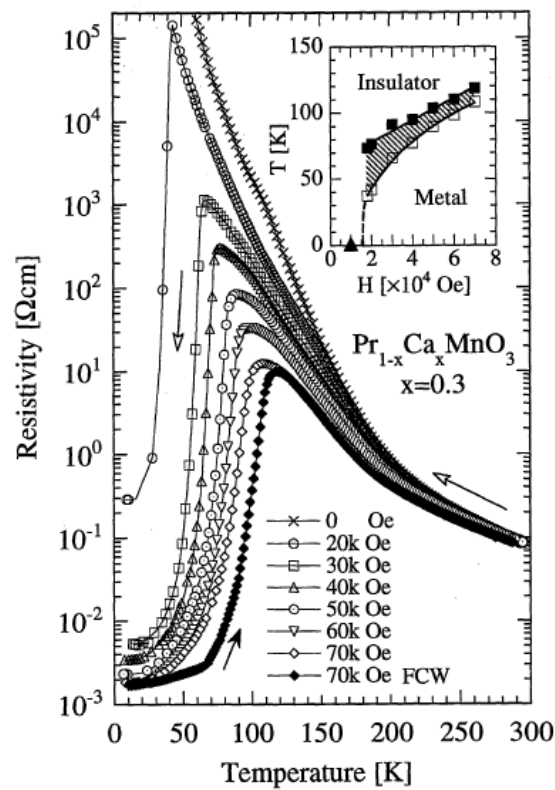


Figure 1.6: Temperature profile of $\text{Pr}_{1-x}\text{Ca}_x\text{MnO}_3$ ($x = 0.3$) crystal. Reproduced from [104].

state, successive transition to charge-ordered insulating phase ($0.3 \leq x \leq 0.5$) and charge-ordered spin canted state ($0.3 \leq x \leq 0.4$) are noticed [97, 98, 102, 103]. Figure 1.6 shows the temperature profile of $\text{Pr}_{1-x}\text{Ca}_x\text{MnO}_3$ ($x = 0.3$) crystal [104]. This crystal for $x = 0.3$ undergoes a phase transition from the charge/orbital ordered insulating state ($T_{CO} \sim 200$ K [105]) to a metallic state under high magnetic field. The resistivity under zero field shows an insulating behavior while the other curves (> 2 T) show a change from

an insulating to metallic phase below critical temperatures. The critical temperature is defined as the temperature with maximum resistivity which increases as the magnetic field intensity increases. The hysteresis observed between cooling (open squares) and warming (filled squares) runs is shown in the inset wherefrom it can be noticed that metal-insulator transition in $\text{Pr}_{1-x}\text{Ca}_x\text{MnO}_3$ ($x = 0.3$) crystal takes place for magnetic field $H > 10$ kOe.

1.2.2.1 $\text{A}_{1/4}\text{A}'_{3/4}\text{BO}_3$ type perovskite

In these perovskite structures, A is a larger cation such as an alkali, alkaline earth, or rare earth cation while A' is a smaller cation, typically a transition metal cation. 1:3 A-site ordering leaves the cubic symmetry intact, cell volume becomes 8 times that of a cubic ABO_3 type perovskite. In order to stabilize the smaller transition metal cations at the

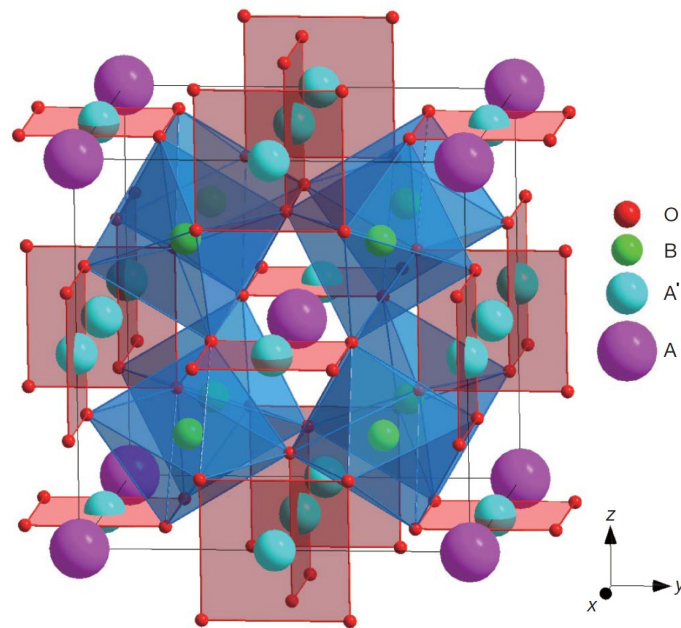


Figure 1.7: Crystal structure of the A-site-ordered quadruple perovskite $\text{AA}'_3\text{B}_4\text{O}_{12}$. Adopted from [106].

A-site of ABO_3 along with the larger cations Ca or La, high pressure is required during the sample preparation of compounds belong to $\text{AA}'_3\text{B}_4\text{O}_{12}$ family. A-cations remain in a much larger 12-coordinate icosahedral environment while A' sites form square planar geometry with nearest four oxygen ions (see Fig. 1.7). B ions sit in octahedral interstice formed by oxygen ions. Fascinating electronic properties of $\text{AA}'_3\text{B}_4\text{O}_{12}$ family depend on

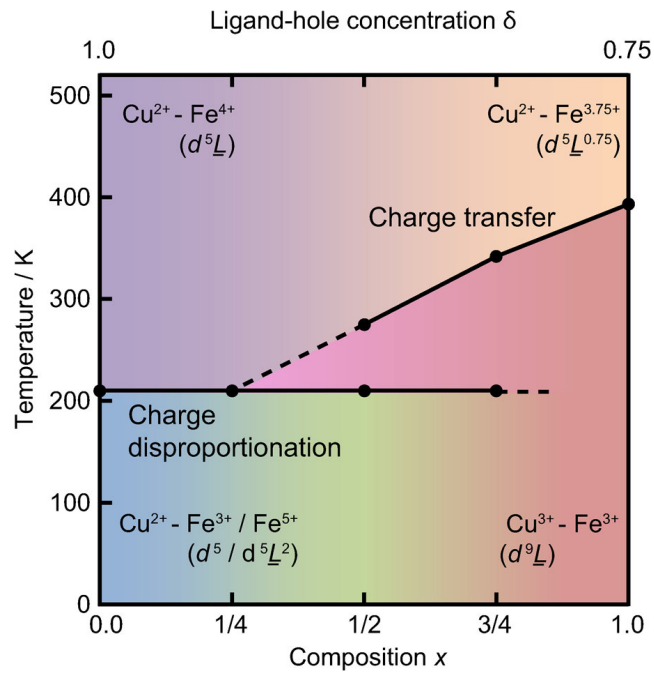


Figure 1.8: Ligand-hole movement in $\text{Ca}_{1-x}\text{La}_x\text{Cu}_3\text{Fe}_4\text{O}_{12}$. For $x = 0$, charge disproportionation is noticed for localized ligand holes at the Fe-site ($\text{CaCu}_3\text{Fe}_4\text{O}_{12}$) while holes start moving towards the Cu site as the La concentration increases. Charge transfer temperature decreases with the increase of ligand-hole concentration δ (decrease of La concentration) while charge disproportionation temperature remains fixed at 210 K. Reproduced from [108].

the proper choice of A' - and B-site cations.

1.2.2.1.1 Transition metal at both A' - and B-sites : Presence of transition metal cations at both A' - and B-sites make them playground of rich varieties of electronic properties depending on the choice of cations. For example, $\text{CaCu}_3\text{Fe}_4\text{O}_{12}$ [107, 108] crystallizes in cubic phase ($Im\bar{3}$, space group no. 204) at room temperature while rock salt type ordering ($Pn\bar{3}$, space group no. 201) is noticed at 90 K. Room temperature structure shows ferromagnetism while ferrimagnetic ordering ($\text{Cu}\uparrow, \text{Fe}\downarrow$) is noticed in the low temperature structure with low Néel temperature (116 K). $\text{CaCu}_3\text{Fe}_4\text{O}_{12}$ shows charge disproportionation ($4\text{Fe}^{4+} \rightarrow 2\text{Fe}^{3+} + 2\text{Fe}^{5+}$) at 210 K similar to simple perovskite CaFeO_3 . This low temperature charge disproportionate state is ferromagnetic and insulating while above 210 K, system switches to a paramagnetic and metallic phase. If Ca^{2+} is substituted by La^{3+} , then A' -B charge transfer ($3\text{Cu}^{2+} + 4\text{Fe}^{3.75+} \rightarrow 3\text{Cu}^{3+} + 4\text{Fe}^{3+}$) is noticed around 393 K which results changes from a high-temperature paramagnetic and metallic phase to a low temperature anti-ferromagnetic and insulating phase (a charge-transferred phase) [106–108].

Such interesting physics is mediated by the distribution of the ligand holes (\underline{L}) which can be seen from Fig 1.8*. Charge disproportion in $\text{CaCu}_3\text{Fe}_4\text{O}_{12}$ results from the localization of the ligand holes at the Fe-sites ($4d^5\underline{L} \rightarrow 2d^5 + 2d^5\underline{L}^2$) while in $\text{LaCu}_3\text{Fe}_4\text{O}_{12}$, charge transfer between Cu and Fe is mediated by the ligand hole transfer from the Fe-site to Cu-site ($3d^9 + 4d^5\underline{L}^{0.75} \rightarrow 3d^9\underline{L} + 4d^5$). At high temperature, itinerant ligand holes are distributed at the Fe-sites forming $d^5\underline{L}^\delta$ ($0 \leq \delta \leq 1 - x/4$) like state. For $T \leq 210\text{K}$ and small La concentration ($0 \leq x \leq 1/4$), charge disproportion is notice in the compound while charge transfer temperature decreases from 393 K as the La concentration starts decreasing from $x = 1.0$ to $x = 1/4$. Both charge disproportion and charge transfer states simultaneously coexist for higher La concentration and low temperature ($T \leq 210\text{K}$) leading to a very complex electronic structure.

Similar type of charge transfer in noticed at higher temperature (428 K) in $\text{BiCu}_3\text{Fe}_4\text{O}_{12}$ [109] resulting semiconducting-antiferromagnetism to paramagnetic metallic phase. This ferrimagnetic transition temperature decreases from 361 K in $\text{LaCu}_3\text{Mn}_4\text{O}_{12}$ to 350 K in $\text{BiCu}_3\text{Mn}_4\text{O}_{12}$. Magnetoresistance is an important property of $\text{ACu}_3\text{Mn}_4\text{O}_{12}$ (A= La, Bi). Temperature driven magnetic ordering is also noticed in $\text{LaMn}_3\text{Cr}_4\text{O}_{12}$ [110] where anti-ferromagnetic ordering of Mn^{3+} spins are noticed around 50 K while anti-ferromagnetic ordering of Cr^{3+} spins take place at higher temperature (150 K). Anti-ferromagnetic ordering of B- and A' -spins take place at lower temperature (76 K for B-site spins, 20 K for A' -site spins) for $\text{LaMn}_3\text{Mn}_4\text{O}_{12}$. $\text{BiMn}_3\text{Mn}_4\text{O}_{12}$ shows different type of ordering. Ferromagnetic ordering of B-site spins are noticed around 59 K while anti-ferromagnetic ordering of A' spins are noticed at 28 K [111]. $\text{CaCu}_3\text{Ru}_4\text{O}_{12}$ shows heavy fermion like characteristic with a Kondo temperature of 200 K [112]. Recently an experimental synthesis suggests $Pnma$ type orthorhombic structure of $\text{AMn}_3\text{V}_4\text{O}_{12}$ where A-site is occupied by Y^{3+} and Lu^{3+} [113]. X-ray diffraction analysis suggests that $\text{La}_{1-x}\text{Na}_x\text{Mn}_3\text{Ti}_4\text{O}_{12}$ crystallized with the $\text{AA}'_3\text{B}_4\text{O}_{12}$ perovskite structure in which the A' -site Mn ions were slightly displaced from the ideal positions [114]. Mn valance is modulated by the Na concentration (x) and B-site bears small amount of Mn signature which decreases with the increase of Na concentration x .

*In this hole presentation, unusual Fe^{4+} , Fe^{5+} and Cu^{3+} states are represented as $d^5\underline{L}$, $d^5\underline{L}^2$ and $d^9\underline{L}$ respectively.

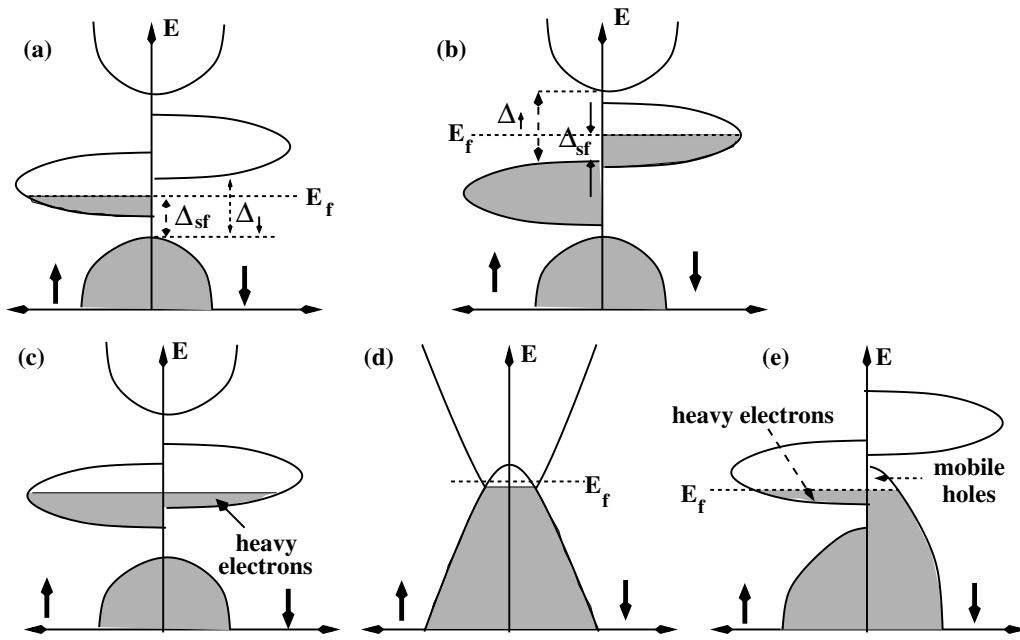


Figure 1.9: Classification of the half-metallicity: DOS of (a) type I_A , (b) type I_B , (c) type III_A , (d) a semi-metal, (e) type IV_A . In case of such half-metals, one spin channel shows metallic behavior, while other spin channel gives rise to insulating or semiconducting ground state [115, 116]. This type of half-metallicity is classified as type I which is further divided into two categories I_A (a) and I_B (b). In their density of states, along with spin gap $\Delta_{\uparrow/\downarrow}$, smaller gap Δ_{sf} exists which causes spin-flip excitation. Sr_2FeMoO_6 is an example of I_B type half-metal. Type I half metal with localize charge carriers are classified as type II half metals. Similar to type I, type II is also divided into two classes II_A and II_B . These localize charge carriers form ‘polarons’. Magnetite is an example of type II_B half metal. In type III, finite density of states at Fermi energy exist from both spin channel. Charge carriers in one spin channel is mobile, while on other spin channel it is found that charge carriers are localize and have no contribution to the transport mechanism. So, we get metallic state in one spin channel, while other spin channel shows insulating solution. $La_{0.7}Sr_{0.3}MnO_3$ is an example of type III_A (c) half metal. (d) In case of semimetals small overlap between valence and conduction bands results small and equal numbers of electrons and holes. Fig. (e) shows DOS of IV type half-metal which is a special case of semimetal where effective mass difference between electrons and holes becomes noticeable. $Tl_2Mn_2O_7$ is an example of semimetal (IV type) where heavy Mn holes are localized at the top of Mn (e_g) state and equal number of light (normal) electrons of TI ($6s$) character are noticed which are mobile. Adopted from [115].

1.2.2.1.2 Transition metal only at A'-site : A number of $AA'_3B_4O_{12}$ perovskite structures have been reported where B-site is occupied by elements other than transition metal cation. Insulating behavior is noticed in $ACu_3Sn_4O_{12}$ (A= Ca, Sr, Pb) [117, 118] while $LaCu_3Sn_4O_{12}$ shows half metallic character. Changes in the electronic structure appears due to changing Cu: $d_{x^2-y^2}$ occupancy. Substitution of La results partial occupied Cu: $d_{x^2-y^2}$ state resulting half-metallic solution. Thus, substitution of La introduces an additional electron which moves towards the Cu site. Half metallicity is an interesting aspect of such transition metal oxides where Kohn-Sham solution of one spin

channel becomes insulating while other spin channel shows metallic character. Fig. 1.9 shows an interesting analysis on the half metallicity. Ferromagnetic ordering is noticed in $\text{CaCu}_3\text{B}_4\text{O}_{12}$ (B= Ge, Sn) below 13 K while anti-ferromagnetic ordering originated from the superexchange interaction through the Cu-O-B-O-Cu path is noticed for B= Ti with a anti-ferromagnetic transition temperature 25 K [119]. Antiferromagnetic interaction is also noticed in $\text{AMn}_3\text{Al}_4\text{O}_{12}$ (A = Y, Yb, Dy) between Mn^{3+} spins with a anti-ferromagnetic transition temperature ranging from 29-40 K [120, 121].

1.2.3 Oxygen deficient perovskite

There are a large number of perovskite structures of the form $\text{A}_n\text{B}_n\text{O}_{3n-\delta}$ have been reported where vacancy at the oxygen site is noticed. Many new oxygen deficient perovskites have been reported after the discovery of high temperature superconductivity. Interesting electronic phenomenon associated with this oxygen deficient A-site ordered perovskite are (i) large magneto-resistance effect in $\text{BaXCo}_2\text{O}_{5+\delta}$ (X = Eu, Gd, $\delta = 0.4$), [122] (ii) metal-insulator transition in $\text{BaYCo}_2\text{O}_{5+\delta}$ ($\delta = 0.5$), [123] (iii) complex charge/ orbital ordering in BaYCo_2O_5 [124]. High temperature superconductor $\text{Ba}_2\text{Ti}_{2-x}\text{Ca}_2\text{Cu}_3\text{O}_{10+\delta}$ ($T_C = 125$ K) [125], $\text{Ba}_3\text{La}_3\text{Ca}_x\text{Cu}_{6+x}\text{O}_y$ ($0 \leq x \leq 3$, $T_C = 80$ K) [126] are well known triple perovskites. Quadruple and quintuple-perovskite structures are crystallized under high pressure. Layered $\text{Ba}_2\text{Gd}_2\text{Ti}_2\text{Cu}_2\text{O}_{11}$ [127], $\text{Ba}_2\text{Ti}_2\text{Ca}_3\text{Cu}_4\text{O}_{12}$ [128] are layered oxygen-deficient quadruple perovskite. $\text{Ba}_2\text{Ln}_2\text{CaTi}_3\text{Cu}_2\text{O}_{14}$ (Ln = Sm, Eu, Gd) is a layered quintuple perovskite structure ($P4/mmm$) with stacking sequences in the order Cu-Ti-Ti-Ti-Cu. [129].

Structure of high temperature superconductors consist of two parts: the charge reservoir block and the conducting block which is further divide into the alternating stack of $[\text{CuO}_2]$ planes and a spacer sheet which is evident from Fig. 1.10. The outmost $[\text{ACuO}_2]$ configuration is termed as 'primary infinite layer cell' while $[\text{A}'\text{CuO}_2]$ configuration where A' is usually a bare sheet in between two neighboring $[\text{CuO}_2]$ planes. Crystal structure of the High temperature superconductors are symbolized as $[\text{M} - m_1 m_2 (n - 1) n]$. Here M is metal element (Bi, Cu, Hg, Tl, Pb, etc.) and m_1 is its layer number (m_1 is the $[\text{MO}]$ layer numbers), m_2 is the number of interfacial layer

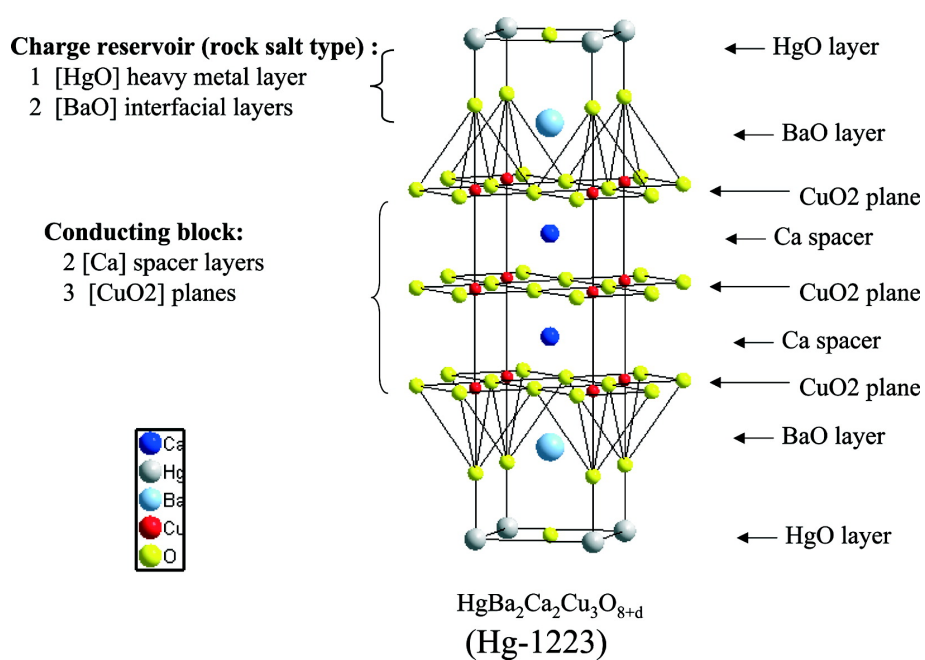


Figure 1.10: Crystal structure of Hg-1223 ($\text{HgBa}_2\text{Ca}_2\text{Cu}_3\text{O}_{8+\delta}$). Reproduced from [130].

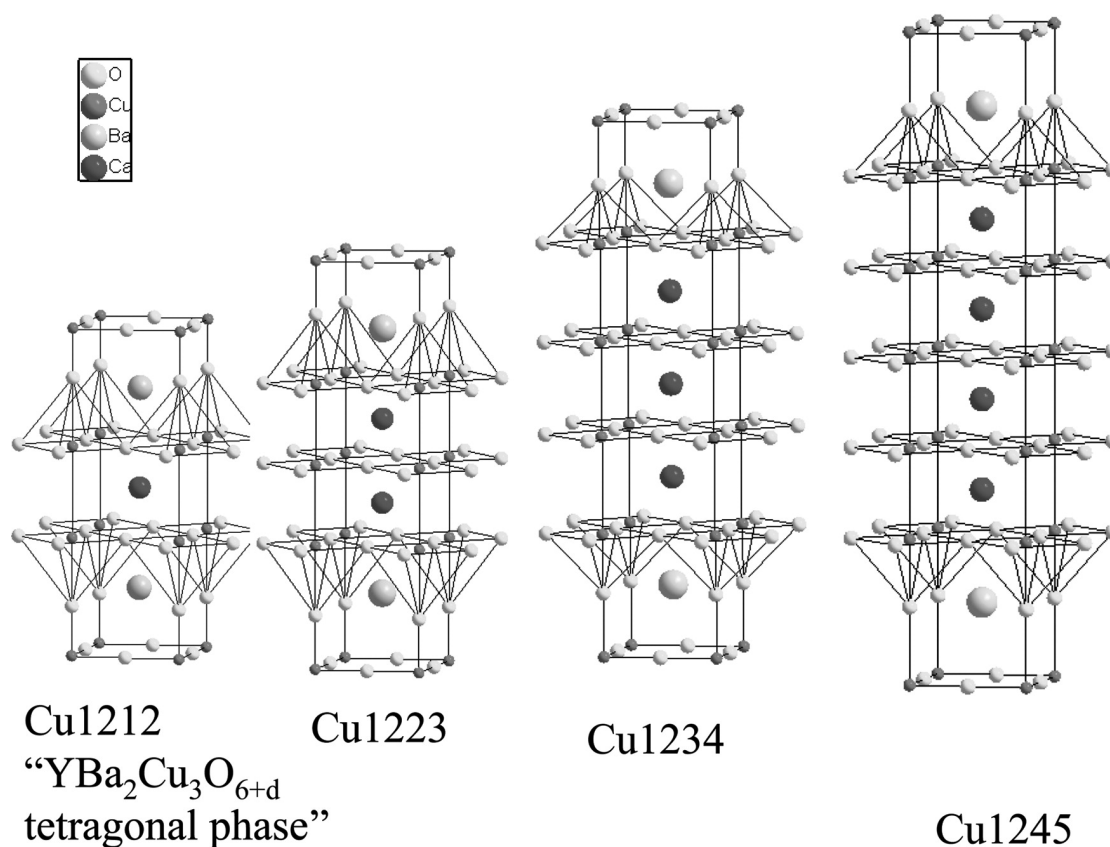


Figure 1.11: Crystal structure of Cu-12(n-1) homologous series. Reproduced from [130].

number (m_2 is the [AO] layer numbers), $(n - 1)$ is number of spacer layer number and n being the number of $[\text{CuO}_2]$ planes in the unit cell. Fig. 1.11 shows the crystal structures of $\text{Cu-}12(n - 1)$ homologous series which crystallize in tetragonal structure with space group $P4/mmm$. Crystallography of $\text{Cu-}12(n - 1)$ has the same features as that of $\text{Hg(Tl)-}12(n - 1)$, replacing the $[\text{Hg(Tl)O}]$ rock salt layer with oxygen deficient $[\text{CuO}_2]_i$ types perovskite layers will lead to $\text{Cu-}12(n - 1)$.

1.2.4 Cation deficient perovskite

A number of perovskite structure have been reported where cationic vacancies at A and B site are noticed. Cation-deficient $A_nB_{n-1}O_{3n}$ is different from the cubic close pack as the structure contains mixed hexagonal and cubic AO_3 stacking sequences [131]. Packing is defined as either 'h' or 'c' type depending on whether the neighboring layers are alike or different. 'h' and 'c' denotes hexagonal and cubic close packing. Such cubic-

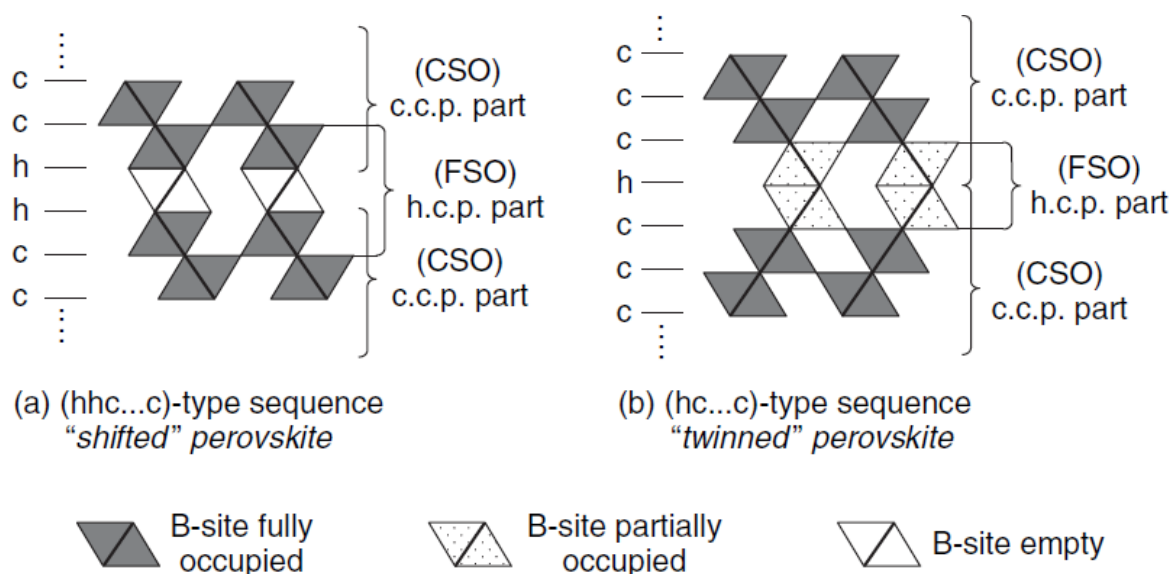


Figure 1.12: Schematic representation of the Shifted and twinned hexagonal perovskite. CSO (FSO) represents corner (face) sharing octahedra. Hexagonal and cubic stacking are represented by the Jagodzinski notation. Similar (different) stacking sequence is represented by letter h (c). Long-range ordering of vacancies are noticed in 'shifted' perovskite. Decrease of the periodicity of vacancies along the c -axis are noticed in twinned hexagonal perovskite. Reproduced from [131].

hexagonal mixing results fcc sharing BO_6 octahedra. Depending on the B-site cation ordering hexagonal perovskite are divide into two categories (i) shifted perovskite and (ii) twinned perovskite as shown in Fig 1.12. $hhc \cdots c$ type of stacking can be described as $(n-1)$

Table 1.4: Microwave dielectric properties of cation-deficient perovskites.

Chemical composition	Compound	Permittivity ϵ_r	Quality factor (GHz)
A ₄ B ₃ O ₁₂	Ba ₃ LaNb ₃ O ₁₂ [132]	43.5	9047
	Ba ₂ La ₂ TiNb ₂ O ₁₂ [133]	42.7	31130
A ₅ B ₄ O ₁₅	Ba ₅ Nb ₄ O ₁₅ [134]	38.4	26337
	Ba ₄ SrNb ₄ O ₁₅ [135]	48	14600
A ₆ B ₅ O ₁₈	Ba ₄ La ₂ Ti ₃ Nb ₂ O ₁₈ [136]	55.1	21273
	Ba ₂ La ₄ Ti ₅ O ₁₈ [137]	46	31839
A ₈ B ₇ O ₂₄	Ba ₈ Ta ₆ NiO ₂₄ [138]	27.5	81758
	Ba ₈ Nb ₄ Ti ₃ O ₂₄ [139]	44-48	21000-23500

corner sharing octahedra at the center of face sharing trimers. hhc...c type stacking is called as shifted perovskite because of periodic shifting of corner sharing octahedra. hc...c type stacking sequence is termed as twinned perovskite where partial occupied face sharing octahedra are noticed around twin plane boundary. Such class of perovskite are important components for the microwave applications. Table 1.4 summarizes the microwave dielectric properties of cation-deficient perovskites.

1.3 Overview of Thesis

The contents of the present thesis are as follows :

Chapter 2 : In this chapter we have discussed the methods for electronic structure calculations performed in this present thesis which includes brief description of the formulation of *first-principles* density functional theory (DFT), different basis set and description of magnetism within DFT.

Chapter 3 : In this chapter we have studied two isostructural A-site ordered cuprate perovskites, CaCu₃Co₄O₁₂ and CaCu₃Cr₄O₁₂. Our first principles analysis suggest that electronic structure of CaCu₃B₄O₁₂ (B= Cr, Co) shows resemblance with high T_c cuprate superconductors despite the lack of superconducting ground state. Both

compounds under study are metallic in agreement with the experimental observation. Metastable Cu^{3+} state is noticed in $\text{CaCu}_3\text{Co}_4\text{O}_{12}$ while Cu in $\text{CaCu}_3\text{Cr}_4\text{O}_{12}$ shows ionic Cu^{2+} like oxidation state. Considering B sublattice, intermediate spin configuration is noticed for Co while Cr shows low spin state. These findings demonstrate that the charge and spin state of Cu, fundamental to the intriguing physical properties the cuprates display, can be effectively altered by a careful choice of the B-site cation on isomorphic lattices that circumvent the chemical disorder and lattice modulation intrinsic to other doping methods.

Chapter 4 : In this chapter we have investigated the changes in the electronic structure of $\text{CaCu}_3\text{B}_4\text{O}_{12}$ as one moves from $3d$ (Co) to $4d$ (Rh) to $5d$ (Ir) element at the B site. $3d$ transition metals show larger electron-electron correlation compared to $4d$ or $5d$ elements, while larger crystal field splitting and spin-orbit interaction play crucial role for $4d$ or $5d$ elements. Our calculations suggest that all three compounds are metallic. Cu in $\text{CaCu}_3\text{Rh}_4\text{O}_{12}$ shows mixed valency while stable ionic Cu^{2+} like oxidation state is noticed in $\text{CaCu}_3\text{Ir}_4\text{O}_{12}$. Low spin state is noticed for Rh and Ir in $\text{CaCu}_3\text{Rh}_4\text{O}_{12}$ and $\text{CaCu}_3\text{Ir}_4\text{O}_{12}$ respectively. Half-metallicity in $\text{CaCu}_3\text{Ir}_4\text{O}_{12}$ is noticed within GGA+U approach while spin-orbit interaction is found to mix up and down spins and destroy half-metallicity.

Chapter 5 : In this chapter we discuss the effect of ligand attachment on Au_8 magic cluster of both planar (2D) and non-planar (3D) geometry. Our result follows that site-selective ligand attachment depends on the coordination as well as the geometry giving rise to ligand-ligand interactions. Although 2D - 3D transition in bare gold cluster takes place in this size range, our first principle analysis suggests that the ligand attachment enhances the structural stability of planar geometry. The above obtained trend is rather different from previously reported theoretical studies on ligated 11 and 13 atom clusters which predict stabilization of 3D-like geometry over 2D-like geometry upon ligation. The difference in the predicted trend between ligated 8-atom cluster in the present study and that for ligated 11 and 13 atom clusters corroborates the fact that structure and bonding

in small clusters crucially depend on their size.

Chapter 6 : In this chapter we focus on buckminsterfullerene, C_{60} . C_{60} has more than 1000 isomers having 12 pentagons and 20 hexagons connected by Stone-Wales mechanism along the potential energy surface. Stone-Wales transformation is the fundamental mechanism for $C_{60}-I_h$ formation which is the most stable C_{60} geometry. C_{60} with C_{2v} symmetry results from a single Stone-Wales transformation. Initially it was noticed that formation of $C_{60}-I_h$ from $C_{60}-C_{2v}$ requires more than 5 eV energy which reduces in the presence of loosely bound additional carbon atoms. In this chapter we discuss the effect of substitutional doping at the active Stone-Wales site. Our first principle analysis concludes that the substitutional doping is much more effective route for C_{60} annealing and fragmentation.

Chapter 7 : This chapter includes summary and outlook of the present work.

Bibliography

- [1] W. D. Knight, K. Clemenger, W. A. de Heer, W. A. Saunders, M. Y. Chou, M. L. Cohen, Phys. Rev. Lett. **52**, 2141 (1984).
- [2] W. A. de Heer, W. D. Knight, M. Y. Chou, M. L., Cohen, Solid State Phys. **40**, 93 (1987).
- [3] N. Goela, S. Gautamb, K. Dharamvir, AIP Conf. Proc. **1349**, 241 (2011);
R. Fournier, J. B. Y. Cheng, A. Wong, J. Chem. Phys. **119**, 9444 (2003).
- [4] W.D. Knight, W.A. de Heer, K. Clemenger, W.A. Saunders, Solid State. Commun. **53** 445 (1985);
W.A. Saunders, K. Clemenger, W.A. de Heer, W.D. Knight, Phys. Rev. B. **32**, 1366 (1985);
M.M. Kappes, M. Schär, P. Radi, E. Schumacher, J. Chem. Phys. **84**, 186 (1986);
W.D. Knight, W.A. de Heer, W.A. Saunders, K. Clemenger, M.Y. Chou, M.L. Cohen, Chem. Phys. Lett. **134**, 1 (1987);
M.L. Cohen, M.Y. Chou, W.D. Knight, W.A. de Heer, J. Phys. Chem. **91** 3141 (1987);
C. Bréchnignac, P. Cahuzac, J.P. Roux, J. Chem. Phys. **87** 229 (1987).
- [5] Y. Li, E. Blaisten-Barojas, D. A. Papaconstantopoulos, Phys. Rev. B. **57**, 15519 (1998).
- [6] M. Y. Chou, A. Cleland, M. L. Cohen, Solid State Commun. **52**, 645 (1984).

- [7] S.-B. Cheng, C. Berkdemir, J. J. Melko, A. W. Castleman, Jr., *J. Am. Chem. Soc.* **136**, 4821 (2014);
J. C. Smith, A. C. Reber, S. N. Khanna, A. W. Castleman, Jr., *J. Phys. Chem. A*, **118**, 8485 (2014).
- [8] R. E. Leuchtner, A. C. Harms, A. W. Castleman Jr, *J. Chem. Phys.* **91** 2753 (1989).
- [9] W. J. Zheng, O. C. Thomas, T. P. Lippa, S. J. Xu, K. H. Bowen, *J. Chem. Phys.* **124** 144304 (2006);
V. Kumar, *Phys. Rev. B* **57**, 8827 (1998);
C. M. Araèjo, S. Li, R. Ahuja, P. Jena, *Phys. Rev. B* **72**, 165101 (2005).
- [10] S. N. Khanna, B. K. Rao, and P. Jena, *Phys. Rev. Lett.* **89**, 016803 (2002);
J. W. Lauher, *J. Am. Chem. Soc.*, **100**, 5305 (1978), C. A. Tolman *Chem. Soc. Rev.*, **1**, 337 (1972).
- [11] E.C. Bain, The nature of martensite. *Trans. Am. Inst. Min. Metall. Pet. Eng.* **70**, 25 (1924);
F. Milstein, H. Fang, J. Marschall, *Philos. Mag. A* **70**, 621 (1994).
- [12] S. Sahoo, A. Hucht, M. E. Gruner, G. Rollmann, P. Entel, A. Postnikov, J. Ferrer, L. Fernández-Seivane, M. Richter, D. Fritsch, S. Sil, *Phys. Rev. B* **82**, 054418 (2010).
- [13] S. Sahoo, M. E. Gruner, A. Hucht, G. Rollmann, P. Entel in "Nanoparticles from the Gasphase: Formation, Structure, Properties" Edited by Phaedon Avouris, Bharat Bhushan, Dieter Bimberg, Klaus von Klitzing, Hiroyuki Sakaki, Roland Wiesendanger, Springer, 2012.
- [14] K. Wade, *Adv. Inorg. Chem. Radiochem.* **18**, 1 (1976);
K. Wade, *J. Chem. Soc. D* **15**, 792 (1971).
- [15] D. M. P. Mingos, *Nature physical science* **236**, 99 (1972).
- [16] Z.-X. Wang, P. V. R. Schleyer, *J. Am. Chem. Soc.* **125**, 10484 (2003);
R. E. Williams, *Inorg. Chem.* **10**, 210 (1971);
S. Heřmánek, *Chem. Rev.* **92**, 325 (1992).

- [17] X. Li, A. Grubisic, S. T. Stokes, J. Cordes, G. F. Gantefor, K. H. Bowen, B. Kiran, M. Willis, P. Jena, R. Burgert, H. Schnöckel, *Science* **315**, 356 (2007);
P. J. Roach, A. C. Weber, W. H. Woodward, S. N. Khanna, A. W. Castleman Jr., *Proc. Natl. Acad. Sci. USA* **104**, 14565 (2007).
- [18] O. Echt, K. Sattler, and E. Recknagel, *Phys. Rev. Lett.* **47**, 1121 (1981).
- [19] S. W. Peter, J. G. King, *Phys. Rev. Lett.* **51**, 1538 (1983).
- [20] P. Sindzingre, M. L. Klein, D. M. Ceperley, *Phys. Rev. Lett.* **63**, 1601 (1989).
- [21] J. Ho, K. M. Ervin, W. C. Lineberger, *J. Chem. Phys.*, **93**, 6987 (1990).
- [22] I. Katakuse, T. Ichihara, Y. Fujita, T. Matsuo, T. Sakurai, H. Matsuda, *Int. J. Mass Spectrom. Ion Processes* **67**, 229 (1985).
- [23] I. Katakuse, T. Ichihara, Y. Fujita, T. Matsuo, T. Sakurai, H. Matsuda, *Int. J. Mass Spectrom. Ion Processes* **74**, 33 (1986).
- [24] H. Häkkinen, M. Moseler, U. Landman, *Phys. Rev. Lett* **89** 033401 (2002).
- [25] D. E. Bergeron, A. W. Castleman Jr, T. Morisato, S. N. Khanna, *Science* **304** 84 (2004).
- [26] D. E. Bergeron, P. J. Roach, A. W. Castleman Jr, N. O. Jones, S. N. Khanna, *Science* **307** 231 (2005).
- [27] X. Li, L. S. Wang, *Phys. Rev. B* **65** 153404 (2002).
- [28] X. Li X, H. Wu, X. B. Wang, L. S. Wang, *Phys. Rev. Lett.* **81** 1909 (1998).
- [29] J. U. Reveles, S. N. Khanna, P. J. Roach, A. W. Castleman, Jr., *Proc. Natl. Acad. Sci. U.S.A.* **103**, 18405 (2006).
- [30] A. J. Stone, D. J. Wales, *Chem. Phys. Lett.* **128**, 501 (1986).
- [31] P.A. Marcos, M.J. Lòpez, A. Rubio, J.A. Alonso, *Chem. Phys. Lett.* **273**, 367 (1997).
- [32] S. J. Austin, P.W. Fowler, D.E. Manolopoulos, F. Zerbetto, *Chem. Phys. Lett.* **235**, 146 (1995).

- [33] J. C. Hanson, C. E. Nordman, *Acta. Crystallogr.* **B32**, 1147 (1976);
S. Mebs, M. Weber, P. Luger, B. M. Schmidt, H. Sakurai, S. Higashibayashi, S. Onogi and D. Lentz, *Org. Biomol. Chem.* **10**, 2218 (2012);
E. Osawa, *Philos. Trans. R. Soc. London, Ser. A* **343**, 1 (1993);
H. Becker, G. Javahery, S. Petrie, P.-C. Cheng, H. Schwarz, L. T. Scott, D.K. Bohme, *J. Am. Chem. Soc.* **115**, 11636 (1993) .
- [34] F. Diederich and R. L. Whetten, *Act. Chem. Res.* **25**, 119 (1992).
- [35] E W. Stephens, L. Mihaly, E L. Lee, R. L. Whetten, S. M. Huang, R. Kaner, E. Diederich, and K. Holczer, *Nature (London)* **351**, 632 (1991);
A. R. Kortan, N. Kopylov, S. H. Glarum, E. M. Gyorgy, A. P. Ramirez, R. M. Fleming, E A. Thiel, and R. C. Haddon. *Nature (London)* **355**, 529 (1992);
M. B. Jost, N. Troullier, D. M. Poirier, J. L. Martins, J. H. Weaver, L. P. F. Chibante, R. E. Smalley, *Phys. Rev. B*, **44**, 1966 (1991);
J.E. Fischer, P.A. Heiney, A.B. Smith III, *Acc. Res. Chem*, **25**, 112 (1992);
V. V. Brazhkin, A. G. Lyapin, S. V. Popova, R. N. Voloshin, Yu. V. Antonov, S. G. Lyapin, Yu. A. Klyuev, A. M. Naletov, N. N. Mel'nik, *Phys. Rev. B* **56**, 11465 (1997).
- [36] W. I. F. David, R. M. Ibberson, T. J. S. Dennis, J. P. Hare, K. Prassides, *Europhys. Lett.*, **18**, 219 (1992);
J. P. Lu, X. -P. Li, R. Martin, *Phys. Rev. Lett.* **68**, 1551 (1992);
G. A. Samara, J. E. Schirber, B. Morosin, L. V. Hansen, D. Loy and A. P. Sylwester, *Phys. Rev. Lett.* **67**, 3136, (1991).
- [37] N. G. Szwacki, A. Sadrzadeh, B. I. Yakobson, *Phys. Rev. Lett.* **98**, 166804 (2007);
S. De, A. Willand, M. Amsler, P. Pochet, L. Genovese, and S. Goedecker, *Phys. Rev. Lett.* **106**, 225502 (2011);
R. R. Zope, T. Baruah, K. C. Lau, A. Y. Liu, M. R. Pederson, B. I. Dunlap, *Phys. Rev. B*, **79**, 161403 (2009).
- [38] C. N. W. Darlington, J. A. Hriljac, K. S. Knight, *Phys. Stat. Sol. (b)* **242**, 854 (2005).

- [39] V. M. Goldsohmidt, *Slcriter Norsk Videnskaps-Akad. Oslo, I, Mct.-Naturv, KL, No. 8* (1926).
- [40] H. Kato, H. Kobayashi, A. Kudo, *J. Phys. Chem. B* **106** 12441 (2002).
- [41] A. Kudo, *J. Hydrogen Energy* **31** 197 (2006).
- [42] M. H. Francombe and B. Lewis, *Acta. Crystallogr.* **11**, 175 (1958).
- [43] A. Kanaria and A. Ratusza, *Phase Transitions* **2**, 7 (1981).
- [44] M. Lukaszewski, M. Pawelczyk, A. Kanaria, *Phase Transitions* **3**, 247 (1983).
- [45] M. Pawelczyk *Phase Transitions*, **8** 273 (1999).
- [46] G. E. Kugel, M. D. Fontana, M. Hafid, K. Roleder, A. Kanaria, M. Pawelczyk, *J. Phys. C. Solid State Phys.* **20** 1217 (1987).
- [47] A. Ratuszna, J. Pawluk, A. Kanaria, *Phase Transitions*, **76**, 611 (2003).
- [48] A. Kanaria, *Ferroelectrics* **205**, 19 (1998).
- [49] P. Sciau, A. Kanaria, B. Dkhil, E. Suard, A. Ratuszna, *J. Phys.: Condens. Matter.* **16**, 2795 (2004).
- [50] B. M. Jacobson, B. E. Collins, F. Fender, *Acta. Crystallogr. B* **32**, 1083 (1976).
- [51] S. Kawashima, M. Nishida, I. Ueda, and H. Ouchi, *J. Amer. Ceram. Soc.* **66**, 421, (1983).
- [52] A. Srinivas, E. D. Dias, G. S. Murthy, *Bull. Mater. Sci.* **20**, 1, 23(1997);
M.T. Sebastian, K.P. Surendran, *J. Eur. Ceram. Soc.* **26**, 1791 (2006).
- [53] Y. I.-C. Chen, H.-F. Cheng, C.-C. Lee, C.-T. Chia, H.-L. Liu, I.-N. Lin, *Journal of Electroceramics*, **13**, 271 (2004).
- [54] I.-T. Kim, Y. H. Kim, S. J. Chung, *J. Mater. Res.* **12**, 518 (1997).
- [55] I.-T. Kim, Y.-H. Kim, S.-J. Chung, *J. Appl. Phys.* **34**, 4096 (1995).

- [56] K. S. Hong, I. T. Kim, C. D. Kim, *J. Am. Ceram. Soc.* **79**, 3218 (1996).
- [57] J.-K. Park, D.-Y. Kim, D. Y. Yoon, *J. Am. Ceram. Soc.* **84**, 218 (2001).
- [58] M. W. Lufaso, *Chem. Mater.* **16**, 2148 (2004).
- [59] F. Galasso, W. Darby, *J. Phys. Chem.* **66**, 131 (1962).
- [60] L. Brixner, *J. Inorg. Nucl. Chem.* **15**, 352 (1960).
- [61] F. Galasso, G. Layden, D. Flichbagh, *J. Chem Phys.* **44**, 2703 (1966).
- [62] V. S. Filipev, E. G. Fesenko, *Sov. Phys. Crystallogr.* **6**, 616 (1962).
- [63] V. S. Filipev, E. G. Fesenko, *Sov. Phys. Crystallogr.* **10**, 243 (1965).
- [64] F. J. Fresia, L. Katz, R. Ward, *J. Am. Chem. Soc.* **81**, 4783 (1959).
- [65] E. G. Steward, H. P. Rooksby, *Acta. Crystallogr.* **4**, 503 (1951).
- [66] F. S. Galasso *Structure and properties of Perovskite compounds*. Pergamon Press, Headington Hill, Oxford (1969).
- [67] R. Zuhmuhlen, J. Petzelt, S. Kamba, G. Kozlov, B. Volkov, B. Gorshunov, D. C. Dube, A. Tagentsev, N. Setter. *J. Appl. Phys.* **77**, 5341 (1995).
- [68] R. Zuhmuhlen, E. L. Colla, D. C. Dube, J. Petzelt, I. M. Reaney, A. Bell, N. Setter, *J. Appl. Phys.* **76**, 5864 (1994).
- [69] R. L. Moreira, L. A. Khalam, M. T. Sebastian, A. Dias, *J. Eur. Ceram. Soc.* **27**, 2803 (2007);
L. A. Khalam, P. S. Anjana, M. T. Sebastian, *Int. J. Appl. Ceram. Technol.* **6** 571 (2009).
- [70] J. B. Philipp, P. Majewski, L. Alff, A. Erb, R. Gross, T. Graf, M. S. Brandt, J. Simon, T. Walther, W. Mader, D. Topwal, and D. D. Sarma, *Phys. Rev. B* **68**, 144431 (2003);
Y. Moritomo, Sh. Xu, A. Machida, T. Akimoto, E. Nishibori, M. Takata, and M. Sakata, *Phys. Rev. B* **61**, R7827 (2000).

- [71] I. Gregoria, J. Petzelt, J. Pokorny, V. Vorlicek, Z. Zikmund, Z. Zurmuhlen, N. Setter, Solid State Commun. **94**, 899(1995).
- [72] Y. Doi, Y. Hinatsu, J. Phys.: Condens. Matter. **13**, 4191 (2001).
- [73] T. Fuji, J. Takahashi, S. Shimada, J. Electroceram. **3**, 387 (1999).
- [74] Y. Moritomo, Sh. Xu, A. Machida, T. Akimoto, E. Nishibori, M. Takata, and M. Sakata, Phys. Rev. B **61**, R7827 (2000).
- [75] M. N. Baibich, J. M. Broto, A. Fert, F. Nguyen Vn Dau, F. Petroff, P. Eitenne, G. Creuzet, P. Friederich, J. Chazelas, Phys. Rev. Lett. **61**, 2472 (1988).
- [76] R. von Helmolt, J. Wecker, B. Holzapfel, L. Schultz, K. Samwer, Phys. Rev. Lett. **71**, 2331 (1993).
- [77] K. Chahara, T. Ohono, M. Kasai, Y. Kozono, Appl. Phys. Lett. **63**, 1990 (1993).
- [78] M. McCormack, S. Jin, T.H. Tiefel, R.M. Fleming, J.M. Phillips and R. Ramesh, Appl. Phys. Lett. **64**, 3045 (1994);
S. Jin, T.H. Tiefel, M. McCormack, R.A. Fastnacht, R. Ramesh and L.H. Chen, Science **264**, 413 (1994);
J. B. Goodenough, Aust. J. Phys. **52**, 155 (1999);
L. Han, C. Chen, J. Mater. Sci. Technol. **26**, 234 (2010).
- [79] W.E. Pickett, D.J. Singh, Phys. Rev. B **53**, 1146 (1996);
A. Urushibara *et al.*, Phys. Rev. B **51**, 14 103 (1995).
- [80] D.J. Singh and W.E. Pickett, Phys. Rev. B **57**, 88 (1998).
- [81] H. Kino, F. Aryasetiawan, I. Solovyev, T. Miyake, T. Ohno, K. Terakura, Physica B: Cond. Matt. **329**, 858 (2003).
- [82] W.E. Pickett, D.J. Singh, J. Magn. Magn. Mater. **172**, 237 (1997).
- [83] P.K. de Boer and R.A. de Groot, Compt. Mat. Res. **10**, 240 (1998).

- [84] S.F. Matar, Prog. Solid State Chem. **31**, 239 (2003);
M. Uehara, S. Mori, C. H. Chen, S.-W. Cheong, Nature **399**, 560 (1999).
- [85] P.K. de Boer, H. van Leuken, R.A. de Groot, T. Rojo, G.E. Barberis, Solid State Comm. **102**, 621 (1997).
- [86] J.S. Kang, T.W. Noh, C.G. Olson, B.I. Min, J. Electron Spectrosc. Rel. Phenom. **114**, 683 (2001);
W. Chérif, M. Ellouze, A.-F. Lehlooh, F. Elhalouani, S.H. Mahmood, J. Magn. Magn. Mater. **324**, 2030 (2012).
- [87] J. P. Zhou, J. T. McDevitt, J. S. Zhou, H. Q. Yin, J. B. Goodenough, Y. Gim, and Q. X. Jia, Appl. Phys. Lett. **75**, 1146 (1999).
- [88] Y. Tokura, Y. Tomioka, H. Kuwahara, A. Asamitsu, Y. Moritomo, M. Kasai: J. Appl. Phys. **79**, 5288 (1996).
- [89] A. Moreo *et al.*, Science **283**, 2034 (1999).
- [90] J. Kanamori, J. Appl. Phys. **31**, 14S (1960).
- [91] E. O. Wollan, W. C. Koehler, Phys. Rev. **100**, 54 (1955).
- [92] P.-G. de Gennes, Phys. Rev. **118**, 141 (1960)
- [93] A. Urushibara, Y. Moritomo, T. Arima, A. Asamitsu, G. Kido, Y. Tokura, Phys. Rev. B **51**, 14103 (1995).
- [94] H. Kawano, R. Kajimoto, M. Kubota, H. Yoshizawa: Phys. Rev. B **53**, R14709 (1996);
H. Kawano, R. Kajimoto, M. Kubota, and H. Yoshizawa, Phys. Rev. B **53** 2202 (1996).
- [95] H. Kuwahara, Y. Tomioka, A. Asamitsu, Y. Moritomo, Y. Tokura, Science **270**, 961 (1995).
- [96] J.B. Goodenough, Phys. Rev. **100**, 564 (1955).

- [97] Z. Jirak, S. Krupicka, Z. Simsa, M. Dlouha, Z. Vlatislav, J. Magn. Mater. **53**, 153 (1985).
- [98] H. Yoshizawa, H. Kawano, Y. Tomioka, Y. Tokura, Phys. Rev. B **52**, R1345 (1995).
- [99] H. Kawano, R. Kajimoto, H. Yoshizawa, Y. Tomioka, H. Kuwahara, Y. Tokura, Phys. Rev. Lett. **78**, 4253 (1997).
- [100] H. Kuwahara, T. Okuda, Y. Tomioka, A. Asamitsu, Y. Tokura, Phys. Rev. Lett. **82**, 4316 (1999).
- [101] Y. Moritomo, T. Akimoto, A. Nakamura, K. Hirota, K. Ohoyama, M. Ohashi, Phys. Rev. B **58**, 5544 (1998).
- [102] Y. Tomioka, A. Asamitsu, Y. Moritomo, Y. Tokura, J. Phys. Soc. Jpn. **64**, 3626 (1995).
- [103] Y. Tomioka, A. Asamitsu, H. Kuwahara, Y. Tokura, Phys. Rev. B **53**, R1689 (1996).
- [104] Y. Tomioka, A. Asamitsu, Y. Moritomo and Y. Tokura, J. Phys. Soc. Jpn. **64**, 3626 (1995).
- [105] H. Yoshizawa, H. Kawano, Y. Tomioka and Y. Tokura, Phys. Rev. B **52**, R13145 (1995).
- [106] Y. W. Long, N. Hayashi, T. Saito, M. Azuma, S. Muranaka and Y. Shimakawa, Nature **458**, 60 (2009).
- [107] I. Yamada, K. Takata, N. Hayashi, S. Shinohara, M. Azuma, S. Mori, S. Muranaka, Y. Shimakawa and M. Takano, Angew. Chem. Int. Ed. **47**, 7032 (2008).
- [108] W.-T. Chen, T. Saito, N. Hayashi, M. Takano and Y. Shimakawa, Sci. Rep. **2**, 449 (2012).
- [109] Y. W. Long, T. Saito, T. Tohyama, K. Oka, M. Azuma and Y. Shimakawa, Inorg. Chem. **48**, 8489 (2009).

- [110] Y. Long, T. Saito, M. Mizumaki, A. Agui, and Y. Shimakawa, *J. Am. Chem. Soc.* **131**, 16244 (2009).
- [111] H. Okamoto, N. Imamura, M. Karppinen, H. Yamauchi, and H. Fjellvag, *Inorg. Chem.* **49**, 8709 (2010).
- [112] A. Krimmel, A. Guenther, W. Kraetschmer, H. Dekinger, N. Buettgen, V. Eyert, A. Loidl, D. V. Sheptyakov, E.-W. Scheidt, W. Scherer, *Phys Rev. B* **80**, 121101(R) (2009).
- [113] Y. Shimakawa, S. Zhang, T. Saito, M. W. Lufaso and P. M. Woodward, *Inorg. Chem.* **53**, 594 (2014).
- [114] T. Tohyama, M. S. Senn, T. Saito, W.-T. Chen, C. C. Tang, J. P. Attfield, Y. Shimakawa, *Chem. Mater.* **25**, 178 (2013).
- [115] J. M. D. Coey, M. Venkatesan, *J. Appl. Phys.* **91**, 8345 (2002).
- [116] J M D Coey, S Sanvito, *J. Phys. D: Appl. Phys.* **37**, 988 (2004).
- [117] 34] H. P. Li, S. H. Lv, D. M. Han, X. J. Liu, J. Meng, *Chem. Phys. Lett.* **494**, 213 (2010).
- [118] H. Shiraki, T. Saito, Y. Shimakawa, *Chem. Mater.* **20**, 7077 (2008).
- [119] M. Mizumaki, T. Saito, H. Shiraki, and Y. Shimakawa, *Inorg. Chem.* **48**, 3499 (2009).
- [120] T. Saito, T. Tohyama, P.M. Woodward, Y. Shimakawa, *Bull. Chem. Soc. Jpn.* **84**, 802 (2011).
- [121] T. Tohyama, T. Saito, M. Mizumaki, A. Agui, Y. Shimakawa, *Inorg. Chem.* **49**, 2492 (2010).
- [122] C. Martin, A. Maignan, D. Pelloquin, N. Nguyen, B. Raveau, *Appl. Phys. Lett.* **71**, 1421 (1997).
- [123] D. Akahoshi and Y. Ueda, *J. Phys. Soc. Jpn.* **68**, 736 (1999).

- [124] T. Vogt, P.M. Woodward, P. Karen, B.A. Hunter, P. Henning, A.R. Moodenbaugh, Phys. Rev. Lett. **84**, 2969 (2000).
- [125] M. Hervieu, C. Michel, A. Maignan, C. Martin, B. Raveau, J. Solid State Chem. **74**, 428 (1988).
- [126] S. Engelsberg, Physica C **176**, 451 (1991).
- [127] A. Gormezano, M. T. Weller, J. Mater. Chem. **3**, 771 (1993).
- [128] M. Hervieu, A. Maignan, C. Martin, C. Michel, J. Provost, B. Raveau, Modern Phys. Lett. B **2**, 1103 (1988).
- [129] M. J. Pack, A. Gormezano, M. T. Weller, Chem. Mater. **9**, 1547 (1997).
- [130] C. Q. Jin, High pressure research **24**, 399(2004).
- [131] G. Trolliard, N. Tenezee, Ph. Boullay, D. Mercurio, J. Solid. State. Chem. **177**, 1188 (2004).
- [132] R. Rawal, A. Feteira, N. C. Hyatt, D. C. Sinclair. , K. Sarma, and N. Mc N. Alford, J. Am. Ceram. Soc. **89**, 332 (2006).
- [133] L. Fanga, S. Mengb, H. Zhangb, Z. Liu, Mater. Lett. **60**, 1147 (2006).
- [134] R. Ratheesh, H. Sreemoolanathan, and M. T. Sebastian, J. Solid. State. Chem. **131**, 2 (1997);
H. Sreemoolanathan, M. T. Sebastian, and P. Mohanan, Mater. Res. Bull. **30**, 653 (1995);
C. Vineis, P. K. Davies, T. Negas, and S. Bell, Mater. Res. Bull. **31**, 431 (1996).
- [135] I. N. Jawahar, P. Mohanan, and M. T. Sebastian, Mater. Lett. **57**, 4043 (2003).
- [136] H. Zhang, L. Fang, R. Dronskowski, P. Mueller, and R. Z. Yuan, J. Solid. State. Chem. **177**, 4007 (2004).
- [137] C. Vineis, P. K. Davies, T. Negas, and S. Bell, Mater. Res. Bull. **31**, 431 (1996).

- [138] S. Kawaguchi, H. Ogawa, A. Kan, and S. Ishihara, *J. Eur. Ceram. Soc.* **26**, 2045 (2006).
- [139] R. Rawal, A. Feteira, N. C. Hyatt, A. R. West, D. C. Sinclair, K. Sarma, and N. McN. Alford, *J. Am. Ceram. Soc.* **89**, 336 (2006).
- [140] F. Galasso, L. Katz, *Acta. Crystallogr.* **14**, 647 (1961).
- [141] F. S. Galasso. *Structure and Properties of Inorganic Solids*. Pergamon Press, NY 1970
- [142] I. N. Jawahar, N. I. Santha, M. T. Sebastian, *J. Mater. Res.* **17**, 3084 (2002).
- [143] Y. Tohdo, K. Kakimoto, H. Ohsato, H. Yamada, T. Okawa, *J. Eur. Ceram. Soc.* **26**, 2039 (2006).
- [144] Z. Yue, F. Zhao, Z. Gui, L. Li, *J. Alloys. Compd.* **395**, 126 (2005).
- [145] J. Pei, Z. Yue, F. Zhao, Z. Gui, L. Li, *J. Alloys Compd.* **459**, 390 (2008).
- [146] D. D. Khalyavin, A. B. Lopes, A. M. R. Senos, P. Q. Mantas, *Chem. Mater.* **18**, 3843 (2006).
- [147] R. Rejini, M. T. Sebastian, *J. Am. Ceram. Soc.* **90**, 2472 (2007).
- [148] J. J. Bian, K. Y. Yan, J. Ji, *J. Eur. Ceram. Soc.* **26**, 1957 (2006).
- [149] J. J. Bian, H. B. Gao, X. W. Wang, *Mater. Res. Bull.* **39**, 2127 (2004).
- [150] M. Abe, K. Uchino, *Mater. Res. Bull.* **10**, 147 (1974).
- [151] K. Yoshii, *J. Solid State Chem.* **149**, 354 (2000).
- [152] D. G. Lim, B. H. Kim, T.-G. Kim, H. J. Jung, *Mater. Res. Bull.* **34**, 1577 (1999).
- [153] M. Kestigian, J. G. Dickinson, R. Waed, *J. Am. Chem. Soc.* **79**, 5598 (1957).
- [154] C. Bbisi, *Ricerca. Sei.* **24**, 1858 (1954).
- [155] G. H. Jonkeb, *Physica* **20**, 1118 (1954).

- [156] H. L. Yakel, Acta. Crystallogr. **8**, 394 (1955).
- [157] J. Guo, C. Dong, L. Yang, G. Fu, J. Solid State Chem. **178**, 58 (2005).
- [158] W. F. Dejong, Z. Krist. **81** , 314 (1932).
- [159] Y. Tomioka, T. Okuda, Y. Okimoto, R. Kumai, and K.-I. Kobayashi, Phys. Rev. B **61**, 422 (2000).
- [160] J.A. Alonso, M.T. Casais, M.J. Martinez-Lope, J.L. Martinez, P. Velasco, A. Muñoz and M.T. Fernández-Dañaz, Chem. Mater. **12**, 161 (2000).
- [161] C. Ritter, M.R. Ibarra, L. Morellon, J. Blasco, J. García, J.M. De Teresa, J. Phys.: Condens. Matter **12**, 8295 (2000).
- [162] B.-G. Kim, Y.-S. Hor and S.-W. Cheong, Appl. Phys. Lett. **79**, 388(2001).
- [163] A. Maignan, B. Raveau, C. Martin and M. Hervieu, J. Solid State Chem. **144**, 224 (1999).

Methodology

In this thesis, first-principle (*ab initio*) electronic structure calculations have been performed on the high performance computing platforms. The aim of *ab-initio* methods is to solve the time independent many body Schrödinger equation for the system under study, expressed as following

$$H\Psi = E\Psi \quad (2.1)$$

where Ψ is the many-body wave-function for the eigen-state E of the system. In the non-relativistic limit, for a system of N_p nuclei and N_e interacting electrons, *many-body* Hamiltonian H can be expressed as

$$\begin{aligned}
 H = & \sum_{i=1}^{N_e} -\frac{\hbar^2}{2m_e} \nabla_{\mathbf{r}_i}^2 + \sum_{I=1}^{N_p} -\frac{\hbar^2}{2M_I} \nabla_{\mathbf{R}_I}^2 \\
 & - \frac{1}{4\pi\epsilon_0} \sum_{i,I=1} \frac{Z_I e^2}{|\mathbf{R}_I - \mathbf{r}_i|} + \frac{1}{2} \frac{1}{4\pi\epsilon_0} \sum_{i>j} \frac{e^2}{|\mathbf{r}_i - \mathbf{r}_j|} \\
 & + \frac{1}{4\pi\epsilon_0} \sum_{I>J} \frac{Z_I Z_J e^2}{|\mathbf{R}_I - \mathbf{R}_J|}
 \end{aligned} \quad (2.2)$$

where m_e is the mass of an electron at r_i and M_I the mass of I^{th} ion at position R_I . Z is the atomic number of ion. Summation over i, j runs over electrons where as summation over I, J runs over nuclei of the system. First and second term in Eq. 2.2 represent the kinetic energy of electrons and ions respectively while third term stands for the electron-ion interaction and fourth term is the electron-electron Coulomb interaction with a factor 1/2 to prevent the double counting. Last term describes ion-ion interaction. Nuclei are much heavier than the electrons and they move much more slowly than electrons. Thus, on

the time scale of nuclei motion, electronic transition occurs instantaneously *ie.* nuclei are treated as fixed particles during electronic motions. Thus, the wave-functions of electrons depend on the ionic positions and not on its velocity. The decoupling of this ionic and electronic motion is described as *adiabatic* or *Born-Oppenheimer* approximation [1]. Simplified Hamiltonian after *Born-Oppenheimer* approximation, can be expressed as

$$H = \sum_{i=1}^{N_e} -\frac{\hbar^2}{2m_e} \nabla_{\mathbf{r}_i}^2 - \frac{1}{4\pi\epsilon_0} \sum_{i,I=1} \frac{Z_I e^2}{|\mathbf{R}_I - \mathbf{r}_i|} + \frac{1}{2} \frac{1}{4\pi\epsilon_0} \sum_{i>j} \frac{e^2}{|\mathbf{r}_i - \mathbf{r}_j|} . \quad (2.3)$$

The problem of solving for electronic wave-functions using Eq. 2.3 remains intractable because of too many electronic degrees of freedom. There exist two distinct ways of approximating the eigen-functions of Hamiltonian of Eq. 2.3, (*i*) wave-function based approach and (*ii*) density based approach.

2.1 Wave function based approach

First wave-function based formalism was proposed by Hartree in 1928 [2] where many body wave-function was expressed as a product of single electronic wave-functions $\Psi_i(\mathbf{r}_i)$ *ie:*

$$\Psi_H(\mathbf{r}_1, \mathbf{r}_2, \mathbf{r}_3 \cdots \mathbf{r}_{N_e}) = \Psi_1(\mathbf{r}_1) \Psi_2(\mathbf{r}_2) \Psi_3(\mathbf{r}_3) \cdots \Psi_{N_e}(\mathbf{r}_{N_e}) . \quad (2.4)$$

Here electron moving in a central potential due to other electrons and the nucleus *ie.* electron-electron interaction is treated in a *mean field* way neglecting the exchange and correlation property completely. The next level of improvement was introduced by Fock in 1930 [3] where $\Psi_H(\mathbf{r}_1, \mathbf{r}_2, \mathbf{r}_3 \cdots \mathbf{r}_{N_e})$ was expressed as a Slater determinant,

$$\Psi_{HF}(\mathbf{r}_1, \mathbf{r}_2 \cdots \mathbf{r}_{N_e}) = \frac{1}{\sqrt{N_e!}} \begin{vmatrix} \Psi_1(\mathbf{r}_1) & \Psi_1(\mathbf{r}_2) & \cdots & \Psi_1(\mathbf{r}_{N_e}) \\ \Psi_2(\mathbf{r}_1) & \Psi_2(\mathbf{r}_2) & \cdots & \Psi_2(\mathbf{r}_{N_e}) \\ \vdots & \vdots & \ddots & \vdots \\ \Psi_{N_e}(\mathbf{r}_1) & \Psi_{N_e}(\mathbf{r}_2) & \cdots & \Psi_{N_e}(\mathbf{r}_{N_e}) \end{vmatrix} . \quad (2.5)$$

Hartree-Fock approach is also known as *self consistent field* method and the *independent particle* method. Using variation principle the Hartree-Fock equation can be expressed as

$$\left[-\frac{\hbar^2}{2m_e} \nabla_{\mathbf{r}_i}^2 + V_{ion}(\mathbf{r}_i) + V^H(\mathbf{r}_i) + V^X \right] \Psi_i(\mathbf{r}_i) = \varepsilon_i \Psi_i(\mathbf{r}_i) \quad (2.6)$$

where Hartree potential,

$$V^H(\mathbf{r}_i) = e^2 \sum_i^{occ} \int \frac{\Psi_i(\mathbf{r}_i)^2}{|\mathbf{r}_i - \mathbf{r}_j|} d\mathbf{r}_i \quad (2.7)$$

and exchange potential,

$$V_i^H \Psi_i(\mathbf{r}_i) = - \sum_i^{occ} \Psi_j(\mathbf{r}_i) \int \Psi^*(\mathbf{r}_j) \frac{e^2}{|\mathbf{r}_i - \mathbf{r}_j|} \Psi_i(\mathbf{r}_j) d\mathbf{r}_j . \quad (2.8)$$

Hartree-Fock method assumes the wave-function can be written as one Slater determinant which is the basic limitation of this approach. Hartree-Fock total energy differs from the exact non-relativistic energy by an amount which is termed as *correlation* energy. Due to mean-field approximation in the self consistent field Hamiltonian, Hartree-Fock method sometimes yields large correlation energy. *Independent particle model* is an important consequence of the Hartree-Fock method which suggests that the electrons are moving in the average field of rest electrons, which is obviously an approximation. In reality the motion of electrons depend on the instantaneous positions of all other electrons.

2.2 Density based approach (Density Functional Theory)

Starting point of Density Functional Theory (DFT) is the Hohenberg-Kohn (HK) formalism which essentially states that stationary many body system can be characterized by the ground state electronic density [4]. HK formalism can be expressed in terms of two basic theorems:

Theorem 1. There is a one-to-one correspondence between the ground-state density $\rho(\mathbf{r})$ of a many electron system and the external potential V_{ext} .

Let us consider two distinct system with same number of electrons (N_e) characterized by external potential V_1^{ext} and V_2^{ext} . Many body wave-function for these two systems can be symbolized as Ψ_1 and Ψ_2 which produce same electronic density $\rho(\mathbf{r})$. Thus,

$$\begin{aligned}\rho(\mathbf{r}) &= N_e \int \Psi_1^*(\mathbf{r}_1, \mathbf{r}_2 \cdots \mathbf{r}_{N_e}) \Psi_1(\mathbf{r}_1, \mathbf{r}_2 \cdots \mathbf{r}_{N_e}) d\mathbf{r}_1 d\mathbf{r}_2 \cdots d\mathbf{r}_{N_e} \\ &= N_e \int \Psi_2^*(\mathbf{r}_1, \mathbf{r}_2 \cdots \mathbf{r}_{N_e}) \Psi_2(\mathbf{r}_1, \mathbf{r}_2 \cdots \mathbf{r}_{N_e}) d\mathbf{r}_1 d\mathbf{r}_2 \cdots d\mathbf{r}_{N_e} .\end{aligned}\quad (2.9)$$

Energy eigen-values can be expressed as :

$$\begin{aligned}E_1 &= \langle \Psi_1 | H_1 | \Psi_1 \rangle \\ &< \langle \Psi_2 | H_1 | \Psi_2 \rangle = \langle \Psi_2 | H_2 | \Psi_2 \rangle + \langle \Psi_1 | [H_1 - H_2] | \Psi_1 \rangle \\ &< E_2 + \int d\mathbf{r} \rho(\mathbf{r}) [V_1^{ext}(\mathbf{r}) - V_2^{ext}(\mathbf{r})] .\end{aligned}\quad (2.10)$$

Eq. 2.10 can also be written as

$$E_2 < E_1 - \int d\mathbf{r} \rho(\mathbf{r}) [V_1^{ext}(\mathbf{r}) - V_2^{ext}(\mathbf{r})] .\quad (2.11)$$

From Eq. 2.10 and 2.11, we can write, $[E_1 + E_2 < E_2 + E_1]$, which describes an unphysical conclusion. Thus, for a given $\rho(\mathbf{r})$, we can have only one value of $V^{ext}(\mathbf{r})$. Thus, for a fixed value of $V^{ext}(\mathbf{r})$, Hamiltonian and the many body wave-function are also fixed by the density. In conclusion, energy functional $E_{V^{ext}}[\rho]$ for a given external potential $V^{ext}(\mathbf{r})$ is a unique functional of density $\rho(\mathbf{r})$.

Theorem 2. Total energy of the system can be written as,

$$\begin{aligned}E_{V_{ext}}[\rho] &= \underbrace{\langle \Psi_1 | \hat{T} + \hat{V} | \Psi_1 \rangle}_{F_{HK}} + \langle \Psi_1 | \hat{V}_{ext} | \Psi_1 \rangle \\ &= F_{HK}[\rho] + \int \rho(\mathbf{r}) V_{ext}(\mathbf{r}) d\mathbf{r} .\end{aligned}\quad (2.12)$$

Here F_{HK} is the Hohenberg-Kohn density functional characterized by the electronic density $\rho(\mathbf{r})$. $E_{V_{ext}}[\rho]$ goes to its minimum value at the ground state for the ground state density $\rho(\mathbf{r})$ corresponding to the external potential V_{ext} . Although Hohenberg-Kohn concluded the dependency of the ground state energy on the density of the interacting electrons,

mathematical expression for the ground state energy was prescribed by Kohn-Sham in 1965 [5]. We may recall the starting from the Hohenberg-Kohn density functional in the following way:

$$\begin{aligned}
 F_{HK} &= T + V + T_0 - T_0 \\
 &= T_0 + V + \underbrace{T - T_0}_{V_C} \\
 &= T_0 + V_H + V_C + \underbrace{V - V_H}_{V_X} \\
 &= T_0 + V_H + \underbrace{V_C + V_X}_{E_{XC}} .
 \end{aligned} \tag{2.13}$$

Here T is the exact kinetic energy functional and T_0 is kinetic energy functional of a non-interacting electron gas. V is the exact electron-electron potential energy functional and V_H is the Hartree contribution. V_X represents the exchange contribution. Here E_{XC} is the exchange-correlation energy functional. We can rewrite the energy functional in the following way:

$$E_{V_{ext}}[\rho] = T_0[\rho] + V_H[\rho] + E_{XC}[\rho] + V_{ext}[\rho] . \tag{2.14}$$

Eq. 2.14 describes non-interacting classical electron gas, subject to potential of the nuclei and exchange and correlation effects. Corresponding Hamiltonian is called as Kohn-Sham Hamiltonian,

$$\begin{aligned}
 \widehat{H}_{KS} &= \widehat{T}_0 + \widehat{V}_H + \widehat{V}_{XC} + \widehat{V}_{ext} \\
 &= -\frac{\hbar^2}{2m_e} \nabla_i^2 + \frac{e^2}{4\pi\epsilon_0} \int \frac{\rho(\mathbf{r}')}{|\mathbf{r} - \mathbf{r}'|} d\mathbf{r}' + \widehat{V}_{XC} + \widehat{V}_{ext} ,
 \end{aligned} \tag{2.15}$$

where \widehat{V}_{XC} is the exchange-correlation functional,

$$\widehat{V}_{XC} = \frac{\delta E_{XC}[\rho]}{\delta \rho} . \tag{2.16}$$

Ground state according to Kohn-Sham approach can be described under the constrain, $\int \rho(\mathbf{r}) d\mathbf{r} = 1$ as,

$$\frac{\delta}{\delta \rho} \left[E_{KS}[\rho] - \lambda N \right] = 0 . \tag{2.17}$$

Here λ is Lagrange multiplier which can be simplified by using Eq. 2.14,

$$\frac{\delta T_0[\rho]}{\delta \rho(\mathbf{r})} + V_{KS}(\mathbf{r}) = \lambda , \quad (2.18)$$

where

$$V_{KS}(\mathbf{r}) = V_s(\mathbf{r}) + V_H(\mathbf{r}) + V_{XC}(\mathbf{r}) = V_s(\mathbf{r}) + \frac{e^2}{4\pi\epsilon_0} \int \frac{\rho(\mathbf{r}')}{|\mathbf{r} - \mathbf{r}'|} d\mathbf{r}' + \frac{\delta E_{XC}}{\delta \rho(\mathbf{r})} , \quad (2.19)$$

where V_s is external potential in the non-interacting frame. In this non-interacting platform, Schrödinger equation becomes:

$$\left[-\frac{\hbar^2}{2m_e} + V_{KS}(\mathbf{r}) \right] \Psi_i = \varepsilon_i \Psi_i , \quad (2.20)$$

where Ψ_i and ε_i are single particle wave-function and energy eigen-values respectively and $\rho(\mathbf{r}) = \sum_{i=1}^{N_e} \Psi_i^*(\mathbf{r}) \Psi_i(\mathbf{r})$. Although Kohn-Sham formalism is exact, solution of the Eq 2.20 is very complicated because of the term V_{XC} in V_{KS} (see Eq. 2.19) whose exact form is unknown quantity and a suitable approximation needs to be sought. Kohn-Sham equation is solved in a iterative manner. Starting from an initial guess of $\rho(\mathbf{r})$, V_{KS} is calculated and Eq. 2.20 is solved to construct the wave-function Ψ_i . This process is repeated until the density is converged.

2.3 Exchange-correlation functional

Simplest approximation to E_{XC} results from the *Local Density functional (LDA)* where exchange and correlation energy at every point in the system has the value that would be given by a homogeneous electron gas having same electron density $\rho(\mathbf{r})$ at that point. Exchange-correlation functional, under LDA scheme can be expressed as,

$$E_{XC}^{LDA}(\rho(\mathbf{r})) = \int \rho(\mathbf{r}) \varepsilon_{xc}(\rho(\mathbf{r})) d\mathbf{r} . \quad (2.21)$$

Within such 'local' approach, exchange and correlation terms can be separated,

$$\varepsilon_{xc}(\rho) = \varepsilon_x(\rho) + \varepsilon_c(\rho) . \quad (2.22)$$

Using correlation energy functional for a free electron gas $\varepsilon_c(\rho)$, explicit form of exchange energy functional can be written as [6, 7],

$$\varepsilon_x = -\frac{3e^2}{4} \left(\frac{3}{\pi}\right)^{1/3} \rho(\mathbf{r})^{1/3} . \quad (2.23)$$

Next step of modification includes both electron density $\rho(\mathbf{r})$ and its gradient $\nabla\rho$ and it is termed as *Generalized Gradient Approximations (GGA)* [8]. Exchange-correlation functional under GGA can be expressed as,

$$E_{XC}^{GGA}(\rho(\mathbf{r}), \nabla\rho(\mathbf{r})) = \int f(\rho(\mathbf{r}), \nabla\rho(\mathbf{r})) d\mathbf{r} . \quad (2.24)$$

Most of the GGA based calculations present in this thesis are performed by using *PBE* functional which was prescribed by Perdew, Burke and Ernzerhof in 1996 [9]. Nowadays more accurate functionals are designed to promote the electronic properties towards the experiments. B3LYP (Becke, three-parameter, Lee-Yang-Parr) and HSE (Heyd-Scuseria-Ernzerhof) are some examples of such hybrid functional [10].

2.4 Basis set

2.4.1 MTO basis set: LMTO, NMTO

Generation of smaller basis set of the accurate molecular orbitals is a serious challenge for the theoreticians. These basis sets help us to express the many body wave-function as a linear combinations of some fixed basis functions like plane waves, partial waves used in cellular, APW, KKR methods. Fixed (energy independent) basis set like plane wave, linear combination of atomic orbitals (LCAO) use a set of linear eigen-value equations given by,

$$(H - \varepsilon O) \cdot \mathbf{b} = 0 . \quad (2.25)$$

Here eigen-values ε are determined in terms of Hamiltonian H , overlap matrix O and expansion coefficient \mathbf{b} . On the other hand, methods of partial waves as in APW, KKR result a set of equation of the form,

$$M(\varepsilon).\mathbf{b} = 0 . \quad (2.26)$$

Eq. 2.25 is a polynomial in ε while secular equation 2.26 has complicated non-linear energy dependence. Although partial wave based methods are quite complicated, they provide some advantages during *ab-initio* electronic structure calculations in terms of accuracy and use of minimal basis set. Within the muffin-tin approximation, such partial wave method provides solution of arbitrary accuracy for close packed systems. On the other hand, it can be seen from Eq. 2.26 that M is a function of ε . So, it becomes necessary to look for the solution of ε_i individually by tracking the roots of the determinant M . Andersen linearized such fixed basis set by using a fixed basis set using a muffin-tin like potential by considering partial waves and their first energy derivatives [11–13]. For these sets of linearized fixed basis sets one needs to solve Eq. 2.25 rather than Eq. 2.26. Linear method combines the basic features of fixed basis and partial wave methods. In LMTO, energy dependent basis set $\chi_{RL}(\mathbf{r})$ is derived from the energy dependent partial waves in the forms of muffin-tin orbitals (*MTOs*). Due to the localize nature of the basis function, first-principle tight-binding method (*TB-LMTO*) is useful during the *self consistent* calculations of electronic structure for the real space construction of model Hamiltonian. TB-LMTO is based on with muffin-tin approximation of the crystal potential which divides the space into atom-centered muffin-tin spheres and the interstitial. Solution of the Schrödinger equation in the spherically symmetric muffin-tin sphere is partial wave while the solution in the interstitial is plane waves which can be expanded in terms of spherical Neumann and Bessel functions. Two stage solution are than joined at the muffin-tin boundary which form the basis function. Finally, linearization of the basis function gives rise to energy dependent LMTO basis sets. In a step towards simplification, these muffin-tin spheres are replaced by space-filling atomic spheres using the atomic-sphere-approximation (*ASA*) [12]. These sets of space-filling atomic spheres are also termed as Wigner-Sitz (*WS*) spheres. Within the *ASA*, crystal Hamiltonian can be divided into two independent parts. First part contains

the structure matrix which depends only on the crystal structure and atomic positions and not on the types of atoms occupying the sites. Second part requires the information about the solution of Schrödinger equation inside each in-equivalent WS spheres with proper boundary conditions. This part depends on the potential parameters for each site. *LMTO* basis functions within the *ASA* have the following form,

$$\chi_{RL}^{\alpha}(\mathbf{r}_R) = \phi_{RL}(\mathbf{r}_R) + \sum_{R'L'} \dot{\phi}_{R'L'}^{\alpha}(\mathbf{r}_{R'}) h_{R'L',RL}^{\alpha} . \quad (2.27)$$

Here L stands for collective *angular-momentum* index (lm). Atomic sites are generated by the position vector \mathbf{R} with $\mathbf{r}_R = \mathbf{r} - \mathbf{R}$. ϕ is a product of a spherical harmonic and solution $\phi_{\nu RL}(|\mathbf{r}_R|)$ to the radial Schrödinger equation *ie.* partial waves inside the sphere centered at \mathbf{R} with energy $\varepsilon_{\nu RL}$ which is the energy of linearization. The functions $\dot{\phi}^{\alpha}$ are linear combination of ϕ and their first energy derivative, $\dot{\phi}$. Label α depends on the actual choice of how the linear combination is performed. Inside the sphere, solution ϕ is normalized while in the interstitial region, ϕ and $\dot{\phi}$ are chosen to be *orthonormal*. Matrix elements of h^{α} can be expressed as,

$$h^{\alpha} = C^{\alpha} - \varepsilon_{\nu} + (\Delta^{\alpha})^{1/2} S^{\alpha} (\Delta^{\alpha})^{1/2} . \quad (2.28)$$

Here C^{α} and Δ^{α} are represented as the diagonal potential matrices which depend on the potential inside the sphere, representation of α and the sphere radius. *Band Centre* parameter C^{α} can be expressed as

$$C^{\alpha} = \varepsilon_{\nu} - \frac{P^{\alpha}(\varepsilon_{\nu})}{\dot{P}^{\alpha}(\varepsilon_{\nu})} . \quad (2.29)$$

Band width parameter Δ^{α} can be represented as

$$\sqrt{\Delta^{\alpha}} = \frac{1}{\dot{P}^{\alpha}(\varepsilon_{\nu})} . \quad (2.30)$$

For a chosen representation α , $P^{\alpha}(\varepsilon_{\nu})$ and $\dot{P}^{\alpha}(\varepsilon_{\nu})$ are the potential function and its energy derivative. Potential function $P^{\alpha}(\varepsilon_{\nu})$ and the representation α are connected by

the logarithmic derivative D_l of the partial wave at the WS sphere boundary,

$$\left\{ P^\alpha(\varepsilon) \right\}^{-1} = \left\{ 2(2l+1) \frac{D_l + l + 1}{D_l(\varepsilon) - 1} \right\} - \alpha . \quad (2.31)$$

Structure matrix S^α depends on the representation and geometrical arrangements of the atomic sites which can be represented in terms of a *canonical* structure constant S^0 ,

$$S^\alpha = S^0(1 - \alpha S^0)^{-1} . \quad (2.32)$$

All such α dependent representation span the same Hilbert space where there exist an exact transformation from one representation to another. Two such representations are γ -representation and the tight binding (TB) representation, β . Due to orthogonality of the basis function, γ -representation can be used to construct the sp^3 hybrid orbitals while in the TB representation, basis functions become very localize. The γ -representation of Hamiltonian correct to second order in energy ($\varepsilon - \varepsilon_\nu$) can be expressed as,

$$H^{(2)} = \varepsilon_\nu + h^\gamma = C^\gamma + (\Delta^\gamma)^{1/2} S^\gamma (\Delta^\gamma)^{1/2} . \quad (2.33)$$

Here ε_ν is the diagonal matrix that contains the linearization energy. Overlap matrix in this γ -representation is a unit diagonal matrix. This representation is also termed as *orthogonal* representation. Transformation from γ to β -representation includes a scaling of potential parameters C , δ of the real space structure constant S^β [13],

$$\beta = \left\{ \begin{array}{ll} 0.3485 & l = 0 \quad (s) \\ 0.05303 & l = 1 \quad (p) \\ 0.010714 & l = 2 \quad (d) \end{array} \right\} . \quad (2.34)$$

Screened structure constants are noticed to be more localized with exponential decay in distance d measured in terms of WS radius W ,

$$S_{l'm}^\beta = A.exp \left[-\lambda_{l'm}^\beta d/w \right] . \quad (2.35)$$

In this representation, TB basis functions become extremely localized only to the nearest neighbor cell. During *self consistency*, it is necessary to go beyond the *ASA* to attend the desired level of accuracy. This can be done by including the *combined correction* which modifies the Hamiltonian in the following way,

$$\begin{aligned} H^{(2)} &= \varepsilon + h^\gamma - (\kappa_\nu^2 + V_0) \partial_{\kappa^2} h^\gamma \\ &= C^\gamma + (\Delta^\gamma)^{1/2} S^\gamma (\Delta^\gamma)^{1/2} - (\kappa_\nu^2 + V_0) \partial_{\kappa^2} h^\gamma, \end{aligned} \quad (2.36)$$

where $\varepsilon = \kappa^2 + V_0$. For open structures, in addition to the atomic spheres, empty spheres are also used to fill up the space.

Although *LMTO* method is highly successful for first-principle *self consistent* electronic structure calculations, essential disadvantages of this method are listed below:

- (i) Inside the sphere the basis is complete to $(\varepsilon - \varepsilon_\nu)$ (1^{st} order) while it is complete to $(\varepsilon - \varepsilon_\nu)^0$ (0^{th} order) in the interstitial region.
- (ii) The non-*ASA* correction like *combined* correction included in the Hamiltonian and overlap matrix, make the formalism computationally heavy and basis function increase for the multi-panel calculation.
- (iii) The expansion of the Hamiltonian H in the orthogonal representation as a power series of two centered tight-binding Hamiltonian h ,

$$\langle \vec{\chi} | (H - \varepsilon_\nu) | \vec{\chi} \rangle = h + hoh + \dots \quad (2.37)$$

is obtained only in *ASA* and excluding *downfolding*. In a step towards an energetically more accurate basis set based on the *MTO* formalism N th order *MTO* basis was introduced which is also free from the disadvantages of *LMTO*. Basis features of the N th order *MTO* basis are:

- (i) It is still muffin-tin potential.
- (ii) Still partial waves ϕ s are used within the atomic sphere.
- (iii) In the interstitial region, instead of Neumann function, N th order *MTO* basis includes screened spherical waves (*SSWs*).
- (iv) Out of partial waves and *SSWs*, N th order *MTO* basis shows *kinked* partial waves (*KPWs*).

(v) Energy-dependent *NMTO* basis is formed by the superposition of *KPW*s evaluated at $(N + 1)$ energy points.

In general, members $R'L'$ of *NMTO* basis sets for a energy mesh $\varepsilon_0, \varepsilon_1 \cdots \varepsilon_N$ are constructed by the superposition,

$$\chi_{R'L'}^N(\mathbf{r}) = \sum_{n=0}^N \sum_{RL \in A} \phi_{RL}(\varepsilon_n, \mathbf{r}) L_{nRL, R'L'}^{(n)} \quad (2.38)$$

of a *kinked* partial waves, $\phi_{RL}(\varepsilon, \mathbf{r})$ at the $(N + 1)$ points which is expressed by the label n of the chosen energy mesh. This expression is the energy quantized form of *Lagrange* interpolation,

$$\chi^N(\varepsilon) \approx \sum_{n=0}^N \phi(\varepsilon_n) l_n^{(N)}(\varepsilon), \quad l_n^{(N)}(\varepsilon) \equiv \prod_{m=0, \neq n}^N \frac{\varepsilon - \varepsilon_m}{\varepsilon_n - \varepsilon_m} \quad (2.39)$$

of a function of energy, $\phi(\varepsilon)$ by N th degree polynomial $\chi^N(\varepsilon)$: The N th degree polynomial $l_n^{(N)}(\varepsilon)$ can be expressed in terms of a matrix $L_{nRL, R'L'}^{(N)}$, the function of energy $\phi(\varepsilon)$, by a Hilbert space with axis $\phi_{RL}(\varepsilon, \mathbf{r})$ and interpolating polynomial $\chi^N(\varepsilon)$ by a Hilbert space with axis $\chi_{R'L'}^{(N)}(\mathbf{r})$.

A *kinked partial wave* is basically a partial wave with a '*kink*' at a central part and tail joined continuously to it. Tail of *kinked partial wave* is called as *screened spherical wave*, $\Psi_{RL}(\varepsilon, \mathbf{r})$, which is the solution in the interstitial region between two *hard spheres* $\Delta\Psi(\varepsilon, \mathbf{r}) = \varepsilon(\varepsilon, \mathbf{r})$ with the boundary condition that $\Psi_{RL}(\varepsilon, \mathbf{r})$ goes to $Y_L(\hat{\mathbf{r}}_R)$ at the central hard sphere, irrespective of energy and to zero (with a *kink*) at all over *hard sphere*. Lagrange coefficient $L_n^{(N)}$, Hamiltonian and the overlap matrices in the *NMTO* basis are expressed in terms of the *KKR* resolvent, $k(\varepsilon)^{-1}$ and its first energy derivative at the energy mesh $\varepsilon_0, \varepsilon_1 \cdots \varepsilon_N$.

Such accurate and compact formalism can form energy-selective and localize *NMTO* basis in terms of a few basis function as suggested by the *downfolding* technique. *Downfolding* mechanism is an energy selective procedure which picks up "few" bands of interest out of the complete band structure by integrating out degrees of freedom which are not of interest. Accuracy of such few band approach depends on N , number of energy points used in the *NMTO* calculation. For isolated downfolded bands, *NMTO* sets spans

the Hilbert space of *Wannier* function and *orthonormal NMTO* construct the Wannier functions. In addition to this, real space representation of the *downfolded* Hamiltonian, in the *NMTO* basis provides the *hopping* matrix elements.

2.4.2 Pseudopotential Method

The basis of this method is the simple observation that only the valence electrons participate in the response of crystal to the perturbation. Unless the perturbation is comparable to the binding energy of the core states, tightly bound core states remain unaffected. Thus it is reasonable to assume that core electrons are *frozen* under perturbation which is the fundamental concept behind the *pseudopotential* [14]. Initially *pseudopotential* concept was originated with the *orthogonalized plane wave* method [15] where the valence wave-function are expanded using plane wave basis that are *orthogonal* to the low lying core states, φ_c ,

$$\phi_{opw}(\mathbf{k} + \mathbf{G}) = \phi_{pw}(\mathbf{k} + \mathbf{G}) - \sum_{\alpha,c} \langle \varphi_c | \phi_{pw}(\mathbf{k} + \mathbf{G}) \rangle \varphi_{\alpha,c} . \quad (2.40)$$

Here ϕ_{pw} is plane wave and ϕ_{opw} is corresponding OPW. Sum is performed on the core state and the atomic sites. Now, consider H be the Hamiltonian with core and valence wave-functions, φ_c and φ_v respectively. Pseudopotential, at this particular stage can be expressed as,

$$\varphi_v^{ps} = \varphi_v + \sum_{\alpha,c} a_{vc} \varphi_{\alpha,c} \quad (2.41)$$

with $a_{vc} = \langle \varphi_{\alpha,c} | \varphi_v^{ps} \rangle$. Considering Schrödinger equation, we obtain,

$$\begin{aligned} H|\varphi_v^{ps}\rangle &= \varepsilon_v |\varphi_v\rangle + \sum_{\alpha,c} a_{vc} \varepsilon_c |\varphi_{\alpha,c}\rangle \\ &= \varepsilon_v |\varphi_v^{ps}\rangle + \sum_{\alpha,c} a_{vc} (\varepsilon_{\alpha,c} - \varepsilon_v) |\varphi_{\alpha,c}\rangle . \end{aligned} \quad (2.42)$$

Here $\varepsilon_{\alpha,c}$ and ε_v are the core and valence state eigen-values respectively. Using expression of a_{vc} , it is possible to simplify Eq. 2.42,

$$\left[H + \sum_{\alpha,c} (\varepsilon_v - \varepsilon_{\alpha,c}) |\varphi_{\alpha,c}\rangle \langle \varphi_{\alpha,c}| \right] \varphi_v^{ps} = \varepsilon_v^{ps} \varphi_v^{ps} . \quad (2.43)$$

Thus, the pseudo states satisfying the Schrödinger like equation includes an additional potential term V^R to the Hamiltonian,

$$V^R = \sum_{\alpha,c} (\varepsilon_v - \varepsilon_{\alpha,c}) |\varphi_{\alpha,c}\rangle \langle \varphi_{\alpha,c}| . \quad (2.44)$$

It can be noted that V^R is energy dependent through $\varepsilon_{v/\alpha,c}$ which is the basis difference between conventional potential and pseudopotential. Adding V^R to the initial potential term results the Phillips-Kleinman pseudopotential [16], V^{PK} ,

$$V^{PK} = V + V^R . \quad (2.45)$$

Outside the core region, as the core wave-function vanish, V^{PK} becomes equal to V . Thus, there exists a radius, r_c around an atom beyond which the contribution of that atom to V^R becomes negligible. Pseudopotential construction is a *linear* scheme as there is a separate and additive contribution from each atomic site α . In addition to this, the pseudopotential is generally much weaker than the original potential because of the additive repulsive (positive) contribution coming from the core region. After Phillips-Kleinman's approach, a lot of efforts were put together to achieve the following goals:

The pseudopotential should be as *soft* as possible *ie.* it should allow expansion of the valance pseudo wave-function using as few plane-waves as possible. Construction of pseudopotential depends on the choice of an reference atomic configuration which is also an indirect statement of the *cutoff* radius r_c . Thus, it can be different for different l -channels. Nodeless pseudopotential must have to reproduce the *all* electron wave-function beyond the cutoff radius, eigen-values corresponding to the pseudo wave-function must be equal to those of all electron solution. In other words, pseudo charge density (charge density obtained from the pseudo wave-function) should reproduce the valance charge density as accurately as possible. In addition to this changes in the core states due to changes in the structural environment (atomic configuration)* should be as negligible as possible *ie.* pseudopotentials are assumed to be *transferable*.

The concept of *norm-conservation* [17, 18] represented an improvement regarding

*For example, pseudopotential of manganese in MnO_4 and MnO_6 network should be invariant.

these criteria. *Norm-conserving* pseudopotentials are so designed that the pseudo wave-function (and potential) become equal to the actual wave-function (and potential) outside some core radius r_c . Inside r_c , pseudo wave-functions deviate from the actual wave-function but the *norm* remains to be the same, *ie.*

$$\int_0^{r_c} dr r^2 \varphi^{PS*}(r) \varphi^{PS}(r) = \int_0^{r_c} dr r^2 \varphi^*(r) \varphi(r) . \quad (2.46)$$

Here wave-functions are referred to the atomic states with spherical symmetry. In addition to this, *norm-conservation* ensures two basic criteria of *all* electronic and pseudo wave-function, φ, φ^{PS} ,

$$\frac{1}{\varphi^{PS}(r_c, E)} \frac{d\varphi^{PS}(r_c, E)}{dr} = \frac{1}{\varphi(r_c, E)} \frac{d\varphi(r_c, E)}{dr} \quad (2.47)$$

for a reference atomic eigen-value, E and this defines an energy range over which this transferability criteria holds adequately which was concluded from the Green's function analysis of Shaw and Harrison [19],

$$-\frac{\partial}{\partial E} \frac{\partial}{\partial r} \ln \varphi(r_c, E) = \frac{1}{r_c^2 \varphi^*(r_c, E) \varphi(r_c, E)} \int_0^{r_c} dr r^2 \varphi^*(r, E) \varphi(r, E) . \quad (2.48)$$

As the wave-function and eigen-value depend on the angular momentum, l , pseudopotential should also be l dependent. Pseudopotential of this type is termed as *semi-local*. *Soft-core, semi-local norm-conserving* pseudo potential for all the elements in the periodic table were developed by Hamann [20] and Bachelet *et al* [21]. Basic of such pseudo potential generation is as follows:

(i). For a particular reference configuration, single atomic electronic properties are calculated using sphericalized atomic program [22]. (ii). Core radius, $r_{c,l}$ are defined for each l . Small values of $r_{c,l}$ result in *hard*[†] but transferable potential. Larger $r_{c,l}$ gives rise to *softer* but less transferable pseudopotential. This leads to *non-local* *ie.* l -dependent model pseudopotential V_{NL} . This non-locality appears only in angular coordinates while it

[†]Too many plane waves are required to represent the pseudo wave-function.

becomes local in radial space (V_l). Thus, semi-local pseudopotential can be expressed as,

$$V_{SL} = \sum_{lm} |Y_{lm}\rangle V_{NL}(r) \langle Y_{lm}| . \quad (2.49)$$

This non-local part is further improved by Kleinman-Bylander transformation [23],

$$V_{NL} = \sum_l V_l^{NL} = \sum_{lm} \frac{|V_l^{SL} \phi_{lm}^{PS}\rangle \langle \phi_{lm}^{ps} V_l^{SL}|}{\langle \phi_{lm}^{PS} | V_l | \phi_{lm}^{PS} \rangle} \quad (2.50)$$

where,

$$V_l^{NL} | \phi_{lm}^{PS} \rangle = \frac{|V_l^{SL} \phi_{lm}^{PS}\rangle \langle \phi_{lm}^{PS} | V_l^{SL} | \phi_{lm}^{PS} \rangle}{\langle \phi_{lm}^{PS} | V_l^{SL} | \phi_{lm}^{PS} \rangle} = V_l^{SL} | \phi_{lm}^{PS} \rangle . \quad (2.51)$$

Vanderbilt and co-workers proposed *ultrasoft* pseudopotential where the pseudo wave-functions are required to be equal to the all electron wave function outside r_c as a consequence of *norm* conservation, but inside r_c pseudo wave-functions are allowed to be as *soft* as possible violating this *norm* conservation criteria [24–26]. Large values of r_c with less plane-wave cutoff (small number of plane waves) can be used in this scheme. Inside r_c , all electron wave-function and pseudo wave-function have different *norm*, while they have same *norm* in the interstitial region, suggesting they are not normalized. In addition to this, pseudo charge density can not be obtained from the computation of $\sum \varphi^* \varphi$ as for *norm* conserving pseudopotential. An augmented term is needed to be added in the core region.

2.4.3 Augmented Plane Wave + local orbital method

Linearized Augmented Plane Wave (*LAPW*) method is a modification of the augmented plane wave (*APW*) method prescribed by Slater [27, 28]. Basic motivation behind *APW* is following:

In *APW* method, the unit cell is portioned into non-overlapping atomic spheres centered around each atomic site and the interstitial region. Near an atomic nucleus the potential and wave-function are similar to an atomic like while in the interstitial region both wave-function and potential are smoother. Atom centered spheres satisfies the radial solution of Schrödinger equation while plane wave is valid in the remaining interstitial region. Radial

solution are *orthogonal* to any eigen-states of the same Hamiltonian which vanishes at the sphere boundary [12, 14],

$$\varphi(\mathbf{r}) = \begin{cases} \frac{1}{\sqrt{\Omega}} \sum_G c_G e^{i(\mathbf{G}+\mathbf{k})\cdot\mathbf{r}} & \mathbf{r} \in I \\ \sum_{lm} A_{lm} u_l(r) Y_{lm}(\hat{\mathbf{r}}) & \mathbf{r} \in S . \end{cases} \quad (2.52)$$

Here φ is a wave-function and Ω is the cell volume and u_l satisfies the following radial equation,

$$\left[-\frac{d^2}{dr^2} + \frac{l(l+1)}{r^2} + V(r) - E_l \right] r u_l(r) = 0 . \quad (2.53)$$

Here c_G and A_{lm} are expansion coefficient, V is spherical component of the potential in the sphere. Equations are expressed in Rydberg unit. Slater pointed out that the plane waves are the solution of Schrödinger equation at constant potential while radial functions are the solution in a spherical potential, provided that E_l becomes an eigen-value. In *APW* method, the continuous property of the wave-function at the sphere boundary is achieved by defining the coefficient A_{lm} in terms of c_G through spherical harmonic expansion of the plane waves. Coefficient for each (l,m) are matched at the sphere boundary which solely depends on the plane wave coefficients c_G and the energy parameter E_l . Several modification of the *APW* method are done by Bross *et al.* [29, 30], Koelling [31], Andersen [12].

linearization: In *LAPW* method, the basis inside the sphere are linear combination of the radial functions $u_l(r) Y_{lm}(\hat{\mathbf{r}})$ and their derivatives with respect to linearization parameter E_l . u_l is defined in the very similar way as in *APW* method. Energy derivatives $\dot{u}_l(r) Y_{lm}(\hat{\mathbf{r}})$ satisfies,

$$\left[-\frac{d^2}{dr^2} + \frac{l(l+1)}{r^2} + V(r) - E_l \right] r \dot{u}_l(r) = r u_l(r) . \quad (2.54)$$

These functions are matched to the values and their derivatives at the sphere boundary.

Plane waves augmented in this way are the *LAPW* basis functions,

$$\varphi(\mathbf{r}) = \begin{cases} \frac{1}{\sqrt{\Omega}} \sum_G c_G e^{i(\mathbf{G}+\mathbf{k})\cdot\mathbf{r}} & \mathbf{r} \in I \\ \sum_{lm} [A_{lm} u_l(r) + B_{lm} \dot{u}_l(r) Y_{lm}(\hat{\mathbf{r}})] & \mathbf{r} \in S . \end{cases} \quad (2.55)$$

Here B_{lm} are coefficient for the energy derivative similar to A_{lm} . *LAPWs* are plane waves in the interstitial (*I*) as for the *APWs* while inside the sphere (*S*) *LAPWs* have more variational freedom than *APWs*. For a small variation in E_l from the band energy ε , a linear combination will construct the *APW* radial function at the band energy,

$$u_l(\varepsilon, r) = u_l(E_l, r) + (\varepsilon - E_l) \dot{u}_l(\varepsilon, r) + \mathcal{O}((\varepsilon - E_l)^2) \quad (2.56)$$

where $\mathcal{O}((\varepsilon - E_l)^2)$ denotes the error which is quadratic in this energy differences.

For a converged plane wave set, *APW* method within *muffin-tin* potential reproduces the correct wave function while *LAPW* basis introduces an error of order $((\varepsilon - E_l)^2)$ in the wave-function which yields an error of order $((\varepsilon - E_l)^4)$ in the band energy. Due to this higher order error, *LAPWs* form a reliable basis set over relatively larger energy range. In *LAPW* method, accurate band energy for a given \mathbf{k} point are obtained with a single diagonalization while *APW* method requires for each bands.

Takeda and Kubler proposed a generalization of the *LAPW* method where N radial functions (each with its own energy parameter E_{li}) are matched to the values and $(N+1)$ energy derivatives of the interstitial plane waves [32]. In this approach, radial errors due to linearization can be removed. *LAPW+lo* expansion consider higher level semi-core states together with the valance state in one *LAPW* calculation instead of two (two energy windows for valance and core states). But matching of higher order derivatives makes the calculation more slowly convergent with respect to the plane wave cutoff than the standard *LAPW* method. Thus, this approach is highly restricted. Singh modified this approach to avoid the matching of higher order derivatives [33]. In this approaches, specially constructed *local* orbitals are added to the basis to perform the relaxation of the linearization without an increase of the plane wave cutoff. This method of construction of *local* orbitals is known as *APW+lo*, was implemented by Sjöstedt *et al.* and proved to be

strongly effective in reduction of the basis set size [34]. In $APW+lo$ implementation, it is possible for augmentation different atoms and angular momentum channels separately. Reduction in Basis set or the plane wave cutoff by the use of $APW+lo$ augmentation results in a great savings in computational cost for the calculation.

Augmenting functions $u_l Y_{lm}$ and $\dot{u}_l Y_{lm}$ are orthogonal to any core states. Local orbital extension in $APW+lo$ takes the form:

$$\chi(\mathbf{r}, \mathbf{k}) = \begin{cases} 0 & \mathbf{r} \in I \\ R_L^{lo}(r) Y_L(\hat{\mathbf{r}}) & \mathbf{r} \in MT \end{cases} . \quad (2.57)$$

Here $R_L^{lo}(r) = a_L^{lo} u_l(r, E_l) + b_L^{lo} \dot{u}_l(r, E_l)$. a_L^{lo} and b_L^{lo} are connected from the fact that χ_L^{lo} should vanish at the muffin-tin (MT) boundary. This new basis functions are referred to as $APW+lo$ will differ in some aspects from the standard $LAPW$ basis function within the MT region. $APW+lo$ basis function has no restriction on their derivatives at the MT boundary which is a difference between $APW+lo$ and standard $LAPW$ basis function. This lo scheme avoids the problem of non-orthogonality that appears in the calculation in which semi-core states are either *frozen* or treated in a separate energy window. During *full potential LAPW (FPLAPW)* calculation, potential and charge density are expanded (i) into lattice harmonics inside each atomic sphere and (ii) as a Fourier series in the interstitial region,

$$V(\mathbf{r}) = \begin{cases} \sum_{lm} V_{lm}(r) Y_{lm}(\hat{\mathbf{r}}) & \mathbf{r} \in MT \\ \sum_{\mathbf{k}} V_{\mathbf{k}} \exp(i\mathbf{k} \cdot \mathbf{r}) & \mathbf{r} \in I , \end{cases} \quad (2.58)$$

where \mathbf{k} stands for the wave vector corresponding to the plane waves. During lattice harmonic expansion in Eq. 2.58, a *local* coordinate system for each atomic sphere is defined depending on the point symmetry of the corresponding atom. This specifies a rotation matrix which relates the *local* and *global* coordinate system of the unit cell. Thus, during computation, smaller l, m values are required for this harmonic expansion which accelerates the speed of the calculation.

2.4.4 Projector Augmented Wave Method

The PAW method is an extension of the APW method and pseudopotential approach that combines both of them into a unified electronic structure method. The main feature of the PAW method is a transformation of the *true* wave-functions with their complete nodal structure onto an *auxiliary wavefunction* which have a rapidly convergent plane wave expansion.

Let us consider $|\Psi_n\rangle$ as one particle wave-function and $|\tilde{\Psi}_n\rangle$ as the corresponding auxiliary wave-function with n as the label for a one particle state which also includes one band index, a k -index and a spin-index. The transformation from the auxiliary wave function to the true physical wave-function is represented as \mathcal{T} [35]:

$$|\Psi_n\rangle = \mathcal{T} |\tilde{\Psi}_n\rangle . \quad (2.59)$$

Variational principle calculations results:

$$\mathcal{T}^\dagger H \mathcal{T} |\tilde{\Psi}_n\rangle = \mathcal{T}^\dagger \mathcal{T} |\tilde{\Psi}_n\rangle \epsilon_n \quad (2.60)$$

a Schrödinger like equation with new Hamiltonian $\tilde{H} = \mathcal{T}^\dagger H \mathcal{T}$ and an overlap operator $\tilde{O} = \mathcal{T}^\dagger \mathcal{T}$ also appear in the equation. Expectation value of an operator A can be determined in terms of either the true wave-function or the auxiliary wave-function,

$$\langle A \rangle = \sum_n f_n \langle \Psi_n | A | \Psi_n \rangle = \sum_n f_n \langle \tilde{\Psi}_n | \mathcal{T}^\dagger A \mathcal{T} | \tilde{\Psi}_n \rangle . \quad (2.61)$$

In the auxiliary wave representation, we have to consider transformed operator $\tilde{A} = \mathcal{T}^\dagger A \mathcal{T}$. This equation is valid only for valance electrons. In the original paper of Blöchl [36], these auxiliary wave-functions are termed as *pseudo wavefunctions* while true physical waves are termed as *all electron wavefunctions*.

In order to reproduce the better nodal structure of the smooth auxiliary wave-function in each atomic region, transformation \mathcal{T} is expressed as sum of identity and atomic contributions S_R :

$$\mathcal{T} = 1 + \sum_R S_R . \quad (2.62)$$

For each atomic sites, S_R adds the differences between the true and auxiliary wave-functions. These local terms S_R are expressed in terms of solution of Schrödinger equation for an isolated atom $|\phi_i\rangle$. Near the nucleus, set of partial waves $|\phi_i\rangle$ will serve as a basis set while the valence wave functions can be expressed as a superposition of the partial waves:

$$\Psi(\mathbf{r}) = \sum_{i \in R} \phi_i(\mathbf{r}) c_i \quad \text{for } |\mathbf{r} - \mathbf{R}_R| < r_{c,R}, \quad (2.63)$$

where we consider only those partial waves that belong to site R ($i \in R$). Core state are treated under the *frozen-core approximation*. Transformation \mathcal{T} will produce wave functions those are orthogonal to the core electronic states. Thus $|\psi_i\rangle$ are the set of atomic partial waves that includes only valence states and are orthogonal to the core wave-functions of the atom. Each partial waves are defined in terms of auxiliary partial waves:

$$\begin{aligned} |\phi_i\rangle &= (1 + S_R) |\tilde{\phi}_i\rangle \quad \text{for } i \in R \\ S_R |\tilde{\phi}_i\rangle &= |\phi_i\rangle - |\tilde{\phi}_i\rangle. \end{aligned} \quad (2.64)$$

Partial waves $|\phi_i\rangle$ and their auxiliary parts $|\tilde{\phi}_i\rangle$ become identical beyond a certain radius $r_{c,R}$:

$$\phi(\mathbf{r}) = \tilde{\phi}_i(\mathbf{r}) \quad \text{for } i \in R \text{ and } |\mathbf{r} - \mathbf{R}_R| > r_{c,R}. \quad (2.65)$$

Before applying the transformation operator to an auxiliary wave-function, it is necessary to expand the auxiliary wave-functions locally into auxiliary partial waves:

$$\tilde{\Psi}(\mathbf{r}) = \sum_{i \in R} \tilde{\phi}_i(\mathbf{r}) c_i = \sum_{i \in R} \tilde{\phi}_i(\mathbf{r}) \langle \tilde{p} | \tilde{\Psi} \rangle \quad \text{for } |\mathbf{r} - \mathbf{R}_R| < r_{c,R}. \quad (2.66)$$

Here $|\tilde{p}\rangle$ are projector functions which shows local character of the auxiliary wave function in the atomic region. It can shown that $\sum_{i \in R} |\tilde{\phi}_i\rangle \langle \tilde{p}_i| = 1$ within $r_{c,R}$. Any auxiliary wave-function $|\tilde{\Psi}\rangle$ can be expanded locally into auxiliary partial waves $|\tilde{\phi}_i\rangle$ if,

$$\langle \tilde{p}_i | \tilde{\phi}_j \rangle = \delta_{i,j} \quad \text{for } i, j \in R. \quad (2.67)$$

From Eq. 2.64 and 2.66, we obtain,

$$S_R | \tilde{\Psi} \rangle = \sum_{i \in R} S_R | \tilde{\phi}_i \rangle \langle \tilde{p}_i | \tilde{\Psi} \rangle = \sum_{i \in R} \left(| \phi_i \rangle - | \tilde{\phi}_i \rangle \right) \langle \tilde{p}_i | \tilde{\Psi} \rangle . \quad (2.68)$$

Thus the transformation operator becomes:

$$\mathcal{T} = 1 + \sum_i \left(| \phi_i \rangle - | \tilde{\phi}_i \rangle \right) \langle \tilde{p}_i | . \quad (2.69)$$

Here the sum runs over all the partial waves of all the atoms. True physical wave function takes the form as following:

$$| \Psi \rangle = | \tilde{\Psi} \rangle + \sum_i \left(| \phi_i \rangle - | \tilde{\phi}_i \rangle \right) \langle \tilde{p}_i | \tilde{\Psi} \rangle = | \tilde{\Psi} \rangle + \sum_R \left(| \Psi_R^1 \rangle - | \tilde{\Psi}_R^1 \rangle \right) \quad (2.70)$$

where

$$| \Psi_R^1 \rangle = \sum_{i \in R} | \phi_i \rangle \langle \tilde{p}_i | \tilde{\Psi} \rangle \quad (2.71)$$

$$| \tilde{\Psi}_R^1 \rangle = \sum_{i \in R} | \tilde{\phi}_i \rangle \langle \tilde{p}_i | \tilde{\Psi} \rangle . \quad (2.72)$$

Far from the atoms the auxiliary wave-functions $\tilde{\Psi}(\mathbf{r})$ become identical to the true wave-function $\Psi(\mathbf{r})$ *ie.* $\tilde{\Psi}(\mathbf{r}) = \Psi(\mathbf{r})$. Far from the atoms, auxiliary wave-functions are expressed in terms of Eq. 2.65 while close to atom, auxiliary wave-functions are expressed as according to Eq. 2.66 which is identical to its one-center expansion *ie.* $\tilde{\Psi}(\mathbf{r}) = \tilde{\Psi}_R^1(\mathbf{r})$. Thus the true wave-function is identical to $\tilde{\Psi}_R^1(\mathbf{r})$ which is build up from the partial waves with proper nodal structure.

Expectation values are obtained from either the reconstructed true wave-functions or directly from the auxiliary wave-functions,

$$\begin{aligned} \langle A \rangle &= \sum_n f_n \langle \Psi_n | A | \Psi_n \rangle + \sum_{n=1}^{N_c} \langle \phi_n^c | A | \phi_n^c \rangle \\ &= \sum_n f_n \langle \tilde{\Psi}_n | \mathcal{T}^\dagger A \mathcal{T} | \tilde{\Psi}_n \rangle + \sum_{n=1}^{N_c} \langle \phi_n^c | A | \phi_n^c \rangle . \end{aligned} \quad (2.73)$$

Here valance states occupations are denoted by f_n and number of core states are represented by N_c . First sum term in Eq. 2.73 runs over the valance states while second

sum is done over the core states $|\phi_n^c\rangle$. Using Eq. 2.70, we obtain:

$$\begin{aligned}
\langle \Psi | A | \Psi \rangle &= \left\langle \tilde{\Psi} + \sum_R (\Psi_R^1 - \tilde{\Psi}_R^1) \middle| A \middle| \tilde{\Psi} + \sum_{R'} (\Psi_{R'}^1 - \tilde{\Psi}_{R'}^1) \right\rangle \\
&= \underbrace{\langle \tilde{\Psi} | A | \tilde{\Psi} \rangle + \sum_R \left(\langle \Psi_R^1 | A | \Psi_R^1 \rangle - \langle \tilde{\Psi}_R^1 | A | \tilde{\Psi}_R^1 \rangle \right)}_{\text{part 1}} \\
&\quad + \underbrace{\sum_R \left(\langle \Psi_R^1 - \tilde{\Psi}_R^1 | A | \tilde{\Psi} - \tilde{\Psi}_R^1 \rangle + \langle \tilde{\Psi} - \tilde{\Psi}_R^1 | A | \Psi_R^1 - \tilde{\Psi}_R^1 \rangle \right)}_{\text{part 2}} \\
&\quad + \underbrace{\sum_{R \neq R'} \langle \Psi_R^1 - \tilde{\Psi}_R^1 | A | \Psi_{R'}^1 - \tilde{\Psi}_{R'}^1 \rangle}_{\text{part 3}} .
\end{aligned} \tag{2.74}$$

Only first part in Eq. 2.74 is evaluated explicitly. Second and third parts are completely neglected. The function $\Psi_R^1 - \tilde{\Psi}_R^1$ vanishes beyond its augmented region because true and auxiliary waves become identical beyond that region. For a sufficiently converged partial wave expansion, $\tilde{\Psi}_R^1 - \tilde{\Psi}_R^1$ vanishes inside its augmentation region. In addition to this, second and third parts in Eq. 2.74 disappear for operators like kinetic energy $-\frac{\hbar^2}{2m_e} \nabla^2$ and real space projection operator $|r\rangle\langle r|$ which produces electron density. But second and third terms has explicit importance for 'truly' non-local operators. Expectation value in Eq. 2.73 can be modified with the help of Eq. 2.74:

$$\begin{aligned}
\langle A \rangle &= \sum_n f_n \left(\langle \tilde{\Psi}_n | A | \tilde{\Psi}_n \rangle + \langle \Psi_n^1 | A | \Psi_n^1 \rangle - \langle \tilde{\Psi}_n^1 | A | \tilde{\Psi}_n^1 \rangle \right) + \sum_{n=1}^{N_c} \langle \phi_n^c | A | \phi_n^c \rangle \\
&= \sum_n f_n \langle \tilde{\Psi}_n | A | \tilde{\Psi}_n \rangle + \sum_{n=1}^{N_c} \langle \tilde{\phi}_n^c | A | \tilde{\phi}_n^c \rangle \\
&\quad + \sum_R \left(\sum_{i,j \in R} D_{i,j} \langle \phi_j | A | \phi_i \rangle + \sum_{n \in R}^{N_{c,R}} \langle \phi_n^c | A | \phi_n^c \rangle \right) \\
&\quad - \sum_R \left(\sum_{i,j \in R} D_{i,j} \langle \tilde{\phi}_j | A | \tilde{\phi}_i \rangle + \sum_{n \in R}^{N_{c,R}} \langle \tilde{\phi}_n^c | A | \tilde{\phi}_n^c \rangle \right) ,
\end{aligned} \tag{2.75}$$

in terms of auxiliary core states $|\tilde{\phi}_n^c\rangle$ where one-center density matrix $D_{i,j}$ can be defined as:

$$D_{i,j} = \sum_n f_n \langle \tilde{\Psi}_n | \tilde{p}_j \rangle \langle \tilde{p}_i | \tilde{\Psi}_n \rangle = \sum_n \langle \tilde{p}_i | \tilde{\Psi}_n \rangle f_n \langle \tilde{\Psi}_n | \tilde{p}_j \rangle . \tag{2.76}$$

These auxiliary core states $|\tilde{\phi}_n^c\rangle$ incorporates the tail of the core wave-function into

the plane wave part. In addition to this, auxiliary core states $|\tilde{\phi}_n^c\rangle$ are not required to be normalized. In this scheme electron density is expressed as:

$$\begin{aligned}
n(\mathbf{r}) &= \tilde{n}(\mathbf{r}) + \sum_R \left(n_R^1(\mathbf{r}) - \tilde{n}_R^1(\mathbf{r}) \right) \\
\tilde{n}(\mathbf{r}) &= \sum_n f_n \tilde{\Psi}_n^*(\mathbf{r}) \tilde{\Psi}_n(\mathbf{r}) + \tilde{n}_c(\mathbf{r}) \\
n_R^1(\mathbf{r}) &= \sum_{i,j \in R} D_{i,j} \phi_j^*(\mathbf{r}) \phi_i(\mathbf{r}) + n_{c,R}(\mathbf{r}) \\
\tilde{n}_R^1(\mathbf{r}) &= \sum_{i,j \in R} D_{i,j} \tilde{\phi}_j^*(\mathbf{r}) \tilde{\phi}_i(\mathbf{r}) + \tilde{n}_{c,R}(\mathbf{r}) ,
\end{aligned} \tag{2.77}$$

where $n_{c,R}$ represents the core density of an atom while $\tilde{n}_{c,R}$ is the auxiliary core density which becomes equal to $n_{c,R}$ outside the atomic region, but smooth inside. During computation, matrix elements of an operator with the auxiliary wave-function may be slowly convergent with the plane wave expansion because the operator is not well behaved. This problem can be solved by adding an ‘‘intelligent zero’’. For a purely localize operator B within an atomic region, identity between the auxiliary wave-function and its own partial wave expansion results:

$$0 = \langle \tilde{\Psi}_n | B | \tilde{\Psi}_n \rangle - \langle \tilde{\Psi}_n^1 | B | \tilde{\Psi}_n^1 \rangle . \tag{2.78}$$

In this situation, operator B is so chosen that it cancels the problematic part (behavior) of the operator A . Operator B is localize in a single atomic region. The plane wave convergence can be improved by adding B to the plane wave part and matrix elements with its one centered expansions which will not affect the converged result. Similar to wave-functions and expectation values total energy can also be expressed in terms of three operators:

$$E[\tilde{\Psi}, R_R] = \tilde{E} + \sum_R \left(E_R^1 - \tilde{E}_R^1 \right) . \tag{2.79}$$

Plane wave part \tilde{E} involves only smooth functions. This part is evaluated on equispaced grids in real space and reciprocal space. In addition to this, computationally \tilde{E} part is the

most important part which shows similarities with the pseudopotential approach,

$$\begin{aligned} \tilde{E} = & \sum_n \left\langle \tilde{\Psi}_n \left| \frac{-\hbar^2}{2m_e} \nabla^2 \right| \tilde{\Psi}_n \right\rangle \\ & + \frac{1}{2} \cdot \frac{e^2}{4\pi\epsilon_0} \int d^3r \int d^3r' \frac{[\tilde{n}(\mathbf{r}) + \tilde{Z}(\mathbf{r})][\tilde{n}(\mathbf{r}') + \tilde{Z}(\mathbf{r}')] }{|\mathbf{r} - \mathbf{r}'|} \\ & + \int d^3r \bar{v}(\mathbf{r}) \tilde{n}(\mathbf{r}) + E_{xc}[\tilde{n}(\mathbf{r})] . \end{aligned} \quad (2.80)$$

Here $\tilde{Z}(\mathbf{r})$ is an angular momentum dependent core density. Remaining parts of the Eq. 2.80 can be evaluated on radial grids in a spherical harmonic expansion. The nodal structure of the wave functions can be expressed in terms of logarithmic radial grid that becomes vary fine near the nucleus,

$$\begin{aligned} E_R^1 = & \sum_{i,j \in R} D_{i,j} \left\langle \phi_j \left| \frac{-\hbar^2}{2m_e} \nabla^2 \right| \phi_i \right\rangle + \sum_{n \in R}^{N_{c,R}} \left\langle \phi_n^c \left| \frac{-\hbar^2}{2m_e} \nabla^2 \right| \phi_n^c \right\rangle \\ & + \frac{1}{2} \cdot \frac{e^2}{4\pi\epsilon_0} \int d^3r \int d^3r' \frac{[n^1(\mathbf{r}) + Z(\mathbf{r})][n^1(\mathbf{r}') + Z(\mathbf{r}')] }{|\mathbf{r} - \mathbf{r}'|} \\ & + E_{xc}[n^1(\mathbf{r})] \end{aligned} \quad (2.81)$$

and

$$\begin{aligned} \tilde{E}_R^1 = & \sum_{i,j \in R} D_{i,j} \left\langle \tilde{\phi}_j \left| \frac{-\hbar^2}{2m_e} \nabla^2 \right| \tilde{\phi}_i \right\rangle \\ & + \frac{1}{2} \cdot \frac{e^2}{4\pi\epsilon_0} \int d^3r \int d^3r' \frac{[\tilde{n}^1(\mathbf{r}) + \tilde{Z}(\mathbf{r})][\tilde{n}^1(\mathbf{r}') + \tilde{Z}(\mathbf{r}')] }{|\mathbf{r} - \mathbf{r}'|} \\ & + \int d^3r \bar{v}(\mathbf{r}) \tilde{n}^1(\mathbf{r}) + E_{xc}[\tilde{n}^1(\mathbf{r})] . \end{aligned} \quad (2.82)$$

The compensation charge density $\tilde{Z}(\mathbf{r}) = \sum_R \tilde{Z}_R(\mathbf{r})$ describes the sum of angular momentum dependent Gauss functions which have an analytically plane wave expansion. $\tilde{Z}(\mathbf{r})$ is localize within atomic region. Plane wave convergence of the total energy is not affected by this auxiliary density. The potential $\bar{v} = \sum_R \bar{v}_R$ which appears in Eq. 2.80 and 2.82 appears in the total energy expression in terms of intelligent zero,

$$\begin{aligned} 0 = & \sum_n f_n \left(\langle \tilde{\Psi}_n | \bar{v}_R | \tilde{\Psi}_n \rangle - \langle \tilde{\Psi}_n^1 | \bar{v}_R | \tilde{\Psi}_n^1 \rangle \right) \\ = & \sum_n f_n \langle \tilde{\Psi}_n | \bar{v}_R | \tilde{\Psi}_n \rangle - \sum_{i,j \in R} D_{i,j} \langle \tilde{\phi}_i | \bar{v}_R | \tilde{\phi}_j \rangle . \end{aligned} \quad (2.83)$$

Thus the potential part just cancels the Coulomb singularity of the potential in the plane wave part. \bar{v} is localize which is evident from the Eq. 2.66.

Plane wave expansion for the auxiliary wave-function must be complete. This plane wave expansion is monitored by the plane wave cutoff defined as $E_{pw} = \frac{1}{2} \hbar^2 G_{max}^2$. Local potential of pseudopotential approach (Eq. 2.44) is identical to corresponding potential of the projector wave method. As the auxiliary density contains auxiliary core density contribution, PAW shows non-linear core correction of the pseudo-potential approach. In addition to this, compensation density $\tilde{Z}(\mathbf{r})$ is non-spherical and depends on the wave functions. Recently, the PAW method has been implemented into a number of the first-principle based codes [37]. Efforts have been put together to modify the PAW method without taking into account the full wave-function for the energy optimization. This approach is termed as “post pseudopotential PAW” which started with the evaluation of hyperfine parameters from a pseudopotential calculation using the PAW reconstruction operator [38] and used in the pseudopotential approach to determine properties like hyperfine parameters that requires the correct wave-functions.

2.5 Spin Density Functional Theory

In the generalization of spin density functional theory (SDFT) [39], the charge density is augmented by magnetization density $m(\mathbf{r})$ which in general forms continuous three dimensional vector field resulting changes in both magnitude and direction of $m(\mathbf{r})$ from place to place. Magnetism, in nature, can be collinear or non-collinear like spin-spirals, helical [40, 41] etc.,.

2.5.1 Collinear Magnetism

The theory of collinear magnetism is based on the two scalar fields, a spin up density $\rho_{\uparrow}(\mathbf{r})$ and a spin down density $\rho_{\downarrow}(\mathbf{r})$, *ie.*

$$\rho(\mathbf{r}) = \rho_{\uparrow}(\mathbf{r}) + \rho_{\downarrow}(\mathbf{r}) \quad (2.84)$$

and

$$m(\mathbf{r}) = \rho_{\uparrow}(\mathbf{r}) - \rho_{\downarrow}(\mathbf{r}) . \quad (2.85)$$

In this situation Hohenberg-Kohn theory suggests that 'true' ground state total energy is a variational functional of both spin densities [39, 42]

$$E = E[\rho, m] = E[\rho_{\uparrow}, \rho_{\downarrow}] . \quad (2.86)$$

It is now possible to construct the single particle Kohn-Sham equation for this spin density function theory. The Coulomb terms remain functional of the total density while T_0 and E_{xc} terms in Eq. 2.19 become functional of two spin densities. Variational principle yields,

$$\left[-\frac{\hbar^2}{2m_e} + V_s(\mathbf{r}) + V_H(\mathbf{r}) + V_{xc,\sigma}(\mathbf{r}) \right] \Psi_{i,\sigma}(\mathbf{r}) = \varepsilon_{i,\sigma} \Psi_{i,\sigma}(\mathbf{r}) \quad (2.87)$$

where σ is the spin index and

$$\rho_{\sigma}(\mathbf{r}) = \sum_{occ} \Psi_{i,\sigma}^*(\mathbf{r}) \Psi_{i,\sigma}(\mathbf{r}) . \quad (2.88)$$

In case of collinear magnetic ordering, two separate sets of Kohn-Sham orbitals are solved for the magnetic ground state. Exchange-correlation term is the only part of the Hamiltonian that includes explicit spin degrees of freedom.

2.5.2 Non-collinear Magnetism

In contrast to a collinear magnetic state where magnetic moments align parallel or anti-parallel to a spin quantization axis, non-collinear magnetic state allows full spatial variation of the spin direction. The concept of decoupled spin dependent Kohn-Sham equation fails for a non-collinear magnetic state. In this case electron density is treated with a 2×2 density matrix [39, 43, 44],

$$\rho(\mathbf{r}) = \rho_0(\mathbf{r})\mathbf{I} + \mathbf{m}(\mathbf{r}) \cdot \boldsymbol{\sigma} . \quad (2.89)$$

Here \mathbf{I} and $\boldsymbol{\sigma}$ are unit matrix and Pauli spin matrix. $\rho_0(\mathbf{r})$ and $\mathbf{m}(\mathbf{r})$ are defined *global* coordinate system. The off-diagonal terms in Eq. 2.89 gives the magnetization perpendicular

to spin quantization axis, say z axis of a Cartesian coordinate system.

In the DFT, variational scheme for the total energy functional with respect to $\rho(\mathbf{r})$ leads to the Kohn-Sham single particle equation for the ground state that is determined from the following Hamiltonian,

$$H = \left[H_{kin} + V_0(\mathbf{r}) \right] \mathbf{I} + V(\mathbf{r}) \cdot \boldsymbol{\sigma} \quad (2.90)$$

where H_{kin} is the kinetic energy term for a non-interacting system, $V_0(\mathbf{r})$ and $V(\mathbf{r})$ are non-magnetic and magnetic part of an effective potential which includes the *external*, *Coulomb*, *exchange-correlation* potential. This effective potential (V_{eff}) is represented within full potential scheme by Weiner [45] and applied in the *local spin density approximation* (LSDA) using the Hedin-Lundqvist exchange-correlation [39]. In LSDA, exchange-correlation potential depends only on the position. From this fact effective potential (V_{eff}) can be expressed in terms of spin $\frac{1}{2}$ rotation matrix $U(\theta(\mathbf{r}), \phi(\mathbf{r}))$, where $\theta(\mathbf{r})$ and $\phi(\mathbf{r})$ are the polar angles of the direction of magnetization $\mathbf{m}(\mathbf{r})$ at a specified point. $U(\theta(\mathbf{r}), \phi(\mathbf{r}))$ transforms the *global* coordinate system to a *local* one parallel to the spin quantization direction. At a given point in space, electron density can be evaluated from the diagonalization of,

$$\rho(\mathbf{r}) = U^\dagger(\theta(\mathbf{r}), \phi(\mathbf{r})) \begin{pmatrix} \rho_+(\mathbf{r}) & 0 \\ 0 & \rho_-(\mathbf{r}) \end{pmatrix} U(\theta(\mathbf{r}), \phi(\mathbf{r})) \quad (2.91)$$

where the effective potential can be expressed as,

$$V_{eff}(\mathbf{r}) = U^\dagger(\theta(\mathbf{r}), \phi(\mathbf{r})) \begin{pmatrix} v_{eff}(\rho_+(\mathbf{r})) & 0 \\ 0 & v_{eff}(\rho_-(\mathbf{r})) \end{pmatrix} U(\theta(\mathbf{r}), \phi(\mathbf{r})) . \quad (2.92)$$

Here $V_{eff}(\rho_\pm(\mathbf{r}))$ is the effective potential of a collinear ferromagnetic electron gas [39]. This transformation is performed all over the crystal space.

In case of atomic sphere approximation, a single local spin direction with a spherically averaged magnetization is defined in each sphere. In case of LAPW basis, plane wave is augmented with a spin dependent LAPW basis in order to avoid discontinuity in this augmented basis set at the muffin tin (MT) boundary [46]. Radial functions $u_l(\mathbf{r})$ and

$\dot{u}_l(\mathbf{r})$ are derived from the radial Schrödinger equations and energy derivative equations at energy point E_l using the non-magnetic part of the spherical potential. In the interstitial region, basis function is augmented by solution of Schrödinger equations and energy derivative equations at the interstitial point E_I . A_{lm} and B_{lm} for both inside MT sphere and interstitial region are derived in the usual way.

Instead it is reasonable to introduce an exchange correlation field corresponds to an internal magnetic field, \mathbf{b}_{xc} [40, 47],

$$\mathbf{b}_{xc}(\mathbf{r}) = -\frac{\partial E_{xc}[\rho, \mathbf{m}]}{\partial \mathbf{m}(\mathbf{r})}. \quad (2.93)$$

Using this auxiliary field, we can rewrite the Kohn-sham equation,

$$\left[-\frac{\hbar^2}{2m_e} + V_s(\mathbf{r}) + V_H(\mathbf{r}) + V_{xc}(\mathbf{r}) - \mathbf{b}_{xc} \cdot \boldsymbol{\sigma} \right] \Psi_i(\mathbf{r}) = \varepsilon_i \Psi_i(\mathbf{r}) \quad (2.94)$$

which is in spinor form with $\Psi(\mathbf{r})$ being a two component spinor,

$$\Psi_i(\mathbf{r}) = \begin{pmatrix} \alpha_i(\mathbf{r}) \\ \beta_i(\mathbf{r}) \end{pmatrix}. \quad (2.95)$$

Here only the last term of the Hamiltonian is spin dependent through the action of Pauli spin matrix vector whose Cartesian components become

$$\sigma_x = \begin{pmatrix} 0 & 1 \\ 1 & 0 \end{pmatrix}, \quad \sigma_y = \begin{pmatrix} 0 & -i \\ i & 0 \end{pmatrix}, \quad \sigma_z = \begin{pmatrix} 1 & 0 \\ 0 & -1 \end{pmatrix}.$$

During iterative cycles, charge and magnetization densities are calculated from the eigen-spinors,

$$\rho(\mathbf{r}) = \sum_{occ} \Psi_i^\dagger(\mathbf{r}) \Psi_i(\mathbf{r}) \quad (2.96)$$

and

$$\mathbf{m}(\mathbf{r}) = \sum_{occ} \Psi_i^\dagger(\mathbf{r}) \boldsymbol{\sigma} \Psi_i(\mathbf{r}). \quad (2.97)$$

This scheme [48] does not includes any geometrical approximations for charge, magnetization, potential or exchange-correlation part modified by the magnetic field (xc magnetic). Nowadays, various electronic structure codes have been implemented taking care of full

potential formalism. x_c magnetic is locally parallel to the magnetization at each point in space

$$\mathbf{b}_{xc}(\mathbf{r}) = -\widehat{\mathbf{m}}(\mathbf{r})\rho(\mathbf{r}) \left[\frac{\partial \varepsilon_{xc}(\rho_{\uparrow}, \rho_{\downarrow})}{\partial m} \right]_{\rho=\rho(\mathbf{r}), m=|\mathbf{m}(\mathbf{r})|}. \quad (2.98)$$

Here $\widehat{\mathbf{m}}$ is a unit vector along magnetization density in space. In addition to this, for magnetic cells, theories have been introduced to deal with the non-commensurate spin density waves [49,50]. In case of so-called spin-spirals, magnetization is rotated in between different cells in the crystal in absence of any spin-orbit coupling. Helical or cycloidal spin density waves have been theoretically justified from the fact that one can introduce general symmetry operations that combine translations with spin rotations which is already applied to some transition metal systems and in rare earth metals.

Bibliography

- [1] M. Born and J. R. Oppenheimer, *Ann. Physik* **84**, 457 (1927).
- [2] D. R. Hartree, *Mathematical Proceedings of the Cambridge Philosophical Society* **24**, 426-437 (1928).
- [3] V. Fock, *Z. Phys.* **61** (1930).
- [4] P. Hohenberg and W. Kohn, *Phys. Rev.* **136**, B864 (1964).
- [5] W. Kohn and L. J. Sham, *Phys. Rev.* **140**, A1133 (1965).
- [6] R. M. Dreizler and E. K. U. Gross, *Density Functional Theory* (Springer, Berlin, 1990).
- [7] R. G. Parr and W. Yang, *Density-Functional Theory of Atoms and Molecules* (Oxford University Press, Oxford, 1989).
- [8] J. P. Perdew and W. Yue, *Phys. Rev. B* **33**, 8800 (1986).
- [9] J. P. Perdew, K. Burke, and M. Ernzerhof, *Phys. Rev. Lett.* **77**, 3865 (1996).
- [10] A.D. Becke, *J. Chem. Phys.* **98**, 5648 (1993);
P.J. Stephens, J.F. Devlin, C.F. Chabalowski, M.J. Frisch, *J. Chem. Phys.* **98** 11623 (1993);
J. Heyd, G. E. Scuseria, and M. Ernzerhof, *J. Chem. Phys.* **118**, 8207 (2003).
- [11] O. Gunnarsson, O. Jepsen, and O. K. Andersen, *Phys. Rev. B* **27**, 7144 (1983).
- [12] O. K. Andersen, *Phys. Rev. B* **12**, 3060 (1975).

-
- [13] O. K. Andersen, O. Jepsen, Phys. Rev. B **52**, 2571 (1984).
- [14] D. Singh, *PlaneWaves, Pseudopotentials and the LAPW Method* (Kluwer Academic, Amsterdam, 1994).
- [15] C. Herring, Phys. Rev. **57**, 1169 (1940).
- [16] J.C. Phillips and L. Kleinman, Phys. Rev. **116**, 287 (1959).
- [17] W.C. Topp and J.J. Hopfield, Phys. Rev. B **7**, 1295 (1974).
- [18] T. Starkloff and J.D. Joannopoulos, Phys. Rev. B **16**, 5212 (1977).
- [19] R.W. Shaw, Jr. and W.A. Harrison, Phys. Rev. **163**, 604 (1967).
- [20] D.R. Hamann, M. Schluter and C. Chiang, Phys. Rev. Lett. **43**, 1494 (1979).
- [21] G.B. Bachelet, D.R. Hamann and M. Schluter, Phys. Rev. B **26**, 4199 (1982).
- [22] D. Liberman, J.T Waber and D.T Cromer, Phys. Rev. **137**, A27 (1965).
- [23] L. Kleinman and D.M. Bylander, Phys. Rev. Lett. **48**, 1425 (1982).
- [24] D. Vanderbilt, Phys. Rev. B **41**, 7892 (1990).
- [25] K. Laasonen, R. Car, C. Lee and D. Vanderbilt, Phys. Rev. B **43**, 6796 (1991).
- [26] K. Laasonen, A. Pasquarello, R. Car, C. Lee and D. Vanderbilt, Phys. Rev. B **47**, 10142 (1993).
- [27] J.C. Slater, Phys. Rev. **51**, 846 (1937).
- [28] J.C. Slater, *Advances in Quantum Chemistry* 1, 35 (1964).
- [29] H. Bross, Phys. Kondens. Mater **3**, 119 (1964).
- [30] H. Bross, G. Bohn, G. Meister, W. Schube and H. Stohr, Phys. Rev. B **2**, 3098 (1970).
- [31] D.D. Koelling, Phys. Rev. B **2**, 290 (1970).

- [32] T. Takeda and J. Kubler, J. Phys. F **9**, 661 (1979).
- [33] D. Singh, Phys. Rev. B **43**, 6388 (1991).
- [34] E. Sjöstedt, L. Nordström and D.J. Singh, Solid State Commun. **114**, 15 (2000).
- [35] Peter E. Blöchl, Johannes Kästner, and Clemens J. Först. *Electronic structure method: Augmented Waves, Pseudopotentials and the Projector Augmented Wave Method. Handbook of Materials Modeling*, edited by Sidney Yip, 1:93-119, 2005.
- [36] P. E. Blöchl, Phys. Rev. B **50**, 17953 (1994).
- [37] G. Kresse and J. Joubert, Phys. Rev. B, **59**, 1758 (1999).
- [38] C.G. Van de Walle and P.E. Blöchl, Phys. Rev. B **47**, 4244 (1993).
- [39] U. von Barth and L. Hedin, J. Phys. C **5**, 1629 (1972).
- [40] L.M. Sandratskii, Adv. Phys. **47**, 91 (1988).
- [41] L.M. Sandratskii, Phys. Rev. B **64**, 134402 (2001).
- [42] H. Eschrig and W.E. Pickett, Solid State Commun. **118**, 123 (2001).
- [43] J. Kübler, K. -H. Höck, J. Sticht, and A. R. Williams, J. Phys. F **18**, 469 (1988).
- [44] L. M. Sandratskii, Adv. Phys. **47**, 91 (1998).
- [45] M. Weinert, J. Math. Phys. **22**, 2433 (1981).
- [46] E. Wimmer, H. Krakauer, M. Weinert, and A. J. Freeman, Phys. Rev. B **24**, 864 (1981);
M. Weinert, E. Wimmer, and A. J. Freeman, Phys. Rev. B **26**, 4571 (1982).
- [47] E. Sjöstedt, and L. Nordström, Phys. Rev. B **66**, 014447 (2002).
- [48] L. Nordstrom and D. J. Singh, Phys. Rev. Lett. **76**, 4420 (1996).
- [49] C. Herring, Phys. Rev. **57**, 1169 (1940).
- [50] L. Sandratskii and R Guletskii, J. Phys. F **16**, L43 (1986).

Zhang-Rice physics and anomalous copper states in A-site ordered perovskites*

3.1 Cuprate superconductors and Zhang-Rice physics

High temperature superconductivity was first observed in 1986 by Bednorz and Müller in a layered copper-oxide perovskite $\text{La}_{2-x}\text{Ba}_x\text{CuO}_4$ ($T_C \sim 30\text{K}$) [1]. Since then a lot of attention was paid to design such cuprate materials. This resulted into superconducting transition temperature increased from 30K to 138K [2]. Although majority of high T_C superconductors are hole doped, experimental database for n doped compounds also exists. $\text{Nd}_{2-x}\text{SrCe}_y\text{CuO}_4$, $\text{Nd}_{2-x}\text{Ce}_x\text{CuO}_4$, $\text{Pr}_{2-x}\text{Ce}_x\text{CuO}_4$ belong to the class of electron doped superconductor [3]. The structure of such cuprate compounds (both hole-doped and electron-doped) contain infinite CuO_2 planes which are the most important structural sub-unit. Due to the crystal field of square planer site symmetry D_{4h} , degeneracy of the 5 d levels of atomic cu is lifted completely, resulting into high lying Cu : $d_{x^2-y^2}$ state with a large energy separation from the rest. Similarly, crystal field of D_{2h} symmetry also removes the degeneracy of oxygen p states [5]. As a result O : p states get splitted into π_{\parallel} , π_{\perp} and σ levels as shown in Fig. 3.1 where both σ and π_{\parallel} are composed of in-plane oxygen orbitals $p(x,y)$ (see Fig. 3.2) and π_{\perp} stands for $p(z)$. Such hybridized $pd\sigma$ states

*This chapter is based on the article : Scientific Reports **3**, 1834 (2013).

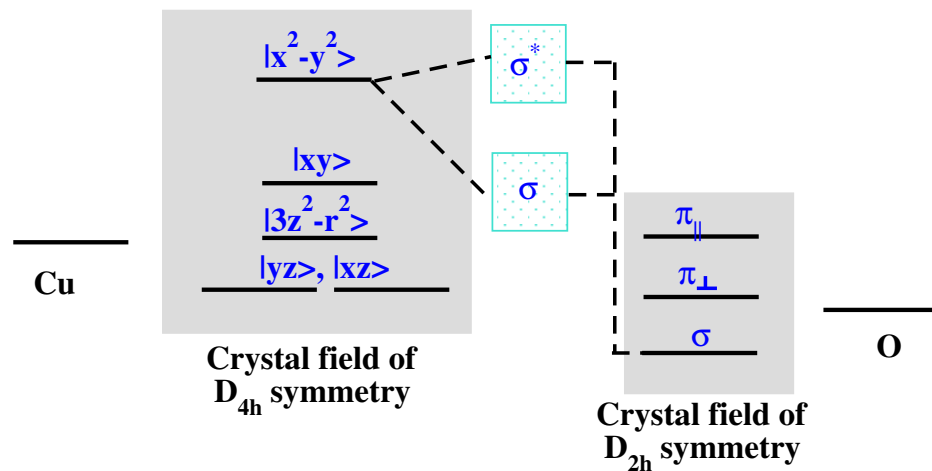


Figure 3.1: Crystal field splitting of Cu : d and O : p states and their covalent bonding as suggested by Damascelli *et al.* [5]. Strong hybridization between Cu : $d_{x^2-y^2}$ and O : p_{σ} results bonding (σ) and anti-bonding (σ^*) bands.

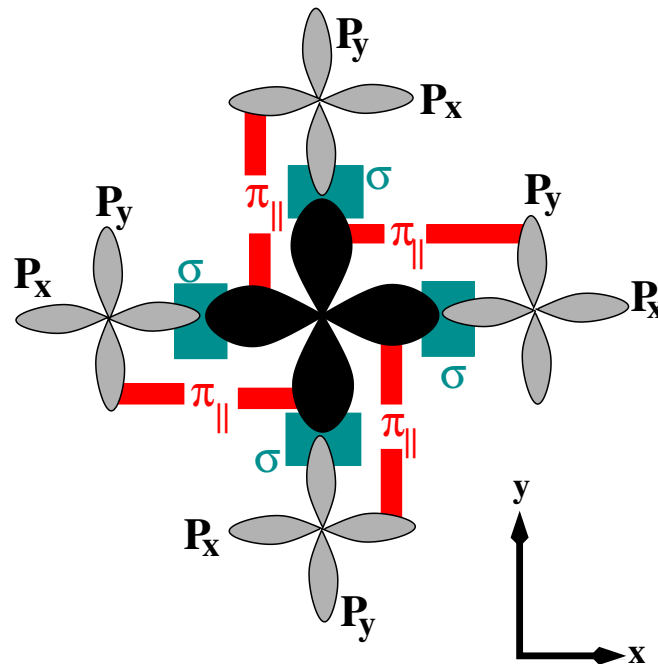


Figure 3.2: σ (cyan) and π (red) bonding in CuO_4 plane resulting from the orbital hybridization between Cu : $d_{x^2-y^2}$ (black) and O : $p_{x,y}$ (gray).

will produce broad bonding (σ) and antibonding (σ^*) bands as shown in Fig. 3.2, 3.3. Small mixing of σ states of oxygen and Cu : d_{3z^2-1} will produce narrow nonbonding band which has small contribution in the conductivity of cuprate superconductor [3]. Due to existence of large onsite Coulomb repulsion Cu : $d_{x^2-y^2}$ splits into two subgroups: upper Hubbard band (UHB) and lower Hubbard band (LHB) [4]. In the undoped case, valence band is formed by hybridized bonding p - d band, mainly of O : $2p$ character. Empty con-

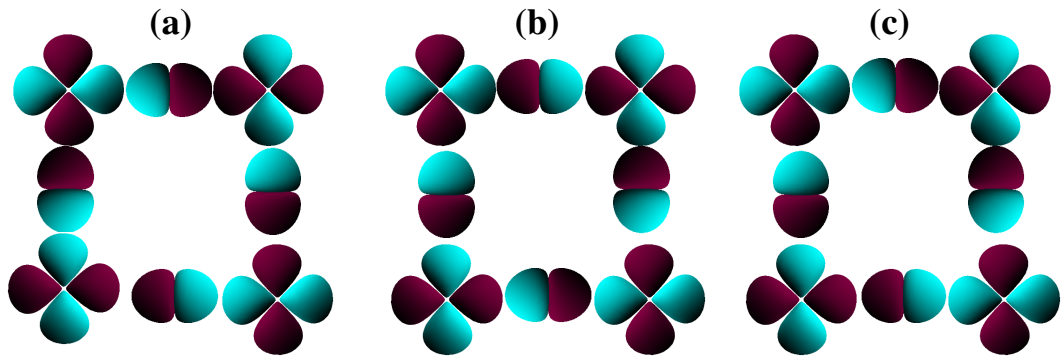


Figure 3.3: Different orbital hybridization (bonding phases) between Cu : $d_{x^2-y^2}$ and O : p (a) bonding (b) anti-bonding (c) non-bonding. Phases of atomic wave-functions are separated by different colours. Adopted from [5].

duction band (UHB) consist of hybridized antibonding p - d states, primarily of Cu : $d_{x^2-y^2}$ character. Valance and conduction bands are separated by charge transfer gap $\Delta = \epsilon_d - \epsilon_p$ (see Fig. 3.4). As $\Delta < U$, undoped cuprates are charge transfer insulators with half filled bands *ie.* one hole per Cu site. Holes mainly occupy Cu : $d_{x^2-y^2}$ state and interact with each other via superexchange [4–6].

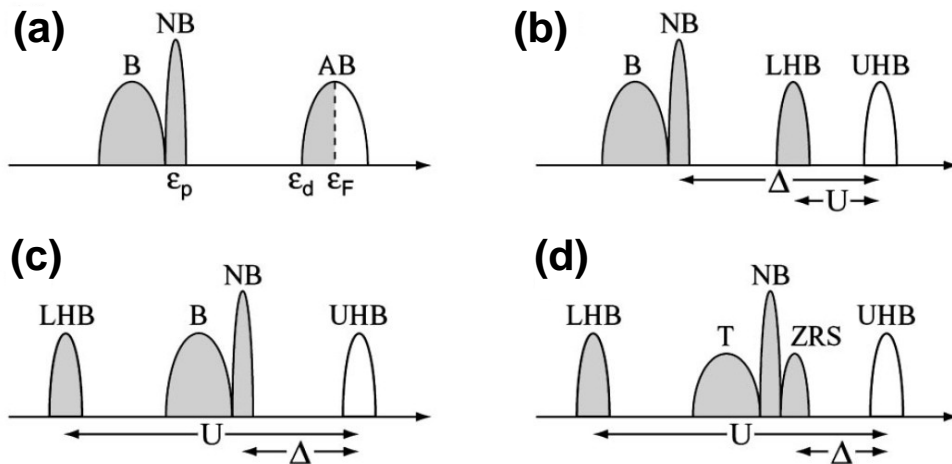


Figure 3.4: Illustration of the p - d model with three bands, bonding (B), anti-bonding (AB) and non-bonding (NB). (a) metallic state for half filled AB band with $U = 0$ (b) $\Delta > U > W$ (band width of $pd\sigma$ hybridized states) results the Mott Hubbard insulator (c) charge-transfer insulator for $U > \Delta > W$. (d) Zhang-Rice singlet-triplet splitting. As a result of hole doping NB band splits into two subgroups: Zhang-Rice triplet (T) and singlet (ZRS) state. Doping of electron (hole) places ϵ_F at UHB (ZRS) (not shown in figure). ϵ_p and ϵ_d stand for band centers of $3d$ and $2p$ bands respectively. Reproduced from [5].

p - d model with 3 bands, Cu : $d_{x^2-y^2}$, O : $p_{x,y}$ shows formation of bands with different bonding characteristic in the CuO_2 plane which is evident from Fig. 3.3, 3.4. In this context, three-band Hubbard model will lead to three different ground state (a) metallic

state of antibonding type for $U = 0$, (b) Mott-Hubbard insulator for $\Delta > U > W$ (band width) and (c) charge transfer insulator for $U > \Delta > W$ as shown in Fig. 3.4. Hole doping results new states for O : $2p$ types hole at the top of valance band while for electron doping introduces $3d_{x^2-y^2}$ types of electrons at the bottom of conduction band [7]. Therefore,

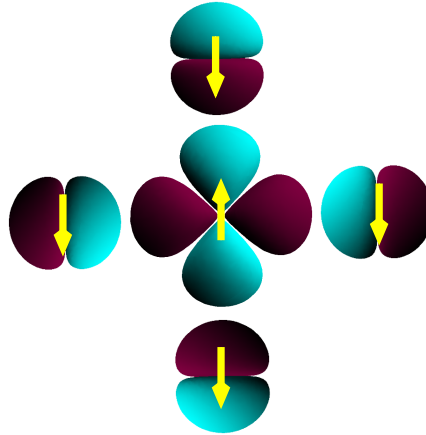


Figure 3.5: Typical Zhang-Rice spin singlet state: $pd\sigma$ antibonding between Cu : $d_{x^2-y^2}$ and O : $p(x,y)$. Doped holes at the $pd\sigma$ hybridized states of O : $p(x,y)$ couple antiferromagnetically with the hole at Cu : $d_{x^2-y^2}$ band.

the cuprate superconductors can be mapped onto an effective single band Hubbard model considering only Cu : $d_{x^2-y^2}$ and O : $p(x,y)$ hybridized orbital. In terms of a single band approach, Zhang-Rice described a simplified picture of the three band $p-d$ model [8–17]. They argued that doped hole at O site is antiferromagnetically coupled with the holes at Cu site (see Fig. 3.5). As a result of such mixing, Cu valency changes to $d^9\bar{L}$ (\bar{L} denotes a ligand (oxygen) hole).[†] In addition to this, anti-symmetry of their wavefunction in spin coordinates suggests that in hole doped superconductors, any carrier excitation originates from this $pd\sigma$ antibonding type spin singlet state.

3.2 Motivation behind the project

With a motivation to synthesis new compounds with square planar coordination of Cu, recent high pressure synthesis was carried out [18]. This resulted into a new type of perovskite

[†]In absence of any p -hole at the transition-metal site, configuration of the undoped compounds with n numbers of d electrons takes the form of $d^n p^6$. In presence of the hole at the oxygen site, the configuration $d^n p^6$ breaks down and we have $d^{n+1} p^5 = d^{n+1} \bar{L}$. The interaction of the p -hole and transition-metal ion takes place in such a way that the *quantum numbers* remain conserved *ie.* total spin remains the same as that of d^n configuration.

structure which also shows such CuO_4 planes like the high T_C cuprate superconductors. General composition of such oxide materials are given by $AA'_3B_4O_{12}$. Both A' and B sites can in general, be occupied by transition metal ions. In the present study we will focus on compounds where the A' site is occupied by copper. Experimental measurements on $\text{CaCu}_3\text{Co}_4\text{O}_{12}$ suggest that this compounds also shows Zhang-Rice like spin singlet state, despite the lack of superconducting ground state [19]. In this chapter we study the electronic properties of this compound intensively. For comparison, we also consider another isostructural compound, $\text{CaCu}_3\text{Cr}_4\text{O}_{12}$.

3.3 Computational Details

The DFT calculations were performed by using the plane wave basis set and pseudo-potentials scheme as implemented in the Vienna *Ab initio* Simulation Package (VASP) [25]. Electron-electron correlation was treated under the generalized gradient approximation (GGA) as suggested by Perdew-Burke-Ernzerhof [26]. Missing correlation beyond GGA was taken into account by means of GGA+U approach in a static mean-field way as implemented by Dudarev *et al.* [22] For the plane wave based calculations, we used projector augmented wave (PAW) potentials [23]. Wave functions were expanded in the plane wave basis set with a kinetic energy cutoff of 600 eV and Brillouin zone summations were carried out with a $6\times 6\times 6$ k-mesh. The U value of 5 eV on Cu site and 4 eV on B site were used for GGA+U calculations while the Hund's rule coupling J was fixed to 0.8 eV. The obtained results were further verified in terms of variation of U parameter. In order to determine the energy positions of the Cu-d, B-d and O-p levels as well as to generate the effective Wannier functions for Cu-d states, we used muffin-tin orbital (MTO) based N-th order MTO (NMTO)-downfolding [24] technique. Starting from a DFT calculations, NMTO-downfolding results at a few-orbital Hamiltonian by integrating out degrees (orbitals) which are not of interest. Our results were verified among the plane wave and LMTO [25] calculations in terms of total energy differences and related electronic properties, like density of states and band structures. All our theoretical results were further verified by experimental resonant soft x-ray absorption spectroscopy.

3.4 Results and Discussions

In order to study the microscopic electronic properties of A-site ordered quadruple perovskite $\text{CaCu}_3\text{Co}_4\text{O}_{12}$ (CCCoO) and $\text{CaCu}_3\text{Cr}_4\text{O}_{12}$ (CCCrO), first we have to understand their structural properties.

3.4.1 Crystal Structure

$\text{AA}'_3\text{B}_4\text{O}_{12}$ crystallizes in body centered cubic structure given by space group symmetry $Im\bar{3}$ (space group number 204). B ions sit within octahedral cage formed by the oxygen ions while Cu-O forms square planer geometry (see Fig. 3.6). BO_6 octahedra are corner shared type. Each oxygen is shared in-between two B ions and a copper ion. In this present study, BO_6 and CuO_4 polyhedra in both CCCoO and CCCrO show "trigonal" distortion which results a small deviation in O-B-O bond angle from 90° . We have used optimized structural parameters for our theoretical purpose. Optimization of atomic positions were carried out keeping the lattice parameters same as obtained in the experiment. Comparison of the optimized and experimental structures of both CCCoO and CCCrO are shown in Table 3.1, 3.2. Theoretically optimized structures show good agreement with the experimental measurements. In the following, we present the calculated electronic structure of the two compounds.

3.4.2 Electronic Structure

In order to assign the spin and valance states of different components correctly, one needs to carry out spin-polarized calculations even through the compound may not be ordered magnetically. Figure 3.7 shows the spin polarized density of states and band structure of $\text{CaCu}_3\text{B}_4\text{O}_{12}$ (B = Cr, Co). Due to octahedral crystal field, five degenerate B : d states are splitted into two subgroups: triply degenerate t_{2g} states and doubly degenerate e_g^σ states. Further due to trigonal distortion, three fold degeneracy of the t_{2g} states are removed partially, giving rise to singly degenerate a_{1g} and doubly degenerate e_g^π states. Square planer crystal field also introduces splitting within the energy level positions of Cu : d states, which results into high lying Cu : $d_{x^2-y^2}$ state with large energy separation from

Table 3.1: Wyckoff Positions of Ca, Cu, B (=Cr, Co) and O in $\text{CaCu}_3\text{B}_4\text{O}_{12}$ (B=Cr, Co). For, CCCrO, theoretically optimized (experimental) values of x, y ie. the free position parameters of oxygen become 0.3017 (0.3055) and 0.1825 (0.1797), while optimized (experimental) values of x, y in CCCoO become 0.3069 (0.3076) and 0.1773 (0.1765).

site	Site Symmetry	Multiplicity	Wyckoff letter	Coordinates
Ca	$m\bar{3}$	2	a	(0, 0, 0)
Cu	mmm	6	b	(0, 1/2, 1/2) (1/2, 0, 1/2), (1/2, 1/2, 0)
B	$\bar{3}$	8	c	(1/4, 1/4, 1/4) (3/4, 3/4, 1/4) (1/4, 3/4, 3/4) (3/4, 1/4, 3/4)
O	m	24	g	(x, y, 0) (x, -y, 0) (-x, y, 0) (-x, -y, 0) (x, 0, y) (x, 0, -y) (-x, 0, y) (-x, 0, -y) (0, x, y) (0, x, -y) (0, -x, y) (0, -x, -y)

Table 3.2: Optimized lattice constants and selected bond-lengths and angles of $\text{CaCu}_3\text{B}_4\text{O}_{12}$ (B=Cr, Co) with the corresponding experimentally measured values within the parentheses.

	CCCrO	CCCoO
B-B bond-length (Å)	3.642 (3.627)	3.598 (3.561)
B-O bond-length (Å)	1.923 (1.926)	1.918 (1.901)
Cu-O bond-length (Å)	1.963 (1.921)	1.887 (1.860)
\angle B-O-B $^\circ$	142.5 (140.6)	139.5 (139.0)
\angle O-B-O ($90\pm\delta$) $^\circ$, $\delta =$	0.38 (0.16)	0.1 (0.2)
\angle O-Cu-O ($90\pm\delta$) $^\circ$, $\delta =$	4.76 (4.52)	4.9 (4.9)
Lattice constant (Å)	7.284 (7.253)	7.197 (7.123)

the rest of the states. From Figure 3.7, strong mixing among Cu : d , B : d (B= Cr, Co) and O : p states can be noticed near the Fermi energy (ϵ_F). Such a strong mixing results into metallic ground state, in agreement with the experimental observations. Considering Cu : d states, we can see that Cu : $d_{x^2-y^2}$ in CCCrO is occupied in majority spin channel, while it is empty in minority spin channel, suggesting Cu^{2+} like oxidation state. Cu :

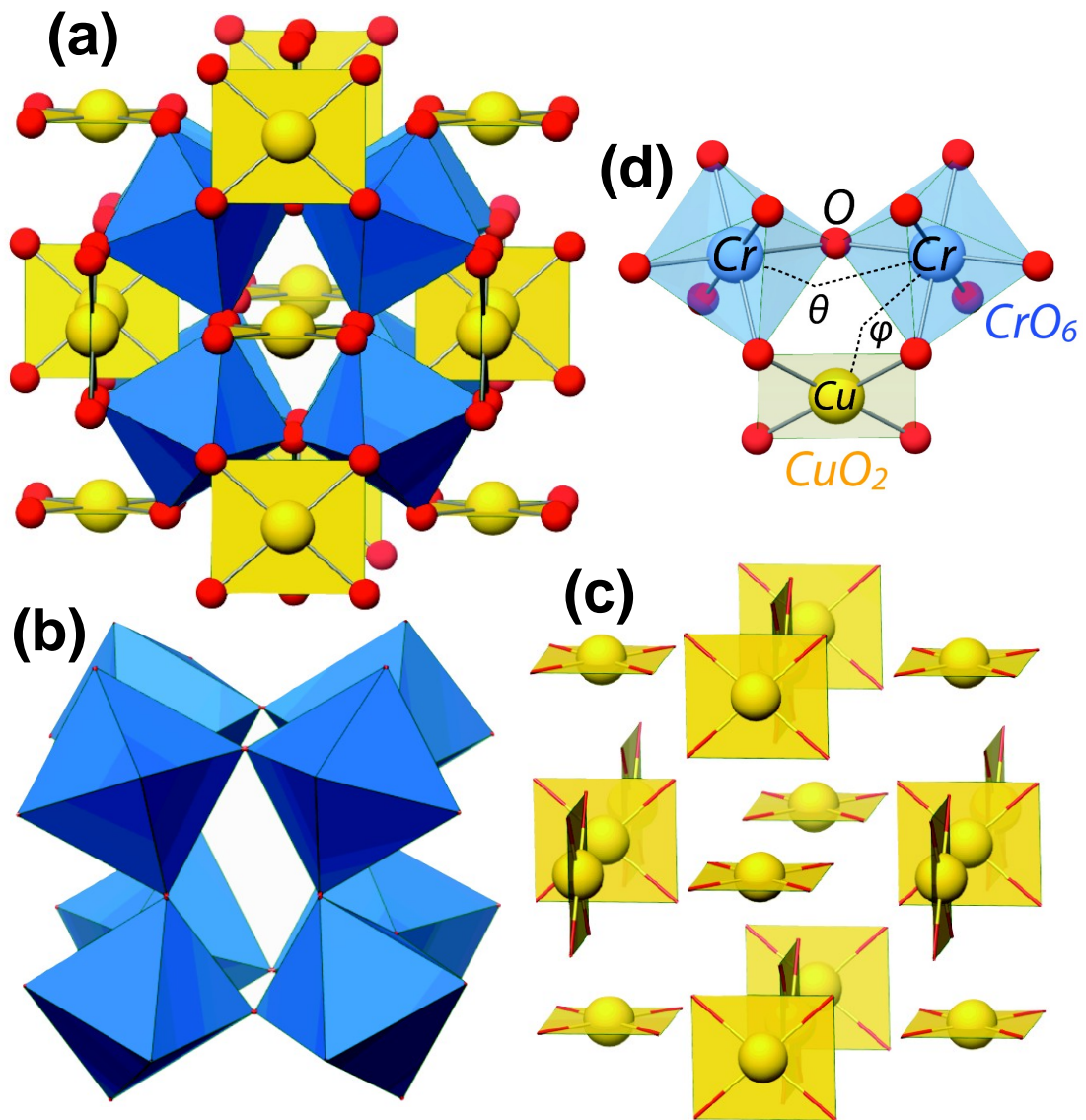


Figure 3.6: Structural building blocks of CCCrO. (a) Crystal structure of CCCrO. (b) CrO₆ octahedra are corner sharing type. (c) All 3 Cu ions form CuO₄ square planer network parallel to Cartesian xy , yz , zx planes. (d) Every oxygen ion is shared in-between two B ions and a Cu ion.

$d_{x^2-y^2}$ in CCCoO compound is empty in either spin channel suggesting metastable Cu³⁺ like behavior. Unoccupied Cu : $d_{x^2-y^2}$ results $\sim 0.07 \mu_B$ moment at Cu site in CCCoO, while single unpaired electron at Cu : $d_{x^2-y^2}$ in CCCrO results in $0.5 \mu_B$ spin moment.

Considering Cr : d states from Figure 3.7, we can see that only occupied states are e_g^π in the minority spin channel resulting low spin configuration of Cr in CCCrO. Two occupied e_g^π electrons give rise to $2.2 \mu_B$ moment at Cr site. Applying similar type of analysis, we can conclude that Co shows intermediate spin configuration resulting from $\sim 1.7 \mu_B$ spin

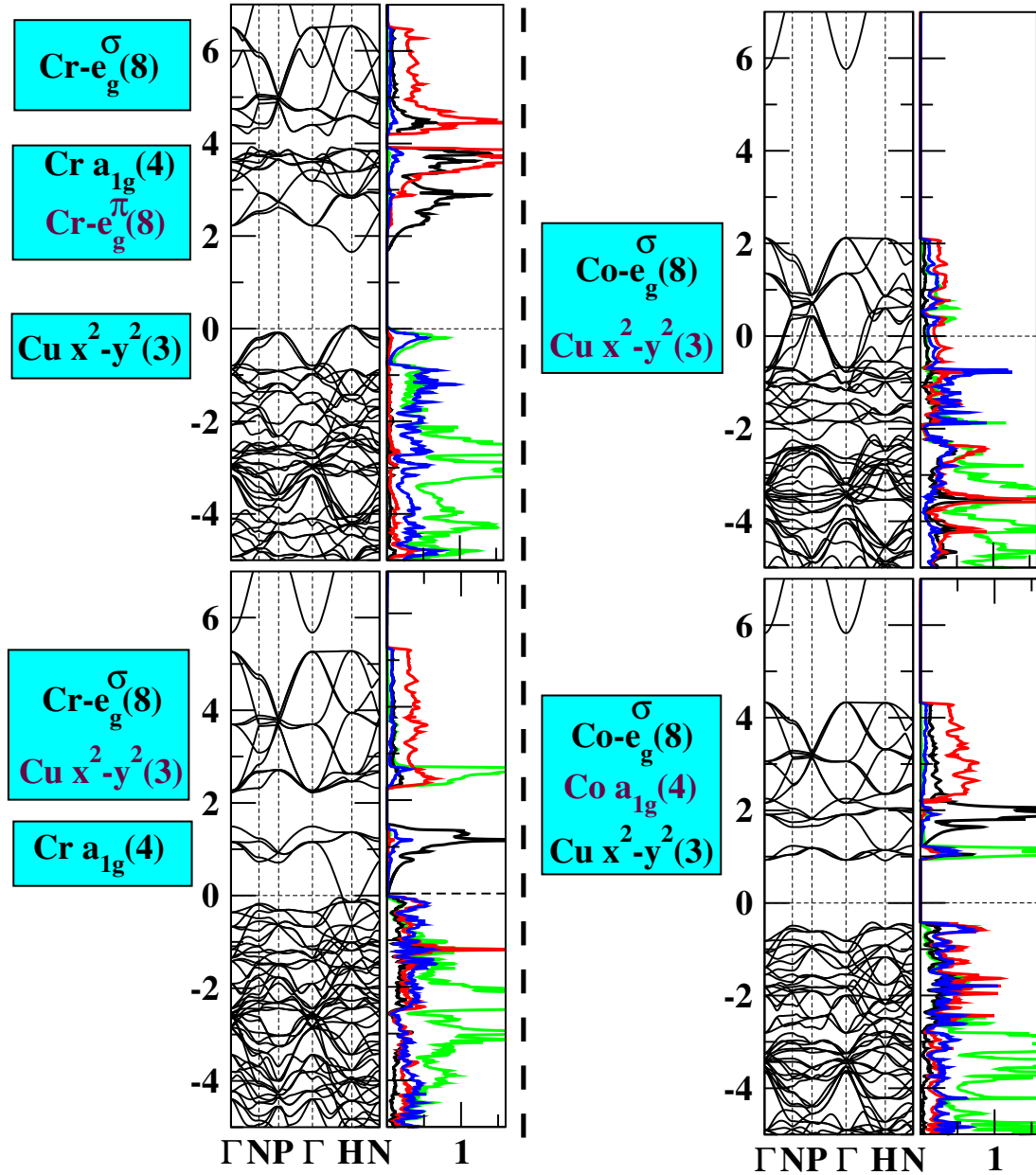


Figure 3.7: Spin polarized density of states and band structure for CCCrO (left panel) and CCCoO (right panel). Black and red line corresponds to B : t_{2g} and B : e_g states respectively. Cu : d and O : p are shown by green and blue colour. Number of bands correspond to an orbital, have been shown by the digit within the parenthesis. Top and bottom panel stands for majority and minority spin channels. Zero energy represents Fermi energy.

moment. Considering nominal valance of Ca and O as 2^+ and 2^- , we get nominal valance of Cr and Co as 4^+ and 3.25^+ respectively *ie.* d electron occupancy for Cr and Co becomes 2 and 5.75 respectively.

In order to determine the precise energy level positions of B : d , Cu : d and O : p states, NMTO downfolding calculations are performed considering B : d , Cu : d and O : p states

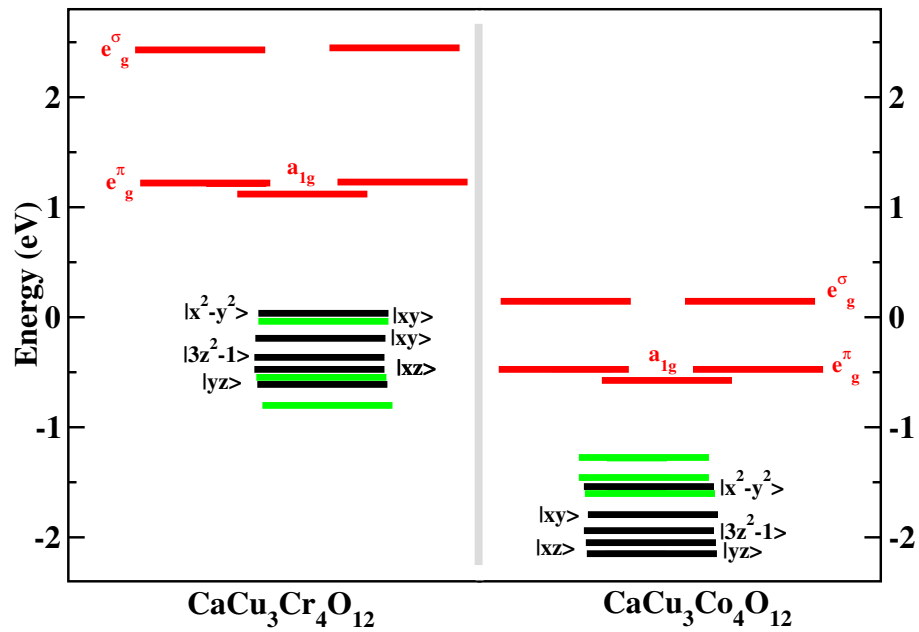


Figure 3.8: Crystal field splitting of B : d (red line), Cu : d (black line) and O : p (green line) states. High T_c cuprate like almost degenerate Cu : d and O : p energy levels can be noticed for either perovskite. Energy is measured with respect to the Cu : $d_{x^2-y^2}$ state of CCCrO compound.

as active and downfolding rest orbitals. From the energy-level position in Fig. 3.8, we can

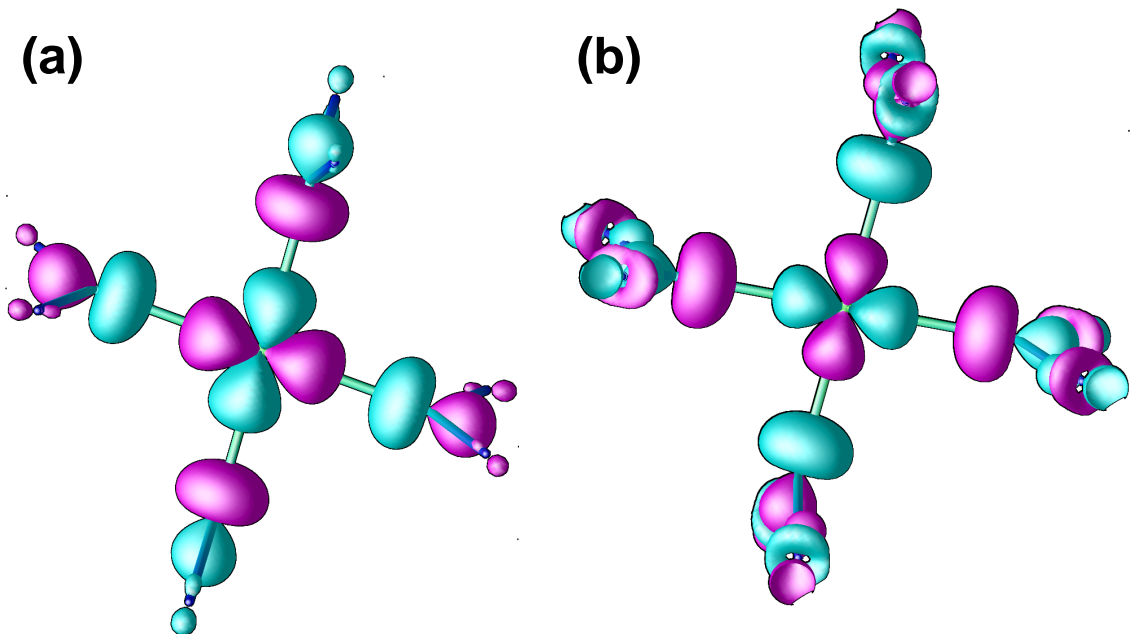


Figure 3.9: Effective Cu : $d_{x^2-y^2}$ Wannier function plot for (a) CCCrO and (b) CCCoO. For a selective isosurface, lobes with different sign have been shown by different colours.

see that Cu : d states are nearly degenerate with oxygen: p orbitals leading to a situation

very similar to that in high T_C cuprates. Such hybridized states further interact with B : d states which is evident from Fig. 3.7. The formation of such a mixed state is also evident in the Wannier function plot of an effective Cu : $d_{x^2-y^2}$ Wannier function obtained by keeping only Cu : $d_{x^2-y^2}$ state active and downfolding or integrating out all the other degrees of freedom (see Fig. 3.9). As clearly seen, the Wannier functions centred at the Cu site have the orbital character of $d_{x^2-y^2}$ symmetry, and the tail is shaped according to the symmetry of the orbitals mixed with it. Both compounds show strong $pd\sigma$ antibonding (see Fig. 3.3) state formed between Cu : $d_{x^2-y^2}$ and O : (p_x, p_y) which further bind to B : d states. For CCCoO, such $pd\sigma$ antibonding states will interact with empty Co : e_g band while Cr : t_{2g} will bind to Cu : $d_{x^2-y^2}$ and O : p_σ antibonding orbitals. Mixing of $pd\sigma$ antibonding orbitals with B : d states is found to be less for CCCrO. Such typical $pd\sigma$ antibonding states, degenerate O : p - Cu : d levels and finite moment at O-site (0.08 (0.20) μ_B for CCCo(Cr)O) bear “Zhang-Rice” like signature similar to the hole doped cuprate superconductors. All our theoretical results are further experimentally verified, as discussed in the following section.

3.4.3 Experimental Observation

Resonant soft x-ray absorption spectroscopy (XAS) is an ideal tool to investigate the microscopic electronic structure of materials [10, 14–16, 26–28]. Results of soft XAS measurements on the Cu $L_{3,2-}$ and O K edges are summarized in Figure 3.10 for $\text{CaCu}_3\text{B}_4\text{O}_{12}$ (B= Cr, Co) along with LaCuO_3 (LCO) and optimally doped superconductor $\text{YBa}_2\text{Cu}_3\text{O}_{7-\delta}$ (YBCO). YBCO and LCO are recalled as the standard references for Cu^{2+} and Cu^{3+} oxidation states respectively. We will discuss the CCCrO compound first. From the absorption line shape of Cr compound, the sharp peak ~ 930 eV corresponds to the transition from ground state d^0 to $\underline{c}d^{10}$ (\underline{c} denotes a core hole) excited d state. This transition introduces a single hole in the Cu $d_{x^2-y^2}$ band. Shoulder seen at 931.5 eV [29, 30], a direct signature of ZR singlet state, is transition from the ground state $d^{10}\underline{L}$ to the $\underline{c}d^{10}\underline{L}$ excited state [10, 13, 15, 27, 28]. In both transitions Cu remains nearly at $2+$ oxidation state, while in the latter case a ligand hole is distributed over neighbouring oxygen ions as shown in Fig. 3.5. Cu L edge spectrum of CCCrO shows excellent similarities with that of YBCO,

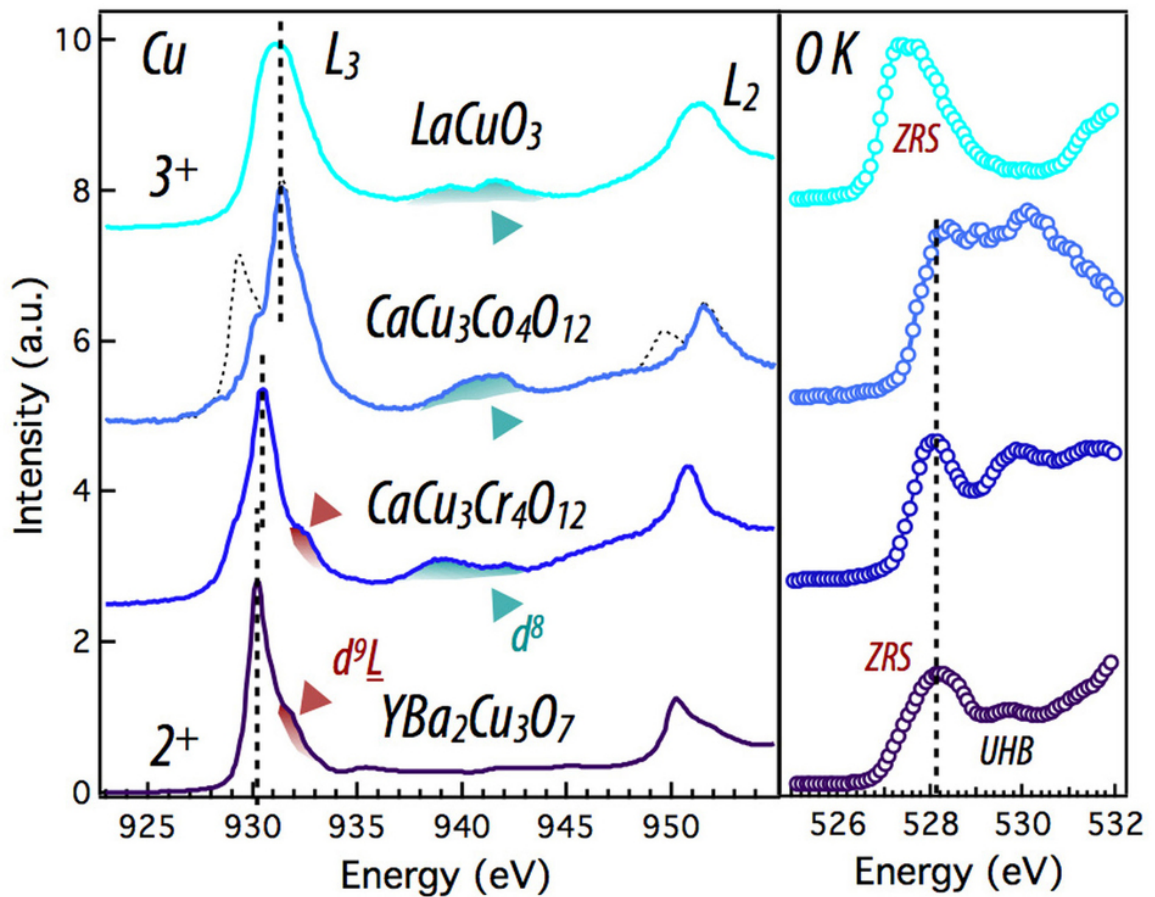


Figure 3.10: Left panel shows the XAS measurements on Cu L_{3,2}- edge for both CCCrO and CCCoO. YBa₂Cu₃O_{7- δ} (YBCO) and LaCuO₃ (LCO) are considered for standard reference for Cu²⁺ and Cu³⁺ oxidation states. Right panel shows O-K edge XAS results. Prepeak \sim 528 eV bears the signature of ZR state.

starting from initial d^9 state followed by ZR shoulder. Similarly it can be seen very easily that the ZR spin singlet state has the dominant contribution to the ground state for both Co and LCO. Absorption line of CCCoO is shifted \sim 1 eV away from the d^9 line which is evident for Cu^{3+} like state. A three peak fit is used for the L₃ data of CCCoO which are centered at 929 eV (impurity peak) [31], 930 eV (d^9) and 931.4 eV (d^9L). This impurity peak is subtracted from the original data which is represented by dotted line in Fig. 3.10. Multiple split peak observed \sim 940 eV corresponds to transition from meta-stable $3d^8$ state to excited cd^9 state. Such ionic Cu³⁺ state is completely absent for YBCO. As seen from O-K edge spectra, prepeak \sim 528 eV shows direct signature of ZR state, which is evident from the comparison with YBCO [14–16, 26].

3.5 Conclusion

Applying first principles GGA+U calculations we have studied two A site ordered perovskite oxides $\text{CaCu}_3\text{B}_4\text{O}_{12}$ (B= Cr, Co). Our calculations reveal that choice of B site cation is an effective tool to manipulate the degree of B-O-Cu hybridization. For CCCoO , Cu shows metastable $3d^8$ ($d^9\bar{L}$) like behavior, while substitution of Co by Cr results into stable ionic Cu^{2+} state. Analysis of energy level position and Wannier function calculations support the direct experimental observation that Zhang-Rice like state present in both compounds, despite the lack of the superconducting ground state. Our findings further demonstrate that the charge and spin state of Cu, fundamental to the intriguing physical properties the cuprates display, can be effectively controlled by a suitable choice of the B-site cation on isomorphic lattices that circumvent the chemical disorder and lattice modulation intrinsic to other doping methods.

Bibliography

- [1] J. G. Bednorz, K. A. Müller, *Z. Phys. B* **64**, 189 (1986).
- [2] G.F. Sun, K.W. Wong, B.R. Xu, Y. Xin, D.F. Lu, *Phys. Lett. A* **192**, 122 (1994).
- [3] N. P. Armitage, P. Fournier, R. L. Greene, *Rev. Mod. Phys.* **82**, 2421 (2010).
- [4] E. Dagotto, *Rev. Mod. Phys.* **66**, 763 (1994).
- [5] A. Damascelli, Z. Hussain, Z.-X. Shen, *Rev. Mod. Phys.* **75**, 473 (2003).
- [6] M. R. Norman, D. P. Pines, C. Kallin, *Adv. Phys.* **54**, 715 (2005).
- [7] D. C. Peets, D. G. Hawthorn, K. M. Shen, Y.-J. Kim, D. S. Ellis, H. Zhang, S. Komiya, Y. Ando, G. A. Sawatzky, R. Liang, D. A. Bonn, and W. N. Hardy, *Phys. Rev. Lett.* **103**, 087402 (2009);
Y. Yamaji and M. Imada, *Phys. Rev. B* **83**, 214522 (2011).
- [8] F. C. Zhang, T. M. Rice, *Phys. Rev. B* **37**, 3759 (1988).
- [9] J. Zaanen, G. A. Sawatzky, J. W. Allen, *Phys. Rev. Lett.* **55**, 418 (1985).
- [10] *Nikolay High-Temperature Cuprate Superconductors*. Berlin: Springer-Verlag, 2010.
- [11] J. Chakhalian, J. W. Freeland, H.-U. Habermeier, G. Cristiani, G. Khaliullin, M. van Veenendaal, B. Keimer, *Science* **318**, 1114 (2007).
- [12] J. Chakhalian, J. W. Freeland, G. Srajer, J. Stremper, G. Khaliullin, J. C. Cezar, T. Charlton, R. Dalgliesh, C. Bernhard, G. Cristiani, H.-U. Habermeier, B. Keimer, *Nat. Phys.* **2**, 244 (2006).

- [13] M. Karppinenab, H. Yamauchia, *Phil. Mag. B* **79**, 2, 343 (1999).
- [14] N. Nücker, J. Fink, J. C. Fuggle, P. J. Durham, W. M. Temmerman, *Phys. Rev. B* **37**, 10 (1988).
- [15] N. Nücker, E. Pellegrin, P. Schweiss, J. Fink, S. L. Molodtsov, C. T. Simmons, G. Kaindl, W. Frentrup, A. Erb, G. Müller-Vogt, *Phys. Rev. B* **51**, 13 (1995)
- [16] P. Kuiper, G. Kruizinga, J. Ghijsen, M. Grioni, P. J. W. Weijs, F. M. F. de Groot, G. A. Sawatzky, H. Verweij, L. F. Feiner, H. Petersen, *Phys. Rev. B* **38**, 10 (1988).
- [17] H-Y Deng, *J. Phys.: Condens. Matter* **21**, 075702 (2009).
- [18] W.-T. Chen, T. Saito, N. Hayashi, M. Takano and Y. Shimakawa, *Sci. Rep.*, **2**, 449 (2012);
H. Etani, I. Yamada, K. Ohgushi, N. Hayashi, Y. Kusano, M. Mizumaki, J. Kim, N. Tsuji, R. Takahashi, N. Nishiyama, T. Inoue, T. Irifune, and M. Takano, *J. Am. Chem. Soc.* **135**, 6100 (2013).
- [19] T. Mizokawa, Y. Morita, T. Sudayama, K. Takubo, I. Yamada, M. Azuma, M. Takano, Y. Shimakawa, *Phys. Rev. B* **80**, 125105 (2009).
- [20] G. Kresse, J. Furthmüller, *Phys. Rev. B* **54**, 11169 (1996).
- [21] J. P. Perdew, K. Burke, M. Ernzerhof, *Phys. Rev. Lett.* **77**, 3865 (1996).
- [22] S. L. Dudarev, G. A. Botton, S. Y. Savrasov, C. J. Humphreys, A. P. Sutton, *Phys. Rev. B* **57**, 1505 (1998).
- [23] P. E. Blöchl, *Phys. Rev. B* **50**, 17953 (1994).
- [24] O. K. Andersen, T. Saha-Dasgupta, *Phys. Rev. B* **62**, R16219 (2000).
- [25] O. K. Andersen, O. Jepsen, *Phys. Rev. Lett.* **53**, 2571 (1984).
- [26] C. T. Chen, F. Sette, Y. Ma, M. S. Hybertsen, E. B. Stechel, W. M. C. Foulkes, M. Schluter, S-W. Cheong, A. S. Cooper, L. W. Ru pp, Jr., B. Batlogg, Y. L. Soo, Z. H. Ming, A. Krol, Y. H. Kao, *Phys. Rev. Lett.* **66**, 104 (1991).

-
- [27] M. Gioni, J. B. Goedkoop, R. Schoorl, F. M. F. de Groot, J. C. Fuggle, F. Schäfers, E. E. Koch, G. Rossi, J.-M. Esteve, R. C. Karnatak, *Phys. Rev. B* **39**, 1541 (1989).
- [28] A. Bianconi, S. Della Longa, C. Li, M. Pompa, A. Congiu-Castellano, D. Udron, A. M. Flank, P. Lagarde, *Phys. Rev. B* **44**, 10126 (1991).
- [29] T. Mizokawa, A. Fujimori, H. Namatame, Y. Takeda, and M. Takano, *Phys. Rev. B* **57**, 16 (1998).
- [30] R. Sarangi, N. Aboelella, K. Fujisawa, W. B. Tolman, B. Hedman, K. O. Hodgson, E. I. Solomon, *J. Am. Chem. Soc.* **128**, 8286 (2006).
- [31] D. D. Sarma, O. Strebel, C. T. Simmons, U. Neukirch, G. Kaindl, R. Hoppe, H. P. Müller, *Phys. Rev. B* **37**, 9784 (1988).

Competition between heavy fermion and Kondo interaction in isoelectronic A-site-ordered perovskites^{*}

4.1 Kondo Lattice and Heavy Fermions

At very low temperature ~ 10 K, electrical resistance of metals usually drops because of low collision rate of conduction electrons. Certain metals like lead, aluminium suddenly lose all their electrical and magnetic properties and switch to superconducting state. Some metals like copper and gold offer a finite resistance even at such low temperature. Superconducting state is not evident for such class of metals. Electrical resistance goes to a saturation value with the decrease of temperature. But the situation gets very complicated when some impurity magnetic ion like Co are added to the system [1]. This time resistance increases as the temperature is lowered further. In 1964 Jun Kondo described this upturn in electrical resistivity. According to Kondo model, scattering of conduction electrons from these localize moments results such peculiar phenomenon. Kondo effect is characterized by a temperature T_K (the Kondo temperature) below which the electrical resistivity starts to increase because of the Kondo-scattering. In materials where these localize moments are arranged in a periodic array are termed as the so-called Kondo lattice.

^{*}This chapter is based on the articles : Nat Commun, **5**, 5818 (2014) and J Mater Sci, **47**, 7660 (2012).

The low-temperature properties of the Kondo lattice exhibits the interplay between the Kondo and RKKY (Ruderman-Kittel-Kasuya-Yosida) interaction where Kondo effect gives rise to non-magnetic ground state while long-range magnetic ordering is characterized by RKKY interaction. Kondo effect arise due to anti-ferromagnetic interaction between the localize spin and surrounding electrons from the Fermi sea. Spin exchange of the conduction electrons results new states near the Fermi energy, termed as the Kondo resonance. As a result of Kondo effect, conduction electrons screen out the localize spin. Such a spin singlet many body state will show no net moment at the Kondo-site. Similar to the Kondo effect, RKKY type interaction between the localize moments is also mediated by the conduction electrons. So, RKKY interaction is not a direct interaction. Sign of the coupling constant (J) between the localize spin and the spins of the electrons from the Fermi sea is oscillatory resulting different magnetic ordering starting from ferro or anti-ferro or spiral ordering [2].

At temperature $T < T_K$, heavy fermion property is noticed in the Kondo lattice where these quasiparticles show Fermi liquid like behavior. Kondo impurity causes the scattering of conduction electrons resulting an upturn in low temperature ($T \leq T_K$) resistivity while the same process in the heavy fermion material shows sudden drop in the resistivity at low temperatures [3]. Doniach argued that heavy fermion material is a dense Kondo lattice system [4]. Every single local moment in the lattice shows Kondo effect while RKKY interaction is noticed between the localize spins characterized by the magnetically ordering temperature T_{RKKY} [3, 4]. This competition between the Kondo and RKKY interaction can be described in the Doniach phase diagram [4]. Tuning the orbital hybridization between the localize spin and conduction electrons causes a phase transition from the magnetically ordered ground state to paramagnetic state passing through a quantum critical point (QCP). Tuning parameters are, in general, external pressure, magnetic field or doping. Fig. 4.1 shows such competition in a series of Ce-115 compounds CeBIn_5 ($B = \text{Co, Rh, Ir}$). Heavy fermion Ce-115 crystallizes in HoCoGa_5 type structure [5]. Incommensurate antiferromagnetically ordering (IC AF) is noticed in CeRhIn_5 with $T_N = 3.8$ K. Magnetic moments in CeRhIn_5 are aligned in ab plane propagating in a spiral along tetragonal c axis. Substitution of Rh by Co or Ir tunes the ground state towards a superconducting state. Coexistence of magnetism and superconductivity makes the electronic structure of $\text{CeRh}_{1-x}\text{B}_x\text{In}_5$ ($B = \text{Co, Ir}$) very complicated. For $B = \text{Ir}$, a second commensurate

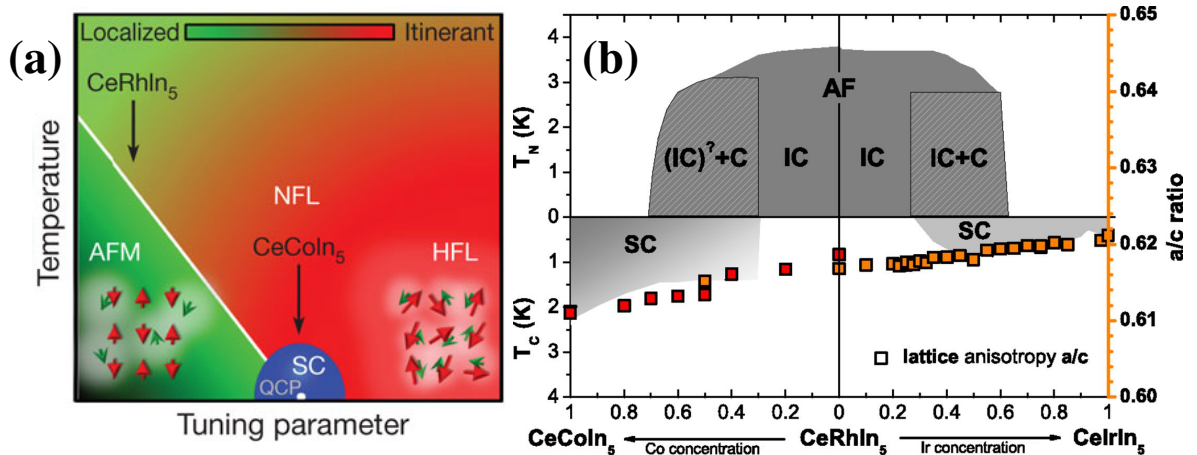


Figure 4.1: Phase diagram of Ce-115 compounds: (a) Antiferromagnetism in CeRhIn_5 places this compound in the RKKY dominated region while it is reported that CeCoIn_5 is very close to the quantum critical point (QCP) [6]. Non-Fermi liquid (NFL) behavior is one of most interesting aspects of the heavy fermion compounds because of the quantum criticality which sometimes results in unconventional superconductivity. Localize f electrons causes antiferromagnetism in CeRhIn_5 while itinerant nature of f electrons are noticed in the heavy Fermi liquid (HFL). (b) Magnetic-ordered and superconducting phases of CeBIn_5 ($B = \text{Co}, \text{Rh}, \text{Ir}$) are shown as function of Co and Ir concentration. Incommensurate antiferromagnetic ordered phases (IC AF) and the commensurate phases (C AF) are colored dark gray and hatched gray, respectively and superconducting (SC) region are marked by light gray. The coexistence of IC and C AF ordering in CeCoIn_5 is shown by a question mark. The temperature scales of T_N and T_C are shown in separate scales (up and down respectively). Lattice anisotropy is shown by the colored squares. Adopted from [5, 7].

magnetic phase is noticed. For $B = \text{Co}$, commensurate magnetic phase is noticed in the sample along with the incommensurate phase which is still a matter of debate. In addition to this lattice anisotropy is also an interesting component regarding the electronic structure of Ce-115 compounds CeBIn_5 ($B = \text{Co}, \text{Rh}, \text{Ir}$). Non-linear dependency of superconducting transition temperature (T_C) on the lattice anisotropy (a/c ratio) is noticed in $B (= \text{Co}, \text{Rh}, \text{Ir})$ rich samples.

4.2 Motivation behind the project

Recent experimental analysis suggests anomalous physical properties of a A-site ordered perovskite oxide $\text{CaCu}_3\text{Ir}_4\text{O}_{12}$, where Kondo like behavior is noticed in localized Cu moments and itinerant Ir-O hybridized states [8]. $\text{CaCu}_3\text{Ir}_4\text{O}_{12}$ shows metal-insulator transition with crossover temperature $\sim 80\text{K}$. Specific heat, magnetic susceptibility of the paramagnetic metallic phase ($T < 80\text{k}$) show non-Fermi liquid behavior indicating nearby quantum critical phenomenon. $\text{CaCu}_3\text{Ir}_4\text{O}_{12}$ exhibits large specific heat at low tempera-

ture (see Fig. 4.2) bearing a heavy fermion like signature. Such a crossover between the

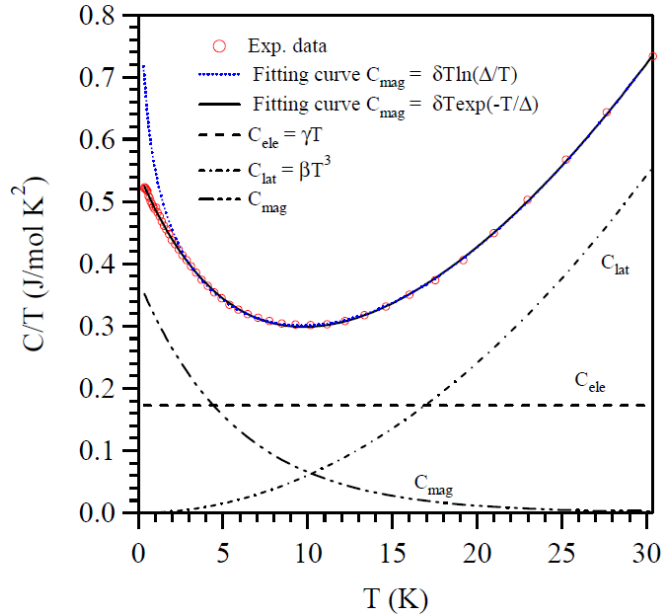


Figure 4.2: Low temperature Specific heat of $\text{CaCu}_3\text{Ir}_4\text{O}_{12}$ showing Heavy-fermion like characteristic. Reproduced from [8].

paramagnetic metallic state and magnetic insulating state is driven by the Cu-O and B-O bond-lengths in $\text{CaCu}_3\text{B}_4\text{O}_{12}$. But the microscopic origin of such anomalous behavior is still unknown. In order to shed light on this interesting aspect, three iso-structural and iso-electronic compounds $\text{CaCu}_3\text{B}_4\text{O}_{12}$ ($\text{B} = \text{Co}, \text{Rh}, \text{Ir}$) has been studied by using first-principle density functional theory. Here Co, Rh and Ir belong to same column of periodic table, with Co, Rh and Ir being $3d$, $4d$ and $5d$ elements respectively. Our study also provides a nice opportunity to study the effect of changing from $3d$ to $4d$ to $5d$ element at the B-site on the electronic properties of the compounds. Earlier studies incorporate the fact that B-site cation in $\text{CaCu}_3\text{B}_4\text{O}_{12}$ emerges wide ranges of varieties in the physical and chemical properties [9–15]. Different ground state in $\text{CaCu}_3\text{B}_4\text{O}_{12}$ result from the strong interplay between the orbital hybridization (W), electron-electron correlation (U) and the charge transfer energy (δ) [16]. Traversing the periodic table from $3d$ to $5d$ transition metal (TM) ions at the B-site in these iso-electronic compounds, the increase of the spatial extent of the valence d orbital (see Fig. 4.3) should cause an increase in W and also a reduction of U due to additional screening effects in the larger bandwidth oxides, along with a change of the charge-transfer energy (see Fig. 4.4). Additionally, the crystal field

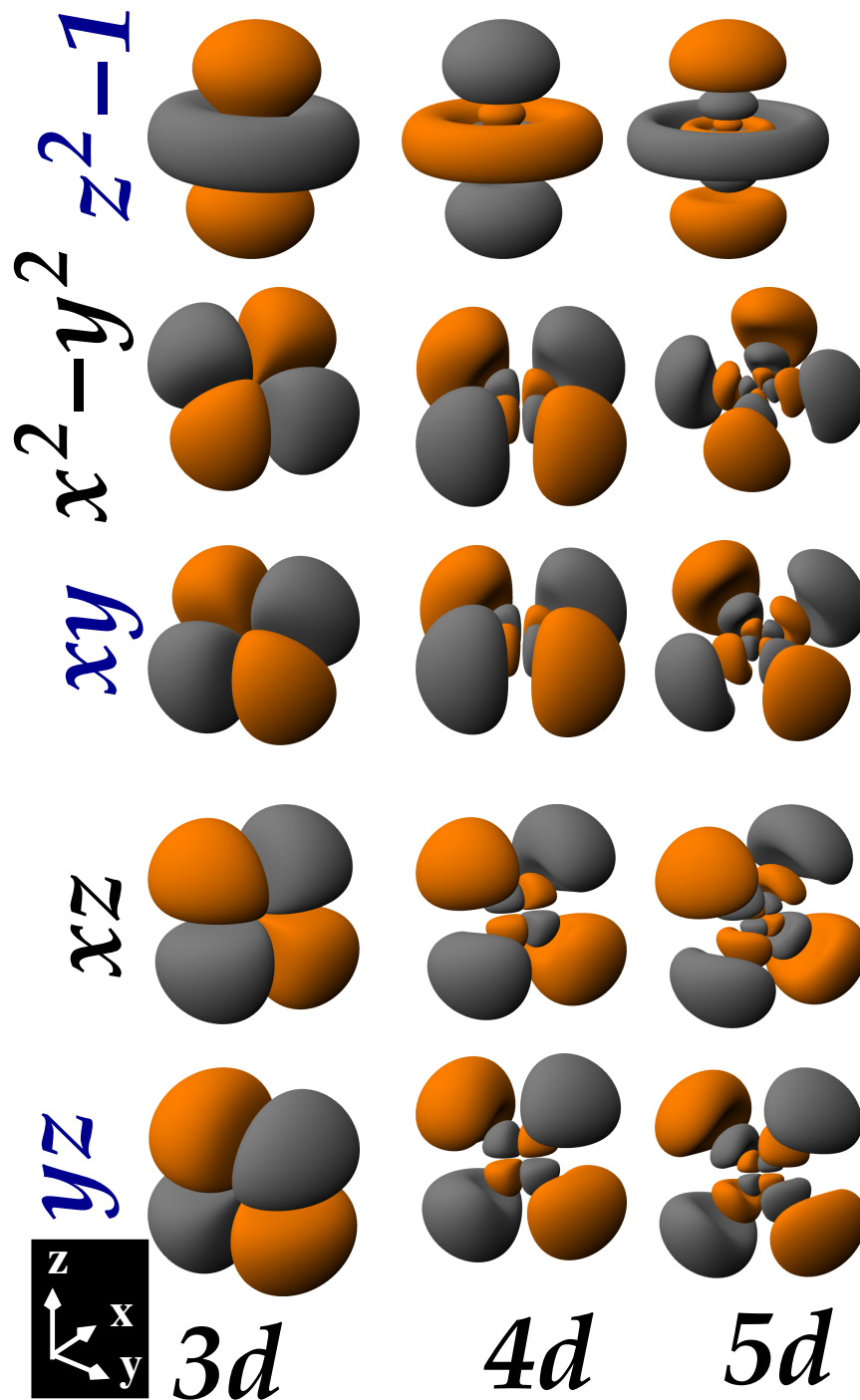


Figure 4.3: $3d$ (left panel) to $4d$ (middle panel) or $5d$ (right panel) atomic orbitals: Positive and negative part of lobes are separated by their colours. As we move from $3d$ to $4d$ or $5d$, much more delocalized nature of d orbitals result larger lattice constant and longer X-O (X= Cu, Co, Rh, Ir) bonds (see table 4.1). Figures are drawn by using *orbital viewer* program [26].

splittings among the five d orbitals increases from $3d$ to $5d$ elements, resulting in most of the 4 and $5d$ oxides acquiring a low spin configuration [17, 18]. Finally, as the spin-orbit

strength (λ) increases with atomic number (Z), λ and U become of comparable strength further complicating the interpretation of microscopic properties of both $\text{CaCu}_3\text{Rh}_4\text{O}_{12}$ and $\text{CaCu}_3\text{Ir}_4\text{O}_{12}$ [19, 20].

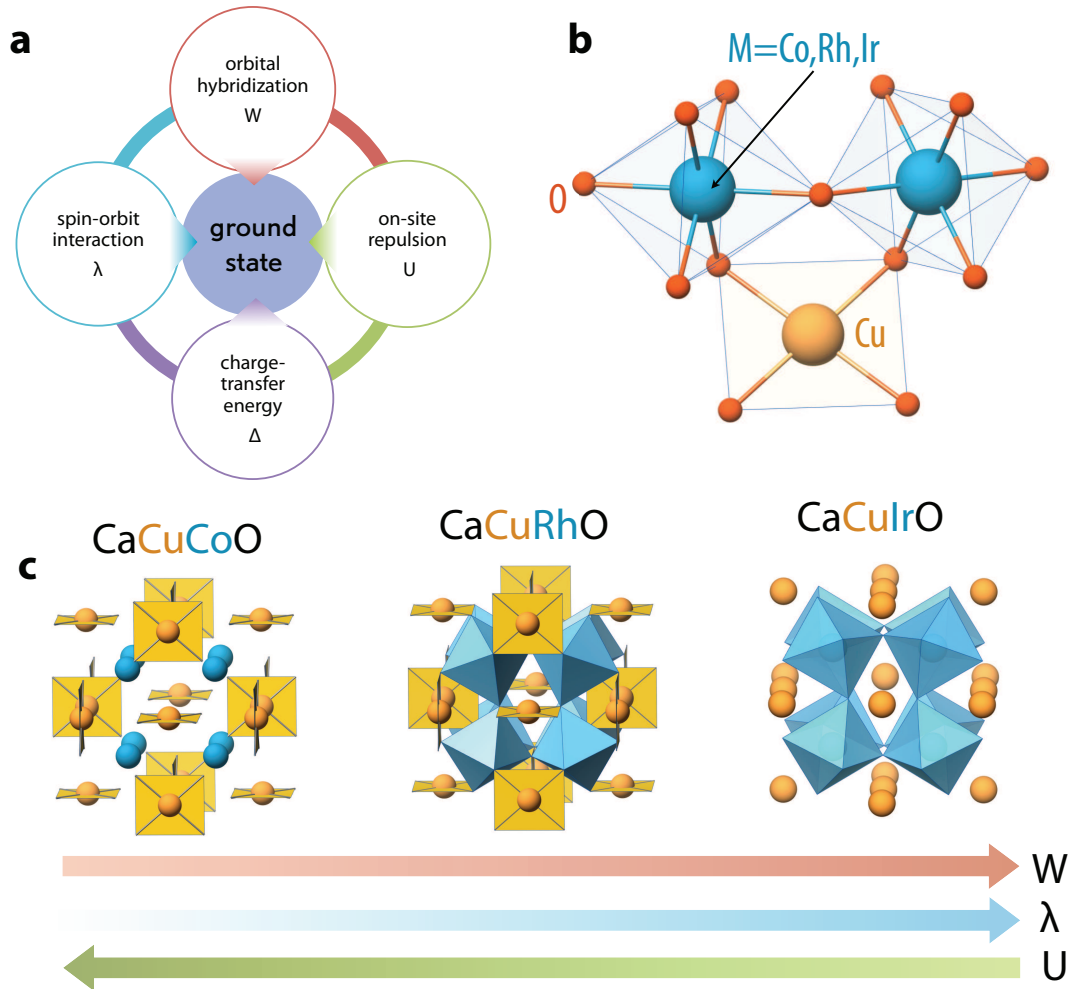


Figure 4.4: (a) Interaction parameters. (b) Cu-O-B local structure in A-site ordered perovskites. (c) Only Cu network and B site network are shown for CaCuCoO and CaCuIrO where both network are shown in CaCuRhO .

4.3 computational detail

All our first-principle DFT calculations have been performed by using plane wave basis set and pseudo potential method as implemented in the Vienna *ab initio* simulation package [21]. The exchange correlation functional was treated under GGA scheme as prescribed by Perdew-Burke-Ernzerhof [22]. Missing correlation beyond GGA was taken through GGA+U

calculation with the "+U" implementation of Dudarev *et al.* [23]. For the plane wave based calculations, we used projector augmented wave [24] potentials. Kinetic energy cutoff of 600 eV was used for the plane wave expansion and reciprocal space integration was performed with $6 \times 6 \times 6$ k mesh. U value of 5 eV was fixed at Cu site, while U value of 4 eV was used at the B site for 3d (Co) element and 1-2 eV was used for 4d (Rh) and 5d (Ir) elements. Obtained results were further verified in terms of variation of "U" parameters. Hund's rule coupling was fixed to 0.8 eV. All the plane wave results were further verified in terms of full potential linearized augmented plane wave (FP-LAPW) method as implemented in WIEN2k [25]. For FP-LAPW calculations, augmented plane wave + $l0$ was chosen as basis set and the expansion of spherical harmonics for radial wave function was taken up to $l=10$. Charge densities and potential were represented by spherical harmonics up to $l=6$. 200 k points in irreducible Brillouin zone were considered and tetrahedron method was applied for Brillouin zone integration [27]. Spin-orbit interactions were included in the calculations via a second variational step using the scalar-relativistic eigen-functions as basis. Energy level positions of Cu: d , B: d and O: p as well as effective Wannier function were calculated by using MTO based Nth order MTO (NMTO) [28] downfolding technique. Starting from full DFT calculations, NMTO downfolding reaches towards a few-orbital Hamiltonian by integrating out all degrees of freedom which are not of interest. Such energy selective effective orbitals serve like Wannier like orbital. NMTO not yet available in its self consistent form, relies on the self consistent potential parameters obtained from linear MTO calculations [29].

4.4 Results and Discussions

4.4.1 Structural details

$\text{CaCu}_3\text{B}_4\text{O}_{12}$ (B=Co, Rh, Ir) crystallize in body centered cubic phase with space group $Im\bar{3}$ (space group number 204). Atomic positions in the cubic $Im\bar{3}$ symmetry are A at the $2a$ site (0, 0, 0), A' at the $6b$ site (0, 1/2, 1/2), B at the $8c$ site (1/4, 1/4, 1/4), and O at the $24g$ site (x, y, 0). B ions form octahedral network with neighboring oxygen ions, while Cu forms CuO_4 square planar geometry. Oxygen ions are shared between two B ions and a

Table 4.1: Optimized lattice constants, oxygen positions and selected bond-lengths and angles of CCCCu, CCRhO, CClrO with the corresponding experimentally measured values within the parentheses.

	CaCu ₃ Co ₄ O ₁₂	CaCu ₃ Rh ₄ O ₁₂	CaCu ₃ Ir ₄ O ₁₂
B-B bond-length (Å)	3.598 (3.561)	3.751 (3.70)	3.777 (3.737)
B-O bond-length (Å)	1.918 (1.901)	2.026 (1.991)	2.028 (1.999)
Cu-O bond-length (Å)	1.887 (1.860)	1.904 (1.889)	1.950 (1.949)
\angle B-O-B ^o	139.5 (139.0)	135.6 (136.3)	137.2 (138.4)
\angle O-B-O (90 \pm δ) ^o , δ =	0.1 (0.2)	1.3 (1.09)	1.7 (1.5)
\angle O-Cu-O (90 \pm δ) ^o , δ =	4.9 (4.9)	8.3 (7.7)	8.3 (7.6)
x, y	0.3069, 0.1773 (0.3076, 0.1765)	0.3080, 0.1660 (0.3076, 0.1680)	0.3047, 0.1687 (0.3039, 0.1718)
Lattice constant (Å)	7.197 (7.123)	7.502 (7.393)	7.554 (7.474)

copper ion as shown in Fig. 4.4. Trigonal distortion is present within BO₆ octahedral subunit resulting a small deviation in O-B-O angle from 90°. Such angular distortion is also noticed in CuO₄ network, which makes O-Cu-O angle different from 90°. We have used theoretical optimized structural parameters for this first principle study. Our symmetry-preserved structural parameters show excellent agreement with experimental XRD measurements (see table 4.1). Next we move on to understand the electronic structure of these compounds.

4.4.2 Electronic structure

Figure 4.5 shows non spin polarized density of states of all compounds calculated within GGA approximation. Due to octahedral crystal field, five fold degeneracy in B: *d* states have been removed partially and we get high lying double degenerate B: *e_g^σ* (*e_g*) states while low lying B: *t_{2g}* states are three fold degenerate. Further due to *trigonal* distortion *t_{2g}* states get split into single degenerate *a_{1g}* and double degenerate *e_g^π*. Similarly square planner crystal field allows a large energy separation in between high lying Cu: *d_{x²-y²}* and the rest. From Fig. 4.5, we can see that metallicity mainly originates from partially filled B: *t_{2g}* states showing less than half filled (*d⁵*) nature. It can also be noticed that *t_{2g}* and *e_g* separation increases as we move from 3*d* (Co) to 4*d* (Rh) to 5*d* (Ir) elements at B site. This energy separation becomes maximum for CClrO, large crystal field splitting could be a reason for such large splitting (~ 3 eV). Most of Cu states are occupied well below

the Fermi energy (~ 2 eV), while some part are unoccupied and lie above ϵ_F . In order to understand the spin-states of $\text{CaCu}_3\text{B}_4\text{O}_{12}$ (B= Co, Rh, Ir) we have performed spin-polarized ferromagnetic density of states and band structure calculated within GGA+U approximation. From Figure 4.6, we can notice that Cu: d , O: p and B: d states are

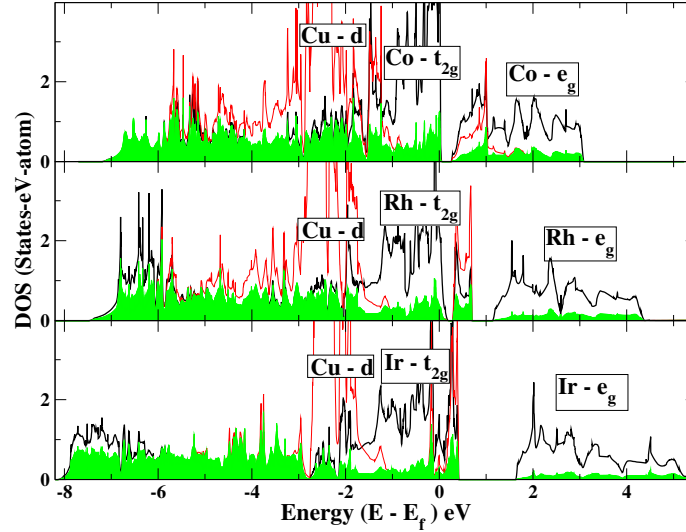


Figure 4.5: Non-spin polarized density of states of CCCoO (top panel), CCRhO (middle panel) and CCIrO (bottom panel). Black and red lines correspond to B: d and Cu: d states, while O: p states are shown by filled green colour. Energy is measured from Fermi energy (ϵ_F).

highly intermixed with each other, the degree of admixture varies between the compounds. For CCCoO, Cu: $d_{x^2-y^2}$ - O: p are highly mixed up with Co: e_g^σ which are completely empty in either spin channel, suggesting Cu^{3+} ($d^9 \underline{L}$) like oxidation state of Cu in CCCoO. Considering Co: d states it is evident that Co: e_g^σ orbitals are slightly occupied in majority spin channel, while in the minority spin channel, only occupied Co: d part is the e_g^π states of Cobalt. Such intermediate spin configuration is also evident from $\sim 1.68 \mu_B$ spin moment at Co site. Moving towards to Rh compound, it can be easily seen that the admixture between Cu: $d_{x^2-y^2}$ - O: p states with Rh: d states has been reduced significantly compared with that of CCCoO. Here, Cu: $d_{x^2-y^2}$ - O: p states is partially occupied in majority spin channel, while these orbitals are completely empty in minority spin channel. Thus, Cu valency in CCRhO is intermediate between 2+ and 3+ ($\sim 2.5+$). Similarly it can be noticed that Rh: e_g^σ states are unoccupied in either spin channel, while a_{1g} is partially populated in minority spin channel, resulting low spin configuration for Rh, which is also evident from $\sim 0.21 \mu_B$ spin moment and largely quenched orbital moment

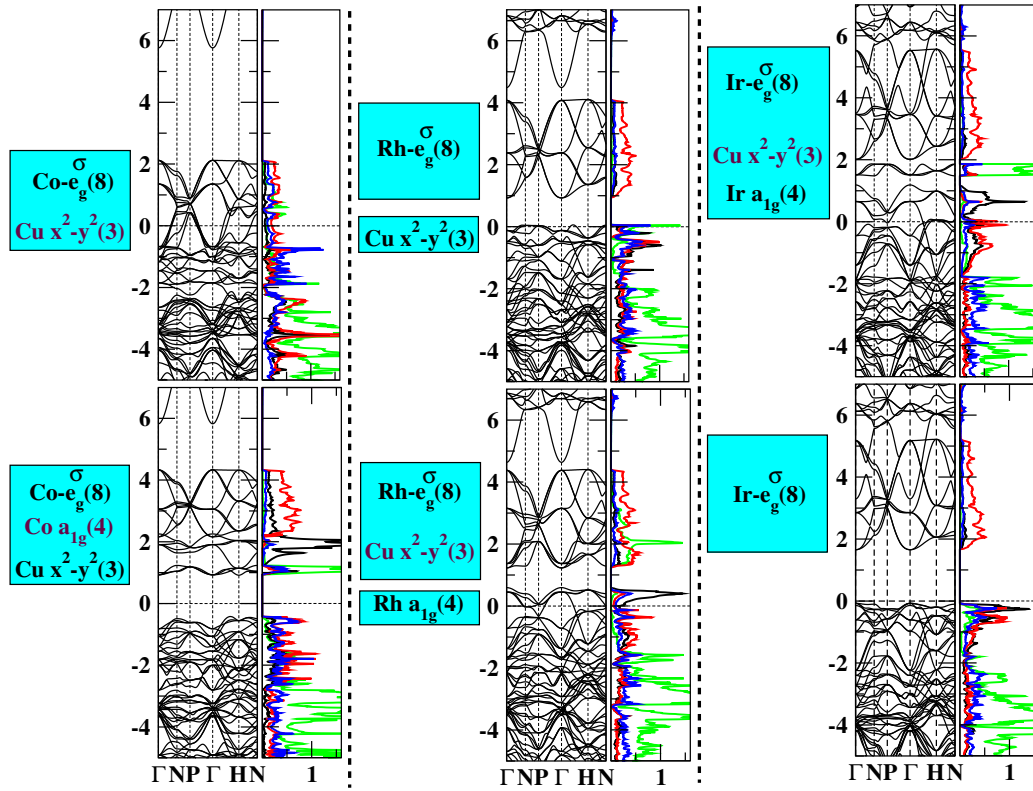


Figure 4.6: Spin polarized DOS and band structure of CaCuCoO (left panel), CCRhO (middle panel) and CClrO (right panel). Top (bottom) panel stands for majority (minority) spin channel. Black, red, green and blue show B: t_{2g} , B: e_g , Cu: d and O: p states. Energy is measured w.r.t Fermi energy (ϵ_F). Number of bands of corresponding character have been shown within parenthesis.

of $0.05 \mu_B$. Finally, we consider CClrO. In contrast to both CCCoO and CCRhO, mixing of Cu: $d_{x^2-y^2}$ -O: p hybridized states with Ir: d has reduced drastically, which results isolated unoccupied Cu: $d_{x^2-y^2}$ in majority spin channel, while in minority spin channel these three Cu: $d_{x^2-y^2}$ states lie just below the Fermi energy (ϵ_F) leading to situation like pure ionic Cu^{2+} oxidation state, also evident from $0.65 \mu_B$ spin moment at Cu site in CClrO. Focusing on the Ir: d states in majority spin channel, it is visible that slightly occupied Ir: a_{1g} state gives rise the metallic behavior of this compound. Such unoccupancy in Ir: a_{1g} orbital introduces $0.45 \mu_B$ spin moment at Ir site and Ir shows low spin configuration like Rh. Oxygens in CClrO shows significant moment ($\sim 0.12 \mu_B$) due to strong hybridization with Ir. Such a d^5 configuration in Ir^{4+} has been studied extensively in recent time where strong spin-orbit coupling (SOC) is found to introduce many interesting properties [19, 20, 30, 31]. The presence of a significant SO interaction is found to mix up and down spins and destroys half-metallicity in CClrO (see Fig. 4.7). Calculated orbital moment at Ir site becomes 0.12

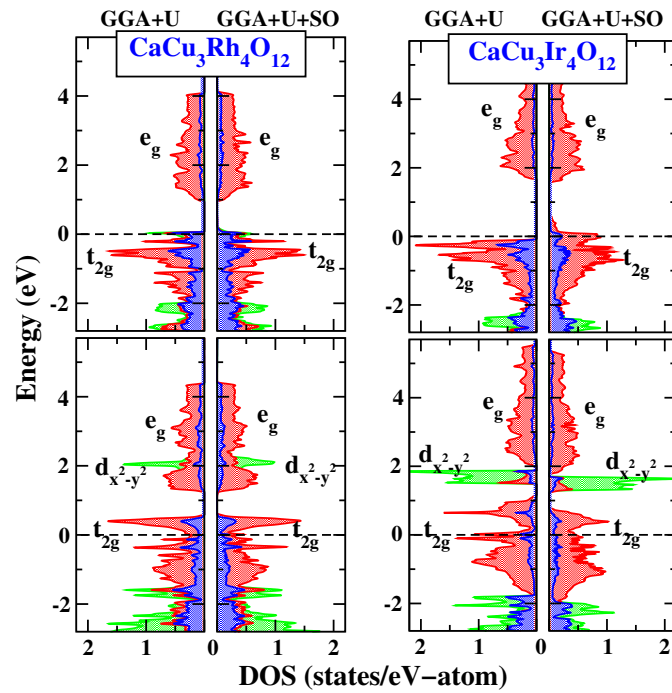


Figure 4.7: Effect of Spin-Orbit coupling. Top (bottom) panels are majority (minority) spin channel. Energy is measured from the Fermi energy. Red, green and blue stand for the DOS of B: d , Cu: d O: p states respectively. Spin-orbit coupling is much more effective for CClrO. Ir: t_{2g} moves towards the Fermi energy and destroys the half-metallicity.

μ_B smaller than the spin moment ($\mu_{orbital}/\mu_{spin} = 0.27$). The large branching ratio of close to 3.8 signifies the presence of a large SOC at the Ir site. The evolution of nominal valance of Cu from $3 + (d^9 \underline{L})$ to $2 +$, as one moves from $3d$ (Co) to $4d$ (Rh) to $5d$ (Ir) elements at the B-site, is monitored by mixing between B-site d states and Cu: $d_{x^2-y^2}$ -

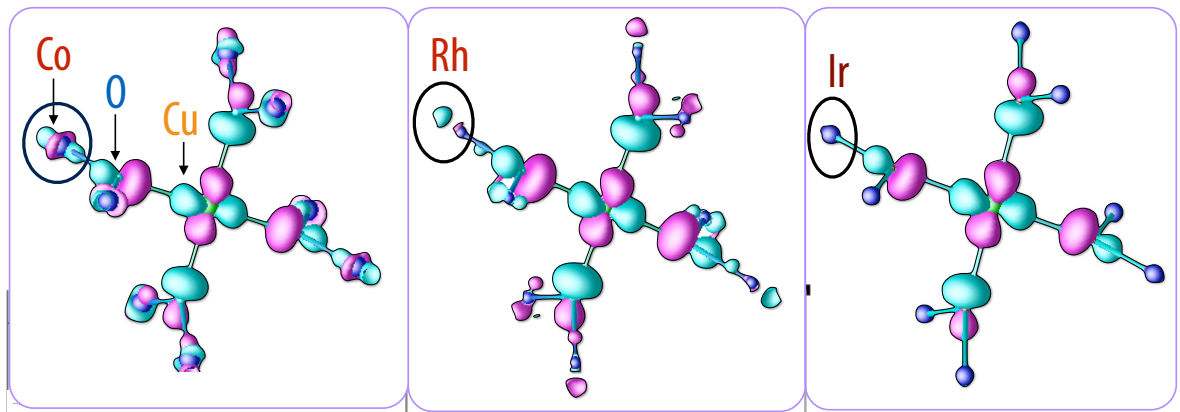


Figure 4.8: Effective Wannier function plot for Cu: $d_{x^2-y^2}$ - O: p hybridized states of all three compounds, CCCoO (left panel), CCRhO (middle panel), CClrO (right panel). Lobes with different signs are coloured as magenta and cyan. Cu, B, O sites are denoted by green, blue and light blue coloured spheres.

O: p states and can be vividly visualized in the effective Wannier function plots shown in Fig. 4.8. As clearly seen, the Wannier function reflecting the $pd\sigma$ type antibonding nature between Cu: d and O: p states, centred at the Cu site have the orbital character of $d_{x^2-y^2}$ symmetry, and the tail is shaped according to the symmetry of the orbitals mixed with it at the B site. Specifically, moving from CCCoO to CCRhO to CCIrO, we find the weight at the tails centred at the B-site progressively diminishes (shown by circle in Fig. 4.8).

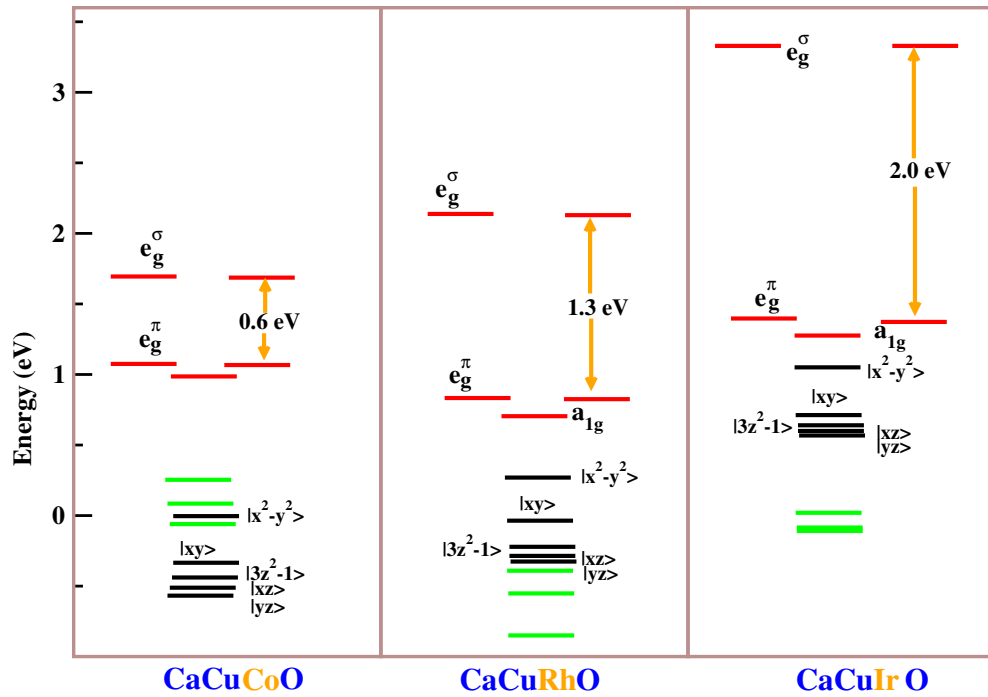


Figure 4.9: Crystal field splitting of B: d , Cu: d and O: p states are shown by red, black and green coloured lines. As we move from $3d$ (left panel) to $4d$ (middle panel) to $5d$ (right panel) element at the B site, B: $[e_g^\sigma - e_g^\pi]$ separation increases, while O: p states are pushed below the Cu: d orbitals. Energy is measured w.r.t Cu: $d_{x^2-y^2}$ state of CCCoO.

The nature of unmixing/ dehybridization effect in between Cu-O and B site in moving from $3d$ to $4d$ to $5d$ element at the B site can also be further elucidated by considering the energy level position of B: d , Cu: d , O: p states as shown in Fig. 4.9. As we move from $3d$ (Co) to $4d$ (Rh) to $5d$ (Ir) element at B site, relative position of Cu: $d_{x^2-y^2}$ with respect to O: p levels increases. Increased crystal field splitting ($e_g^\sigma - e_g^\pi = a_{1g}$ splitting) at B site just push down the O: p states, resulting weaker and weaker hybridization between Cu and B site as those ions communicate via the intervening oxygen. In addition to this, Cu: $d_{x^2-y^2}$ state is energetically degenerate with the σ state of oxygen, indicating strong $pd\sigma$ type anti-bonding in CCCoO. Such un-mixing of Cu: d and O: p states empathize

a key difference between CClrO and $\text{CaCu}_3\text{Ru}_4\text{O}_{12}$, where for $\text{CaCu}_3\text{Ru}_4\text{O}_{12}$ it was found that the suspected Kondo-like physics was unlikely due to a strong admixing of Cu with O [32, 33]. Similar to that of high- T_c cuprates, for CCCoO, the O p states are positioned above Cu: $d_{x^2-y^2}$, placing Cu in to a negative charge transfer regime, which promotes a high- T_c cuprate-like $d^9 \underline{L}$ state similar to the Zhang-Rice singlet state. As we move from CCCoO to CCRhO to CClrO, the progressive weakening of covalency between the B sublattice and Cu-O sublattice has been noticed. As a result, the O: $p_{x,y}$ hole, doped within CuO_4 plane of CCCoO, causing Zhang-Rice akin spin singlet state, is completely removed to B site for CClrO. The movement of the oxygen hole from the CuO_4 plane to the B sublattice as indicated from our theoretical side, has been further proved in the following by experimental XAS measurements.

4.4.3 Experimental observation

Soft X-ray absorption spectroscopy (XAS) is an ideal tool to determine the oxidation states of both B and Cu site in CCCoO, CCRhO and CClrO. First we will discuss the evaluation of the Cu electronic structure. From Cu- L_3 edge spectroscopy (Fig. 4.10), the sharp peak ~ 930 eV stands for the transition from the d^9 ground state, featuring a hole in the Cu: $d_{x^2-y^2}$ band, to the $\underline{c}d^{10}$ (\underline{c} denotes a core hole at Cu: $2p$ core state) excited state. Shoulder present at 931.5 eV shows a direct signature of Zhang-Rice (ZR) spin singlet state [34–36], is a transition from ground state $d^9 \underline{L}$ to $\underline{c}d^{10} \underline{L}$ excited state. During this transition, Cu mainly remains at $2+$ (Cu: d^9) state, while a ligand hole is distributed over the neighbouring O sites. The interaction in-between core and ligand hole prompted by the photon absorption results an electronic transition from Cu: $2p$ state to unoccupied $d_{x^2-y^2}$ state. Such Co-O mixing is also noticed in CCRhO, where the ZR signature is still present, giving rise to a mixed valency for Cu ($\sim 2.6+$) in CCRhO. Both CCCoO and CCRhO, ground state is mainly described by the ZR like state [37, 38]. Moving towards CClrO, it is clearly seen that $d^9 \underline{L}$ state is no longer present and Cu shows pure ionic $2+$ like oxidation state [34, 39–42]. Multiple split peak appearing ~ 940 eV is due to transition from the meta-stable d^8 state to $\underline{c}d^9$ state. So, in conclusion, ZR spin singlet state, a pair of hole antiferromagnetically coupled within CuO_4 square planer network is the ground state for

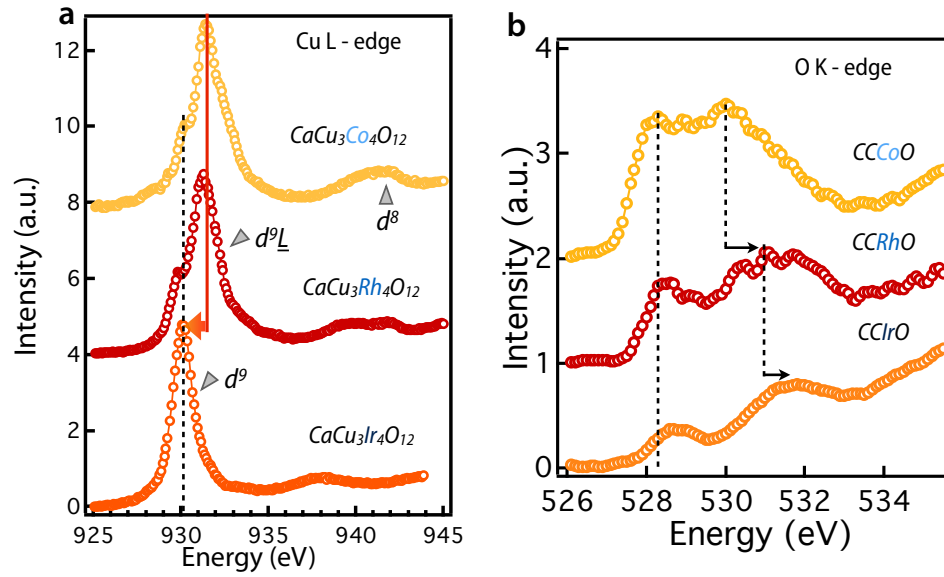


Figure 4.10: (a) Cu-L edge soft XAS of all the compounds. The dotted line is the spectrum before the subtraction of the impurity peak. The dashed line stands for the energy of the d^9 peak. (b) O-K edge spectra shows reduction of spectral intensity as we move from $3d$ (Co) to $4d$ (Rh) to $5d$ (Ir) element at the B site of $\text{CaCu}_3\text{B}_4\text{O}_{12}$. Dashed line at 528 eV shows the energy of O prepeak associated with doped hole.

CCoO, while for CIrO, presence of $5d$ orbital results movement of the hole from Cu site to B (Ir) site [41–45]. Such dehybridization in Cu-O orbitals can also be explained in terms of O-K edge XAS data. Prepeak ~ 528 eV shows oxygen specific signature for $d^9 \underline{L}$ state. As we move from $3d$ (Co) to $4d$ to $4d$ element at the B site the prepeak intensity \sim

Table 4.2: Comparison between theoretical and experimental spin magnetic moments at B, Cu site in $\text{CaCu}_3\text{B}_4\text{O}_{12}$ (B= Co, Rh, Ir).

	$\text{CaCu}_3\text{Co}_4\text{O}_{12}$	$\text{CaCu}_3\text{Rh}_4\text{O}_{12}$	$\text{CaCu}_3\text{Ir}_4\text{O}_{12}$
Cu-site (theory)	3^+	2.5^+	2^+
Cu-site (experimental)	$(2.90 \pm 0.15)^+$	$(2.63 \pm 0.10)^+$	$(2.03 \pm 0.10)^+$
B-site (theory)	3.25^+	3.6^+	4^+
B-site (experimental)	3.25^+	$(3.64 \pm 0.10)^+$	4^+

528 eV decreases, suggesting reduction of ligand hole on oxygen *ie.* available empty states at O site decreases for the presence of higher order d orbitals [46–49]. For CIrO, this prepeak disappears completely, indicating hole is no longer bond to the Cu site which is the mirror image of our crystal-field splitting diagram and effective Wannier function plot (see Fig. 4.8, 4.9). The Ir L_3 edge ($2p_{3/2} \rightarrow 5d$ transition) to L_2 edge ($2p_{1/2} \rightarrow 5d$ transition) branching ratio was found to be 3.79 which is close to our finding (~ 3.8).

4.5 Unified Picture

Finally our *ab initio* calculations along with the spectroscopic results motivates us to build a unified framework to explain the emergent physical behaviour of CaCuCoO, CaCuRhO and CaCuIrO. Although an earlier study utilizing electron energy loss spectroscopy found small changes between $3d \rightarrow 4d \rightarrow 5d$ transition metal ion at the B-site of A-site ordered perovskites, CaCu₃B₄O₁₂ (B= Ir, Ru, Ti) [8], our study reveals that upon ascending a column of the periodic table from Ir to Co, the Cu: $d_{x^2-y^2}$ orbital occupation changes from pure ionic $3d_{x^2-y^2}^9$ ($S= 1/2$) for CClrO to the non-magnetic cuprate Zhang-Rice-like state with $3d^9 \underline{L}$ ($S= 0$) for CCCoO. In addition to it, these localized and magnetically active Cu d states in CClrO shift towards the Fermi surface representing a drastic change in orbital hybridization compared with both CCRhO and CCCoO. Significant change in the Cu orbital occupation results in the mixed valence intermediate spin state of $\text{Co}^{3.25+}$, mixed valence Rh $\sim 3.6+$, but ionic $\text{Ir}^{4+}(5d^5)$. These findings allow us to place the three compounds under discussion in the context of the Doniach phase diagram as shown in Fig. 4.11, where the fundamental control parameter is the average occupation $\langle n_{Cu} \rangle$ of the Cu: $d_{x^2-y^2}$ orbital modulated by the mixed B-site d - and O: p hybridized bands. In the Doniach Phase diagram, ground state is defined by the competition between RKKY-type magnetic exchange between magnetic holes on Cu with the Kondo screening by conduction carries from the B-O sublattices. For CClrO, with a $S = 1/2$ d hole localized on Cu, the large magnetic exchange is comparable in strength with the Kondo screening, resulting in the strongly enhanced effective mass observed with transport and thermal measurements. Thus, Cheng *et al.* [8] placed CClrO into the heavy fermion regime I in Fig. 4.11 with the antiferromagnetic local moment short-range magnetism. In moving from Ir to Rh and Co, the Kondo energy scale begins to increase because of the collective hybridization of Cu d -holes into the ZR singlets. With the strong reduction in the Cu: $d_{x^2-y^2}$ orbital occupation, both CCRhO and CCCoO enter the regime II of mixed valency (or Kondo liquid phase) in Fig. 4.11. Unlike regime I, in the mixed valence regime quantum fluctuations between different electronic configurations are highly significant; in this regime, the local electronic and magnetic structure of Kondo centres (Cu) are defined by the redistribution of electrons between Cu d states and electrons from the strongly hybridized d - and p -states of Rh (Co)

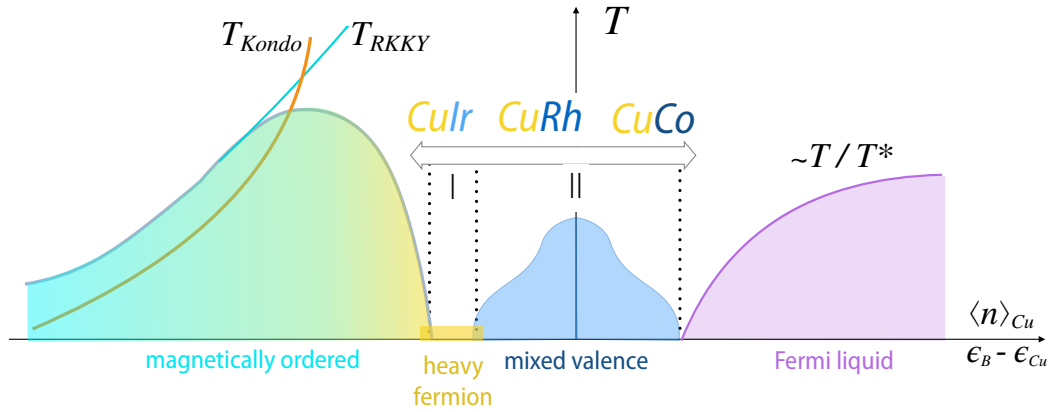


Figure 4.11: Doniach phase diagram of Kondo lattice $\text{CaCu}_3\text{B}_4\text{O}_{12}$ plotted as a function of cu occupancy $\langle n_{Cu} \rangle$. Energy associated with Kondo effect is $T_{K(Kondo)} \propto \left[\exp\left(-\frac{1}{JN(E_F)}\right) \right]$, while magnetic ordering temperature in RKKY interaction becomes $T_{RKKY} \propto \left[J^2 N(E_F) \right]$. $N(E_F)$ is the DOS at Fermi energy E_F , while J is coupling constant in between the impurity spin and conduction electrons. Since both energy, $K_B T_K$ and $K_B T_{RKKY}$, depend on coupling constant J , an unified phase diagram considering both interactions, was established by Doniach. For small values of $|J|$ ($T_{RKKY} \gg T_K$), the RKKY interaction dominates and results a magnetically ordered ground state. For strong coupling *ie.* larger values of J , system becomes non-magnetic because of Kondo effect. In the paramagnetic state, each site scatters electrons with a phase shift of $\sim \pi/2$ [3]. RKKY and Kondo characteristic energies become comparable for a critical value J_C . For $J \gg J_C$ ($T_K \gg T_{RKKY}$), Kondo effect compensates local moment resulting non-magnetic ground state. In the vicinity of the critical point ($J = J_C$), non-Fermi liquid behavior is observed. Physical properties around this critical point show anomalous temperature dependence of low temperature physical properties, like specific heat, resistivity, magnetic susceptibility. Landau Fermi-Liquid is formed below a characteristic temperature T^* . As we move from the deep below Fermi energy to its above, sequence of phases that appears in the system are the following: RKKY-dominated magnetically ordered state \rightarrow heavy fermion state \rightarrow mixed valence state \rightarrow completely nonmagnetic state.

and O, that is, $|3d^9, S = 1/2\rangle$ versus $|3d^9 \underline{L}, S=0\rangle$. The conjectured microscopic framework that links the electronic and magnetic ground state of the A-site perovskites with macroscopic physical behaviour opens a path in designing emergent ordered phases with heavy fermion behaviour, quantum criticality and unconventional superconductivity in the magnetic Kondo lattice of cuprate-like moments.

4.6 Conclusion

We have studied the electronic structure of three iso-structural A-site ordered perovskite oxides $\text{CaCu}_3\text{B}_4\text{O}_{12}$ ($B = \text{Co}, \text{Rh}, \text{Ir}$). Our calculations reveal that B-site cations strongly control the mixing of Cu: d , O: p and B: d states. Localize hole at the Cu^{2+} site shows heavy-fermion like character. As we move from $5d$ to $4d$ element at the B-site, O: p states

are pushed towards the Cu: d states *ie.* Kondo site spin starts interacting with the holes from the O: p states which increases the Kondo coupling strength [50]. Such a Kondo like

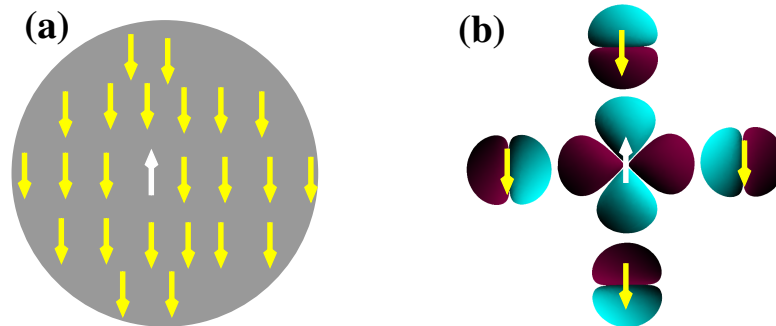


Figure 4.12: Many-body spin singlet state (a) Kondo effect arising from the anti-parallel alignment of the itinerant carrier spin (yellow arrow) and impurity spin (white arrow) (b) Cu: $d_{x^2-y^2}$ -O: p hybridized state in a CuO_4 plane forms Zhang-Rice state. Wavefunction of opposite phases are separated by their colours.

spin singlet becomes more prominent for CCCoO where Kondo screening gives rise to the many-body Zhang-Rice like spin singlet state [50] as shown in Fig. 4.12. In other words, as we move from $5d$ to $4d$ to $3d$ element at the B-site of $\text{CaCu}_3\text{B}_4\text{O}_{12}$, Kondo like coupling strength increases progressively. Hole at the oxygen site forms Zhang-Rice singlet state for $\text{B} = \text{Co}, \text{Rh}$ while for CCIrO , this hole goes to Ir site. As a result, itinerant carriers from Ir-O hybridized states in CCIrO place this compound in the heavy fermion region of the Doniach phase diagram, while Kondo effect gives rise to mixed valency in both CCRhO and CCCoO .

Bibliography

- [1] L. Kouwenhoven and L. Glazman, Phys. World **14**, **1**, 33 (2001).
- [2] Y.-J. Zhao, T. Shishidou, and A. J. Freeman, Phys. Rev. Lett. **90**, 047204 (2003);
F. Qu and P. Hawrylak, Phys. Rev. Lett. **96**, 157201 (2006).
- [3] P. Coleman, arXiv:cond-mat/0612006.
- [4] S. Doniach, Physica B **91**, 231 (1977);
N. Read, D. M. Newns, and S. Doniach, Phys. Rev. B **30**, 3841 (1984);
Y. ōnuki, R. Settai, K. Sugiyama, T. Takeuchi, T. C. Kobayashi, Y. Haga, and E. Yamamoto, J. Phys. Soc. Jpn. **73**, 769 (2004).
- [5] T. Willers, F. Strigari, Z. Hu, V. Sessi, N. B. Brookes, E. D. Bauer, J. L. Sarrao, J. D. Thompson, A. Tanaka, S. Wirth, L. H. Tjeng, and A. Severing, Proc. Nat. Acad. Sci. U.S.A. **112**, 2384 (2015).
- [6] V. A. Sidorov, M. Nicklas, P. G. Pagliuso, J. L. Sarrao, Y. Bang, A. V. Balatsky, and J. D. Thompson, Phys. Rev. Lett. **89**, 157004 (2002);
J. Paglione, M. A. Tanatar, D. G. Hawthorn, Etienne Boaknin, R. W. Hill, F. Ronning, M. Sutherland, Louis Taillefer, C. Petrovic, and P. C. Canfield, Phys. Rev. Lett. **91**, 246405 (2003);
J. Paglione, T. A. Sayles, P.-C. Ho, J. R. Jeffries and M. B. Maple, Nature Physics **3**, 703 (2007);
R. R. Urbano, B. -L. Young, N. J. Curro, J. D. Thompson, L. D. Pham, and Z. Fisk, Phys. Rev. Lett. **99**, 146402 (2007).

- [7] P. Aynajian, E. H. da Silva Neto, A. Gyenis, R. E. Baumbach, J. D. Thompson, Z. Fisk, E. D. Bauer, A. Yazdani, *Nature* **486**, 201 (2012).
- [8] J.-G. Cheng, J.-S. Zhou, Y.-F. Yang, H. D. Zhou, K. Matsubayashi, Y. Uwatoko, A. MacDonald, J. B. Goodenough, *Phys. Rev. Lett.* **111**, 176403 (2013);
Y. Xina, H.D. Zhou, J.G. Cheng, J.S. Zhou, J.B. Goodenough, *Ultramicroscopy* **127** 94 (2013).
- [9] C. McGuinness, J. E. Downes, P. Sheridan, P.-A. Glans, K. E. Smith, W. Si, P. D. Johnson, *Phys. Rev. B* **71**, 19511 (2005).
- [10] H. Shiraki, T. Saito, T. Yamada, M. Tsujimoto, M. Azuma, H. Kurata, S. Isoda, M. Takano, Y. Shimakawa, *Phys. Rev. B* **76**, 140403(R) (2007).
- [11] I. Yamada, K. Takata¹, N. Hayashi, S. Shinohara, M. Azuma, S. Mori, S. Muranaka, Y. Shimakawa, M. Takano, *Angew. Chem. Int. Ed.* **47**, 7032 (2008).
- [12] Y. Morita, T. Sudayama, K. Takubo, H. Shiraki, T. Saito, Y. Shimakawa, T. Mizokawa, *Phys. Rev. B* **81**, 165111 (2010).
- [13] N. Hollmann, Z. Hu, A. Maignan, A. GÃijnthner, L.-Y. Jang, A. Tanaka, H.-J. Lin, C. T. Chen, P. Thalmeier, L. H. Tjeng, *Phys. Rev. B* **87**, 155122 (2013).
- [14] W.-T. Chen, T. Saito, N. Hayashi, M. Takano, Y. Shimakawa, *Sci. Rep* **2**, 449 (2012).
- [15] I. Yamada, S. Ishiwata, I. Terasaki, M. Azuma, Y. Shimakawa, M. Takano, *Chem. Mater.* **22**, 5328 (2010).
- [16] J. Zaanen, G. A. Sawatzky, J. W. Allen, *Phys. Rev. Lett.* **55**, 418 (1985).
- [17] B. J. Kim, Hosub Jin, S. J. Moon, J.-Y. Kim, B.-G. Park, C. S. Leem, Jaejun Yu, T. W. Noh, C. Kim, S.-J. Oh, J.-H. Park, V. Durairaj, G. Cao, E. Rotenberg, *Phys. Rev. Lett.* **101**, 076402 (2008).
- [18] G. Cao, J. Bolivar, S. McCall, J. E. Crow, R. P. Guertin, *Phys. Rev. B* **57**, R11039 (1998).

- [19] D. Haskel, G. Fabbris, Mikhail Zhernenkov, P. P. Kong, C. Q. Jin, G. Cao, M. van Veenendaal, *Phys. Rev. Lett.* **109**, 027204 (2012).
- [20] B. J. Kim, Hosub Jin, S. J. Moon, J.-Y. Kim, B.-G. Park, C. S. Leem, Jaejun Yu, T. W. Noh, C. Kim, S.-J. Oh, J.-H. Park, V. Durairaj, G. Cao, E. Rotenberg, *Phys. Rev. Lett.* **101**, 076402 (2008).
- [21] G. Kresse and J. Furthmüller, *Phys. Rev. B* **54**, 11169 (1996).
- [22] J. P. Perdew, K. Burke, M. Ernzerhof, *Phys. Rev. Lett.* **77**, 3865 (1996).
- [23] S. L. Dudarev, G. A. Botton, S. Y. Savrasov, C. J. Humphreys, A. P. Sutton, *Phys. Rev. B* **57**, 1505 (1998).
- [24] P. E. Blöchl, *Phys. Rev. B* **50**, 17953 (1994).
- [25] P. Blaha, K. Schwarz, G. Madsen, D. Kvasnicka, J. Luitz in *An Augmented Plane Wave+Local Orbitals Program for Calculating Crystal Properties* ed. Schwarz K. Technische Universität Wien (2001).
- [26] <http://www.orbitals.com/orb/ov.htm>
- [27] P. E. Blöchl, P. E., O. Jepsen, O. K. Andersen, *Phys. Rev B* **49**, 16223 (2004).
- [28] O. K. Andersen, T. Saha-Dasgupta, *Phys. Rev. B* **62**, R16219 (2000).
- [29] O. K. Andersen, O. Jepsen, *Phys. Rev. Lett.* **53**, 2571 (1984).
- [30] M. A. Laguna-Marco, D. Haskel, N. Souza-Neto, J. C. Lang, V. V. Krishnamurthy, S. Chikara, G. Cao, and M. van Veenendaal, *Phys. Rev. Lett.* **105**, 216407 (2010).
- [31] W. Witczak-Krempa, G. Chen, Y. B. Kim, L. Balents, *Annu. Rev. Condens. Mater. Phys.* **5**, 57 (2014).
- [32] S. Tanaka, H. Takatsu, S. Yonezawa, Y. Maeno, *Phys. Rev. B* **80**, 035113 (2009).
- [33] M. Mizumaki, T. Mizokawa, A. Agui, S. Tanaka, H. Takatsu, S. Yonezawa, Y. Maeno, *J. Phys. Soc. Jpn* **82**, 024709 (2013).

- [34] J. Chakhalian, J. W. Freeland, G. Srajer, J. Stremper, G. Khaliullin, J. C. Cezar, T. Charlton, R. Dalgliesh, C. Bernhard, G. Cristiani, H.-U. Habermeier, B. Keimer, Nat. Phys. **2**, 244 (2006).
- [35] N. Nücker, E. Pellegrin, P. Schweiss, J. Fink, S. L. Molodtsov, C. T. Simmons, G. Kaindl, W. Frentrup, A. Erb, G. Müller-Vogt, Phys. Rev. B **51**, 13 (1995).
- [36] M. Gioni, J. B. Goedkoop, R. Schoorl, F. M. F. de Groot, J. C. Fuggle, F. Schäfers, E. E. Koch, G. Rossi, J.-M. Esteva, R. C. Karnatak, Phys. Rev. B **39**, 1541 (1989).
- [37] T. Mizokawa, A. Fujimori, H. Namatame, Y. Takeda, M. Takano, Phys. Rev. B **57**, 16 (1998).
- [38] R. Sarangi, N. Aboeella, K. Fujisawa, W. B. Tolman, B. Hedman, K. O. Hodgson, E. I. Solomon, J. Am. Chem. Soc. **128**, 8286 (2006).
- [39] Talia Eldar-Geva, Philip J.M Lowe, Vivien MacLachlan, B.Sc.a, Luk Rombauts, M.D., Ph.D.a, David L Healy, Ph.D.a., Rev. Mod. Phys. **70**, 1039 (1998).
- [40] J. Chakhalian, J. W. Freeland, H.-U. Habermeier, G. Cristiani, G. Khaliullin, M. van Veenendaal, B. Keimer, Science **318**, 1114 (2007).
- [41] Y Tokura, Rep. Prog. Phys. **69**, 797 (2006).
- [42] M. McCormack, S. Jin, T. H. Tiefel, R. M. Fleming, Julia M. Phillips and R. Ramesh, Appl. Phys. Lett. **64**, 3045 (1994).
- [43] Ritimukta Sarangi, Nermeen Aboeella, Kiyoshi Fujisawa, William B. Tolman, Britt Hedman, Keith O. Hodgson, Edward I. Solomon, J. Am. Chem. Soc. **128**, 8286 (2006).
- [44] Z Hua, G Kaindl, S.A Ward, D Reinen, F.M.F de Groot, B.G Müller, Chem. Phys. **232**, 63 (1998).
- [45] G. Kaindl, O. Streb, A. Kolodziejczyk, W. Schäfer, R. Kiemel, S. Löss, S. Kemmler-Sack, R. Hoppe, H.P. Müller, D. Kissel, Phys. B Condens. Matter **158**, 446 (1989).

- [46] C. T. Chen, F. Sette, Y. Ma, M. S. Hybertsen, E. B. Stechel, W. M. C. Foulkes, M. Schuster, S-W. Cheong, A. S. Cooper, L. W. Rupp, Jr., B. Batlogg, Y. L. Soo, Z. H. Ming, A. Krol, and Y. H. Kao, Phys. Rev. Lett. **66**, 104 (1991).
- [47] N. Nücker, J. Fink, J. C. Fuggle, P. J. Durham, W. M. Temmerman, Phys. Rev. B **37**, 5158 (1988).
- [48] N. Nücker, E. Pellegrin, P. Schweiss, J. Fink, S. L. Molodtsov, C. T. Simmons, G. Kaindl, W. Frentrup, A. Erb, and G. Müller-Vogt, Phys. Rev. B **51**, 8529 (1995).
- [49] P. Kuiper, G. Kruizinga, J. Ghijsen, M. Grioni, P. J. W. Weijs, F. M. F. de Groot, G. A. Sawatzky, H. Verweij, L. F. Feiner, and H. Petersen, Phys. Rev. B **38**, 6483 (1988).
- [50] M. Yu. Kagan and K. I. Kugel, Usp. Fiz. Nauk **171**, 577 (2001) [Phys. Usp. **44**, 553 (2001)];
Q. Yin, A. Gordienko, X. Wan, S. Y. Savrasov, Phys. Rev. Lett. **100**, 066406 (2008);
R. Eder, P. Wröbel, Phys. Rev. B **84**, 035118 (2011);
J. Moreno, S. Qin, P. Coleman, L. Yu, Phys. Rev. B **64**, 085116 (2001).

A first principles density functional investigation of ligand-protected eight atom gold nanoclusters*

5.1 Background

Relativistic effect is an important aspect for gold. $1s$ electron of gold reaches a speed about 58% of that of light and electronic mass at this $1s$ orbital also increases by an amount of 20%. Thus the $1s$ orbital shrinks and similar effect takes place for s orbitals of higher quantum number. The relativistic to nonrelativistic ratios of the orbital radii (described by $\langle r \rangle_R / \langle r \rangle_{NR}$) for neutral gold becomes 0.880 for $1s$, 0.873 for $2s$, 0.900 for $3s$, 0.911 for $4s$, 0.907 for $5s$, 0.827 for $6s$ [1]. Thus, $6s$ orbital shrinks more than $1s$. Fig. 5.1 shows a plot of $\langle r \rangle_R / \langle r \rangle_{NR}$ of the $6s$ orbital for several elements from the periodic table. This radial function shows a minima at gold and platinum. Similar contraction also takes place for p orbital. Contraction of s or p results from the direct relativistic effect while indirect relativistic orbital expansion also plays crucial role in gold cluster stability [2]. d or f orbitals are hardly affected because of the centrifugal potential $I(I + 1)/r^2$ where I is the azimuthal quantum number and r is the radius. As a result, effective potential of d or f orbital is more effectively screened due to such relativistic contraction of s , p orbitals. As a result of such interesting relativistic effect, $6s$ orbital of gold shrinks while $5d$ is pushed

*This chapter is based on the article : AIP Advances **1**, 032150 (2011).

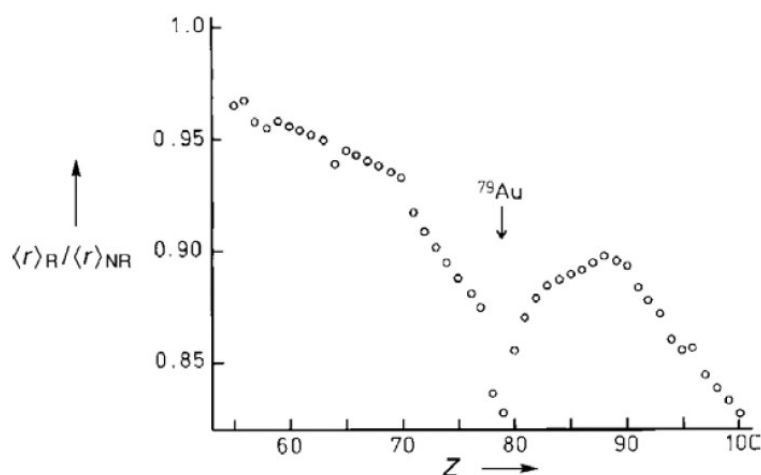


Figure 5.1: Relativistic effect on the $6s$ orbital. Reproduced from [3].

away from the nucleus. Study of Au cluster thus forms an active area of research. The properties exhibited by the gold clusters are found to be extremely sensitive to the size, structure and dimension of the cluster. This led to extensive research to determine the size N at which the 3D geometries become energetically more favorable over the 2D geometries. Several experimental and theoretical studies have predicted this number to fall in a range from 6 to 13 [4–16]. For anionic and cationic gold clusters the 2D-3D transitions are observed to occur at $N = 13$ and $N = 8$, respectively. Theoretical calculations for neutral clusters have predicted the transition to occur at six [4], seven [5, 6], eight [7, 8], as well as in the range from 11-15 atom clusters [9–16]. It has been anticipated that the different methods and models adopted to determine the cluster size at which the 2D-3D transition takes place can possibly be one of the reasons for the large spread in the obtained results (from 6-15). Gold clusters are reported to retain their planar structures to cluster sizes larger compared to Ag and Cu clusters which remain planar upto 7 atom cluster sizes only [17]. This has been anticipated to occur due to the relativistic effect in gold which results in a strong sd -hybridization leading to a delocalization of the d-electrons over the volume of the cluster which in turn produces a stronger d-d interaction of neighboring Au atoms [17].

However, the clusters observed in experiments are prepared in ligand-resolved solution. “passivators”, originally employed to check the growth of the clusters which otherwise would grow to large sizes, appear to play a more active role in terms of determining the

structure of the cluster primarily by influencing the surface geometry through a change of surface chemistry. This has led to several theoretical studies involving cluster together with ligands. Considering small Au atoms, particularly those falling in the range of crossover transition between 2D-like to 3D-like geometry theoretical studies have been carried out for 11-atom and 13-atom clusters [18, 19]. The studies indicate that the structure of small gold clusters are altered substantially in the presence of ligands, in the sense the planar geometries predicted by calculations for bare clusters were found to be stabilized in 3D-like geometries upon ligation. The rationale for the stabilization of markedly different geometries were traced to Au-ligand covalency.

5.2 Motivation behind the project

In 2008, Au_8 has been prepared by etching with “excess”[†] glutathione [32]. Strong bluish-green luminescence has been noticed in glutathione capped Au_8 with excitation and emission maxima 370 and 465 nm respectively. Such fluorescent property suggests that glutathione capped Au_8 complex is not metallic. But the experimental structural analysis has not been provided for this magic cluster which have also been predicted by several studies to be a possible case for 2D-3D crossover. In the present study based on first principles density functional theory (DFT) calculations, we investigate the effect of ligand capping on the results of the earlier studies on the stabilization of 2D and 3D geometries. In this present study, we have considered the ligand molecule as ethyl mercaptan (CH_3-CH_2SH), a small structure of glutathione ($HO_2CCH_2NHCOCH(NH_2)CH_2CH_2CONHCH(CO_2H)-CH_2SH$), the ligand which was used for the synthesis of the 8-atom clusters [32].

5.3 Computational Details

All our calculations were performed by using the PWscf (plane wave self consistent field) code of the QUANTUM ESPRESSO [33, 34] distribution. The wave functions in this

[†]During etching in presence of “excess” thiol, structural composite follows two distinct mechanism: during first mechanism, unstable gold-thiol molecules form Au-SR (SR : sulfur S within an organic radical R) polymers [30]. Second mechanism is the formation of stable gold nanoclusters with smaller size. Such a process of conversion of larger unstable nanoclusters to smaller stable size is termed as “core-size conversion” [31].

code are expanded in a basis consisting of plane waves. An energy cut-off of 680 eV was chosen for the plane wave based wave functions to converge the binding energies. Relativistic spin-orbit coupling increases the binding energies of all clusters. But the relative stability between different structures was not significantly altered. Thus, Scalar relativistic ultrasoft pseudopotentials [35] was considered for the calculations. Exchange correlation functional was treated under LDA scheme as parametrized by Perdew and Zunger [36]. We checked our results for Perdew-Burke-Ernzerhof Generalized Gradient Approximation (PBE-GGA) [37]. The inter-periodic image distance was maintained at $\sim 8 \text{ \AA}$ for all systems.

Binding energy per gold atom was calculated by the mathematical expression :

$$E_B = -\frac{E_{Au_8} - 8 \times E_{Au}}{8} \quad (5.1)$$

where E_{Au_8} is the total energy of the 8 atom gold cluster, E_{Au} is the energy of an isolated Au atom. The interaction energy E_I of the ligand capped molecules was defined as:

$$N_{Lig} \times E_I = E_{(Au_8+N_{Lig})} - E_{Au_8} - E_{N_{Lig}} \quad (5.2)$$

where $E_{(Au_8+N_{Lig})}$ is the total energy of the Au_8 cluster covered with N number of ligand chains and E_{Lig} is the total energy of the isolated ligand. The ionization potentials (IP) and the electron affinities (EA) have been calculated as:

$$IP = E_{N-1} - E_N \quad (5.3)$$

$$EA = E_N - E_{N+1} \quad (5.4)$$

where E_{N-1} , E_{N+1} and E_N are the total energies of the anionic, cationic and neutral clusters respectively. For vertical IPs and EAs, the total energies were obtained at the optimized coordinates of the neutral cluster with a difference in the number of electrons and for adiabatic IPs and EAs, the geometries were relaxed. *s-d* hybridization index is calculated according to Ref [38]:

$$H_{sd} = \sum_{i=1}^{occ.} \sum_{l=1}^8 w_{i,s}^l w_{i,d}^I \quad (5.5)$$

where $w_{i,s}^l$ and $w_{i,d}^I$ are the squares of the projections of the i -th Kohn-Sham orbital onto the s and d spherical harmonics respectively, centered on the I -th atom integrated over a sphere whose radius is equal to half the nearest neighbor bond distances of the cluster.

5.4 Results and Discussions

In order to study the gold-sulfur interface of $Au_8(SR)_n$ ($R = CH_3 - CH_2H$), we have to understand their structural properties. Thus, at first, we will discuss the optimized structures.

5.4.1 Structural stability of clusters

8 gold ions can be rearranged in various ways. We started our calculations by considering only minimum energy configuration of Au_8 available in literature [12, 38–42]. Considering planar 2D geometry of Au_8 we found that edge-bridge rhombus (star) structure (left structure of top panel in Fig 5.2) is most stable among the planar geometry. Binding energies were calculated by using the formula 5.1. Binding energy of triangle-capped hexagonal (hex) structure (second figure of top panel in Fig 5.2) is 0.01 eV/atom was found to be less compared to that of “star” structure. From the binding energy concept, we can clearly conclude that rest two 2D planar geometry of Au_8 are much more unstable, thus they have been put aside in this current project. From the stability point of view, both star and hex structure are in tough competition, irrespective of basis set or exchange correlation functional or choice of pseudopotentials [12, 40, 41, 43], while bicapped distorted octahedron is reported to be the only stable non-planar 3D geometry of Au_8 [12, 40, 43]. So, in the following discussions, we will focus on only star, hex and 3D bicapped-distorted octahedron structure of 8 atom gold nanocluster.

In order to study the ligand capped structures, first we have to know the amount of ligand coverage *ie.* number of ligand chains to be attached as well as the preferable gold

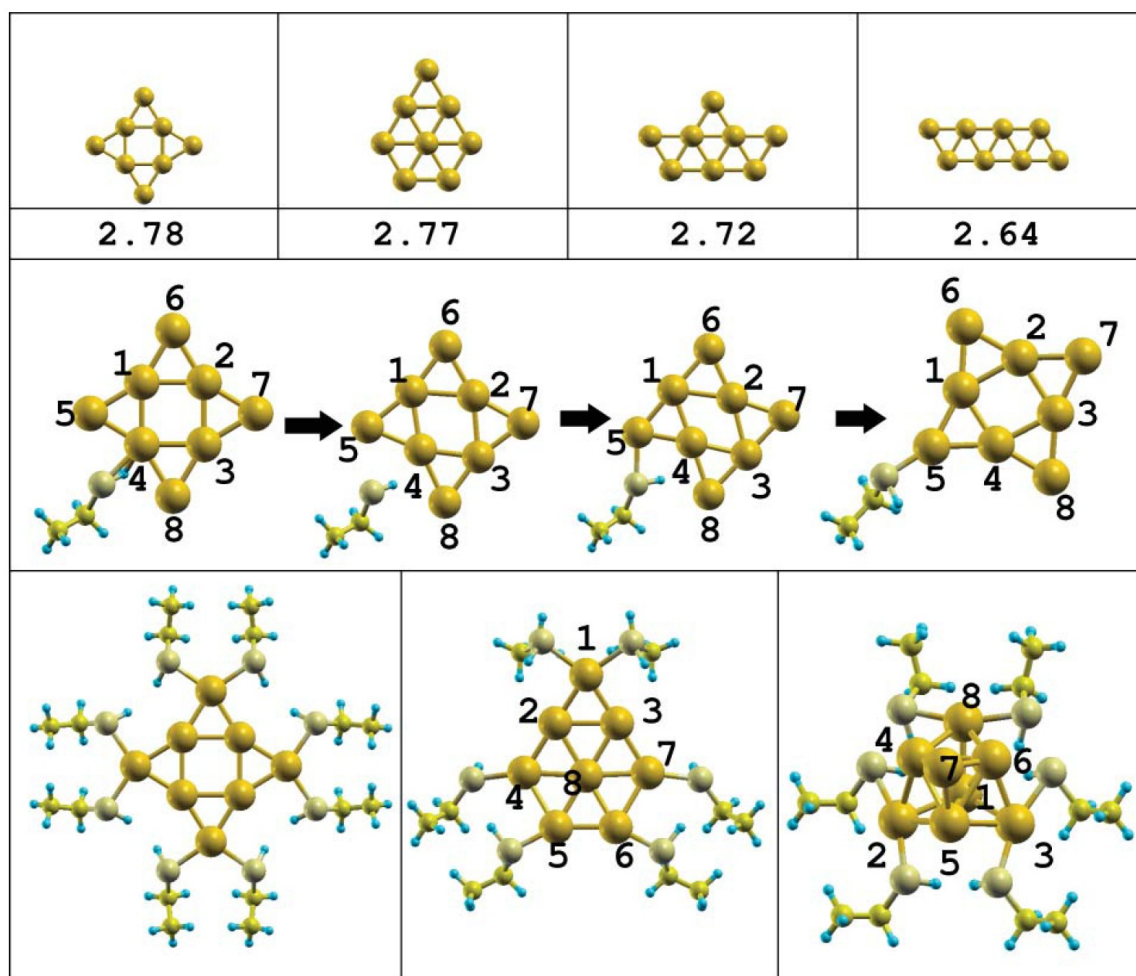


Figure 5.2: Toppanel :: planner (2D) geometry of bare gold nanoclusters with corresponding binding energy E_B (eV/atom). Left and second left structures are termed as star and hex. Middlepanel :: inactivity of 4 nearest neighbor gold site to a mercaptan chain. If we attach any ligand chain to some corner site, after force optimization, ligand chain goes to nearest top site. Bottompanel :: ligand capped cluster configurations. From left to right: four double ligand chains attached to the four top atoms of the star cluster, six ligand chains attached to selective atoms of the hex cluster and the 3D cluster capped by three double ligand chains.

sites for the ligand molecules. Considering star structure, it can be seen that (see Fig. 5.2) this structure has two in-equivalent sites, corner site (pointed as 1, 2, 3, 4) and top site (pointed as 5, 6, 7, 8). Top sites have two nearest Au ions, while corner ions are shared in between 4 gold ions. Single ligand chain attached to the a site, increases the stability of the complex, while ligation at corner site detaches the mercaptan molecule from that site and after force optimization, we found that the ligand chain is attached to a top site, nearest to that corner site (see Fig. 5.2). In conclusion, gold ion with 4 or higher order nearest neighbors is less inactive to the ligand chain. To check the higher order ligand

activity of the star structure, we considered Au-S to be 2.38 Å [44] and \angle S-Au-S as 160° [45]. Our calculations suggested that top site of star structure can attach, at best two ligand molecule, so that full ligaton resulted in the structure shown in the left figure of bottom panel in Fig. 5.2. Optimization reduces the Au-S bond-lengths to 2.47 Å, while \angle S-Au-S is changed to 111.02°. Next we focus on the hex structure. Atom sitting at the top of the triangle (marked as 1 in middle of the bottom panel in Fig. 5.2) has two nearest neighbors, thus two ligand chain can be attached to that site, which after optimization increases the stability. Atom 2 and 3 don't react with the mercaptan chain, may be due to the absence of any dangling bond (4 nearest neighbors). Atom sites 4, 5, 6 and 7 attach maximum single chain of mercaptan, while site 8 with 5 nearest neighbors doesn't react with ligand. Thus, full ligand coverage results into the structure shown in the middle diagram of bottom panel in Fig. 5.2. Finally we consider the non-planner geometry of Au₈. Within this structure, sites marked as 2, 3, 7 and 8 have 3 nearest neighbors, while 1, 4, 5 and 6 sites are located at more than 3 nearest neighbors positions. Considering sites 2, 3, 7 and 8, except site marked as 7, rest attach two ligand chains, site 7 does not prefer to attach any ligand. Thus, three nearest neighbor sites in non-planner geometry attach a pair of ligands which is energetically restricted for planner geometry like the hex structure. In hex structure separation between 2 three nearest neighbor sites is \sim 2.62 Å, while same for 3D becomes 4.38 Å *ie.* ligand capped non-planner structure is much more closely packed with ligand chains leading to less ligand-ligand interaction.

5.4.2 Energetics

Energetics of bare and ligand capped systems are summarized in table 5.1. Numbers within the bracket stand for results obtained within PBE-GGA. Bare planner 2D hex and non-planner (3D)structures become energetically degenerate within LDA. Although 2D hex and 3D structures are covered with 6 number of mercaptan chains, E_I of ligand capped hex structure is greater than 3D structure by 0.18 eV per ethyl mercaptan chain. PBE-GGA also shows similar type of trend. Then we will discuss about the first adiabatic and vertical ionization potentials (IP) and electron affinities (EA) of both bare and ligand capped complex system by using equation 5.3 and 5.4. The vertical IPs and EAs are

Table 5.1: Binding energies E_B (in eV/atom) of bare clusters (B) and the interaction energies E_I (in eV/ligand) of the ligand capped clusters (WL). E_g is the HOMO-LUMO energy gap in eV. The numbers within the brackets for $E_B(B)/E_I(WL)$ indicate results obtained using PBE-GGA

Structure	$E_B(B)/E_I(WL)$	E_g
Star (B)	2.78 (2.06)	1.17
Hex (B)	2.77 (2.02)	0.77
3d (B)	2.77 (2.03)	2.01
Star (WL)	0.88 (0.31)	1.41
Hex (WL)	1.16 (0.49)	1.34
3D (WL)	0.98 (0.33)	1.18

Table 5.2: Adiabatic and vertical ionization potential (AIP, VIP) and electron affinity (AEA, VEA) (in eV) of the bare (B) and ligated (WL) star, hex and 3D clusters.

Structure	VIP	AIP	VEA	AEA
Star (B)	5.67	5.59	3.23	3.29
Star (WL)	2.78	2.65	0.62	0.63
Hex (B)	5.33	5.31	3.37	3.41
Hex (WL)	3.93	3.55	1.28	1.49
3d (B)	5.55	5.54	2.44	2.68
3D (WL)	4.01	3.70	1.60	1.83

calculated with a difference in electron count keeping the same structure between the two calculations. The adiabatic IPs and EAs are obtained by optimization of the structures. Relaxation lowers the IPs and increases the EAs (see Table 5.2) irrespective of bare or ligand-capped clusters. Both EAs and IPs decreases compared with the bare component, indicating that the ligand capping increases the stability of the structures. Such reduction is weaker for 3D geometry compared to planar structures. Thus, passivation is stronger for the planar geometry suggesting that ligand capped planar geometry is much more stable compared to the non-planar (3D) structure

5.4.3 *sd* hybridization

Stability of the individual cluster and their ligand capped complexes can be explained in terms of the *sd* hybridization index. Calculated *sd* hybridization index for bare star, hex and non-planar structure become 1.98, 2.10 and 1.75 respectively. Thus, *sd* hybridization

become stronger for planar 2D geometry. Ligand capped molecules show decrease in the value of sd hybridization index [46]. After ligand attachment, sd hybridization index for star, hex and 3D complexes become 1.24, 1.48, 1.16 respectively. Although values of sd hybridization decreases after ligation, the trend remains almost same for both bare and ligand capped structures.

5.4.4 Density of states

Next we discuss about the density of states (DOS) of each bare cluster system and their ligand capped complexes. From Fig. 5.3, it can be easily seen that $S-[s,p]$ and $C-p$ states appear at lower energies, which also hybridize with $Au-d$ states resulting from the bonding nature of Au and the ligand molecule. HOMO-LUMO gaps for both star and hex complexes increases after ligand attachment, while for non-planar geometry, this energy gap gets reduced. Thus, attachment of ligand increases the stability for planar geometry over the 3D structure. The quantitative values of HOMO-LUMO gaps are summarized in table 5.1.

5.4.5 HOMO-LUMO charge densities

Now, we focus on the charge densities accumulated at the HOMO and LUMO. This analysis will mainly reflect the DOS nature. From Fig. 5.4, it is seen that corner centered HOMO states of bare star structure shows dominant $Au: d_{x^2-y^2}$ nature while same for top sites bears mainly $Au: d_{xy}$ character. This feature remains almost same after ligand attachment. For hex structure, center atom of the hexagon shows mainly $Au: d_{x^2-y^2}$ character. This HOMO charge density remains more or less similar when ligands are attached. Considering non-planar structure, HOMO states are mainly centered on the sites marked as 2, 3, and 8 which moves to the site 7 after ligation. Next we will discuss about LUMO charge densities. Considering star structure, sd hybridized LUMO charges, centered on the 4 top sites, move to the ligand site after ligation *ie.* all dangling bonds of this bare gold cluster are successfully passivated by the ethyl mercaptan chains. The edge atoms of the hex cluster which in bare condition show accumulation of sd -hybridized charge density, similarly get rid of the accumulated charge upon ligand attachment by shifting them to the ligand chains. The sites where ligand is not attached, such sd -hybridization character

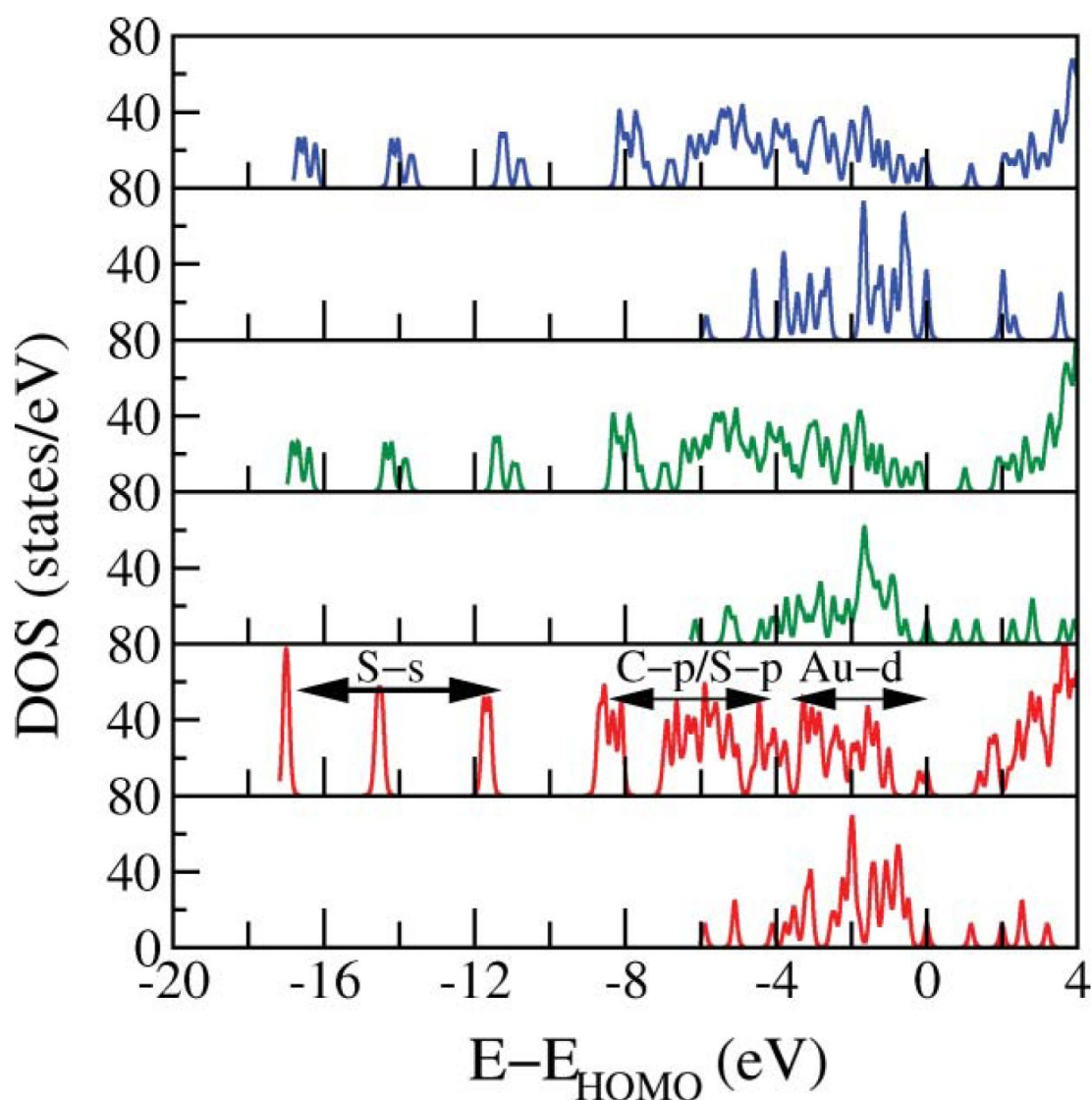


Figure 5.3: From top to bottom, the DOS corresponds to ligated 3D, bare 3D, ligated hex, bare hex, ligated star and bare star, respectively.

is retained though weakened a bit. For the bare 3D structure, the LUMO charge density shows sd -hybridized nature on four atoms. A significant difference appears in the LUMO charge density distribution of the ligated 3D cluster. In this case, the charge density does not move completely from the Au atoms to the ligand chains. Instead it has moved to the central atoms of the cluster. Presence of such unpassivated dangling bonds results the lowering of the HOMO-LUMO gap E_g . The energetics of the ligand capped clusters are therefore mostly governed by the LUMO charge densities, the movement of which in the presence of ligands results in an increase (or decrease) of the energy gap (Fig. 5.3).

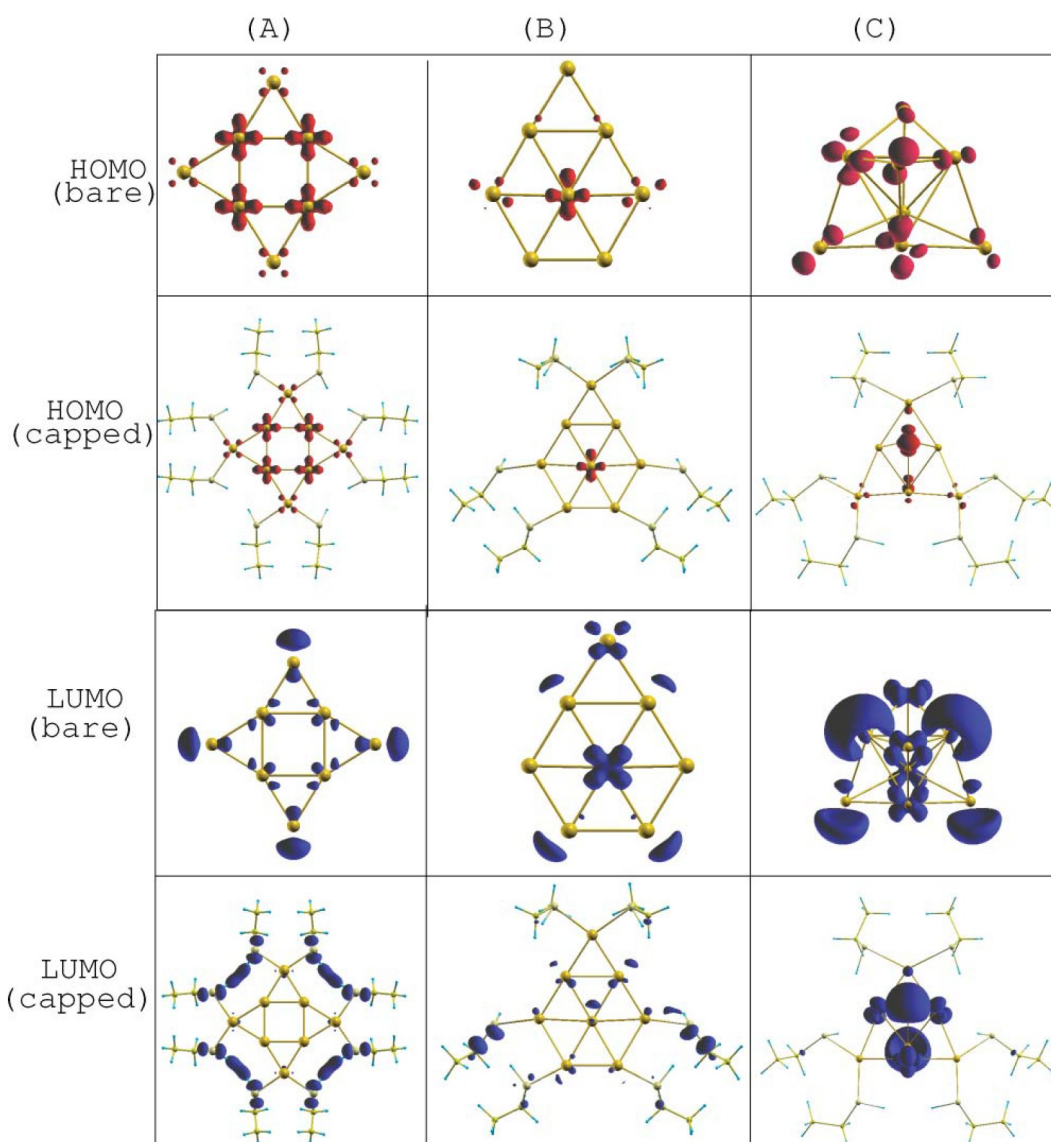


Figure 5.4: HOMO and LUMO charge density distributions have been plotted at one-third the maximum of iso-value for bare and ligand protected star (panel A), hex (panel B) and 3D (panel C) clusters.

5.4.6 Bonding charge density

In order to study the bonding nature of the ligand molecule and gold cluster, we have studied the bonding charge densities or the charge density differences. Bonding charge density ρ_{diff} has been calculated by using the mathematical expression 5.6,

$$\rho_{\text{diff}} = \rho_{\text{complex}} - \left(\rho_{\text{cluster}} - \sum_{i=1}^{n_{\text{lig}}} \rho_{\text{ligand}(i)} \right) \quad (5.6)$$

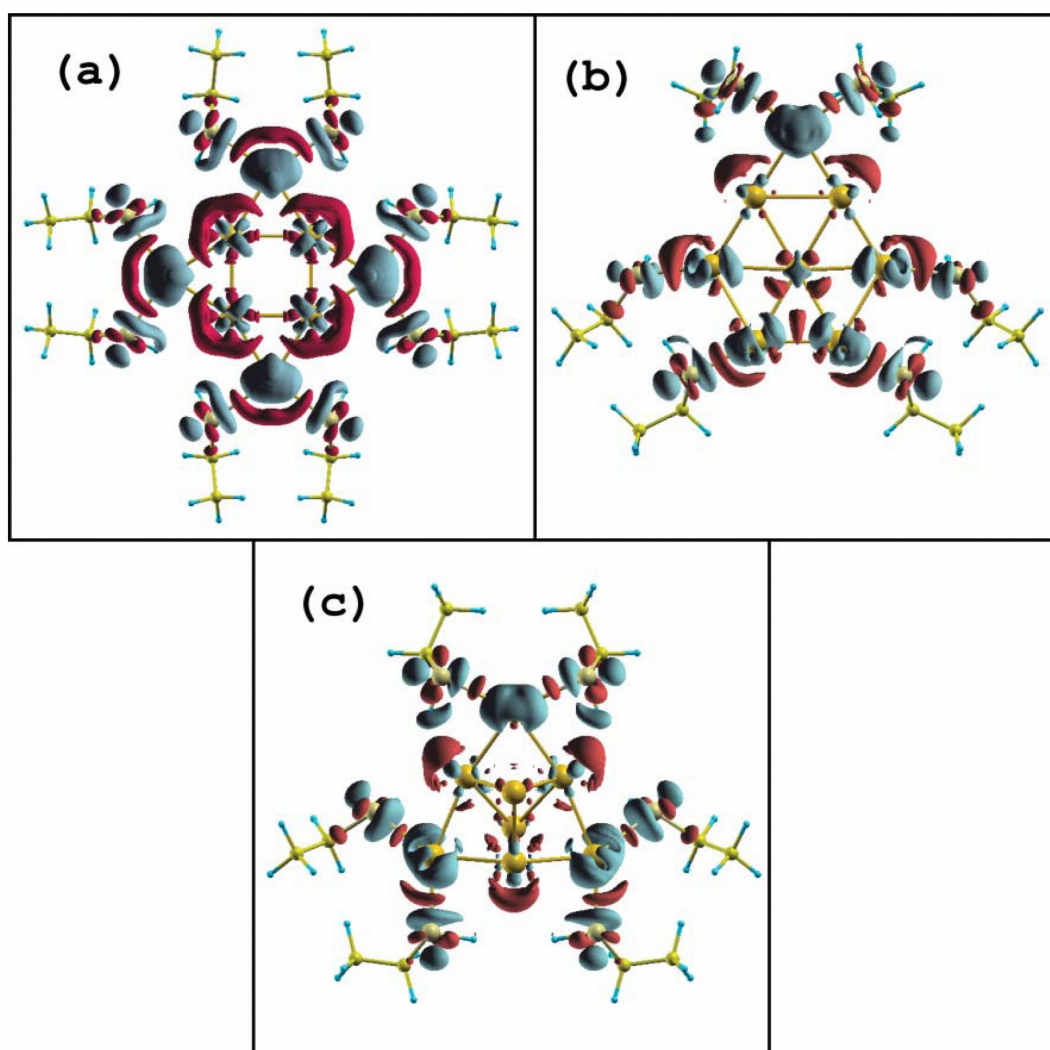


Figure 5.5: Charge density difference plots for one-third the maximum of iso-value of star (a) hex (b) and 3D (c) ligand-protected clusters. Charge accumulated and depleted regions have been shaded by Red and cyan colors .

where ρ_{complex} is the charge density of ligand capped complexes, ρ_{cluster} stands for charge density of bare cluster and ρ_{ligand} is ligand charge density. All sets of values are calculated within same structural supercell. So, in other words, during the calculations, we first calculate the charge density of the ligand-cluster complex (ρ_{complex}). Then using the same supercell we calculate the charge densities of individual ligands ($\rho_{\text{ligand}, i}$, $i = \text{ligand number}$) and the bare cluster (ρ_{cluster}). Fig. 5.5 shows bonding charge density plots, in which red and cyan regions denote charge accumulated and charge-depleted regions respectively. These plots shares important electronic aspect regarding the charge-accumulated regions. Charge transfer from the metal cluster to the Au-S bonds results in a strong covalent

bond between the Au and S atoms. Ligand protected star cluster shows strong charge accumulation in the Au-S bonds as well as in the S-S bridges. The six-ligand protected hex cluster shows similar types of behavior *ie.* charge lost from the Au and S atoms accumulate at the center of the bond between Au and S atoms. This accumulation is stronger for the 2D hex system than the 3D structure (Fig. 5.5) supporting the enhanced stability of the 2D systems over the 3D.

5.5 Conclusion

Applying first principles DFT calculations we have studied the effect of ligand attachment to 8-atom Au-clusters. This magic numbered cluster has already been experimentally synthesized. We have chosen the ligand molecule to be ethyl mercaptan which is similar to the sulfur tail of glutathione, the ligand which was used for the synthesis of the 8-atom clusters [32]. In the experimental scenario, the solvent molecules interact with the tail part of the ligands leaving the cluster-ligand interaction unperturbed, as the cluster-ligand interaction (bonding) involves only the head part of the ligand [47,48]. During our study this solvent effect is neglected completely and simplified form of ligand molecule is considered with shortened tail part. Our study in this respect represents mainly the cluster-ligand interaction through the bonding nature of gold and sulfur. Our studies suggests that attachment of ethyl mercaptan ligands to Au_8 increases the stability of the planar geometries over that of the non-planar structure.

Bibliography

- [1] P. Schwerdtfeger, M. Lein,.: Theoretical Chemistry of Gold-from Atoms to Molecules, Clusters, Surfaces, and the Solid State. *Gold Chemistry: Applications and Future Directions in the Life Sciences*. Wiley-VCH Verlag GmbH & Co. KGaA: Weinheim, Germany; pp. 183-246 (2009).
- [2] S J Rose, I P Grant and N C Pyper, *J. Phys. B: At. Mol. Phys.* **11** 1171 (1978); P. Pyykkö , J. P. Desclaux, *Acc. Chem. Res.*, **12**, 276 (1979).
- [3] P. Pyykkö, *Angew. Chem. Int. Edn.* **43**, 4412 (2004).
- [4] Y. Dong, M. Springborg, *Eur. Phys. J. D.* **43**, 15 (2007).
- [5] J. Wang, G. Wang, G. Zhao, *J. Phys. Rev. B.* **66**, 035418 (2002).
- [6] P. K. Jain, *Struc. Chem.* **16**, 421 (2005).
- [7] H. Häkkinen, U. Landman, *Phys. Rev. B(R).* **62**, 2287 (2000).
- [8] R. M. Olson, S. Varganov, M. S. Gordon, H. Metiu, S. Chretien, P. Piecuch, K. Kowalski, S. A. Kucharski, M. Musial, *J. Am. Chem. Soc.* **127**, 1049 (2005).
- [9] L. Xiao, L. Wang, *Chem. Phys. Lett.* **392**, 452 (2004).
- [10] J. Wang, J. Jellinek, J. Zhao, Z. Chen, R. B. King, P. von R. Schleyer, *J. Phys. Chem. A* **109**, 9265 (2005).
- [11] E. M. Fernandez, J. M. Soler, I. L. Garzon, L. C. Balbas, *Phys. Rev. B.* **70**, 165403 (2004)

- [12] H. Häkkinen, B. Yoon, U. Landman, X. Li, H-J. Zhai, L-S Wang, *J. Phys. Chem. A* **107**, 6168 (2003).
- [13] L. Xiao, B. Tollberg, X. Hu, L. Wang, *J. Chem. Phys.* **124**, 114309 (2006).
- [14] X-B Li, H-Y. Wang, X-D. Yang, Z-H. Zhu, Y-J. Tang, *J. Chem. Phys.* **126**, 084505 (2007).
- [15] J. C. Idrobo, W. Walkosz, S. F. Yip, S. Ogut, J. Wang, J. Jellinek, *Phys. Rev. B.* **76**, 205422 (2007).
- [16] B. Assadollahzadeh, P. Schwerdtfeger, *J. Chem. Phys.* **131** 064306 (2009).
- [17] H. Häkkinen, M. Moseler, U. Landman, *Phys. Rev. Lett.* **89**, 033401 (2002).
- [18] K. Spivey, J. I. Williams, L. Wang, *Chem. Phys. Lett.* **432**, 163 (2006).
- [19] G. Shafai, S. Hong, M. Bertino, T. S. Rahman, *J. Phys. Chem. C.* **113**, 12072 (2009).
- [20] E. F. Finney, R. Finke, *Jour. Colloid and Interface Science*, **317**, 351 (2008).
- [21] J. D. Aiken III, R. Finke, *Jour. Molecular Catalysis A: Chemical* **145**, 1 (1999).
- [22] G. Mills, M. S. Gordon, H. Metiu, *J. Chem. Phys.* **118**, 4198 (2003).
- [23] P. Pyykkö, *Nature Nanotechnology* **2**, 273 (2007).
- [24] M-C. Daniel, D. Astruc, *Chem. Rev.* **104**, 293 (2004).
- [25] S. Creager et al., *J. Am. Chem. Soc.* **121**, 1059 (1999).
- [26] D. Kruger, H. Fuchs, R. Rousseau, D. Marx and M. Parrinello, *Phys. Rev. Lett.* **89**, 186402 (2002).
- [27] P. R. Nimmala, V. R. Jupally, A. Dass, *Langmuir*, **30**, 2490 (2014).
- [28] M. Zhu, H. Qian, R. Jin, *J. Am. Chem. Soc.* **131**, 7220 (2009).
- [29] Y. Pei, Y. Gao, N. Shao, X. C. Zeng, *J. Am. Chem. Soc.*, **131**, 13619 (2009).

- [30] T. G. Schaaff, R. L. Whetten, *J Phys Chem B* **103**, 9394 (1999).
- [31] P. R. Nimmala, V. R. Jupally, A. Dass, *Langmuir*, **30**, 2490 (2014).
- [32] M. A. H. Muhammed, S. Ramesh, S. S. Sinha, S. K. Pal, T. Pradeep, *Nano Res.* **1**, 333 (2008).
- [33] <http://www.pwscf.org>
- [34] P. Giannozzi, S. Baroni, N. Bonini, M. Calandra, R. Car, C. Cavazzoni, D. Ceresoli, G. L. Chiarotti, M. Cococcioni, I. Dabo, A. D. Corso, S. d. Gironcoli, S. Fabris, G. Fratesi, R. Gebauer, U. Gerstmann, C. Gougoussis, A. Kokalj, M. Lazzeri, L. Martin-Samos, N. Marzari, F. Mauri, R. Mazzarello, S. Paolini, A. Pasquarello, L. Paulatto, C. Sbraccia, S. Scandolo, G. Sclauzero, A. P Seitsonen, A. Smogunov, P. Umari, R. M Wentzcovitch, *J. Phys. Cond. Matt.* **21**, 395502 (2009).
- [35] D. Vanderbilt, *Phys. Rev. B(R)* **41**, 7892 (1990).
- [36] J. P. Perdew, A. Zunger, *Phys. Rev. B.* **23**, 5048 (1981).
- [37] J. Perdew, K. Burke, M. Ernzerhof, *Phys. Rev. Lett.* **77**, 3865 (1996).
- [38] E. M. Fernandez, J. M. Soler, I. L. Garzon, L. C. Balbas, *Phys. Rev. B.* **70**, 165403 (2004).
- [39] L. Xiao, L. Wang, *Chem. Phys. Lett.* **392**, 452 (2004).
- [40] L. Xiao, B. Tollberg, X. Hu, L. Wang, *J. Chem. Phys.* **124**, 114309 (2006).
- [41] X-B Li, H-Y. Wang, X-D. Yang, Z-H. Zhu, Y-J. Tang, *J. Chem. Phys.* **126**, 084505 (2007).
- [42] F. Remacle, E. S. Kryachko, *J. Chem. Phys.* **122**, 44304 (2005).
- [43] R. M. Olson, S. Varganov, M. S. Gordon, H. Metiu, S. Chretien, P. Piecuch, K. Kowalski, S. A. Kucharski, M. Musial, *J. Am. Chem. Soc.* **127**, 1049 (2005).
- [44] H. Häkkinen, M. Walter, H. Gronbeck, *J. Phys. Chem. B.* **110**, 9927 (2006).

-
- [45] P. D. Jadzinsky, G. Calero, C. J. Ackerson, D. A. Bushnell, R. D. Kornberg, *Science*. **318**, 430 (2007).
- [46] G. K. Wertheim, J. Kwo, B. K. Teo, K. A. Keating, *Solid. State. Comm.* **55**, 357 (1985).
- [47] M. Anand, M. McLeod, W. Bell, B. Roberts, *J. Phys. Chem. B* **109** 22852 (2005).
- [48] M. Schulz-Dobrick, K. Sarathy, M. Jansen, *J. Am. Chem. Soc.* **127** 12816 (2005).

Substantial reduction of Stone-Wales activation barrier in fullerene*

6.1 Stone-Wales transformation

Stone-Wales transformation [1,2] is often discussed in describing the growth of fullerene, carbon nanotubes. During Stone-Wales transformation a hexagon-hexagon sharing [6, 6] bond is rotated by an angle 90° , so that pentagon-hexagon within a pyracyclene change their positions as shown in Fig. 6.1. During fullerene growth, heptagons (7 edges) are formed to move the pentagons (5 edges) by the formation of (7, 5) heptagon-pentagon pair which passes away after the shifting of pentagon. Figure 6.1 (a) shows Stone-Wales transformation for the rearrangement of pentagons and hexagons while creation of two (7, 5) pairs are shown in Fig. 6.1(b). With the help of Stone-Wales mechanism in Fig. 6.1(b), creation (annihilation) of a (7, 5) pair in the presence of a pentagon has been shown in Fig. 6.1(c). Movement of this (7, 5) pair and the pentagon around the fullerene surface have been shown in Fig. 6.1(d). Thus, during the growth process, heptagons formation describes the pentagons movement around the surface of fullerenes.

*This chapter is based on the article : Phys. Rev. B **84**, 205404 (2011).

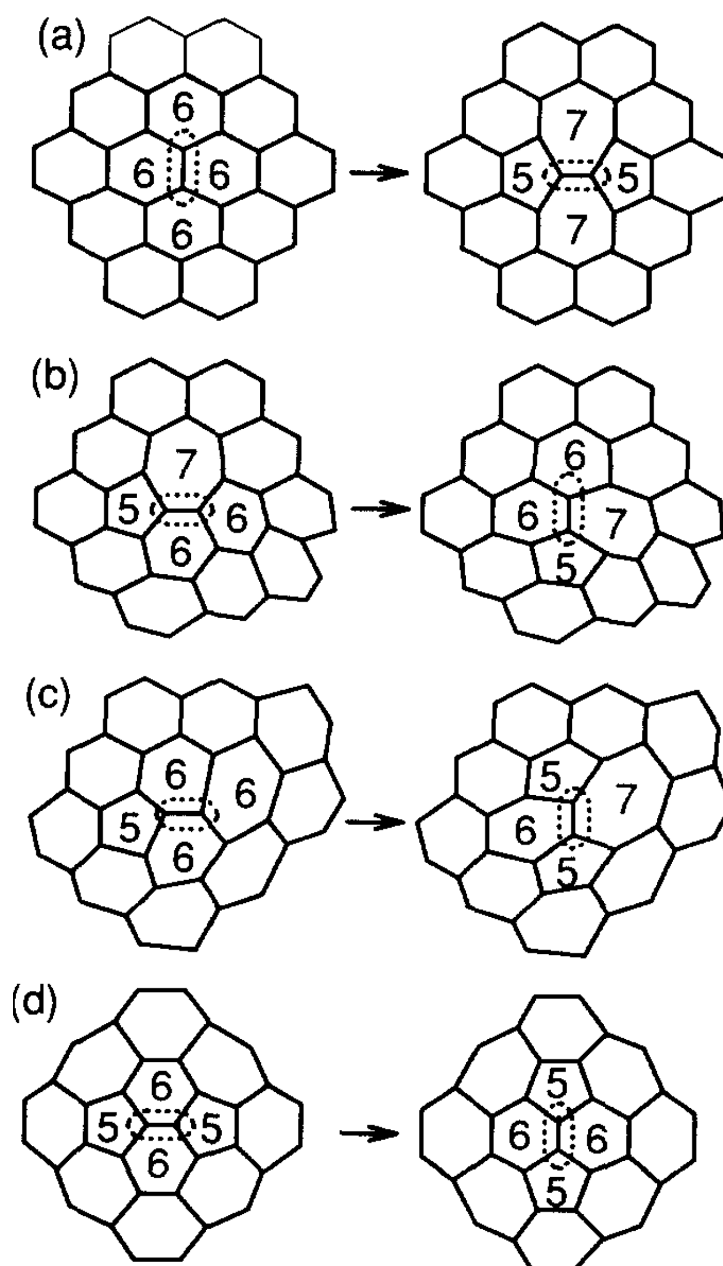


Figure 6.1: Preliminary steps for the Stone-Wales transformation. (a) $(5,6,5,6) \rightarrow (6,5,6,5)$ (b) $(6,6,6,6) \rightarrow (7,5,7,5)$ (c) $(5,6,6,6) \rightarrow (6,5,7,5)$ (d) $(5,7,6,6) \rightarrow (6,6,7,5)$. Reproduced from [3].

6.2 Motivation behind the project

Stone-Wales transformation of buckminsterfullerene (BF) changes the structural symmetry from I_h to C_{2v} which contains a pair of adjacent pentagons. Thus, SW transformation is the fundamental mechanism for I_h - C_{60} formation, which lies at the global minimum of the complex potential energy surface. C_{2v} - C_{60} is ~ 1.6 eV less stable than I_h - C_{60} [4–6].

Although reactant ($C_{2v}\text{-}C_{60}$) and product ($I_h\text{-}C_{60}$) of the Stone-Wales transformation are both stable structures, this transition requires large potential energy barrier ~ 5.4 eV (see Fig. 6.2) [5,7]. Thus the formation of BF from the annealing of carbon cluster was a serious

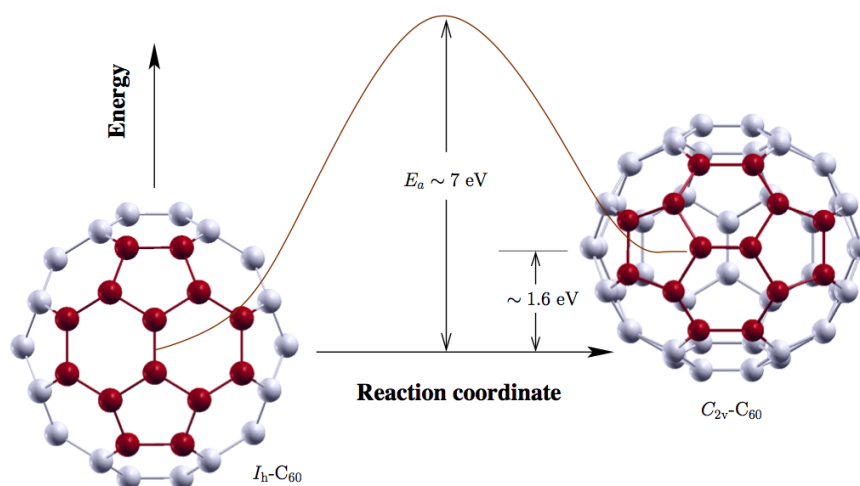


Figure 6.2: Stone-Wales mechanism for $I_h\text{-}C_{60} \rightarrow C_{2v}\text{-}C_{60}$ transition. The pyracyclene region is shown by red colour.

challenge from the theoretical perspective. Initial molecular dynamics failed to reach BF by annealing carbon clusters [8–10]. Product becomes distorted hollow cage of 60 carbon atoms satisfying ‘isolated pentagon rule’ [10]. Afterwards, a lot of effort were put together to explain the ideal mechanism for nucleation of C_{60} cluster. Successful molecular dynamics simulations for fullerene annealing and fragmentation was achieved from the Stone-Wales rearrangement [15,16]. Eggen *et al* [17–19] prescribed the energy path for SW transition. They proposed an auto-catalysis mechanism for fullerene annealing where presence of extra loosely bound carbon atom located in the region of paired pentagons, catalyzes this SW transformation. Thus, SW activation energy barrier can be reduced under experimental condition. In 2000, Slanina *et al.* studied a variety of elements and concluded that such auto-catalysis mechanism can be enhanced for nitrogen atom during catalyzing the SW transformation [20]. In contrast, endohedral doping (K, Ca, and La) shows relatively less activity towards the barrier-height reduction [5]. These metal ions are encapsulated within the hollow carbon cage of fullerene and the activation energy barrier for $I_h\text{-}C_{60} \rightarrow C_{2v}\text{-}C_{60}$ transition was noticed to be reduced by an amount of 0.30, 0.55 and 0.80 eV for K, Ca and La atoms respectively. In this chapter we will discuss the effect of substitutional doping at the active SW site. Boron was chosen as such substituent. Boron doped heterofullerenes

have been synthesized successfully where their hydrogen storage activity was attracted considerable attention [21–23].

6.3 Computational Details

Our calculations were carried out using density functional theory implemented in the Vienna *Ab-initio* Simulation Package (VASP) code [24] with the Perdew-Burke-Ernzerhof exchange-correlation functional [25] and projector augmented wave pseudopotential [26]. Energetics have also been further verified in terms of Heyd-Scuseria-Ernzerhof (HSE06) [27–29] functional. GGA functional underestimates the Kohn-Sham band gap whereas Hartree-Fock method overestimates. The PBE exchange term in HSE06 is split into a short range and a long-range part. 25% of short range part is replaced by a short range Hartree-Fock term while the PBE correlation part remains unchanged. The spatial decay of $1/r$ Coulomb potential in the Hartree-Fock exchange interaction is simplified by the screening effect. The screening parameter was fixed at 0.2 Å. This functional obtains improved information on energies and band gaps than PBE, [27, 30] and locate the stable structures with higher precision. The kinetic energy cutoff was chosen to be 800 eV. Symmetry unrestricted geometry optimizations were performed until the force on each atom was less than 0.005 eV/Å, and the reciprocal space integration were carried out at the Γ point.

Transition state and minimum energy path (MEP) were calculated by using Nudged Elastic Band (NEB) [31, 32] method which is an updated version of the chain of state model connecting two known potential energy minima with springs having same force constant k . Here each state \mathbf{R}_i is a replica (image) of the system's configuration. These replicas are generated by linear interpolation between the initial and final points stable structures. Interpolating path between two end-point and intermediate images is used as an initial guess for the pathway. The chain of state acts like an elastic band where the end points are fixed. The intermediate states (images) are then relaxed in such a way that minimizes the “object function” $S[\mathbf{R}_0, \mathbf{R}_1, \dots, \mathbf{R}_N]$. Optimized band passes through the potential energy minima at the saddle point and joins the end points of the elastic band following the MEP. This object function depends on the

spring constant and potential. Simplest form of the object function consist of the potential of the images ($V(\mathbf{R}_i)$) and the spring constant of the harmonic springs (k) connecting two adjacent images:

$$S[\mathbf{R}_0, \mathbf{R}_1, \dots, \mathbf{R}_N] = \sum_{n=1}^{N-1} V(\mathbf{R}_i) + \sum_{n=1}^N \frac{1}{2} k (\mathbf{R}_i - \mathbf{R}_{i-1})^2 \quad (6.1)$$

The “object function” is optimized with respect to the intermediate images $\mathbf{R}_0, \mathbf{R}_1 \dots \mathbf{R}_N$.

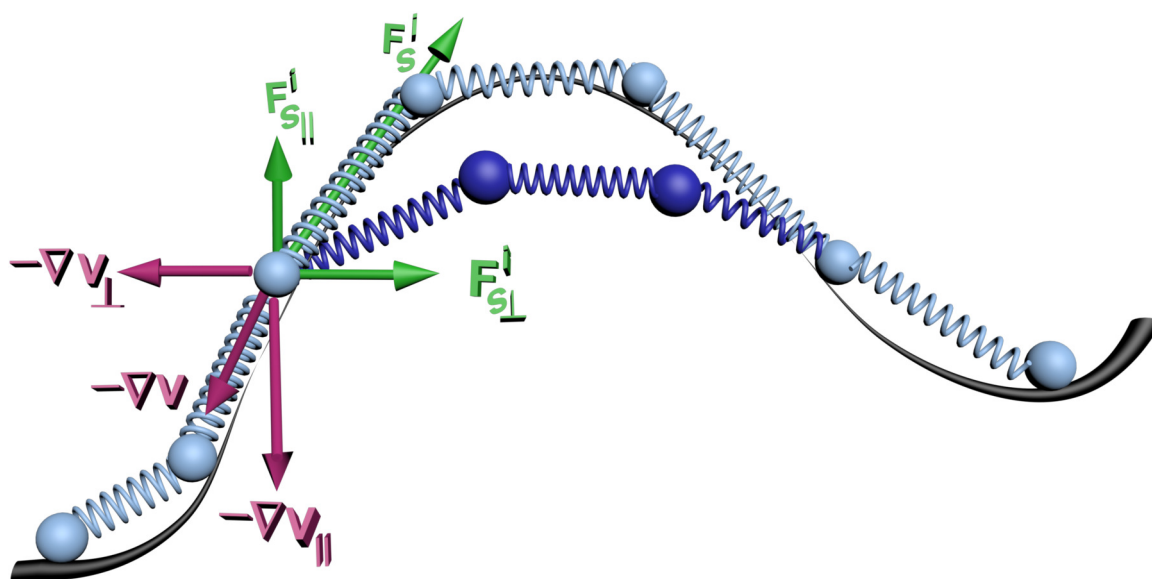


Figure 6.3: Schematic diagram of the NEB method: Initially images are created and held together by means of springs (light blue color). Their discrete representation defines the MEP which is shown by black trajectory. But $\mathbf{F}_{S\perp}^i$ (acting on i^{th} image) moves down the images from the MEP introducing “corner cutting”, while due to $\nabla V_{||}$, images slide down along the MEP (deep blue color). Thus, to avoid such discrepancy, $\mathbf{F}_{S\perp}^i$ and $\nabla V_{||}$ are projected out from the calculation. So that, NEB force on i^{th} image becomes: $F^i = -\nabla V_{\perp} + F_{S||}^i$

Various existing chain of states methods differ in the particular form of the object function and optimization method for the minimization. During optimization of the “object function” two effect compete with one another, (i) the images along the chain tend towards the potential energy minima while (ii) the harmonic spring try to place the images approximately equidistant along a straight line. For a suitable force constant, optimized elastic band approximately follows the minimum energy path (MEP) for the transition. Main problem of such a straightforward approach is the harmonic spring which tend to align along straight path. As a result elastic band tries to pull the path away from the MEP and saddle point. Another important point is that the images along the elastic band

try to slide down along the chain due to the force resulting from the PES. In the NEB approach as shown in Fig. 6.3, this ‘corner cutting’ near about the saddle point and ‘sliding down’ problems are solved by ‘nudging’ the elastic band where the normal component of the spring force and parallel component of ‘true’ physical force are smartly ignored. Hence the NEB force on the i^{th} image becomes,

$$\mathbf{F}_i = -\nabla V(\mathbf{R}_i)_\perp + \mathbf{F}_i^s \hat{\mathcal{T}}_\parallel \hat{\mathcal{T}}_\parallel \quad (6.2)$$

where $\nabla V(\mathbf{R}_i)$ is the gradient of the energy with respect to the atomic coordinates of the i^{th} image and \mathbf{F}_i^s is the spring force acting on the i^{th} image. Unit tangent at i^{th} image can be obtained from the normalization of

$$\mathcal{T}_i = \frac{\mathbf{R}_i - \mathbf{R}_{i-1}}{|\mathbf{R}_i - \mathbf{R}_{i-1}|} + \frac{\mathbf{R}_{i+1} - \mathbf{R}_i}{|\mathbf{R}_{i+1} - \mathbf{R}_i|} \quad (6.3)$$

ie. $\hat{\tau}_i = \tau_i/|\tau_i|$. Such an expression of the unit tangent $\hat{\tau}_i$ ensures that the images are equispaced even in the region of high curvature. Thus, the spring force that maintain the spacing between the images approximately fixed, may be redefined as

$$\mathbf{F}_{i\parallel}^s = k[|\mathbf{R}_{i+1} - \mathbf{R}_i| - |\mathbf{R}_i - \mathbf{R}_{i-1}|] \hat{\tau}_i \quad (6.4)$$

Computation of ∇V for the various images of the system can be done in parallel on a cluster of computers where separate node handling is done for each one of the images. Each node only needs to receive coordinates and energy of adjacent images to evaluate the spring force and to carry out the force projections for the image under consideration. In order to obtain an estimate of the saddle point, interpolation method is used between the images of the converged elastic band. The climbing image nudged elastic band (CI-NEB) method [33] is a modification of the NEB method which describes the saddle point structure with higher accuracy. At first few steps of NEB calculations are performed and then the highest energy image along the NEB path is determined. In this CI-NEB method, spring force on the image with highest energy is neglected while inverted parallel component

of the true physical force is considered only,

$$\begin{aligned}\mathbf{F}_{i_{max}}^{CI-NEB} &= -\nabla V(\mathbf{R}_{i_{max}}) + 2\nabla V(\mathbf{R}_{i_{max}})_{\parallel} \\ &= -\nabla V(\mathbf{R}_{i_{max}}) + 2\nabla V(\mathbf{R}_{i_{max}}) \cdot \hat{\mathcal{T}}_{i_{max}} \cdot \hat{\mathcal{T}}_{i_{max}}\end{aligned}\quad (6.5)$$

During CI-NEB optimization, spacing between the images will be different on both sides. Springs with variable force constant are used to increase the parallel forces near the saddle point helping to place the climbing image at the exact saddle point. As the climbing image moves towards the saddle point, images on one side come closer to each other while spacing between the images on the other side increases. According to CI-NEB method, energy barrier is no longer needed to be obtained from the interpolation among images as we have an image sitting at the top of the MEP. Since all images are relaxed simultaneously, no additional computational cost is needed to pay for the upturn of the image along the MEP.

6.4 Results and Discussions

In order to study the effect of boron substitution on the Stone-Wales (SW) barrier height we have to locate the two end point structures. Thus, first of all we will discuss about the structural and electronic properties of $C_{60-x}B_x$ ($x = 0, 1, 2$).

6.4.1 $C_{60-x}B_x$ ($x = 0, 1, 2$): Structure and Electronic properties

I_h - C_{60} shows two types of bond lengths: smaller [6,6] bonds (1.399 Å) and larger [6, 5] bonds (1.453 Å). First isomer C_{2v} - C_{60} is ~ 1.6 eV less stable compared to I_h - C_{60} [4–6]. Bond lengths of both I_h - and C_{2v} - C_{60} are shown in Fig. 6.4. When one of the Carbon atoms in [6,6] bonds of C_{60} is replaced by boron, both [6,6] and [6,5] bonds are increased as shown in Fig. 6.4. Due to presence of such foreign host element, wide range of variation in the bond length of pentagonal and hexagonal rings of boron centered pyracyclene are noticed [7]. Similar feature is also observed in the boron centered pyracyclene of $C_{60-x}B_x$ ($x = 2$) where the [6,6] bond length of boron-boron dimer is further increased compared to the [6,6] carbon-boron dimer in case of $C_{60-x}B_x$ ($x = 1$). Thus the boron substitution

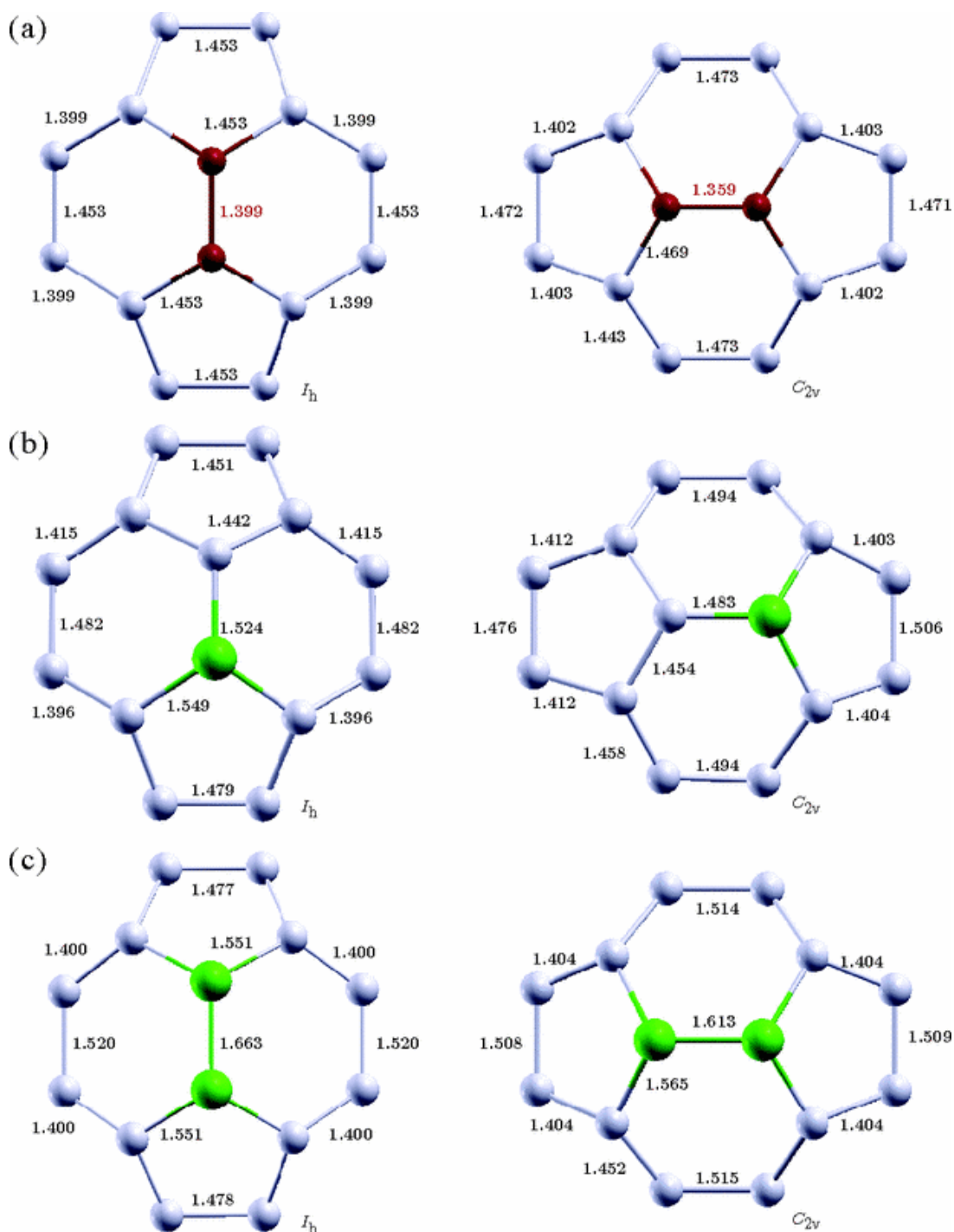


Figure 6.4: Local pyracyclene region for the optimized (a) C_{60} , (b) $C_{59}B$, and (c) $C_{58}B_2$ in I_h and C_{2v} symmetries. Bond lengths are shown in Å. Boron is shown by green colour within the local light blue colored pyracyclene. The [6, 6] rotating dimer bond length decreases substantially in the C_{2v} symmetric structure and induces a significant local distortion.

significantly destroy the inherent structural symmetry of C_{60} which should strongly influence the microscopic electronic structure. Highest occupied molecular orbital (HOMO) of I_h-C_{60} is five fold degenerate while lowest unoccupied molecular orbital (LUMO) shows three fold degeneracy. Substitution of boron causes a shifting of degeneracy in both HOMO and LUMO states. HOMO-LUMO energy gap (E_g) for $I_h-C_{60-x}B_x$ ($x = 0$) becomes 1.63 eV as shown in Fig. 6.5. Successive boron doping results successive reduction of Kohn-Sham energy gap, while discrepancy has been noticed for $C_{2v}-C_{60-x}B_x$ ($x = 1$) which shows higher HOMO-LUMO gap compared to pristine $C_{2v}-C_{60-x}B_x$ ($x = 0$). Conventional DFT

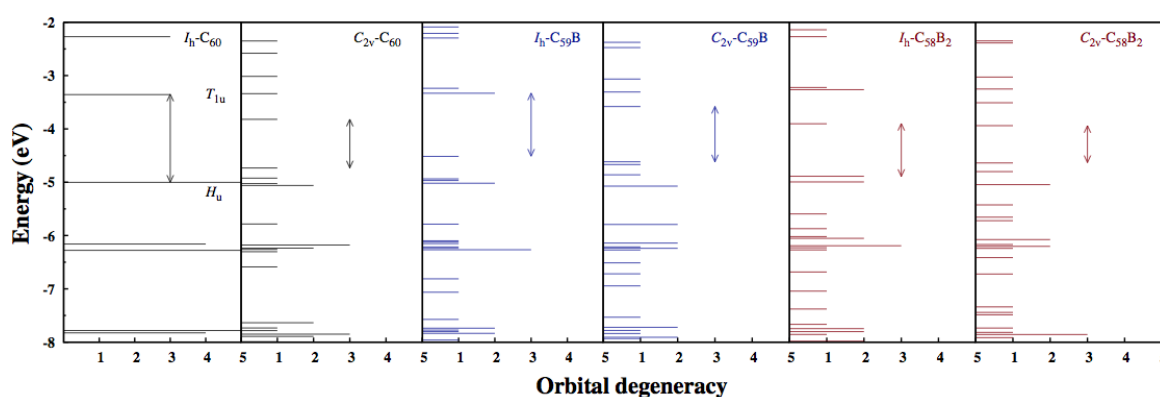


Figure 6.5: Orbital degeneracy in $C_{60-x}B_x$ ($x = 0, 1, 2$) for both I_h and C_{2v} symmetries.

usually underestimate the HOMO-LUMO energy gap which is lower than the quasi particle gap [34–36]. For a system of N interacting electrons, quasi particle energy gap can be obtained from the difference between ionization potential (IP)[†] and electron affinity (EA)[‡]. According to DFT (PBE) calculations, IP and EA of $I_h-C_{60-x}B_x$ ($x = 0$) are turned out to be 7.32 eV and 2.75 eV respectively [34–37]. Quasi particle gap 4.57 eV agrees well with the previous reported results [34–36]. Substitution of boron reduces the IP and increases the EA for $C_{60-x}B_x$ ($x = 1, 2$) as shown in table 6.1. Thus the heterofullerenes show enhanced redox character compared to pristine $C_{60-x}B_x$ ($x = 0$).

6.4.2 Activation barrier: Effect of substitutional B doping

SW activation energy barrier in fullerene is comparatively less than the carbon nano tube and graphene due to the strain present in structure [6]. Rotating C-C dimer shows peculiar

[†]IP = $[E(N-1)-E(N)]$

[‡]EA = $[E(N)-E(N+1)]$, $E(N)$ is the total energy of N electron system.

Table 6.1: Energetics of $C_{60-x}B_x$ ($x = 0, 1, 2$) in eV unit where $\Delta E = E_{[I_h:C_{60-x}B_x]} - E_{[C_{2v}:C_{60-x}B_x]}$, $E_g = E_{HOMO} - E_{LUMO}$.

	ΔE	$E_g(I_h)$	$E_g(C_{2v})$	IP (I_h)	EA (I_h)
Pristine- C_{60}	1.57	1.63	0.91	7.32	2.75
$C_{59}B$	1.67	1.18	1.04	7.00	3.71
$C_{58}B_2$	1.75	0.98	0.70	7.21	3.27

behavior during this SW transition. Bond length of C-C dimer in I_h - $C_{60-x}B_x$ ($x = 0$) is 1.399 Å while in C_{2v} - $C_{60-x}B_x$ ($x = 0$) it is reduced to 1.359 Å. But at the transition state, C-C dimer bond length becomes 1.248 Å which pops out the fullerene surface by an amount ~ 0.21 Å [6, 7, 38]. At this saddle point, $C_{60-x}B_x$ ($x = 0, 1, 2$) shows an imaginary phonon which is a characteristic of first-order transition state. This imaginary phonon mode decreases after boron doping [962, 377 and 167 cm^{-1} for $C_{60-x}B_x$ ($x = 0, 1, 2$) respectively]. Calculated SW barrier height for $I_h \rightarrow C_{2v}$ transition in pristine $C_{60-x}B_x$ ($x = 0$) becomes 6.88 eV which reduced by an amount of ~ 2.1 eV after substitution of a single boron atom (see Fig. 6.6). Maximum reduction in this activation barrier height takes place for double boron doping (see table 6.2). Although $C_{60-x}B_x$ ($x = 1$) is a spin doublet system^S, magnetism has negligible effect on the SW activation barrier. Spin polarized activation barrier is ~ 0.10 eV lower than non-spin polarized calculation. Similar type of trend was noticed for $[C_{60-x}B_x]^+$ ($x = 0$). Although $[C_{60-x}B_x]^+$ ($x = 0$) is isoelectric to $[C_{60-x}B_x]$ ($x = 1$), SW barrier height for $[C_{60-x}B_x]^+$ ($x = 0$) is much higher (~ 2 eV) than $[C_{60-x}B_x]$ ($x = 1$). Thus doped boron not only contributes a hole, but also introduces additional strain into the structure which is also evident from the optimized local pyracyclene region in Fig. 6.4. When carbon atoms of the rotating dimer are substituted by boron, SW barrier height ($I_h \rightarrow C_{2v}$ transition) becomes 2.54 eV which is the minimum value of SW activation barrier in C_{60} reported till date. Similar type of trend in the SW activation barrier was also noticed for HSE06 functional [27] where the barrier height calculation are performed with higher accuracy (see table 6.2). Origin of such SW barrier height reduction is anyway related to the microscopic properties of the [6,

^S $C_{60-x}B_x$ ($x = 0$) is close shell spin singlet system, while for $x = 1$, single hole is doped within the system. As a result spin-polarized calculation lowers the total energy by 80 meV with respect to the non-spin-polarized calculation. On the other hand, $x = 2$ again forms a spin singlet system.

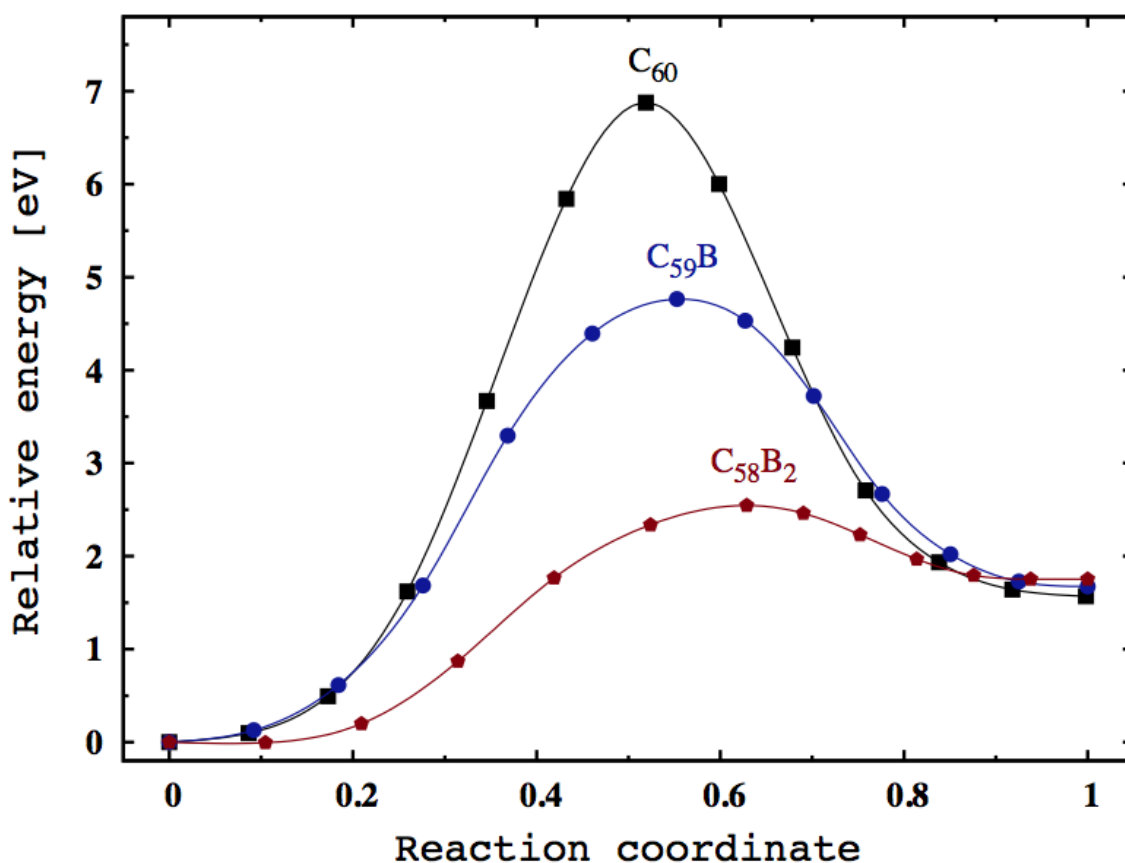


Figure 6.6: SW barrier height is plotted against the angular distortion *ie.*, in-plane rotation angle of the [6, 6] dimer. SW activation energy barrier for $I_h \rightarrow C_{2v}$ transition is 6.88 for C_{60} , while same mechanism for $C_{2v} \rightarrow I_h$ transition takes place at ~ 5.3 eV.

Table 6.2: SW activation energy barrier for $I_h \rightarrow C_{2v}$ transition. $\delta E_a [=E_a(C_{60})-E_a(X)]$ is the reduction in the activation barrier compared to pristine C_{60}

	<i>Activation barrier</i> (eV)		δE_a (eV)
	PBE	HSE06	PBE (HSE06)
C_{60}	6.88	7.61	
C_{60}^+	6.40	7.05	0.48 (0.56)
$C_{59}B$	4.76	5.22	2.12 (2.39)
$C_{58}B_2$	2.54	2.80	4.34 (4.81)

[6] rotating dimer of the pyracylene. Let's now focus to the electronic structure of this [6, 6] dimer. First of all we will discuss about the bond strength of this particular [6, 6] dimer in $C_{60-x}B_x$ [$x = 0, 1, 2$]. As shown in Fig. 6.4, this rotating [6, 6] dimer is a C-B bond for $x = 1$ and for $x = 2$, it switches to a boron dimer. Total binding energy of a system is the total bonding energy distributed among all bonds required for structural stability. Thus,

the bond strength of the rotating [6, 6] dimer for $x = 0, 1, 2$ can be expressed as

$$\begin{aligned} E_{C-C} &= E_{C_{60}}^{\text{tot}}/90 \\ E_{C-B} &= [E_{C_{59}B}^{\text{tot}} - 87 \times E_{C-C}] / 3 \\ E_{B-B} &= [E_{C_{58}B_2}^{\text{tot}} - 85 \times E_{C-C} - 4 \times E_{C-B}] \end{aligned} \quad (6.6)$$

Here E^{tot} is total binding energy of the system under consideration. Our calculations yield E_{C-C} (5.87 eV) > E_{C-B} (4.74 eV) > E_{B-B} (3.75 eV)

Due to weaker C-B bonds surrounding the [6,6] rotating dimer, the SW rotation becomes easier for the heterofullerenes which is also evident from the bonding charge density analysis (see Fig. 6.7). Substitution of boron introduces ionic character in the C-B bonds. Bonding

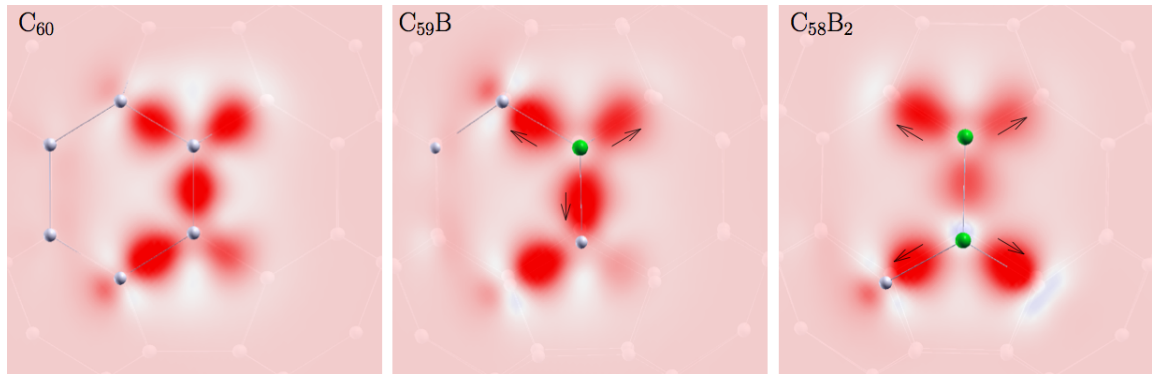


Figure 6.7: Bonding charge densities $\Delta\rho$ for pristine C_{60} , single, and double B-doped heterofullerenes. The B atoms are shown in green. Here $\Delta\rho = \rho^{\text{tot}}(\mathbf{r}) - \rho^{C_{58}}(\mathbf{r}) - \rho^X(\mathbf{r}) - \rho^Y(\mathbf{r})$, where X-Y represents the rotating C-C, C-B, and B-B dimers for C_{60} , $C_{59}B$, and $C_{58}B_2$ structures, respectively. For pristine C_{60} , the charge accumulation centers (red) appear at the middle of the bond, which indicate covalent C-C bonds. As a result of B doping, the charge accumulation centers shift toward the C atoms (shown with the arrows) resulting ionic C-B character.

charge density moves towards the C atoms. Bader charge analysis [39] also suggests that each B atom loses $\sim 1|e|$ charge to the neighbouring carbon atoms. Thus, as a result of boron doping [6, 6] rotating dimer is bound with the hollow carbon cage with some[¶] weak bonds. So, the SW rotation is promoted for such B heterofullerenes. Such a bond weakening at and around the rotating [6, 6] dimer has also strong influence on the phonon frequency, as the bond stiffness (k) is related to the phonon frequency (ν), $\nu \propto \sqrt{k}$. As boron doping mainly affects the atoms around the dimer, we will focus only the pyracyclene around this [6, 6] dimer. Due to bond softening, phonon frequencies are starting to shift

[¶]for $C_{60-x}B_x$ ($x = 1$), [6, 6] C-B dimer is bonded with 2 weak C-B bonds, while for $C_{60-x}B_x$ ($x = 2$), 4 such C-B bonds bound this [6, 6] dimer with C_{58} hollow cage.

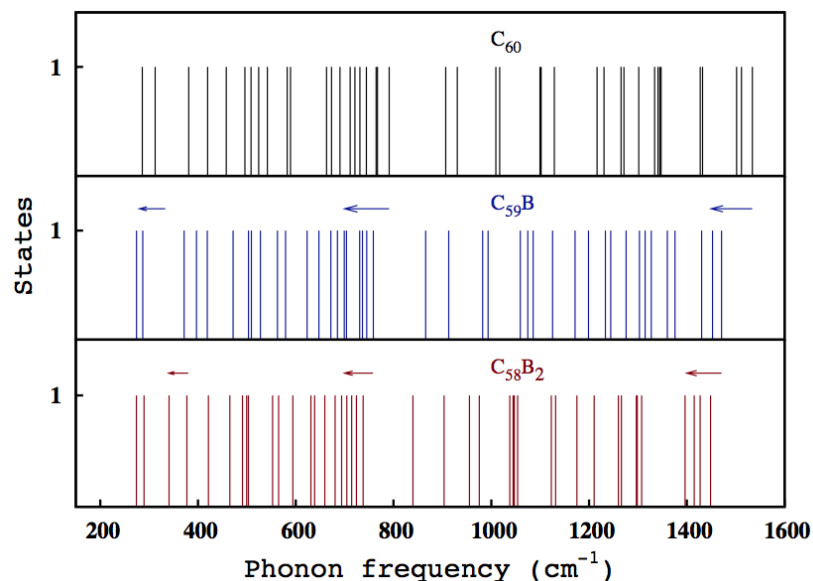


Figure 6.8: Phonon modes in the 14-atom pyracyclene around the rotating dimer are shown for I_h symmetry.

towards the lower frequencies as shown in Fig. 6.8. In a single sentence, this “softening” effect arises due to the bond-strength and additional strain introduced by the foreign host.

6.4.3 Reaction rate and characteristic time scale

At temperature well below the melting point, harmonic approximation to the transition state theory (HTST) can be used to understand the reaction mechanism associated with the reaction. Reaction rate can be expressed in terms of energy and normal mode frequencies at the saddle point and initial state [40].

$$k^{\text{HTST}} = \frac{\prod_i^{3N} \nu_i^{\text{I}}}{3N-1 \prod_i \nu_i^{\text{TS}}} e^{-(E_a/k_B T)}, \quad (6.7)$$

where $E_a = (E^{\text{TS}} - E^{\text{I}})$ is the activation energy with E^{I} (E^{TS}) being the energy corresponding to the initial (transition) state and ν_i are the corresponding normal mode frequencies. Within the harmonic approximation, entropic effect of the reaction rate is included in the prefactor involving the zero temperature phonon frequencies. Imaginary phonon mode appearing at the transition state is excluded. Characteristic time scale can be calculated

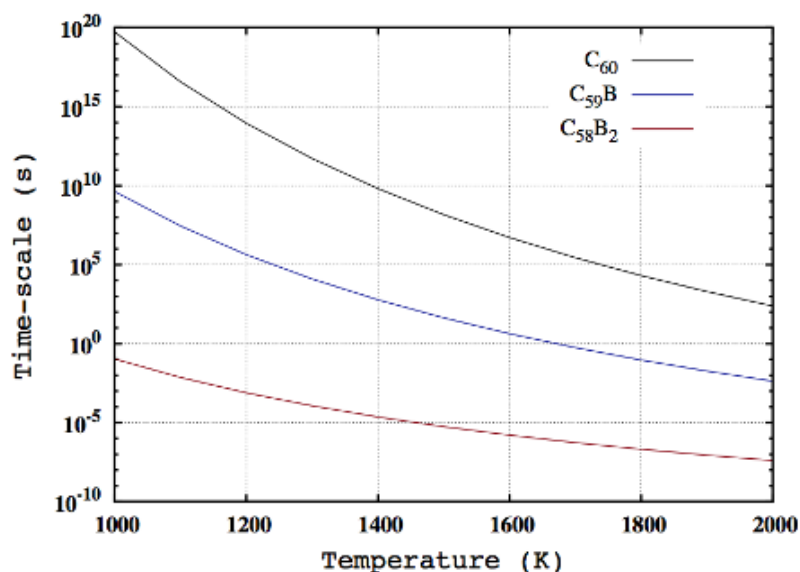


Figure 6.9: $I_h \rightarrow C_{2v}$ transition rate.

from the reaction rate k^{HTST} as $\tau = 1/k^{HTST}$. Characteristic time required for $I_h \rightarrow C_{2v}$ reaction is shown in Fig. 6.9 where SW transition is plotted as a function of temperature. From this diagram it is clear that SW transition in heterofullerenes are enormously accelerated and requires a second and microsecond for $C_{60-x}B_x$ ($x = 1, 2$) respectively. On the other hand, reverse transition $C_{2v} \rightarrow I_h$ is $e^{\Delta E/k_B T}$ times faster than the forward transition. Thus, formation of $I_h-C_{60-x}B_x$ is highly promoted for such heterofullerenes.

6.5 Conclusion

Stone-Wales (SW) activation barrier for I_h-C_{60} formation is very high (~ 5.3 eV). This large barrier height can be reduced in presence of extra carbon atom. The growth of fullerene results from the autocatalysis by such loosely bound carbon atoms. In this chapter we have shown that substitutional doping at the SW sites is a much more effective route for such mechanism. Our calculations reveal that presence of a single boron at the active SW site reduces this activation barrier by an amount of ~ 2.2 eV, while company of another boron at the nearest SW active site minimize this energy cost to ~ 0.76 eV which is the minimum value of the SW activation energy barrier reported till date. First-principle analysis suggest that such low energy path is tracked down by the bond-softening mechanism and additional strain introduced by the substituent. Along this newly prescribed energy path for SW

transition, time scale for the [6, 6] dimer rotation is also reduced.

Bibliography

- [1] A. Stone and D. Wales, Chem. Phys. Lett. **128**, 501 (1986).
- [2] D. J. Wales, M. A. Miller, and T. R. Walsh, Nature (London) **394**, 758 (1998).
- [3] Riichiro Saito, G. Dresselhaus, M.S. Dresselhaus, Chem. Phys. Lett., **195**, 537 (1992).
- [4] S. J. Austin, P. W. Fowler, D. E. Manolopoulos, G. Orlandi, F. Zerbetto, J. Phys. Chem. **99**, 8076 (1995).
- [5] W. I. Choi, G. Kim, S. Han, J. Ihm, Phys. Rev. B **73**, 113406 (2006).
- [6] J.-Y. Yi, J. Bernholc, J. Chem. Phys. **96**, 8634 (1992).
- [7] H. F. Bettinger, B. I. Yakobson, and G. E. Scuseria, J. Am. Chem. Soc. **125**, 5572 (2003).
- [8] J. R. Chelikowsky, Phys. Rev. Lett. **67**, 2970 (1991).
- [9] J. R. Chelikowsky, Phys. Rev. B **45**, 12062 (1992).
- [10] X. Jing, J. R. Chelikowsky, Phys. Rev. B **46**, 5028 (1992).
- [11] E. Osawa, Z. Slanina, K. Honda, and X. Zhao, Fullerene Sci. Technol. **6**, 259 (1998).
- [12] R. K. Mishra, Y. T. Lin, S. L. Lee, Chem. Phys. Lett. **313**, 437 (1999).
- [13] R. K. Mishra, Y. T. Lin, S. L. Lee, J. Chem. Phys. **112**, 6355 (2000).
- [14] J. W. Mintmire, Science **272**, 45 (1996).

- [15] C. Xu, G. E. Scuseria, *Phys. Rev. Lett.* **72**, 669 (1994).
- [16] I. Laszlo, *Fullerene Sci. Technol.* **5**, 375 (1997).
- [17] B. R. Eggen, M. I. Heggie, G. Jungnickel, C. D. Latham, R. Jones, P. R. Briddon, *Science* **272**, 87 (1996).
- [18] B. R. Eggen, C. D. Latham, M. I. Heggie, B. Jones, P. R. Briddon, *Synth. Met.* **77**, 165 (1996).
- [19] B. R. Eggen, M. I. Heggie, G. Jungnickel, C. D. Latham, R. Jones, P. R. Briddon, *Fullerene Sci. Technol.* **5**, 727 (1997).
- [20] Z. Slanina, X. Zhao, F. Uhlik, M. Ozawa, E. J. Osawa, *Organomet. Chem.* **599**, 57 (2000).
- [21] H. J. Muhr, R. Nesper, B. Schnyder, R. Kötz, *Chem. Phys. Lett.* **249**, 399 (1996); T. Guo, C. Jin, and R. E. Smalley, *J. Phys. Chem.* **95**, 4948 (1991).
- [22] Y. Zhao, Y.-H. Kim, A. C. Dillon, M. J. Heben, and S. B. Zhang, *Phys. Rev. Lett.* **94**, 155504 (2005).
- [23] Y.-H. Kim, Y. Zhao, A. Williamson, M. J. Heben, and S. B. Zhang, *Phys. Rev. Lett.* **96**, 016102 (2006).
- [24] G. Kresse and J. Hafner, *Phys. Rev. B* **47**, 558 (1993); G. Kresse J. Furthmüller, *ibid.* **54**, 11169 (1996).
- [25] J. P. Perdew, K. Burke, M. Ernzerhof, *Phys. Rev. Lett.* **77**, 3865 (1996).
- [26] P. E. Blöchl, *Phys. Rev. B* **50**, 17953 (1994).
- [27] J. Heyd, G. E. Scuseria, and M. Ernzerhof, *J. Chem. Phys.* **118**, 8207 (2003); A. F. Izmaylov, G. E. Scuseria, and M. J. Frisch, *ibid.* **125**, 104103 (2006).
- [28] J. Paier, M. Marsman, K. Hummer, G. Kresse, I. C. Gerber, and J. G. Ángyán, *J. Chem. Phys.* **124**, 154709 (2006).
- [29] J. Heyd, G. E. Scuseria, and M. Ernzerhof, *J. Chem. Phys.* **124**, 219906 (2006).

- [30] V. Eyert, Phys. Rev. Lett. **107**, 016401 (2011).
- [31] H. Jónsson, G. Mills, K. W. Jacobsen, " Nudged elastic band method for finding minimum energy paths of transitions" in *Classical and Quantum Dynamics in Condensed Phase Simulations*, edited by BJ Berne, G. Ciccotti, DF Coker (World Scientific, Singapore, 1998), p. 385 .
- [32] G. Henkelman, H. Jónsson, J. Chem. Phys. **113**, 9978 (2000).
- [33] G. Henkelman, B. P. Uberuaga, H. Jónsson, J. Chem. Phys. **113**, 9901 (2000).
- [34] X. Blase, C. Attaccalite, and V. Olevano, Phys. Rev. B **83**, 115103 (2011).
- [35] I. V. Hertel, H. Steger, J. de Vries, B. Weisser, C. Menzel, B. Kamke, and W. Kamke, Phys. Rev. Lett. **68**, 784 (1992).
- [36] L.-S. Wang, J. Conceicao, C. Jin, and R. Smalley, Chem. Phys. Lett. **182**, 5 (1991).
- [37] J. D. Sau, J. B. Neaton, H. J. Choi, S. G. Louie, and M. L. Cohen, Phys. Rev. Lett. **101**, 026804 (2008).
- [38] R. L. Murry, D. L. Strout, G. K. Odom, and G. E. Scuseria, Nature (London) **366**, 665 (1993).
- [39] R. F. W. Bader, *Atoms in Molecules-A Quantum Theory* (Oxford University Press, Oxford, 1990); G. Henkelman, A. Arnaldsson, and H. Jónsson, Comput. Mater. Sci. **36**, 354 (2006)
- [40] G. H. Vineyard, J. Phys. Chem. Solids **3**, 121 (1957).

Conclusion and scope for future study

The aim of the present thesis is to understand the electronic properties of 3D crystalline solids and 0D nanoclusters. In the context of crystalline solids, we have paid our attention to the transition metal oxide based perovskite compounds. All our calculations have been performed by using *first principles* density functional theory. In this chapter we will summarize the important findings regarding the 3D and 0D systems. First we shall discuss about the crystalline perovskite compounds and then we will highlight on the 0D nanoclusters considered in the present thesis.

7.1 Crystalline perovskite

In this present thesis, crystalline perovskite compounds have been discussed in chapters 3 and 4. All the perovskite compounds considered in the thesis belong to $AA'_3B_4O_{12}$ family which crystallize in $Im\bar{3}$ symmetry. Tunable B-O-Cu interaction in these compounds is the important aspect. In the following, we provide the gist of our study on these compounds which include $CaCu_3B_4O_{12}$ ($B = Co, Cr, Rh, Ir$).

Recent experimental analysis shows heavy fermion like signature in $CaCu_3Ir_4O_{12}$, where Kondo like behavior is noticed in localized Cu moments and itinerant Ir-O hybridized states. Metal-insulator transition is also noticed with crossover temperature 80K. Specific heat, magnetic susceptibility of the paramagnetic metallic phase ($T < 80k$) show non-Fermi liquid behavior indicating nearby quantum critical phenomenon [1]. These localized and magnetically active Cu d states in $CaCu_3Ir_4O_{12}$ shift towards the Fermi surface representing a drastic change in orbital hybridization compared with

$\text{CaCu}_3\text{B}_4\text{O}_{12}$ (B= Co, Cr, Rh). Significant change in the Cu orbital occupation results in the mixed valence intermediate spin state of $\text{Co}^{3.25+}$, mixed valence Rh $\sim 3.6+$, but ionic $\text{Ir}^{4+}(5d^5)$ and $\text{Cr}^{4+}(5d^2)$. GGA+U calculation suggests half-metallic ground state for $\text{CaCu}_3\text{Ir}_4\text{O}_{12}$. The presence of a significant spin-orbit interaction is found to mix up and down spins and destroys half-metallicity. Inclusion of spin-orbit coupling (SOC) allows for the non-collinear arrangement of spins. We have therefore carried out spin-polarized calculations assuming collinear as well as non-collinear spin arrangements. The calculated magnetic moments at various atomic sites, obtained in non-collinear calculations, turn out to be very similar to that obtained assuming simple collinear arrangement of spins.

Upon ascending a column of the periodic table from $5d$ to $3d$ element at the B-site, the Cu: $d_{x^2-y^2}$ orbital occupation was found to change from pure ionic $3d_{x^2-y^2}^9$ ($S= 1/2$) for $\text{CaCu}_3\text{Ir}_4\text{O}_{12}$ to the non-magnetic cuprate Zhang-Rice-like state with $3d^9 \underline{L}$ ($S= 0$) for $\text{CaCu}_3\text{B}_4\text{O}_{12}$ (B= Co, Cr). As we move from $3d$ to $4d$ to $5d$ elements at the B-site, t_{2g} - e_g separation increases because of larger ligand field effect and O: p states are also pushed away from the Cu: d states. Degenerate $3d_{x^2-y^2}^9$ and O: p states along with the $pd\sigma$ antibonding state noticed in the $3d_{x^2-y^2}$ effective Wannier function plot shows the signature of Zhang-Rice like Kondo state which corresponds to the XAS peak at 931.5 eV.

Localize hole at the Jahn-Teller active Cu^{2+} site shows heavy-fermion like character for the $5d$ element at the B-site. As we move from $5d$ to $4d$ element at the B-site, O: p states are pushed towards the Cu: d states *ie.* Kondo site spin starts interacting with the holes from the O: p states which increases the Kondo coupling strength. Such a Kondo like spin singlet becomes more prominent for $3d$ elements at the B-site where Kondo screening gives rise to the many-body Zhang-Rice like spin singlet state. In other words, as we move from $5d$ to $4d$ to $3d$ element at the B-site of $\text{CaCu}_3\text{B}_4\text{O}_{12}$, Kondo like coupling strength increases progressively. Hole at the oxygen site forms Zhang-Rice singlet state for B= Co, Cr, Rh while for $\text{CaCu}_3\text{Ir}_4\text{O}_{12}$, this hole goes to Ir site.

7.2 Nanoclusters

Next we will focus on the low dimensional structural composites. Chapters 5 and 6 describe the study of the nano-clusters. In chapter 5, we have discussed the attachment of sulfur

ligand on previously reported planar and non-planar geometry of eight atom gold nano cluster (Au_8) while chapter 6 describes geometric transformation in C_{60} .

7.2.1 Gold nanoclusters

Applying first principles DFT calculations we have studied the effect of ligand attachment to 8-atom Au-clusters. This magic numbered cluster has already been experimentally synthesized. We have chosen the ligand molecule to be ethyl mercaptan which is similar to the sulfur tail of glutathione, the ligand which was used for the synthesis of the 8-atom clusters [Muhammed *et al.*, Nano Res. **1**, 333 (2008)]. We have analyzed the site-selective attachment of ligand chains which we show to depend on the coordination as well as the specificities of the geometry giving rise to ligand-ligand interactions. The relative stability of the bare and ligated clusters are studied based on binding and interaction energies, *sd*-hybridization, DOS, HOMO-LUMO charge distributions and charge density differences. Considering the chosen geometries, our studies indicate that for 8 atom clusters, attachment of ethyl mercaptan ligands increases the stability of the 2D like geometries over that of the 3D like geometries. The above obtained trend is rather different from previously reported theoretical studies on ligated 11 and 13 atom clusters which predict stabilization of 3D-like geometry over 2D-like geometry upon ligation [2]. The difference in the predicted trend between ligated 8-atom cluster in the present study and that for ligated 11 and 13 atom clusters corroborates the fact that structure and bonding in small clusters crucially depend on their size. In particular the metal-ligand covalency, which is the primary cause of the difference in geometrical properties between ligated and bare clusters, depends on the nature of the local environment of the Au atom in the bare cluster in which the ligand has been attached or in other words the geometry of the bare cluster and also on the nature of the ligand, as been stressed in several studies.

7.2.2 C_{60}

Stone-Wales transformation of buckminsterfullerene (BF) changes the structural symmetry from I_h to C_{2v} which contains a pair of adjacent pentagons. Thus, SW transformation is the fundamental mechanism for I_h - C_{60} formation, which lies at the global minimum

of the complex potential energy surface. $C_{2v}-C_{60}$ is ~ 1.6 eV less stable than I_h-C_{60} . Although reactant ($C_{2v}-C_{60}$) and product (I_h-C_{60}) of the Stone-Wales transformation are both stable structures, this transition requires large potential energy barrier ~ 5.4 eV. Our calculations reveal that presence of a single boron at the active SW site reduces this activation barrier by an amount of 2.2 eV, while company of another boron at the nearest SW active site minimize this energy cost to 0.76 eV which is the minimum value of the SW activation energy barrier reported till date. For C_{60} , the C-C bonding is completely covalent, the bonding charge accumulates at the centers of the bond. This picture deviates for B-doped cases, where the charge accumulation centers move toward the C atom for C-B bonds, imparting ionic character to the C-B bonds. Bader charge analysis shows that each B atom loses an $\sim 1|e|$ charge to the neighboring C atoms. This bond softening mechanism is also established from the bonding charge analysis. Due to B doping, phonon frequencies gradually shift to the lower frequencies. This indicates that the bonds get softer. In addition to this, B doping also introduces additional strain in the structure. Such low energy path is tracked down by the bond-softening mechanism and additional strain introduced by the substituent. Along this newly prescribed energy path for SW transition, time scale for the [6, 6] dimer rotation is also reduced.

7.3 Future Scope of Work

(i) **CaCu₃B₄O₁₂**: In this present thesis, B-site substitution in CaCu₃B₄O₁₂ is described as an effective tool to manipulate the orbital degrees of freedom resulting different oxidation state for copper. Recent experimental measurements suggests that A-site substitution has also similar types of effects [S. Zhang *et al.* J. Am. Chem. Soc. **135**, 6056 (2013)] which could be rechecked in future for the compounds under study CaCu₃Ir₄O₁₂ (B= Co, Cr, Rh, Ir). Recently novel A-site ordered quadruple perovskite has been synthesized where A-site is occupied by transition metal cation. MnCu₃V₄O₁₂ crystallizes with space group symmetry $Im\bar{3}$ with lattice constant $a = 7.267$ Å at room temperature [3]. Mn²⁺ is surrounded by 12 equidistant oxide ions to form a regular icosahedro. Similar type of structure has been reported for Cu²⁺Cu₃²⁺V₄⁴⁺O₁₂ [4]. These novel structures should also be an interesting topic for future theoretical study.

(ii) **Gold nanoparticles:** In the experimental scenario, the solvent molecules interact with the tail part of the ligands leaving the cluster-ligand interaction unperturbed, as the later interaction involves only the head part of the ligand. In this present study we have considered the simplified form of ligand with shortened tail part. In future, same analysis for the geometries with the full long tail structure and the ligand-solvent molecule interaction, possibly modeled through classical force field of the ligand will be an interesting topic.

(iii) **C₆₀ related:** In future, it may be an another interesting topic to check the effect of boron substitution on the inter-transformation between graphene and fullerene [5].

Bibliography

- [1] J.-G. Cheng, J.-S. Zhou, Y.-F Yang, H. D. Zhou, K. Matsubayashi, Y. Uwatoko, A. MacDonald, J. B. Goodenough, Phys. Rev. Lett.
- [2] G. Shafai, S. Hong, M. Bertino, T. S. Rahman, J. Phys. Chem. C. **113**, 12072 (2009);
H. Häkkinen, M. Walter, H. Gronbeck, J. Phys. Chem. B. **110**, 9927 (2006).
111, 176403 (2013);
Y. Xina, H.D. Zhou, J.G. Cheng, J.S. Zhou, J.B. Goodenough, Ultramicroscopy, **127**, 94 (2013).
- [3] Y. Akizuki, I. Yamada, K. Fujita, N. Nishiyama, T. Irifune, T. Yajima, H. Kageyama, K. Tanaka, Inorg. Chem., **52**, 11538 (2013).
- [4] Yasuhide Akizuki *et al.* Angew. Chem. Int. Ed. **54**, 10870 (2015).
- [5] A. Chuvilin, U. Kaiser, E. Bichoutskaia, N. A. Besley, A. N. Khlobystov, Nature Chem. **2**, 450 (2010);
J. Zhang, F. Bowles, D. Bearden, W. Ray, T. Fuhrer, Y. Ye, C. Dixon, K. Harich, R. Helm, M. Olmstead, A. Balch and H. Dorn, Nat. Chem., **5**, 880 (2013);
W. Neng, L. Shuang-ying, X. Jun, M. Matteo, Z. Yi-long, W. Shu, S. Li-tao H. Qing-an, Nanoscale, **6**, 11213 (2014).

– Reprints –



Zhang-Rice physics and anomalous copper states in A-site ordered perovskites

SUBJECT AREAS:

ELECTRONIC PROPERTIES
AND MATERIALS

SUPERCONDUCTING PROPERTIES
AND MATERIALS

SPECTROSCOPY

ELECTRONIC STRUCTURE

Received
18 January 2013

Accepted
24 April 2013

Published
13 May 2013

Correspondence and requests for materials should be addressed to D.M. (dmeys@uark.edu) or T.S.-D. (t.sahadasgupta@gmail.com)

D. Meyers¹, Swarnakamal Mukherjee², J.-G. Cheng^{3,4,5}, S. Middey¹, J.-S. Zhou³, J. B. Goodenough³, B. A. Gray¹, J. W. Freeland⁶, T. Saha-Dasgupta² & J. Chakhalian^{1,7}

¹Department of Physics, University of Arkansas, Fayetteville, AR 72701, ²Department of Condensed Matter Physics and Materials Science, S. N. Bose National Centre for Basic Sciences, Kolkata 700098, India, ³Texas Materials Institute, ETC 9.102, University of Texas at Austin, Austin, Texas 78712, ⁴Institute for Solid State Physics, University of Tokyo, 5-1-5 Kashiwanoha, Kashiwa, Chiba Japan 277-8581, ⁵Beijing National Laboratory for Condensed Matter Physics, and Institute of Physics, Chinese Academy of Sciences, Beijing 100190, China, ⁶Advanced Photon Source, Argonne National Laboratory, Argonne, Illinois 60439, USA, ⁷Division of Physics and Applied Physics, School of Physical and Mathematical Sciences, Nanyang Technological University, Singapore 637 371, Singapore.

In low dimensional cuprates several interesting phenomena, including high T_c superconductivity, are deeply connected to electron correlations on Cu and the presence of the Zhang-Rice (ZR) singlet state. Here, we report on direct spectroscopic observation of the ZR state responsible for the low-energy physical properties in two isostructural A-site ordered cuprate perovskites, $\text{CaCu}_3\text{Co}_4\text{O}_{12}$ and $\text{CaCu}_3\text{Cr}_4\text{O}_{12}$ as revealed by resonant soft x-ray absorption spectroscopy on the Cu $L_{3,2}$ - and O K-edges. These measurements reveal the signature of Cu in the high-energy $3+ (3d^8)$, the typical $2+ (3d^9)$, as well as features of the ZR singlet state (*i.e.*, $3d^9\bar{L}$, \bar{L} denotes an oxygen hole). First principles GGA + U calculations affirm that the B-site cation controls the degree of Cu-O hybridization and, thus, the Cu valency. These findings introduce another avenue for the study and manipulation of cuprates, bypassing the complexities inherent to conventional chemical doping (*i.e.* disorder) that hinder the relevant physics.

The many-body ZR singlet state¹⁻⁹, a doped hole on the oxygen site coupled antiferromagnetically with a hole on the copper site, can be manipulated with conventional solid-state chemistry methods by partial removal of oxygen or by non-isovalent cation exchange (*e.g.* $\text{La}^{3+} \rightarrow \text{Sr}^{2+}$). Such chemical routes of manipulation make the doped cuprates prone to chemical disorder causing strong structural distortions or even changes in crystal symmetry, which in turn may severely alter the properties associated with Cu d -electron derived electronic and magnetic structures. En route to the goal of realizing the ZR state without chemical disorder or lattice distortion, while the majority of the Cu oxide compounds have the Cu ions in the B-site of the perovskite ABO_3 structure, the A-site ordered perovskites with chemical formula $(\text{ACu}_3)\text{B}_4\text{O}_{12}$ are intriguing candidates for investigation due to the unique Cu A-site arrangement (see Fig. 1(a)). In this structure, a surprisingly rich set of interesting physics phenomena¹⁰⁻¹⁶ have been demonstrated by replacement of the B-site $3d$ transition metal ion via experiment and theory including colossal dielectric constant^{17,18}, ferrimagnetism¹⁹, charge, orbital, and spin ordering²⁰, non-fermi liquid behavior²¹, enhanced electronic correlations²² and possibly the Zhang-Rice state²³. In addition, previous reports hinted at the presence of a mixed-valency on Cu for B = Cr and Co^{23,24}. Despite the large variation in the B-site ions, all the members of this family belong to the same space group $Im\bar{3}$ built upon two sub-lattices of octahedral BO_6 units and the planar CuO_4 units (see Fig. 1(b)-(c)). As seen in Fig. 1(a and d), the two structural units are connected *via* apical oxygens to form a $\text{BO}_6 - \text{CuO}_4 - \text{BO}_6$ cluster. In this configuration, the effect of the B-site cation has been shown to be two-fold: first, its valence state controls the nominal valence state of the A'-site Cu ion and second, most importantly, its tendency for covalent mixing alters the charge distribution between Cu d - and O p -states^{11,15}. The structural similarity of the local ionic environment of Cu in these ordered perovskites with that of high T_c cuprates, and, in close analogy to chemical doping, the above-mentioned B-site's potential to engineer the electronic structure prompts one to use the A-site ordered perovskites to gain unique insight into the development of the cuprate electronic structure. Construction of such manipulated valencies suggests the ability to tune the formation of ligand holes on oxygen and possibly to achieve the formation of the Zhang-Rice singlet state - an important ingredient for high temperature superconductivity.

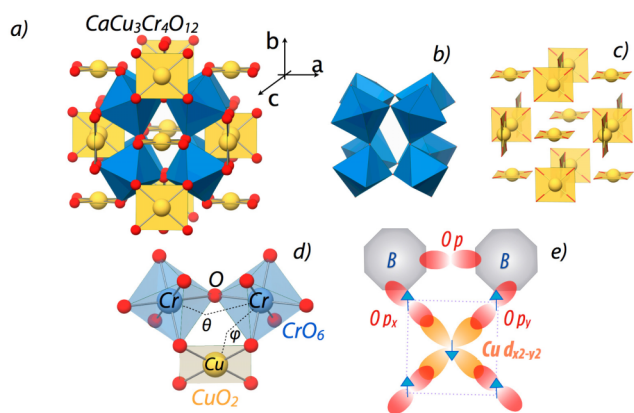


Figure 1 | Crystal structure of A-site ordered perovskites. (a) The entire crystal structure of $\text{CaCu}_3\text{Cr}_4\text{O}_{12}$. (b) CrO_6 octahedral sub-lattice. (c) CuO_4 distorted square planar sub-lattice. (d) Cr-Cr and Cr-Cu exchange pathways and (e) a sketch of B-site electronic states coupled to the ZR singlet state on Cu.

Results

Resonant x-ray absorption spectroscopy (XAS) in the soft X-ray regime is an ideal tool, extensively used in the past, to investigate the Cu and O electronic structure and the effects of electron-electron correlations in high T_c cuprates^{2,6–8,25–27}. Results of our soft XAS measurements on the Cu $L_{3,2}$ - and O K-edge are shown in Fig. 2 for the two A-site ordered perovskites $\text{CaCu}_3\text{Co}_4\text{O}_{12}$ (CCCoO) and $\text{CaCu}_3\text{Cr}_4\text{O}_{12}$ (CCCrO) along with that of the optimally doped superconducting $\text{YBa}_2\text{Cu}_3\text{O}_{7-\delta}$ (YBCO) and metallic LaCuO_3 (LCO) perovskite with a unique formal Cu^{3+} ($3d^8$) oxidation state. From the absorption line shape in Fig. 2, it is readily apparent that in CCCoO and CCCrO a mixed valency of Cu is present; we will discuss the CCCrO compound first. The sharp peak ~ 930 eV corresponds to the transition from the d^9 ground state, featuring a single hole in the Cu e_g band, to the $\bar{c}d^{10}$ (here \bar{c} denotes a core hole) excited state. The shoulder seen at 931.5 eV, a signature of the ZR singlet state, is a transition from the ground state $d^9\bar{L}$ to the $\bar{c}d^{10}\bar{L}$ excited state^{2,5,7,26,27}. The key difference between these two transitions being that while the Cu still maintains a nearly $2+$ (or d^9) valency, a ligand hole is distributed over the neighboring oxygens as illustrated in Fig. 1(e). The interaction between this ligand hole and the core hole created by the photon absorption raises the energy required to promote the core electron to the unoccupied state in the e_g band resulting in the observed high-energy state marked by red arrows. Furthermore, to corroborate this, we show the absorption data on LCO with the formal Cu charge state of $3+$. Indeed, in-line with our previous statement, the main feature of the LCO XAS around the L_3 -edge at ~ 931.5 eV is the transition from the $d^9\bar{L}$ state, thus making the ZR state the dominant contribution to the ground state in good agreement with previous reports^{28,29}. The aforementioned doped ligand holes are the charge carriers essential to the physics of high T_c cuprates; for instance, in hole doped cuprates the superconducting transition temperature is strongly dependent on the amount of doping present^{2,30,31}. To clarify the connection between these compounds and the high-temperature superconducting cuprates, XAS data was taken for an optimally doped YBCO sample. As seen in Fig. 2, the Cu L-edge spectrum of CCCrO shows remarkable resemblance to YBCO, namely the dominant d^9 initial states followed by the higher energy ZR state shoulder. This result highlights the capacity of the A-site ordered cuprate perovskites to *mimic the effects of chemical doping* without provoking unwanted lattice and stoichiometry deviations inherent to conventional chemical doping. In addition, the multiplet split peak at ~ 940 eV corresponds to a transition from

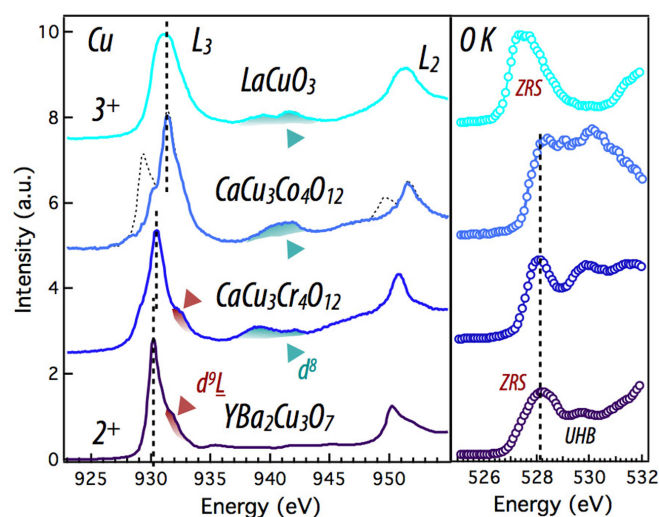


Figure 2 | XAS measurements on Cu L- and O K-edges. Left panel displays the Cu L-edge for all samples with the Zhang-Rice and d^8 ground states highlighted. LCO and YBCO are shown as references for Cu $3+$ and Cu $2+$ respectively, highlighting the change in valence for Cu with B-site change^{36,37}. Right panel shows the corresponding O K-edge spectra displaying the Zhang-Rice ligand hole state. In LCO, the higher energy peak around ~ 940 eV is due to the presence of the unusual Cu d^8 state. In CCCoO, a previously reported impurity peak around 929 eV³² is subtracted from both the L_3 and L_2 edges by fitting to a Voigt function. This peak corresponds to the d^9 peak observed on the other samples, however it has a very small spectral weight ($\sim 1/50$ ratio between d^9 and $d^9\bar{L}$ states).

the metastable $3d^8$ state to the cd^9 excited state, indicating the presence of the ionically Cu^{3+} state entirely absent in YBCO.

Next, we turn our attention to the CCCoO electronic structure. As clearly seen in Fig. 2, CCCoO shows a dominant white absorption line analogous to CCCrO, but, surprisingly, it is shifted ~ 1 eV away from the d^9 white line of CCCrO and YBCO. When compared with the formally Cu^{3+} compound LCO (shown immediately above it in Fig. 2) it becomes readily apparent that the Cu ground state is predominantly of $d^9\bar{L}$ character, implying a dominant Cu^{3+} formal valence as in LCO. To quantify the prevalence of the $d^9\bar{L}$ state, a three peak fit is used for the L_3 data, which are centered at 929.3 eV (impurity)³², 930 eV (d^9), and 931.4 eV ($d^9\bar{L}$) which gave a very small spectral weight ratio of $.0203 \left(\frac{d^9}{d^9\bar{L}}\right)$. The impurity peak was subtracted from the original data (dotted line) for clarity. Further demonstrating the $3+$ formal valence, the multiplet split peak at ~ 940 eV provides strong evidence for the admixture of the d^8 state. When considered alongside CCCrO, CCCoO also contains all three Cu states, but with obviously significantly different weights, further testifying to the ability of the B-site to effectively hole dope the Cu sites.

Because of the large degree of charge transfer between oxygen and copper and its importance to the ZR state, studies of the O K-edge can lend supporting information about the electronic structure of Cu. As seen in Fig. 2(b), O K-edge data in all samples show the oxygen specific signature of the $3d^9\bar{L}$ state, a necessary ingredient of the ZR state, which is particularly evident from the comparison to the well studied case of YBCO, where the ligand hole on oxygen appears as a large, doping dependent pre-peak around 528 eV^{6–8,25}. This observation of the pre-peak intensity indicates that the ZR state is the first ionization state at the Fermi energy. This further evidences our conclusion on the presence of the ZR state inferred from the Cu L-edge analysis.

Although our prime focus is on the electronic structure of Cu and O, Co and Cr $L_{3,2}$ -edge absorption can serve to independently

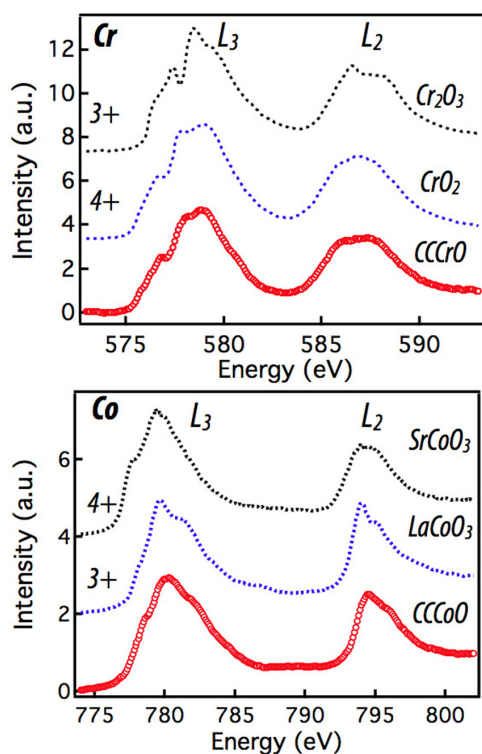


Figure 3 | XAS measurements on the Cr and Co L-edges. (a) The Cr L-edge along with 3+ and 4+ references from³³, the CCCrO and the 4+ reference samples show strong similarities. (b) The Co L-edge with valence references from³⁴ showing a similar, but not identical line shape. No standards were available meaning any energy shift between the samples could not be analyzed, all spectra were shifted to ~ align the white lines.

validate the Cu oxidation state. With this goal in mind, we performed L-edge XAS measurements on Co and Cr and compared this to the previous results on reference Cr and Co compounds. As shown in Fig. 3(a), a direct comparison to the Cr^{3+} and Cr^{4+} absorption confirms that in CCCrO the Cr valency is 4+ or very close to it³³. This verifies the conclusion that, in this compound, if Cr is 4+ then Cu must be $\sim 2+$ (assuming O^{2-} and Ca^{2+}). Any deviation of Cr valency towards 3+ must then be compensated by raising the Cu charge state, thus Cu must be 2+ or very close to it, consistent with the Cu L-edge results. The Co L-edge data shown in Fig. 3(b) bear strong similarities with previous studies of LaCoO_3 , which consists of ionically bound Co^{3+34} . Specifically, strong, high energy multiplet shoulders on the L_3 and L_2 white lines are present in both CCCoO and LaCoO_3 . In variance to this, Co^{4+} shows a smaller shoulder shifted to even higher energy. While the high energy side of the CCCoO Co L-edge is consistent with Co^{3+} , the low energy multiplet peak does not match either 3+ or 4+, implying CCCoO is neither ionically pure 3+ or 4+. Based upon the Cu L-edge conclusion of the Cu^{3+} charge state, we can independently assess the Co valency to be $\sim 3.25+$. In this context, the Co L-edge data is compatible with the Cu L-edge results and implies the presence of a mixed 3+/4+ Co valency, although it cannot confirm the exact 3.25+ valence state needed to conserve charge. Lending further support to this conclusion, Co L edge data in total electron yield (TEY) mode is shown in the Supplemental Figure S1.

To gain further understanding of the B-site influence on the unusual electronic states on Cu, we performed first-principles spin-polarized DFT calculations within the GGA + U approximation. Fig. 4 summarizes the first-principles results for CCCoO and CCCrO, respectively. Note, although no long-range magnetic ordering is reported in these compounds, spin-polarized calculations are

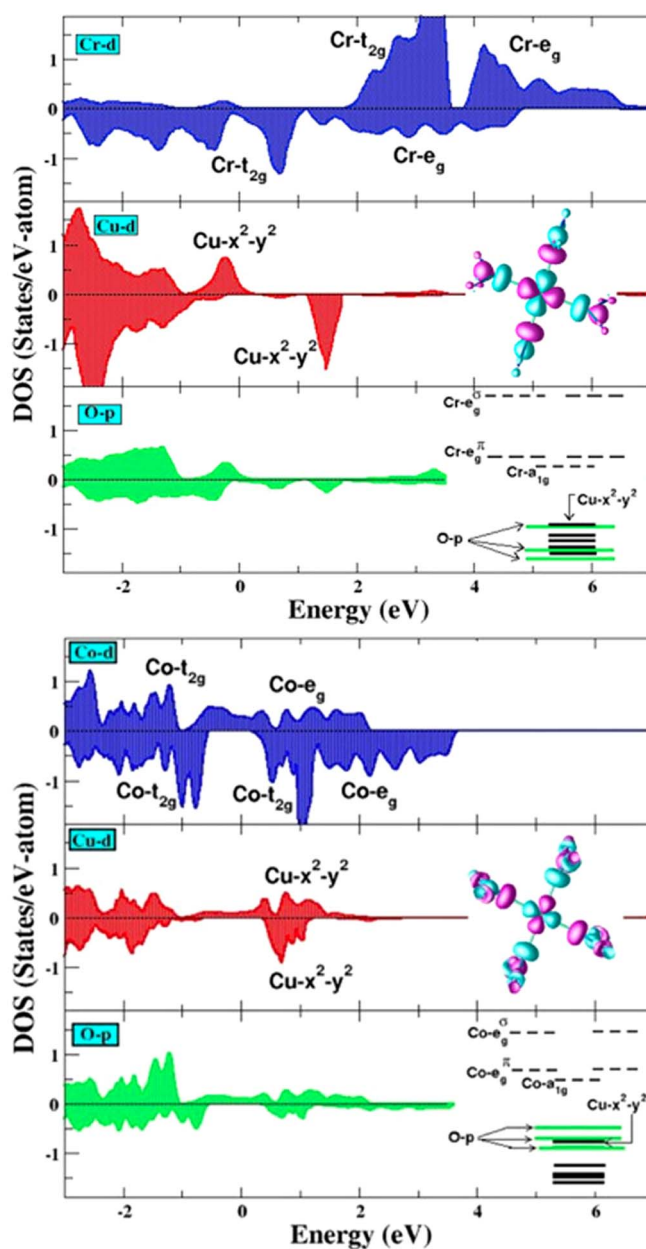


Figure 4 | The GGA + U density of states, projected onto Co d (Cr d), Cu d and O p states for the A-site ordered perovskites. (a) $\text{CaCu}_3\text{Co}_4\text{O}_{12}$ ((b) $\text{CaCu}_3\text{Cr}_4\text{O}_{12}$) compound. The positive and negative values in y-axis correspond to density of states in up and down spin channels, respectively. The zero of the energy is set at E_F . The features due to dominant contributions of various degrees of freedom have been marked. The inset in the middle panel shows the plot of the effective $\text{Cu } x^2 - y^2$ Wannier function, calculated by NMTO-downfolding. Shown are the isosurface function with lobes of opposite signs are colored differently. The inset in the bottom panel shows the relative positions of Co d, Cu d and O p energy levels.

essential for proper assignment of both charge and spin states of various constituents¹⁵. The three panel Fig. 4(a) and (b) show an inspection of the calculated density of states (DOS) projected onto B-d (B=Co/Cr), Cu-d and O-p states respectively. A direct inspection of the states in the vicinity to the Fermi energy, E_F demonstrates the existence of strong mixing between B and Cu d-states and O p-states. This strong covalency effect makes both CCCoO and CCCrO systems metallic, in agreement with experimental observations. In addition, as shown in the inset of Fig. 4(a)–(b), the octahedral crystal field



of the oxygen atoms around the B ion splits the B- t_{2g} states from the B- e_g (e_g^σ) states; the trigonal distortion present in the BO_6 octahedra breaks the t_{2g} levels further into doubly degenerate, e_g^π and singly degenerate a_{1g} states. The distorted square planar environment of oxygen atoms surrounding the Cu ion, on the other hand, lifts the 5-fold degeneracy of Cu d-levels, with large energy separation of Cu $d_{x^2-y^2}$ state from the rest. Here we note that the nominal d^8 (i.e. Cu^{3+}) would imply empty Cu: $d_{x^2-y^2}$ states in both spin up and spin down channels, and for d^9 Cu: $d_{x^2-y^2}$ states would be occupied in one of the spin channels and be empty in the other spin channel. From the DOS plots shown in Fig. 4(a) and (b), we find that Cu: $d_{x^2-y^2}$ states are empty in the down spin channel, while in the up spin channel it is indeed close to being empty for $CCCoO$, but mostly occupied for $CCCrO$. We note that DFT calculation deals with single configuration nature of the wavefunction and therefore, delivers the state with most dominant weight. Interestingly enough, the dominance of Cu 3+ state in $CCCoO$ and Cu 2+ state in $CCCrO$ is evident even at the level of single configuration theory. This result lends strong theoretical support for the conclusion inferred from our XAS measurements that the Cu state is predominantly in the 3+ state for $CCCoO$ and closer to 2+ for $CCCrO$.

Next, we discuss the calculated magnetic states in connection to Cu. First, we note that occupancy of the square planar Cu d-states according to the formal valence of d^8 would give rise to a paired electronic configuration with zero magnetic moment at Cu sites, while that of formal valence of d^9 would give rise to one unpaired electron with magnetic moment of $1 \mu_B$ in the fully spin polarized limit. In comparison, the calculation yields magnetic moments on Cu site $0.07 \mu_B$ for $CCCoO$ and $0.50 \mu_B$ for $CCCrO$, thus lending additional validation of our experimental conclusion on the exotic 3+ state for $CCCoO$ and closer to 2+ valency in $CCCrO$. Moreover, from the simple ionic charge count, the nominal 3+ and 2+ valences of Cu (assuming Ca^{2+} and O^{2-}), would set the formal valences of the B-site ion to 3.25+ and 4+ respectively, and result in d-electron occupancies of 5.75 for Co and 2 for Cr. The computed magnetic moment at the Cr site is $2.2 \mu_B$, in good agreement with the nearly 2+ valence of Cu and 4+ valence of Cr in $CCCrO$. The d-occupancy of 5.75 on Co can lead to either low or high spin magnetic state; our computed Co magnetic moment of $\sim 1.7 \mu_B$, however, is in conformity with the intermediate rather than low- or high-spin state.

By examining the energy level positions, as calculated in DFT, shown in the insets in the bottom panels of Figs. 4(a–b), we find that Cu $d_{x^2-y^2}$ energy level is nearly degenerate with O- p states, leading to a situation very similar to that in high T_c cuprates. This electronic configuration naturally supports strong mixing of Cu $d_{x^2-y^2}$ and O p_x and p_y states by forming a strong $pd\sigma$ antibonding combination, which may further bind to d-states at the B site as shown in Fig. 1(e). The formation of such a mixed state is also evident in the Wannier function plot of an effective Cu $x^2 - y^2$ Wannier function obtained by keeping only Cu $d_{x^2-y^2}$ state active and downfolding or integrating out all the other degrees of freedom (see inset of the middle panel of Fig. 4). We notice that for the Co compound mixing of Cu-O hybridized states with B-site d-states is much stronger compared to that of Cr compound, which is driven by the strong hybridization of empty Cu $d_{x^2-y^2}$ orbital of Cu 3+ state with empty Co, e_g orbitals. In $CCCrO$, this leads to vanishing contribution of the B-site states for the selected iso-surface value of the Wannier plot, showing the typical Cu-O antibonding wavefunction, making the situation more like high T_c cuprates with dominant Cu 2+ state. The strong mixing between Cu $d_{x^2-y^2}$ and O p states, which is a prerequisite for formation of the ZR state - observed as the feature around 931 eV in Cu L-edge spectra, is further corroborated by the presence of a $0.2 \mu_B$ fraction of the magnetic moment on the O site and $0.5 \mu_B$ on Cu. We thus conclude that the formation of a ZR like many-body state

similar to what is observed on the high T_c cuprates is indeed highly favorable in these systems with enhanced probability for the Cr compound.

Discussion

In summary, resonant soft X-ray absorption data on Cu L_{3,2}- and O K-edges revealed the presence of the ZR singlet state in the symmetrically invariant A-site-ordered cuprate compounds, $CaCu_3Co_4O_{12}$ and $CaCu_3Cr_4O_{12}$. Additionally, the data demonstrated the existence of a mixed valency for Cu modulated by the electronic state of the B-site cation and reflected in the d^9 , d^9L , and the metastable d^8 states of Cu d-electrons. First principles $GG\ddot{A} + U$ calculations further validate the notion that within the A-site ordered perovskite family, the choice of B-site cation is an effective tool to manipulate the degree of B-Cu-O hybridization, adjusting the Cu valency towards the unusual 3+ valence state in $CCCoO$ and away from 3+ closer to the stable 2+ valency in $CCCrO$. Additionally, Wannier function calculations support this direct experimental observation that in the $CCCrO$ compound the ZR many-body state is particularly favorable and controls the low-energy physics. These findings demonstrate that the charge and spin state of Cu, fundamental to the intriguing physical properties the cuprates display, can be effectively altered by a careful choice of the B-site cation on isomorphous lattices that circumvent the chemical disorder and lattice modulation intrinsic to other doping methods.

Methods

Experimental details. Polycrystalline $CaCu_3B_4O_{12}$ (B = Cr and Co) samples were prepared under high-pressure and high-temperature (HPHT) conditions with a Walker-type multianvil module (Rockland Research Co.). For B = Cr, stoichiometric amounts of CaO , CuO , and CrO_2 powders were thoroughly mixed and then subjected to a HPHT treatment at 7 GPa and 900°C for 30 minutes. For B = Co, a precursor containing Ca, Cu, and Co ions in the 1 : 3 : 4 molar ratio obtained via a sol-gel route was mixed with 30 wt.% $KClO_4$ acting as an oxidizing agent and then subjected to a HPHT treatment at 9 GPa and 1000°C for 30 minutes. The resultant KCl was washed away with deionized water. Details about the sample assembly and procedures for the HPHT experiment can be found in a previous paper³⁵. Phase purity of the above samples was examined with powder X-ray diffraction (XRD) at room temperature with a Philips Xpert diffractometer (Cu K α radiation). The B = Co sample contains a small amount of cobalt and copper oxides. The cubic lattice parameter was calculated to be $a = 7.2385(5)$ and $7.1259(3)$ Å for M = Cr and Co, respectively. Reitveld refinement for the two a-site ordered compounds is available in the Supplemental Figure S2.

LCO was synthesized under high oxygen pressure to the rhombohedral symmetry, details of which can be found elsewhere³⁶. YBCO was grown with pulsed laser deposition, the details of which can also be found elsewhere³⁷.

In order to elucidate the transformation of the Cu valency across these compounds, soft XAS measurements were carried out at the soft x-ray branch at the 4-ID-C beamline in the bulk-sensitive total fluorescence yield (TFY) mode and TEY mode in the Advanced Photon Source at Argonne National Laboratory. Measurements were taken on the Cu L-edge and O-K edge for all samples. All measurements were accompanied by a CuO standard, which allows precise alignment of the energy for oxidation state comparison. The Co and Cr L-edges were also obtained for the corresponding samples. All measurements shown were obtained in TFY mode; except, the Cr L edge data and all the Cr reference absorption data were taken in TEY mode.

Computational details. In the first-principles DFT calculations we have used the plane wave basis set and pseudo-potentials as implemented in the Vienna Ab-initio Simulation Package (VASP)³⁸. The exchange-correlation function was chosen to be that of generalized gradient approximation (GGA) implemented following the parametrization of Perdew-Burke-Ernzerhof³⁹. The electron-electron correlation beyond GGA was taken into account through improved treatment of $GGA + U$ calculation within the $+U$ implementation of Dudarev *et al.*⁴⁰. For the plane wave based calculations, we used projector augmented wave (PAW)⁴¹ potentials. The wave functions were expanded in the plane wave basis with a kinetic energy cutoff of 600 eV and Brillouin zone summations were carried out with a $6 \times 6 \times 6$ k-mesh. The U value of 5 eV on Cu site and 4 eV on B site were used for $GGA + U$ calculations while the Hund's rule coupling J was fixed to 0.8 eV. The obtained results were verified in terms of variation of U parameter.

In order to estimate the positions of the Cu-d, B-d and O-p energy levels as well as the plots of the effective Wannier functions for B-d states, we used muffin-tin orbital (MTO) based N-th order MTO (NMTO)⁴²-downfolding calculations. Starting from a full DFT calculations, NMTO-downfolding arrives at a few-orbital Hamiltonian by integrating out degrees which are not of interest. It does so by



defining energy-selected, effective orbitals which serve as Wannier-like orbitals defining the few-orbital Hamiltonian in the *downfolded* representation. NMTO technique which is not yet available in its self-consistent form relies on the self-consistent potential parameters obtained out of linear muffin-tine orbital (LMTO)⁴³ calculations. The results were cross-checked among the plane wave and LMTO calculations in terms of total energy differences, density of states and band structures.

- Zaanan, J., Sawatzky, G. A. & Allen, J. W. Band gaps and electronic structure of transition-metal compounds. *Phys. Rev. Lett.* **55**, 418 (1985).
- Plakida, Nikolay. *High-Temperature Cuprate Superconductors*. Berlin: Springer-Verlag, 2010.
- Chakhalian, J. *et al.* Orbital Reconstruction and covalent bonding at an oxide interface. *Science* **318**, 1114–1117 (2007).
- Chakhalian, J. *et al.* Magnetism at the interface between ferromagnetic and superconducting oxides. *Nat. Phys.* **2**, 244–8 (2006).
- Karpinen, M & Yamauchi, H. The doping routes and distribution of holes in layered cuprates: a novel bond-valence approach. *Phil. Mag. B* **79**, 2, 343–66 (1999).
- Nücker, N., Fink, J., Fuggle, J. C., Durham, P. J. & Temmerman, W. M. Evidence for holes on oxygen sites in the high T_c superconductors $\text{La}_{2-x}\text{Sr}_x\text{CuO}_4$ and $\text{YBa}_2\text{Cu}_3\text{O}_{7-y}$. *Phys. Rev. B* **37**, 10 (1988).
- Nücker, N. *et al.* Site-specific and doping-dependent electronic structure of $\text{YBa}_2\text{Cu}_3\text{O}_x$ probed by O1s and Cu 2p x-ray-absorption spectroscopy. *Phys. Rev. B* **51**, 13 (1995).
- Kuiper, P. *et al.* X-ray absorption study of the O 2p hole concentration dependence on O stoichiometry in $\text{YBa}_2\text{Cu}_3\text{O}_x$. *Phys. Rev. B* **38**, 10 (1988).
- Zhang, F. C. & Rice, T. M. Effective hamiltonian for the superconducting Cu oxides. *Phys. Rev. B* **37**, 3759–3761 (1988).
- Xiang, H. P., Liu, X. J., Meng, J. & Wu, Z. J. Structural stability and magnetic coupling in $\text{CaCu}_3\text{Co}_4\text{O}_{12}$ from first principles. *J. Phys.: Condens Matter* **21**, 045501 (2009).
- Shimakawa, Y. A-site-ordered perovskites with intriguing physical properties. *Inorg. Chem* **47**, 8562–70 (2008).
- Alippi, P. & Fiorentini, V. Magnetism and unusual Cu valency in quadruple perovskites. *Eur. Phys. J. B* **85**, 82 (2012).
- Tran, T. T., Takubo, K., Mizokawa, T., Kobayashi, W. & Terasaki, I. Electronic structure of $\text{CaCu}_3\text{Ru}_4\text{O}_{12}$ studied by x-ray photoemission spectroscopy. *Phys. Rev. B* **73**, 193105 (2006).
- Shiraki, H., Saito, T., Azuma, M. & Shimakawa, Y. Metallic behavior n A-site-ordered perovskites $\text{ACu}_3\text{V}_4\text{O}_{12}$ with $A = \text{Na}^+$, Ca^{2+} , and Y^{3+} . *J. Phys. Soc. Jpn.* **77**, 6 (2008).
- Mukherjee, S., Sarkar, S. & Saha-Dasgupta, T. First Principles study of $\text{CaCu}_3\text{B}_4\text{O}_{12}$ ($B = \text{Co}, \text{Rh}, \text{Ir}$). *J. Mater. Sci.* **47**, 7660–4 (2012).
- Long, Y. W. *et al.* Temperature-induced A-B intersite charge transfer in a A-site-ordered $\text{LaCu}_3\text{Fe}_4\text{O}_{12}$ perovskite. *Nature* **458**, 60 (2009).
- McGuinness, C. *et al.* X-ray spectroscopic study of the electronic structure of the high-dielectric-constant material $\text{CaCu}_3\text{Ti}_4\text{O}_{12}$. *Phys. Rev. B* **71**, 19511 (2005).
- Lin, Y., Chen, Y. B., Garret, T., Liu, S. W. & Chen, C. L. Epitaxial growth of dielectric $\text{CaCu}_3\text{Ti}_4\text{O}_{12}$ thin films on (001) LaAlO_3 by pulsed laser deposition. *Appl. Phys. Lett.* **81**, 631–3 (2002).
- Yamada, I. *et al.* A perovskite containing quadrivalent iron as a charge-disproportionated ferrimagnet. *Angew. Chem. Int. Ed* **47**, 7032–5 (2008).
- Prodi, A. *et al.* Charge, orbital and spin ordering phenomena in the mixed valence manganite $(\text{NaMn}^{3+}_3)(\text{Mn}^{3+}_2\text{Mn}^{4+}_2)\text{O}_{12}$. *Nat. Mater.* **3**, 48–52 (2004).
- Tanaka, S., Shimazui, N., Takatsu, H., Yonezawa, S. & Maeno, Y. Heavy-Mass Behavior of Ordered Perovskites $\text{ACu}_3\text{Ru}_4\text{O}_{12}$ ($A = \text{Na}, \text{Ca}, \text{La}$). *J. Phys. Soc. Jpn.* **78**, 024706 (2009).
- Hollmann, N. *et al.* Correlation effects in $\text{CaCu}_3\text{Ru}_4\text{O}_{12}$ arXiv: 1211.2984v1.
- Mizokawa, T. *et al.* Metallic versus insulating behavior in the A-site ordered perovskite oxides $\text{ACu}_3\text{Co}_4\text{O}_{12}$ ($A = \text{Ca}$ and Y) controlled by Mott and Zhang-Rice physics. *Phys. Rev. B* **80**, 125105 (2009).
- Subramanian, M. A., Marshall, W. J., Calvarese, T. G. & Sleight, A. W. Valence degeneracy in $\text{CaCu}_3\text{Cr}_4\text{O}_{12}$. *J. Phys. and Chem. Solids* **64**, 1569–71 (2003).
- Chen, C. T. *et al.* Electronic States in $\text{La}_{2-x}\text{Sr}_x\text{CuO}_{4+\delta}$ probed by soft-x-ray absorption. *Phys. Rev. Lett.* **66**, 1 (1991).
- Griani, M. *et al.* Studies of copper valence states with Cu L_3 x-ray absorption spectroscopy. *Phys. Rev. B* **39**, 3 (1989).
- Bianconi, A. *et al.* Linearly polarized Cu L_3 -edge x-ray-absorption near-edge structure of $\text{Bi}_2\text{CaSr}_2\text{Cu}_2\text{O}_8$. *Phys. Rev. B* **44**, 18 (1991).
- Mizokawa, T., Fujimori, A., Namatame, H., Takeda, Y. & Takano, M. Electronic structure of tetragonal LaCuO_3 studied by photoemission and x-ray-absorption spectroscopy. *Phys. Rev. B* **57**, 16 (1998).
- Sarangi, R. *et al.* X-ray absorption edge spectroscopy and computational studies on LCuO_2 species. *J. Am. Chem. Soc.* **128**, 8286–96 (2006).
- LeBoeuf, D. *et al.* Electron pockets in the Fermi surface of hole-doped high- T_c superconductors. *Nature* **450**, 533–6 (2007).
- Ando, Y., Komiya, S., Segawa, K., Ono, S. & Kurita, Y. Electronic phase diagram of high- T_c cuprate superconductors from a mapping of the in-plane resistivity curvature. *Phys. Rev. Lett.* **93**, 267001 (2004).
- Sarma, D. D. *et al.* Electronic structure of high- T_c superconductors from soft-x-ray absorption. *Phys. Rev. B* **37**, 16 (1988).
- Debkov, Y. S. *et al.* Correlations in the electronic structure of half-metallic ferromagnetic CrO_2 films: An x-ray absorption and resonant photoemission spectroscopy study. *Phys. Rev. B* **72**, 060401(R) (2005).
- Medling, S. *et al.* Evolution of magnetic oxygen states in Sr-doped LaCoO_3 . *Phys. Rev. Lett.* **109**, 157204 (2012).
- Cheng, J.-G., Zhou, J.-S. & Goodenough, J. B. Evolution of ferromagnetism in orthorhombic perovskites $\text{Sr}_{1-x}\text{Pb}_x\text{RuO}_3$. *Phys. Rev. B* **81**, 134412 (2010).
- Zhou, J.-S., Archibald, W. & Goodenough, J. B. Approach to Curie-Weiss paramagnetism in the metallic perovskites $\text{La}_{1-x}\text{Nd}_x\text{CuO}_3$. *Phys. Rev. B* **61**, 3196–3199 (2000).
- Gray, B. A. *et al.* arXiv:1301.3736.
- Kresse, G. & Furthmüller, J. Efficient iterative schemes for ab initio total-energy calculations using a plane-wave basis set. *Phys. Rev. B* **54**, 11169 (1996).
- P. Perdew, J., Burke, K. & Ernzerhof, M. Generalized Gradient Approximation Made Simple. *Phys. Rev. Lett.* **77**, 3865 (1996).
- Dudarev, S. L., Botton, G. A., Savrasov, S. Y., Humphreys, C. J., & Sutton, A. P. Electron-energy-loss spectra and the structural stability of nickel oxide: An LSDA + U study. *Phys. Rev. B* **57**, 1505 (1998).
- Blöchl, P. E. Projector augmented-wave method. *Phys. Rev. B* **50**, 17953 (1994).
- Andersen, O. K. & Saha-Dasgupta, T. Muffin-tin orbitals of arbitrary order. *Phys. Rev. B* **62**, R16219 (2000).
- Andersen, O. K. & Jepsen, O. Explicit, First-Principles Tight-Binding Theory. *Phys. Rev. Lett.* **53**, 2571 (1984).

Acknowledgements

JC is supported by DOD-ARO Grant No. 0402-17291. JSZ and JBG is supported by NSF Grant No. DMR-1122603. TS-D would also like to thank, CSIR and DST, India for funding. Work at the Advanced Photon Source, Argonne is supported by the U.S. Department of Energy, Office of Science under Grant No. DEAC02-06CH11357. Thanks to Dr. Bogdan Dabrowski for the $\text{SrCoO}_{2.9}$ ($\sim 4+$) sample. JGC acknowledges the support from the Japan Society for the Promotion of Science (Grant No. 12F02023) and the Chinese Academy of Sciences.

Author contributions

D.M., J.W.F. and J.C. acquired the experimental data. S.M. and T.S.-D. did the theoretical calculations. J.G.C., J.S.Z. and J.B.G. grew the samples. S.M. and B.A.G. analyzed data and provided notes on the initial versions of the manuscript. D.M., T.S.-D. and J.C. wrote the final version of the manuscript.

Additional information

Supplementary information accompanies this paper at <http://www.nature.com/scientificreports>

Competing financial interests: The authors declare no competing financial interests.

License: This work is licensed under a Creative Commons Attribution-NonCommercial-NoDerivs 3.0 Unported License. To view a copy of this license, visit <http://creativecommons.org/licenses/by-nc-nd/3.0/>

How to cite this article: Meyers, D. *et al.* Zhang-Rice physics and anomalous copper states in A-site ordered perovskites. *Sci. Rep.* **3**, 1834; DOI:10.1038/srep01834 (2013).

ARTICLE

Received 25 Jun 2014 | Accepted 11 Nov 2014 | Published 17 Dec 2014

DOI: 10.1038/ncomms6818

Competition between heavy fermion and Kondo interaction in isoelectronic A-site-ordered perovskites

D. Meyers¹, S. Middey¹, J.-G. Cheng^{2,3}, Swarnakamal Mukherjee⁴, B.A. Gray¹, Yanwei Cao¹, J.-S. Zhou³, J.B. Goodenough³, Yongseong Choi⁵, D. Haskel⁵, J.W. Freeland⁵, T. Saha-Dasgupta⁴ & J. Chakhalian¹

With current research efforts shifting towards the *4d* and *5d* transition metal oxides, understanding the evolution of the electronic and magnetic structure as one moves away from *3d* materials is of critical importance. Here we perform X-ray spectroscopy and electronic structure calculations on A-site-ordered perovskites with Cu in the A-site and the B-sites descending along the ninth group of the periodic table to elucidate the emerging properties as *d*-orbitals change from partially filled *3d* to *4d* to *5d*. The results show that when descending from Co to Ir, the charge transfers from the cuprate-like Zhang-Rice state on Cu to the t_{2g} orbital of the B site. As the Cu *d*-orbital occupation approaches the Cu^{2+} limit, a mixed valence state in $\text{CaCu}_3\text{Rh}_4\text{O}_{12}$ and heavy fermion state in $\text{CaCu}_3\text{Ir}_4\text{O}_{12}$ are obtained. The investigated *d*-electron compounds are mapped onto the Doniach phase diagram of the competing RKKY and Kondo interactions developed for the *f*-electron systems.

¹Department of Physics, University of Arkansas, Fayetteville, Arkansas 72701, USA. ²Beijing National Laboratory for Condensed Matter Physics, and Institute of Physics, Chinese Academy of Sciences, Beijing 100190, China. ³Texas Materials Institute, ETC 9.102, University of Texas at Austin, Austin, Texas 78712, USA. ⁴Department of Condensed Matter Physics and Materials Science, S.N.Bose National Centre for Basic Sciences, Kolkata 700098, India. ⁵Advanced Photon Source, Argonne National Laboratory, Argonne, Illinois 60439, USA. Correspondence and requests for materials should be addressed to D.M. (email: dmeyers@uark.edu) or to T.S.-D. (email: t.sahadasgupta@gmail.com).

Transition metal (TM) oxides host a diversity of fascinating phenomena^{1–6}. Several possible formal oxidation states of the TM ions coupled with the innate ability to stabilize those states by structural network of oxygens give rise to a striking change in the TM–O orbital hybridization W , electron–electron correlations U and the charge transfer energy Δ ⁷; the subtle competition between W , U and Δ across the $3d$ group of the periodic table is then responsible for a vast landscape of interesting magnetic and electronic ground states^{1,4,8}. In traversing the periodic table within groups of the $3d \rightarrow 4d \rightarrow 5d$ TM blocks, the additional degree of freedom, the spin–orbit (SO) interaction, λ gets activated and is predicted to foster a multitude of exotic electronic and topological phases of correlated matter^{9–15}.

Although the vast majority of these compounds contain TM ions at the B -site of the ABO_3 perovskite structure, it is now possible to synthesize a new family of compounds with formula unit $(AA_3')B_4O_{12}$, Fig. 1a, where the perovskite A -site is partially occupied by a TM ion, labelled A' . Among this class of materials, $(ACu_3)B_4O_{12}$ with Cu in the A' site have garnered considerable attention because of the presence of CuO_4 planes. Structurally, this family of compounds consists of two different magnetically active sublattices of TM ions: BO_6 octahedral units (forming a three-dimensional octahedral network as in the typical ABO_3 perovskite lattice) and the planar CuO_4 units coupled with BO_6 units via an apical oxygen (see Fig. 1a). Depending on the choice of B -site ion, the materials exhibit exciting properties including giant dielectric constant ($B = Ti$), exotic ferromagnetism ($B = Ge$,

Sn, Fe), valence fluctuation ($B = V$), Mott physics ($B = Ru$) and inter-site charge order ($B = Fe$) to name a few^{16–22}. They are also of particular interest owing to the preservation of the cubic lattice symmetry ($IM\bar{3}$), despite large variations of the B -site ion including utilizing different TM series ($3d$ or $4d$ or $5d$) of the periodic table²³. This provides a unique platform to investigate the emergence of the electronic and magnetic states; for example, in recent work on $(CaCu_3)B_4O_{12}$ ($B = Cr, Co$), it has been demonstrated that the Zhang-Rice quantum state (essential for hole doped high- T_c superconductivity) can be realized in these compounds, despite the lack of the superconducting ground state^{24–26}.

Very recently, Cheng *et al.* showed that this class of materials displays a crossover between the magnetic insulating and paramagnetic metallic states, depending on the Cu–O and B –O bond lengths²⁷. It was further suggested that the $CaCu_3Ir_4O_{12}$ (CCIrO) compound, with the bond length within the crossover region, possesses anomalous electronic and magnetic properties arising presumably due to the interaction between the localized Cu and itinerant Ir states²³. However, the mechanism by which the electronic structure transforms to create this emergent behaviour in CCIrO is not microscopically understood. In order to shed light on this interesting aspect, three *isostructural* and *isoelectronic* compounds whose B -site spans the ninth group of the periodic table, $(CaCu_3)B_4O_{12}$ ($B = Co, Rh, Ir$), were synthesized. Within the proposed phase diagram of Cheng *et al.*, $B = Co$ occupies the paramagnetic metallic state, whereas CCIrO is at the crossover region as reflected for instance in anomalous d.c. transport properties shown in Fig. 1b (refs 22,27).

In this paper, we investigate the electronic and magnetic structure of this new class of materials by a combination of resonant soft and hard X-ray absorption spectroscopy (XAS) on the Cu L-edge, O K-edge, and B -site L- and K-edges. Complementary first-principles calculations corroborate the experimental findings, providing microscopic understanding. Our results reveal that the unusual physical properties of these compounds are microscopically controlled by the degree of Cu $3d_{x^2-y^2}$ orbital occupancy and the strength of the B –O covalency.

Results

Spectroscopic results. First, we discuss the evolution of the electronic structure of Cu. The Cu L₃-edge XAS are presented in Fig. 2a (total fluorescence yield (TFY) available in supplementary Fig. 1). In accord with the previously reported results²⁴ for $CaCu_3Co_4O_{12}$ (CCCoo), the main absorption line at 931.4 eV arises due to absorption from the $d^9\bar{L} \rightarrow \underline{c}d^{10}\bar{L}$ transition, where \bar{L} stands for a ligand hole whereas \underline{c} indicates a hole in the Cu $2p$ core states. The low-energy shoulder around 930 eV arises from the $d^9 \rightarrow \underline{c}d^{10}$ transition; the d^9 transition accounting for 10% of the total peak area, indicating that there is a large Cu–O hybridization present in CCCoo. The line shape of the Cu L₃ absorption edge for $CaCu_3Rh_4O_{12}$ (CCRhO), containing the $4d$ element Rh at the B -site, also contains a lesser and yet still significant $d^9\bar{L}$ contribution, giving a Cu valence of $\sim 2.6+$. The transport behaviour for this compound is quite similar to CCCoo and points to CCRhO also being paramagnetic metallic (Fig. 1b). On the other hand, for CCIrO, the $d^9\bar{L}$ state is no longer present and the L₃ line shape is almost analogous to that recorded from purely ionic $d^9 Cu^{2+}$ charge state, agreeing with an earlier report utilizing electron energy loss spectroscopy^{23,23,28–30}. This implies that the hole is no longer interacting with the Cu $\underline{c}d^{10}$ final state, showing a significant reduction of the hole contribution to the hybridized orbital between Cu and O. Furthermore, the small multiplet split peak seen around ~ 940 eV for all Cu L₃-edge spectra is due to a transition from the metastable $3d^8$ (Cu^{3+}) to

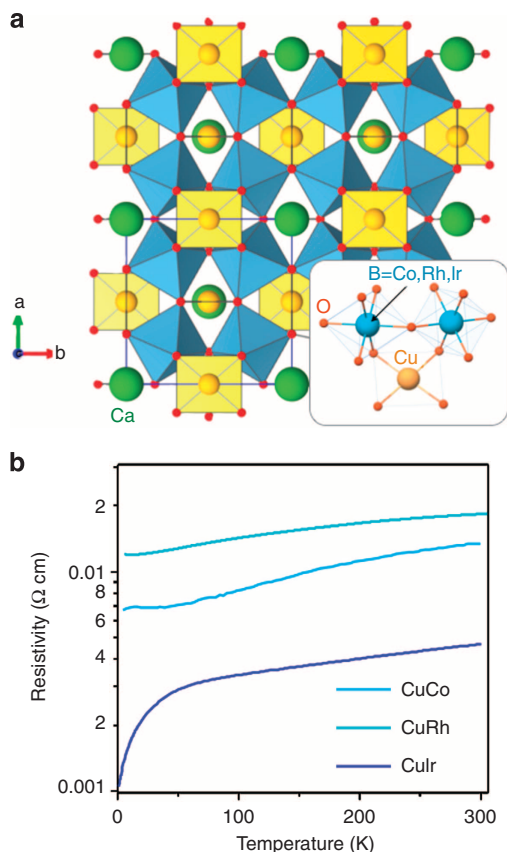


Figure 1 | Structure and properties of A-site-ordered perovskites. (a) Crystal structure of A-site-ordered perovskites. Connection between CuO_4 planes and IrO_6 octahedra shown in the bottom right corner. (b) Temperature-dependent transport data for the $B = Co, Rh, Ir$ samples displaying the anomalous behaviour for CCIrO. CCCoo data taken from ref. 22. CCIrO data taken from ref. 27.

the cd^9 state; the small decrease in this $3d^8$ peak spectral weight in going from Co to Ir also indicates movement towards the ionic $3d^9$ state of Cu^{2+} . Taken as a whole, the Cu L_3 -edge data directly illustrate that in the presence of $4d$ or $5d$ orbitals, it is energetically more favourable to transfer the hole on to the B -site instead of stabilizing the Cu^{3+} state, suggesting a strong change in covalency, as tabulated in Table 1.

In the past, the electronic structure of Cu has been extensively studied in the context of high- T_c superconducting cuprates, where it was also found that the reduction of ligand hole weight on Cu causes a decrease of the pre-peak intensity around 528 eV in the O K-edge XAS spectrum^{32–35}. To track the movement of the hole in the present series of samples, we obtained O K-edge XAS spectra shown in Fig. 2b, with the post-edge normalized to 1 (at 540 eV). As immediately seen, the decrease of the relative intensity of the pre-peak indeed scales with the reduction of the ligand hole on Cu, implying a marked change in both bandwidth, W , and the charge transfer gap, Δ . The decrease of the pre-peak intensity can be rationalized in terms of a decreasing availability of empty states as the hole concentration on O decreases in moving from Co to Rh to Ir. Although the high-energy shoulder on the Cu L_3 peak disappears entirely for CClrO, the oxygen pre-peak does not, which indicates the hybridization between the B -site and O is also significant, as Cu^{2+} will not contribute to the pre-peak. The results of the O K-edge spectroscopy are thus in excellent agreement with the Cu L-edge observations. Another interesting observation is that the energy separation between the pre-peak and the peak around 530 eV increases from Co to Ir. The shift towards higher energy will be discussed in detail in the

theory section and is attributed to the gradually increasing separation of the B -site bands (CCCoO) and both the B -site and Cu bands (CCRhO and CClrO) from the O $2p$ band.

The movement of the hole away from Cu naturally implies a change in valency of the B -site ion. To verify this proposition and to corroborate the previous findings, we performed XAS on the L- and K-edges of Ir and Rh, respectively (Co was measured previously and found to be in the $\sim 3.25+$ state, after subtraction of an impurity peak²⁴). Moving to the $4d$ compound, Rh K-edge XAS spectra have been simultaneously collected from the CCRhO sample and a standard $SrRhO_3$ reference sample. Although the line shape from CCRhO shares similarities with $SrRhO_3$ (Rh^{4+}), the difference in energy at 80% of the normalized absorption was found to be ~ 0.68 eV lower relative to $SrRhO_3$, Fig. 3a (ref. 36). Based on this shift, and the shift of ~ 1.9 eV between Rh^{3+} and Rh^{4+} (see Supplementary Fig. 2), we conclude that the Rh valence state is indeed strongly mixed between $3+$ and $4+$, with a value of $3.64 \pm (\pm 0.1)$. In conjunction with the Cu and O soft XAS, the entire Rh data set strongly supports the notion that the hole still largely resides on the O anion, but spreads to the hybridized orbital with Rh. Finally, the Ir L_3 edge ($2p_{3/2} \rightarrow 5d$ transition) recorded from CClrO and $SrIr(4+)O_3$ is shown in Fig. 3b. As seen, the remarkably similar line shape and the energy peak position both confirm that Ir is in the $4+$ state. The L_3 to L_2 branching ratio was found to be 3.79 (analysis shown in Supplementary Fig. 2)^{9,11}. This value is similar to that found in several other iridate compounds and signifies a large SO coupling (SOC) as expected for a $5d$ compound^{9,11,37,38}. Overall, the Ir L-edge data are in excellent agreement with the Cu L-edge data stating the d^9 Cu^{2+} ground state, with a much smaller d^8 contribution compared with the Rh and Co compounds; thus, in the CClrO compound, the hole is now almost entirely transferred from the Cu $3d$ -O $2p$ state to the Ir $5d$ -O $2p$ hybridized orbital. The obtained valences for the B -sites are also listed in Table 1.

Table 1 | Experimental and theoretical values for the valence of Cu and the B -site for each compound.

	CCCoO	CCRhO	CClrO
Cu (experimental)	$(2.90 \pm 0.15)^+$	$(2.63 \pm 0.1)^+$	$(2.03 \pm 0.1)^+$
B -site (experimental)	3.25^+ (ref. 24)	$(3.64 \pm 0.1)^+$	4^+
Cu (theory)	3^+	2.5^+	2^+
B -site (theory)	3.25^+	3.6^+	4^+

Density functional theory (DFT) results. Calculating the spin-polarized electronic structure of the three compounds, as a common feature, we find that the Cu d , Bd and O p states are admixed, although the degree of admixture varies between the three

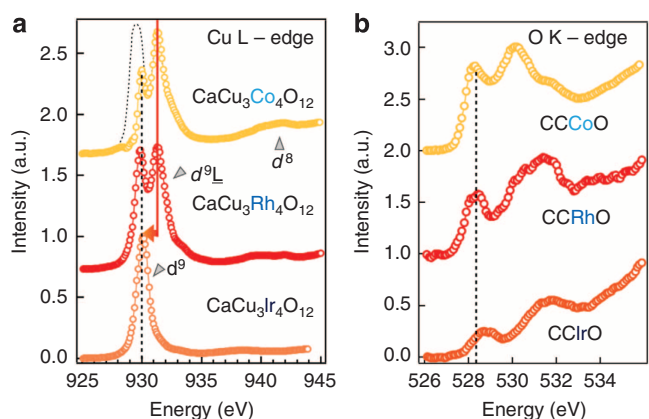


Figure 2 | Changing Cu and O valency as a function of B -site. (a) Soft XAS on the Cu L-edge for all samples showing the changing Cu valence. The dotted line is the spectrum before the subtraction of the impurity peak (note that CCCoO TFY data and explanation of impurity peak originally given in ref. 24). The dashed line indicates the energy of the d^9 peak. (b) XAS on the O K-edge showing both the reduction of the pre-peak on O and the shifting of the O $2p$ -Cu $3d$ and O $2p$ - B -site d hybridized orbitals. The dashed line here indicates the energy of the O pre-peak associated with a doped hole.

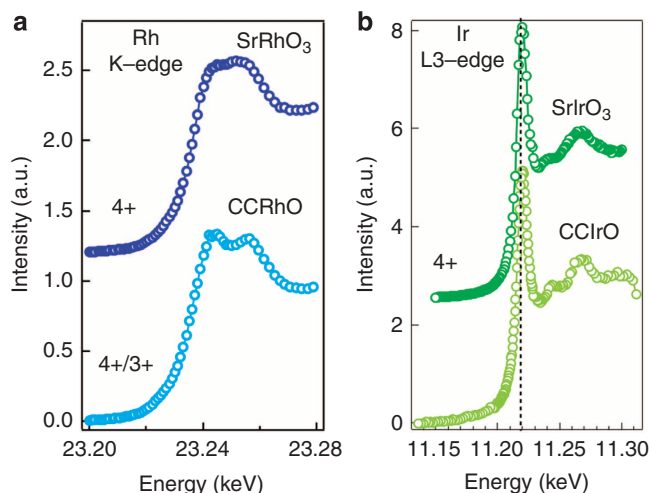


Figure 3 | Changing valency of the B -sites by hard XAS. (a) Hard XAS Rh K-edge measurements on the CCRhO and $SrRhO_3$ ($4+$) standard. (b) XAS on the Ir L_3 -edge for both CClrO and $SrIrO_3$ standard evidencing the nearly identical line shape and position indicating the $4+$ valency. The dashed line shows the excellent agreement of the peak positions.

compounds. Site-projected partial density of states is shown in Supplementary Fig. 3 (ref. 39). A direct inspection of the plot for CCCoO reveals that the Cu $d_{x^2-y^2} - O(p)$ states, which are strongly admixed with Co $e_g (e_g^\sigma)$ states, are empty in both spin-up and spin-down channels, thus lending strong support for the $\text{Cu}^{3+} (d^9 \underline{L})$ valence in CCCoO. This yields a mixed valence of $3.25+$ on Co and the intermediate spin state with a magnetic moment of $\sim 1.68 \mu_B$. Moving towards the CCRhO compound, the admixture between the Cu $d_{x^2-y^2} + O$ state and Rh states becomes markedly reduced compared with that of CCCoO. In this compound, the calculated Cu valence is found to be mixed between $2+$ and $3+$ ($\sim 2.5+$), with Rh valence close to $3.6+$. Unlike Co, magnetically Rh is found to be in the low spin state with a spin moment of $0.21 \mu_B$ and largely quenched orbital moment of $0.05 \mu_B$. Finally, we consider the CCIrO. In sharp contrast to both Co and Rh, the mixing of the Cu $d_{x^2-y^2} - O p$ states and the Ir d states is drastically reduced. This results in an almost pure Cu $d_{x^2-y^2} - O p$ state occupied in one spin channel and empty in another, implying a Cu^{2+} valence and nominal Ir^{4+} valence. The spin moments at Ir and Cu sites are found to be $0.45 \mu_B$ and $0.65 \mu_B$, respectively, with a rather large spin moment of $0.12 \mu_B$ on O, arising from strong hybridization with Ir. We note that ionic Ir^{4+} is in the $5d^5$ configuration and has extensively been discussed in view of the interplay of strong SOC and correlation physics^{9–15}. The large branching ratio of close to 3.8 signifies the presence of a large SOC at the Ir site, which is found to be common among many of the compounds of Ir^{4+} in an octahedral environment, even when the compound is metallic as in IrO_2 (ref. 38). The orbital moment at the Ir site, calculated within the generalized gradient approximation (GGA) + U + SO, turned out to be $0.12 \mu_B$, smaller than the spin moment with $m_{\text{orbital}}/m_{\text{spin}}$ being 0.27. This is curious when compared with the values obtained in cases like BaIrO_3 (ref. 11). The structure and coupling mechanisms are, however, rather different between compounds like Sr_2IrO_4 or BaIrO_3 and the present one. In the former examples, magnetic interactions are one- or two-dimensional Ir–Ir, whereas here they are Cu–Ir with three-dimensional connectivity. The dominance of hybridization produces an additional induced spin moment at the Ir site because of the presence of the magnetic ion Cu, a behaviour qualitatively similar to the case of $\text{La}_2\text{CoIrO}_6$, discussed in recent literature³⁷. The presence of a significant SO interaction is found to mix up and down spins and destroys half-metallicity in CCIrO. We note here that inclusion of SOC allows for the non-collinear arrangement of spins. We have therefore carried out spin-polarized calculations assuming collinear as well as non-collinear spin arrangements. The calculated magnetic moments at various atomic sites, obtained in non-collinear calculations, turn out to be very similar to that obtained assuming simple collinear arrangement of spins. The spin magnetic moments are found to be similar to that obtained from collinear calculations within 1–2%, whereas the orbital magnetic moments are found to differ from that in collinear calculation by a maximum of 0.5%, providing confidence in the general conclusion drawn from the electronic structure calculations on the various valence and spin states, irrespective of the assumed spin arrangements.

The evolution of the nominal valence of Cu from predominant $3+$ ($d^9 \underline{L}$) to $2+$, as one moves from $3d$ (Co) to $4d$ (Rh) to $5d$ (Ir) elements at the B -site, is controlled by mixing between B -site d states and Cu $d_{x^2-y^2} - O p$ states and can be vividly visualized in the effective Wannier function plots shown in Fig. 4a (upper panel). As clearly seen, the Wannier functions centred at the Cu site have the orbital character of $d_{x^2-y^2}$ symmetry, and the tail is shaped according to the symmetry of the orbitals mixed with it.

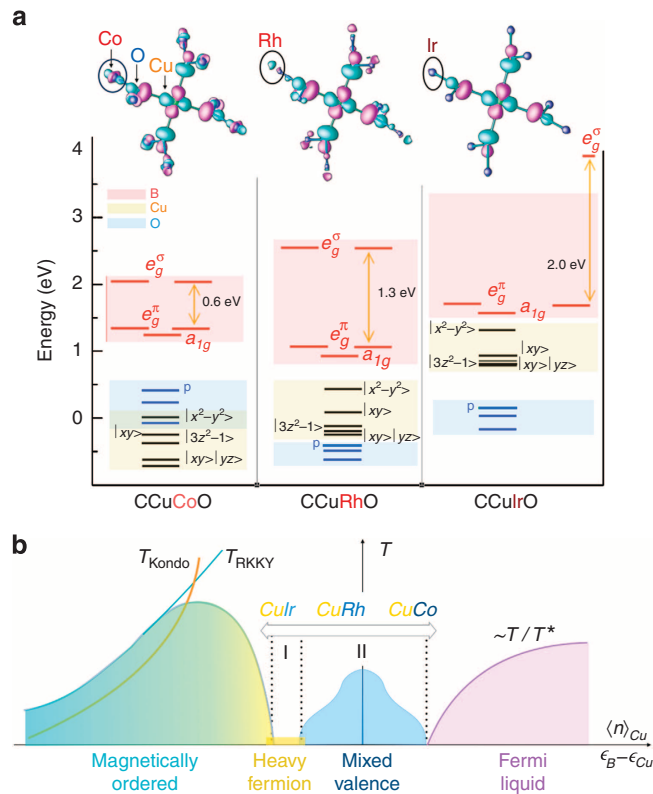


Figure 4 | Theoretical calculations and Doniach phase diagram. (a) Top panels: plots of effective Wannier functions for O p , Cu $d_{x^2-y^2}$ orbitals for CCCoO, CCRhO and CCIrO. Plotted are the constant value surfaces with lobes of different signs coloured as cyan and magenta. The Cu, B- and O-sites are shown as green, red and blue coloured balls. Bottom panels: energy level positions of Cu d , B d and O p states for CCCoO, CCRhO and CCIrO. (b) Doniach phase diagram showing the dependency on the Cu occupation.

Specifically, moving from CCCoO to CCRhO to CCIrO, we find the weight at the tails centred at the B -site (marked by a circle) progressively diminishes.

Microscopically, the nature of this peculiar unmixing/dehybridization effect between Cu–O and B -site in moving from $3d$ to $4d$ to $5d$ element at the B -site can be further elucidated by considering the energy level positions of $B d$, Cu d and O p states (see Fig. 4a (bottom panel)). As mentioned above, the octahedral crystal field coupled with the trigonal distortion separates the $B d$ states into doubly degenerate e_g^σ , e_g^π and singly degenerate a_{1g} ones, whereas the square planar geometry of the CuO_2 plane breaks the Cu d states into Cu $d_{x^2-y^2}$ and the rest, with Cu $d_{x^2-y^2}$ being of the highest energy. In progressing from CCCoO to CCRhO to CCIrO, the relative position of Cu $d_{x^2-y^2}$ with respect to O p states increases, driven by the pushing down of O p states because of the increased crystal field splitting ($e_g^\sigma - e_g^\pi/a_{1g}$ splitting) at the B -site. This, in turn, makes the hybridization between the Cu sublattice and B sublattice weaker and weaker as those ions communicate via the intervening oxygen. This highlights a key difference between CCIrO and $\text{CaCu}_3\text{Ru}_4\text{O}_{12}$, where for the latter it was found that the suspected Kondo-like physics was unlikely due to a strong mixing of Cu with O^{40,41}. Similar to that of high- T_c cuprates, for CCCoO, the O p states are positioned above Cu $d_{x^2-y^2}$, placing Cu in to a negative charge transfer regime, which promotes a high- T_c cuprate-like $d^9 \underline{L}$ state akin to the Zhang-Rice singlet state^{24–26,42}. The progressive weakening of covalency between the B sublattice and Cu–O sublattice, as one moves from CCCoO to CCRhO to CCIrO,

makes the spread of the effective Cu $d_{x^2-y^2}$ Wannier function (top panel of Fig. 4a) in the case of Ir dramatically reduced compared with either Co or Rh.

Unified picture. Finally, the element-resolved spectroscopic results combined with the *ab-initio* calculations prompts us to build a unified framework to explain their emergent physical behaviour. Although an earlier study utilizing electron energy loss spectroscopy found small changes between 3–4–5 *d* A-site-ordered perovskites from different columns²³, our study reveals that upon ascending a column of the periodic table from Ir to Co, the Cu $3d_{x^2-y^2}$ orbital occupation changes from practically ionic $3d_{x^2-y^2}^9$ ($S = 1/2$) for CCIrO to the non-magnetic cuprate Zhang-Rice-like state with $3d_{x^2-y^2}^9$ ($S = 0$) for CCCoO, as supported by experimentally and theoretically deduced valences listed in Table 1. Along with it, these localized and magnetically active Cu *d* states in CCIrO shift towards the Fermi surface demonstrating a rapid change in hybridization compared with both CCRhO and CCCoO. On the opposite end, such a drastic change in the Cu orbital occupation results in the *mixed valence* intermediate spin state of Co^{3.25+}, mixed valence Rh $\sim 3.7+$ but ionic Ir⁴⁺ ($5d^5$). These findings allow us to place the three compounds under discussion in the context of the Doniach phase diagram depicted in Fig. 4b, where the fundamental control parameter is the average occupation $\langle n \rangle_{\text{Cu}}$ of the $d_{x^2-y^2}$ orbital modulated by the hybridization from the strongly mixed *B*-site *d*- and *O* *p*-bands^{43–45}. In the modern version of the Doniach phase diagram, interesting physics involving heavy fermions manifests itself as a competition between the Kondo liquid and spin liquid behaviour mediated by chemical doping, whereas very little attention has been given to the mixed valency regime, particularly in *d*-electron systems and in the absence of doping^{43–48}. In this framework, the overall ground state is defined by the competition between RKKY-type magnetic exchange between magnetic holes on Cu with the Kondo screening by conduction carriers from the *B*-O sublattices. For CCIrO, with a $S = 1/2$ *d*-hole localized on Cu, the large magnetic exchange is comparable in strength with the Kondo screening, resulting in the strongly enhanced effective mass observed with transport and thermal measurements²⁷. Thus, Cheng *et al.* firmly placed CCIrO into the heavy fermion regime I in Fig. 4b with the antiferromagnetic local moment short-range magnetism^{23,27}. In moving from Ir to Rh and Co, the Kondo energy scale begins to gain because of the collective hybridization of Cu *d*-holes into the ZR singlets. With the strong reduction in the Cu $d_{x^2-y^2}$ orbital occupation, both CCRhO and CCCoO enter the regime II of mixed valency (or Kondo liquid phase) in Fig. 4b. Unlike regime I, in the mixed valence regime quantum fluctuations between different electronic configurations are highly relevant; in this regime, the local electronic and magnetic structure of Kondo centres (Cu) is defined by the redistribution of electrons between Cu *d* states and electrons from the strongly hybridized *d*- and *p*-states of Rh (Co) and O, that is, $|3d_{x^2-y^2}^9, S = 1/2\rangle$ versus $|3d_{x^2-y^2}^9, S = 0\rangle$. The conjectured microscopic framework that links the electronic and magnetic ground state of the *A*-site perovskites with macroscopic behaviour opens a path in designing emergent-ordered phases with heavy fermion behaviour, quantum criticality and unconventional superconductivity in the magnetic Kondo lattice of cuprate-like moments.

To summarize, we performed XAS measurements and first-principles calculations on a series of *A*-site-ordered perovskites, chemical formula $\text{CaCu}_3\text{B}_4\text{O}_{12}$, spanning one period of the periodic table. Surprisingly, we find that the materials fit well within the Doniach phase diagram, being controlled by the hole count on Cu, leading to the conclusion that the competition

between RKKY and Kondo effects is responsible for the anomalous behaviour observed in the CCIrO compound.

Methods

Sample preparation. All samples used in the present study were prepared under high-pressure and high-temperature conditions with a Walker-type multianvil module (Rockland Research Co.). The *A*-site-ordered perovskites CCCoO, CCRhO and CCIrO were obtained under $P = 9$ GPa and $T = 1,000$ – $1,300$ °C; the reference perovskites SrRhO₃ and SrIrO₃ were obtained at 8 GPa, 1,200 °C and 6 GPa, 1,000 °C, respectively. About 30 wt.% KClO₄ acting as oxidizing agent were added for synthesizing the compounds containing Co and Rh. The resultant KCl was washed away with deionized water. Phase purity of the above samples was examined with powder X-ray diffraction at room temperature with a Philips Xpert diffractometer (Cu K_α radiation). All the *A*-site-ordered perovskites adopt a cubic $IM\bar{3}$ structure with lattice parameter increasing progressively from $a = 7.1259(3)$ Å for $M = \text{Co}$ to $a = 7.3933(1)$ Å for $M = \text{Rh}$, and to $a = 7.4738(1)$ Å for $M = \text{Ir}$. On the other hand, the reference perovskites crystallize into the orthorhombic $Pbnm$ structure with unit-cell parameters $a = 5.5673(1)$ Å, $b = 5.5399(2)$ Å and $c = 7.8550(2)$ Å for SrRhO₃, and $a = 5.5979(1)$ Å, $b = 5.5669(1)$ Å and $c = 7.8909(1)$ Å for SrIrO₃, respectively.

X-ray measurements. XAS measurements were carried out on the polycrystalline samples in the soft X-ray branch at the 4-ID-C beamline in the bulk-sensitive TFY and total electron yield modes, with a 0.1 eV (0.3 eV) resolution at the O K-edge (Cu L-edge), at the Advanced Photon Source in Argonne National Laboratory. Measurements were taken on the Cu L-edge and O K-edge for all samples, and all measurements shown here were obtained in total electron yield mode (TFY available in Supplementary Fig. 1). To measure the *4d* and *5d* *B*-site valences, hard XAS measurements with a 1.5(3) eV resolution were taken at the 4-ID-D beamline in transmission (fluorescence) mode for Ir (Rh).

Computational details. In the first-principles DFT calculations, we have primarily used the plane wave basis set and pseudo-potentials as implemented in the Vienna *Ab-initio* Simulation Package⁴⁹. The exchange-correlation function was chosen to be that of the GGA implemented following the parametrization of Perdew-Burke-Ernzerhof⁵⁰. The electron–electron correlation beyond GGA was taken into account through improved treatment of GGA + *U* calculation within the + *U* implementation of Dudarev *et al.*⁵¹ For the plane wave-based calculations, we used projector augmented wave⁵² potentials. The wave functions were expanded in the plane wave basis with a kinetic energy cutoff of 600 eV and Brillouin zone (BZ) summations were carried out with a $6 \times 6 \times 6$ k-mesh. A *U*-value of 5 eV on Cu site was used. For the *U*-value on the *B* site, a value of 4 eV was used for the 3d element Co and 1–2 eV was used for *4d* and *5d* elements, Rh and Ir. The obtained results were verified in terms of variation of *U* parameter. The Hund's rule coupling *J* was fixed to 0.8 eV. The plane wave results were verified in terms of full-potential linearized augmented plane wave method as implemented⁵³ in WIEN2k. For FLAPW calculations, we chose the augmented plane wave + *lo* as the basis set and the expansion in spherical harmonics for the radial wave functions was taken up to $l = 10$. The charge densities and potentials were represented by spherical harmonics up to $l = 6$. For BZ integration, we considered about 200 k-points in the irreducible BZ and modified tetrahedron method was applied⁵⁴. The commonly used criterion for the convergence of basis sets relating the plane wave cutoff, K_{max} , and the smallest atomic sphere radius, R_{MT} , $R_{\text{MT}} \cdot K_{\text{max}}$ was chosen to be 7.0. Spin-orbit coupling has been included in the calculations in scalar relativistic form as a perturbation to the original Hamiltonian.

To estimate the positions of the Cu *d*, *B d* and *O p* energy levels as well as the plots of the effective Wannier functions for *B d* states, we used muffin-tin orbital (MTO)-based *N*-th order MTO (NMTO)⁵⁵-downfolding calculations. Starting from full DFT calculations, NMTO-downfolding arrives at a few-orbital Hamiltonian by integrating out degrees, which are not of interest. It does so by defining energy-selected, effective orbitals, which serve as Wannier-like orbitals defining the few-orbital Hamiltonian in the *downfolded* representation. NMTO technique, which is not yet available in its self-consistent form, relies on the self-consistent potential parameters obtained out of linear MTO⁵⁶ calculations. The results were cross-checked among the calculations in three different basis sets in terms of total energy differences, density of states and band structures.

References

- Imada, M., Fujimori, A. & Tokura, Y. Metal-insulator transitions. *Rev. Mod. Phys.* **70**, 1039–1263 (1998).
- Chakhalian, J. *et al.* Magnetism at the interface between ferromagnetic and superconducting oxides. *Nat. Phys.* **2**, 244–248 (2006).
- Chakhalian, J. *et al.* Orbital Reconstruction and covalent bonding at an oxide interface. *Science* **318**, 1114–1117 (2007).
- Tokura, Y. Critical features of colossal magnetoresistive manganites. *Rep. Prog. Phys.* **69**, 797–851 (2006).
- McCormack, M., Jin, S., Tiefel, T. H., Fleming, R. M. & Phillips, J. M. Very large magnetoresistance in perovskite-like La-Ca-Mn-O thin films. *Appl. Phys. Lett.* **64**, 3045–3047 (1994).

6. Wang, J. *et al.* Epitaxial BiFeO₃ multiferroic thin film heterostructures. *Science* **299**, 1719–1722 (2003).
7. Zaanen, J., Sawatzky, G. A. & Allen, J. W. Band gaps and electronic structure of transition-metal compounds. *Phys. Rev. Lett.* **55**, 418–421 (1985).
8. Tokura, Y. & Nagaosa, N. Multiferroics as quantum electromagnets. *Science* **69**, 1481–1482 (2006).
9. Haskel, D. *et al.* Pressure tuning of the spin-orbit coupled ground state in Sr₂IrO₄. *Phys. Rev. Lett.* **109**, 027204 (2012).
10. Kim, B. J. *et al.* Novel $J_{\text{eff}}=1/2$ Mott state induced by relativistic spin-orbit coupling in Sr₂IrO₄. *Phys. Rev. Lett.* **101**, 076402 (2008).
11. Laguna-Marco, M. A. *et al.* Orbital magnetism and spin-orbit effects in the electronic structure of BaIrO₃. *Phys. Rev. Lett.* **105**, 216407 (2010).
12. Witzak-Krempa, W., Chen, G., Kim, Y. B. & Balents, L. Correlated quantum phenomena in the strong spin-orbit regime. *Annu. Rev. Condens. Mater. Phys.* **5**, 57–82 (2014).
13. Cao, G., Bolivar, J., McCall, S., Crow, J. E. & Guertin, R. P. Weak ferromagnetism, metal-to-nonmetal transition, and negative differential resistivity in single-crystal Sr₂IrO₄. *Phys. Rev. B* **57**, 11039(R) (1998).
14. Cao, G. *et al.* Anomalous magnetic and transport behavior in the magnetic insulator Sr₃Ir₂O₇. *Phys. Rev. B* **66**, 214412 (2002).
15. Ashcroft, N. W. & Mermin, N. D. *Solid State Physics, Dorothy Garbose Crane*. 659Saunders College Publishing, (1976).
16. McGuinness, C. *et al.* X-ray spectroscopic study of the electronic structure of the high-dielectric-constant material CaCu₃Ti₄O₁₂. *Phys. Rev. B* **71**, 19511 (2005).
17. Shiraki, H. *et al.* Ferromagnetic cuprates CaCu₃Ge₄O₁₂ and CaCu₃Sn₄O₁₂ with A-site ordered perovskite structure. *Phys. Rev. B* **76**, 140403(R) (2007).
18. Yamada, I. *et al.* A perovskite containing quadrivalent iron as a charge-disproportionated ferrimagnet. *Angew. Chem. Int. Ed.* **47**, 7032–7035 (2008).
19. Morita, Y. *et al.* Valence fluctuations and correlated metallic states in A-site ordered perovskite oxides ACu₃V₄O₁₂ (A = Na, Ca, and Y). *Phys. Rev. B* **81**, 165111 (2010).
20. Hollmann, N. *et al.* Correlation effects in CaCu₃Ru₄O₁₂. *Phys. Rev. B* **87**, 155122 (2013).
21. Chen, W.-T. *et al.* Ligand-hole localization in oxides with unusual valence Fe. *Sci. Rep.* **2**, 449 (2012).
22. Yamada, I. *et al.* Synthesis, structure, and physical properties of A-site ordered perovskites ACu₃Co₄O₁₂ (A = Ca and Y). *Chem. Mater.* **22**, 5328–5332 (2010).
23. Xin, Y. *et al.* Study of atomic structure and electronic structure of an AA₃B₄O₁₂ double-perovskite CaCu₃Ir₄O₁₂ using STEM imaging and EELS techniques. *Ultramicroscopy* **127**, 94–99 (2013).
24. Meyers, D. *et al.* Zhang-Rice physics and anomalous copper states in A-site ordered perovskites. *Sci. Rep.* **3**, 1834 (2013).
25. Mizokawa, T. *et al.* Metallic versus insulating behavior in the A-site ordered perovskite oxides ACu₃Co₄O₁₂ (A = Ca and Y) controlled by Mott and Zhang-Rice physics. *Phys. Rev. B* **80**, 125105 (2009).
26. Zhang, F. C. & Rice, T. M. Effective hamiltonian for the superconducting Cu oxides. *Phys. Rev. B* **37**, 3759–3761 (1988).
27. Cheng, J.-G. *et al.* Possible Kondo Physics near a metal-insulator crossover in the A-Site ordered perovskite CaCu₃Ir₄O₁₂. *Phys. Rev. Lett.* **111**, 176403 (2013).
28. Achkar, A. J. *et al.* Bulk sensitive X-ray absorption spectroscopy free of self-absorption effects. *Phys. Rev. B* **83**, 081106(R) (2011).
29. Sarangi, R. *et al.* X-ray absorption edge spectroscopy and computational studies on LCuO₂ species. *J. Am. Chem. Soc.* **128**, 8286–8296 (2006).
30. Hu, Z. *et al.* On the electronic structure of Cu(III) and Ni(III) in La₂Li_{1/2}Cu_{1/2}O₄, Nd₂Li_{1/2}Ni_{1/2}O₄, and Cs₂KCuF₆. *Chem. Phys.* **232**, 63–74 (1998).
31. Kaindl, G. *et al.* Correlation between oxygen-hole concentration and T_c in YBa₂Cu₃O_{7-δ} from Cu-L_{III} X-ray absorption. *Phys. B Condens. Matter* **158**, 446–449 (1989).
32. Chen, C. T. Electronic states in La_{2-x}Sr_xCuO_{4+δ} probed by soft-X-Ray absorption. *Phys. Rev. Lett.* **66**, 104–107 (1991).
33. Nücker, N., Fink, J., Fuggle, J. C., Durham, P. J. & Temmerman, W. M. Evidence for holes on oxygen sites in the high T_c superconductors La_{2-x}Sr_xCuO₄ and YBa₂Cu₃O_{7-y}. *Phys. Rev. B* **37**, 5158–5163 (1988).
34. Nücker, N. *et al.* Site-specific and doping-dependent electronic structure of YBa₂Cu₃O_x probed by O 1s and Cu 2p X-ray-absorption spectroscopy. *Phys. Rev. B* **51**, 8529–8542 (1995).
35. Kuiper, P. *et al.* X-ray absorption study of the O 2p hole concentration dependence on O stoichiometry in YBa₂Cu₃O_x. *Phys. Rev. B* **38**, 6483–6489 (1988).
36. Zeng, Z., Greenblatt, M., Subramanian, M. A. & Croft, M. Large Low-Field Magnetoresistance in perovskite-type CaCu₃Mn₄O₁₂ without double exchange. *Phys. Rev. Lett.* **82**, 3164–3167 (1999).
37. Kolchinskaya, A. *et al.* Magnetism and spin-orbit coupling in Ir-based double perovskites La_{2-x}Sr_xCoIrO₆. *Phys. Rev. B* **85**, 224422 (2012).
38. Clancy, J. P. *et al.* Spin-orbit coupling in iridium-based 5d compounds probed by X-ray absorption spectroscopy. *Phys. Rev. B* **86**, 195131 (2012).
39. Mukherjee, S., Sarkar, S. & Saha-Dasgupta, T. First principles study of CaCu₃B₄O₁₂ (B = Co, Rh, Ir). *J. Mater. Sci.* **47**, 7660–7664 (2012).
40. Mizumaki, M. *et al.* Oxygen hole state in A-site ordered perovskite ACu₃Ru₄O₁₂ (A = Na, Ca, and La) probed by resonant X-ray emission spectroscopy. *J. Phys. Soc. Jpn* **82**, 024709 (2013).
41. Tanaka, S., Takatsu, H., Yonezawa, S. & Maeno, Y. Suppression of the mass enhancement in CaCu₃Ru₄O₁₂. *Phys. Rev. B* **80**, 035113 (2009).
42. Ushakov, A. V., Streltsov, S. V. & Khomskii, D. I. Crystal field splitting in correlated systems with negative charge-transfer gap. *J. Phys. Condens. Matter* **23**, 445601 (2011).
43. Yang, Y.-I. & Pines, D. Emergent states in heavy-electron materials. *Proc. Natl Acad. Sci. USA* **109**, 3060–3066 (2012).
44. Süllo, S., Aronson, M. C., Rainford, B. D. & Haen, P. Doniach Phase diagram, revisited: from ferromagnet to fermi liquid in pressurized CeRu₂Ge₂. *Phys. Rev. Lett.* **82**, 2963–2966 (1999).
45. Si, Q. Global magnetic phase diagram and local quantum criticality in heavy fermion metals. *Phys. B Condens. Matter* **378**, 23–27 (2006).
46. Yoshida, K. Magnetic properties of Cu-Mn alloys. *Phys. Rev* **106**, 893–898 (1957).
47. Pandey, A., Mazumdar, C., Ranganathan, R. & Dattagupta, S. Magnetism in ordered metallic perovskite compound GdPd₃B_xC_{1-x}. *J. Mag. Mag. Mat.* **321**, 2311–2317 (2009).
48. Feng, J., Xiao, B., Zhou, R. & Pan, W. Electronic and magnetic properties of double perovskite slab-rocksalt layer rare earth strontium aluminates natural superlattice structure. *J. Appl. Phys.* **114**, 143907 (2013).
49. Kresse, G. & Furthmüller, J. Efficient iterative schemes for ab initio total-energy calculations using a plane-wave basis set. *Phys. Rev. B* **54**, 11169–11186 (1996).
50. Perdew, J. P., Burke, K. & Ernzerhof, M. Generalized Gradient Approximation Made Simple. *Phys. Rev. Lett.* **77**, 3865–3868 (1996).
51. Dudarev, S. L. *et al.* Electron-energy-loss spectra and the structural stability of nickel oxide: An LSDA + U study. *Phys. Rev. B* **57**, 1505–1509 (1998).
52. Blöchl, P. E. Projector augmented-wave method. *Phys. Rev. B* **50**, 17953–17979 (1994).
53. Blaha, P., Schwartz, K., Madsen, G. K. H., Kvasnicka, D. & Luitz, J. in *An Augmented Plane Wave + Local Orbitals Program for Calculating Crystal Properties* (ed. Schwarz, K.) (Technische Universität Wien, 2001).
54. Blöchl, P. E., Jepsen, O. & Andersen, O. K. Improved tetrahedron method for Brillouin-zone integrations. *Phys. Rev. B* **49**, 16223 (2004).
55. Andersen, O. K. & Saha-Dasgupta, T. Muffin-tin orbitals of arbitrary order. *Phys. Rev. B* **62**, R16219 (2000).
56. Andersen, O. K. & Jepsen, O. Explicit, first-principles tight-binding theory. *Phys. Rev. Lett.* **53**, 2571–2574 (1984).

Acknowledgements

J.C. is supported by DOD-ARO Grant No. 0402-17291. J.-S.Z. and J.B.G. are supported by NSF Grant No. DMR-1122603. T.S.-D. thank CSIR and DST, India, for funding. Work at the Advanced Photon Source, Argonne, is supported by the US Department of Energy, Office of Science under Grant No. DEAC02-06CH11357. J.-G.C. acknowledges the support from NSFC and MOST (Grant Nos. 11304371, 2014CB921500) and the Strategic Priority Research Program of the Chinese Academy of Sciences (Grant No. XDB07000000). We thank Dr Shalinee Chikara and Professor Gang Cao for sharing data on reference samples Rh₂O₃ and Sr₂RhO₄. J.C. acknowledges useful discussions with D. Khomskii.

Author contributions

D.M., S. Middey, Y. Choi, D.H., B.A.G., J.W.F. and J.C. acquired the experimental data. S. Mukherjee and T.S.-D. did the theoretical calculations. J.-G.C., J.-S.Z. and J.B.G. grew the samples. D.M. and S.Middey analysed data. All authors discussed the results. D.M., S. Middey, Y. Cao., T.S.-D. and J.C. wrote the manuscript.

Additional information

Supplementary Information accompanies this paper at <http://www.nature.com/naturecommunications>

Competing financial interests: The authors declare no competing financial interests.

Reprints and permission information is available online at <http://ngp.nature.com/reprintsandpermissions/>

How to cite this article: Meyers, D. *et al.* Competition between heavy fermion and Kondo interaction in isoelectronic A-site-ordered perovskites. *Nat. Commun.* 5:5818 doi: 10.1038/ncomms6818 (2014).

First-principles study of $\text{CaCu}_3\text{B}_4\text{O}_{12}$ (B=Co, Rh, Ir)

Swarnakamal Mukherjee · Soumyajit Sarkar ·
T. Saha-Dasgupta

Received: 14 February 2012 / Accepted: 23 April 2012 / Published online: 9 May 2012
© Springer Science+Business Media, LLC 2012

Abstract Employing first-principles density functional theory based calculations we investigated the change in electronic structure of $\text{CaCu}_3\text{B}_4\text{O}_{12}$ compounds as one moves from $3d$ (Co) to $4d$ (Rh) to $5d$ (Ir) element at B site. Our study sheds light on valences of Cu and B ions as one moves from $3d$ to $4d$ to $5d$ based compounds. The valence of Cu in Co and Rh compound turn out to be that of less known $3+$ state, while that in Ir compound turn out to be commonly known $2+$ state. Our first-principles study provide microscopic understanding of these different valences of Cu, in terms of changes in the mixing of Cu $x^2 - y^2$ and B- a_{1g} states, driven by changes in the crystal field and spin splitting. The stronger crystal field splitting for $4d$ and $5d$ elements compared to $3d$ at B site drive the low-spin state at Rh and Ir site as opposed to intermediate spin in case of Co.

Introduction

Recently A site ordered perovskite oxides $\text{AA}'_3\text{B}_4\text{O}_{12}$ have attracted considerable attention due to their interesting and intrinsic properties. For example $\text{CaCu}_3\text{Mn}_4\text{O}_{12}$ shows large magnetoresistance even at low magnetic field [1], while $\text{CaCu}_3\text{Ti}_4\text{O}_{12}$ [2] is an antiferromagnetic insulator and has large dielectric constant. Therefore, it is clear that substitution at the B site induces drastic changes in the electronic structure of such compounds. In order to study the effect of

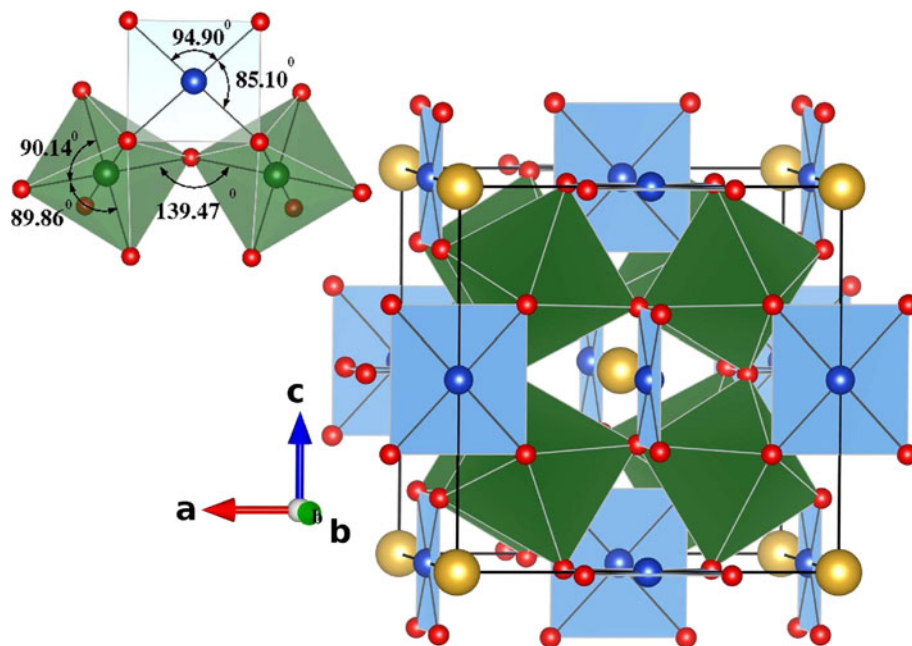
substitution at the B site, on the electronic structure we have carried out a first-principles study on a series of compounds $\text{CaCu}_3\text{B}_4\text{O}_{12}$ (B=Co, Rh, Ir). Note that Co, Rh, and Ir belong to the same column of the periodic table, with Co, Rh, and Ir being $3d$, $4d$ and $5d$ elements, respectively. This provides a nice opportunity to study the effect of changing from a $3d$ to a $4d$ to a $5d$ element at B site on the physical properties of the compounds. Among these three compounds, while $\text{CaCu}_3\text{Co}_4\text{O}_{12}$ and $\text{CaCu}_3\text{Ir}_4\text{O}_{12}$ compounds have been synthesized, [3–5] $\text{CaCu}_3\text{Rh}_4\text{O}_{12}$ compound is yet to be synthesized. Very few first-principles calculations exist on these compounds. The physical properties of $\text{CaCu}_3\text{Ir}_4\text{O}_{12}$ is yet to be measured. The measurement of physical properties of $\text{CaCu}_3\text{Co}_4\text{O}_{12}$ compound, has established its metallic character, conduction being dominated by Co- d state. Rietveld refinement of synchrotron powder X-ray diffraction suggests $3+$ valence of Cu ion in square-planar geometry making the situation interesting.

Structural details

$\text{CaCu}_3\text{B}_4\text{O}_{12}$ (B=Co, Rh, Ir) compounds crystallize in body-centered cubic symmetry with space group $Im\bar{3}$ (space group number 204). B atoms sit in octahedral environment created by O ions and Cu atoms remain at center of a CuO_4 square-planar environment. BO_6 octahedra corner share with each other. Each O ion is shared by two BO_6 octahedra and one CuO_4 square plane as shown in the inset of Fig 1. In spite of the underlying cubic symmetry of the compounds, the space group allows for trigonal distortion to be present in BO_6 octahedra. In addition to this, there is also distortion present in square-planar environment, which makes O–Cu–O angle different from 90° .

S. Mukherjee · S. Sarkar · T. Saha-Dasgupta (✉)
S. N. Bose National Centre for Basic Sciences Salt Lake,
Kolkata 700098, India
e-mail: tanusri@bose.res.in

Fig. 1 Conventional unit cell ($z = 2$) of $\text{CaCu}_3\text{Co}_4\text{O}_{12}$. Yellow, blue, green, and red atoms represent Ca, Cu, Co (Rh/ Ir), and O ions, respectively. CoO_6 octahedra and CuO_4 square-planar environment are represented by green octahedra and blue square, respectively. The inset shows separately CoO_6 octahedra and CuO_4 square plane along with the distortion angles (Color figure online)



Computational details

Calculations have been carried out in the plane wave basis as implemented in the VASP code [6] and the muffin-tin orbital (MTO) based linear MTO (LMTO) [7] and N-th order MTO (NMTO) [8] basis. The exchange correlation functional was chosen to be generalized gradient approximation (GGA) [9]. The missing electron–electron correlation beyond GGA was taken into account through improved approximation of $\text{GGA} + U$ in the sense of static, mean field theory. For the plane wave calculations, we used projector augmented wave (PAW) [10] potentials and the wave functions were expanded in the plane wave basis with a kinetic energy cutoff of 600 eV. Reciprocal space integrations were carried out with a k mesh of $6 \times 6 \times 6$. The $\text{GGA} + U$ calculations were performed with the $+U$ implementation of Dudarev et al. [11] We have used U value of 5 eV on Cu site and 4 eV on B site while the Hund's rule coupling J was fixed to 0.8 eV. Ideally one would expect U to vary at B site as one moves from $3d(\text{Co})$ to $4d(\text{Rh})$ to $5d(\text{Ir})$ series. The choice of U value of 4 eV though appropriate for Co, one would expect it to be reduced for Rh and Ir. However, in the absence of a good prescription of how exactly it would vary, we have kept it fixed. We have checked the validity of our obtained results in terms of reduced value of U ($U = 2$ eV) for Rh and Ir. We found that the basic conclusions in terms of valence states of B and Cu ions remain unchanged though the precise values of quantities like magnetic moments etc., change. In the following, we, therefore, report results obtained with uniform choice of U value of 4 eV at B site. U value at Cu site in a square-planar geometry is expected

to be 4–8 eV and chosen to be 5 eV [12]. The obtained results were verified in terms of variation of U parameter. The NMTO-downfolding calculation has been used to determine the crystal field splitting at Cu and B sites. For this purpose, NMTO-downfolding calculations were carried out keeping only the Cu- d and B- d states active and downfolding all the other states, including O- p states. The on-site block of the real space Hamiltonian in Cu- d , B- d basis, gives the crystal field splitting.

Results

Structural optimization

Among the three compounds we have studied, for $\text{CaCu}_3\text{Co}_4\text{O}_{12}$ [3, 4] and $\text{CaCu}_3\text{Ir}_4\text{O}_{12}$ $\text{CaCu}_3\text{Ir}_4\text{O}_{12}$ [5] compounds experimentally measured structural parameters are available in the literature. We first carried out structural optimization for $\text{CaCu}_3\text{Co}_4\text{O}_{12}$ and $\text{CaCu}_3\text{Ir}_4\text{O}_{12}$ compounds and compared with experimental results. This comparison turned out to be reasonable (see Table 1), validating our optimization scheme. In the next step, we have carried out geometry optimization for $\text{CaCu}_3\text{Rh}_4\text{O}_{12}$ compound to get their structural parameters since for this compound the experimental results are not available. For this purpose, we have replaced Ir by Rh in $\text{CaCu}_3\text{Ir}_4\text{O}_{12}$ and carried out structural optimization. Similarly we have done another set of calculation starting from the $\text{CaCu}_3\text{Co}_4\text{O}_{12}$ compound. The structural parameters obtained from the two sets of calculations agree with each other within the accuracy of our calculation. We have used

Table 1 Optimized lattice constants and selected bond-lengths and bond-angles of $\text{CaCu}_3\text{B}_4\text{O}_{12}$ (B=Co, Rh, Ir) compounds with the corresponding experimentally measured values within the parentheses.[3–5]

	$\text{CaCu}_3\text{Co}_4\text{O}_{12}$	$\text{CaCu}_3\text{Rh}_4\text{O}_{12}$	$\text{CaCu}_3\text{Ir}_4\text{O}_{12}$
B–B bond-length (Å)	3.598 (3.561)	3.751	3.777 (3.737)
B–O bond-length (Å)	1.918 (1.901)	2.026	2.028 (1.999)
Cu–O bond-length (Å)	1.887 (1.860)	1.904	1.950 (1.949)
$\angle\text{B-O-B}^\circ$	139.5 (139.0)	135.6	137.2 (138.4)
$\angle\text{O-B-O}$			
$(90 \pm \delta)^\circ$, $\delta =$	0.1 (0.2)	1.3	1.7 (1.5)
$\angle\text{O-Cu-O}$			
$(90 \pm \delta)^\circ$, $\delta =$	4.9 (4.9)	8.3	8.3 (7.6)
Lattice constant (Å)	7.197 (7.123)	7.502	7.554 (7.474)

the theoretically optimized structural parameters of three compounds in all calculations, described in the following.

Non-spin polarized electronic structure

Figure 2 shows the non-spin polarized density of states (DOS) for all the three compounds calculated within GGA. Due to the presence of octahedral environment, B-*d* states in BO_6 octahedra get split into two manifolds, t_{2g} and e_g . Within the non-spin polarization scheme, t_{2g} states are partially occupied lying around E_f consistent with less than half filled (d^5) nature of *d* occupancies of B ion, and the e_g states are completely empty lying above E_f . The energy separation between t_{2g} and e_g states is maximum for Ir compound (~ 3 eV), where as in $\text{CaCu}_3\text{Co}_4\text{O}_{12}$ those two manifolds are at closest separation, reflecting the larger B–O covalency in moving from 3*d*(Co) to 4*d*(Rh) to 5*d*(Ir) metal ions. Cu-*d* states are mostly occupied and are well

below (~ 2 eV) the Fermi energy (E_f), with some unoccupied states lying just above E_f . In order to determine the precise positions of B and Cu *d* energy levels, NMTO-downfolding calculations are carried out keeping Cu-*d* and B-*d* states active and downfolding all other states, including O-*p* states. On-site block of real space Hamiltonian in Cu-*d* and B-*d* basis gives energy level splitting of Cu-*d* and B-*d* states. The octahedral crystal field splits B-*d* levels into t_{2g} and e_g^σ . Further due to trigonal distortion t_{2g} manifold (as shown in Fig. 3) of B ions get split between doubly degenerate e_g^π and singly degenerate a_{1g} . As we move from 3*d* to 4*d* to 5*d* element at B site, the energy separation between a_{1g} and e_g^σ levels increases. The *d* levels at Cu site get split into xz , yz , $3z^2 - 1$, xy and $x^2 - y^2$ in order of increasing energy with large separation between $x^2 - y^2$ and rest. The relative position of highest lying Cu-*d* level, which is of $x^2 - y^2$ character, with respect to a_{1g} of corresponding B-*d* state changes as one move from 3*d* to 4*d* to 5*d* element at B site. The difference between Cu- $x^2 - y^2$ and B- a_{1g} energies, is smallest for Ir compound and biggest for Co compound.

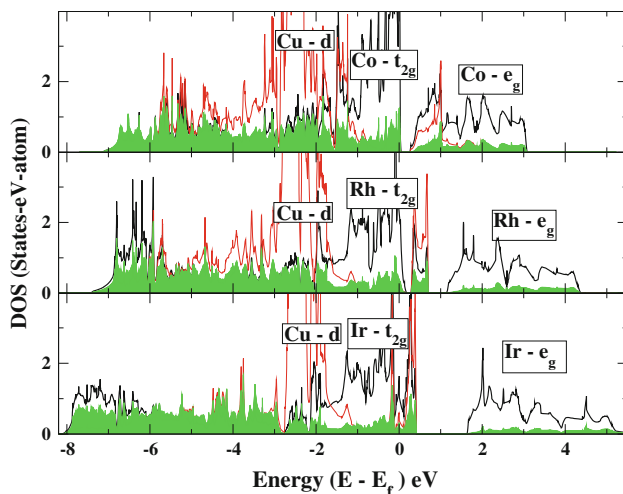


Fig. 2 Non-spin polarized DOS calculated within GGA using LMTO basis. The *top*, *middle*, and *bottom* panel represents DOS for $\text{CaCu}_3\text{Co}_4\text{O}_{12}$, $\text{CaCu}_3\text{Rh}_4\text{O}_{12}$, and $\text{CaCu}_3\text{Ir}_4\text{O}_{12}$, respectively. The *black* and *red* lines represent the B-*d* and Cu-*d* states, respectively. The *filled area* represents O-*p* states. Energy is plotted with respect to the Fermi Energy (E_f) (Color figure online)

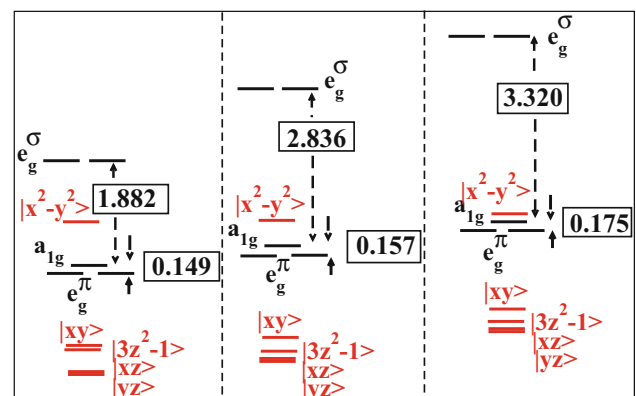


Fig. 3 The crystal field splitting of B-*d* (marked in *black* lines) and Cu-*d* (marked in *red* lines) states, computed by NMTO-downfolding technique. The *left*, *middle*, and *right* panels represent splitting of B and Cu-*d* states in $\text{CaCu}_3\text{Co}_4\text{O}_{12}$, $\text{CaCu}_3\text{Rh}_4\text{O}_{12}$ and $\text{CaCu}_3\text{Ir}_4\text{O}_{12}$, respectively. All the energies are in eV unit (Color figure online)

Spin polarized electronic structure calculation within GGA and GGA + *U*

Table 2 shows the magnetic moments calculated within GGA for all the three compounds. Out of the three compounds, only CaCu₃Co₄O₁₂ converges to a proper, magnetic ground state with reasonable value of magnetic moment. The magnetic moment at Co site is found to be appreciable (0.7 μ_B) while that at Cu site is found to be negligibly small.

On applying Hubbard *U* at both A' and B site, ground state of all the three compounds converges to a magnetic ground state. Table 3 shows the magnetic moments for all the three compounds calculated within GGA + *U*. Magnetic moment at B site increases due to application of Hubbard *U*. Co ion in CaCu₃Co₄O₁₂ shows largest moment (1.71 μ_B), where as Rh ion in CaCu₃Rh₄O₁₂ shows least moment (0.14 μ_B). This may be expected as we move from 3*d* to 4*d* element at B site the band width would increase and hence the magnetism will be less favored. It is however, interesting to note that in CaCu₃Ir₄O₁₂ compound, where the B ion is an 5*d* element, moment at B site is larger compared to that in CaCu₃Rh₄O₁₂ compound. In addition to this, Cu ion in CaCu₃Ir₄O₁₂ compound shows appreciable magnetic moment which is not the case in both CaCu₃Co₄O₁₂ and CaCu₃Rh₄O₁₂ compounds. In order to understand the origin of this, in Fig. 4 we show the DOS and corresponding band structure calculated within GGA + *U* for CaCu₃Co₄O₁₂, CaCu₃Rh₄O₁₂ and CaCu₃Ir₄O₁₂. From band structure plots, and the corresponding DOS plots, we find that for Cu states, the *x*² - *y*² state is empty and rest of the states to be

Table 2 Magnetic moments in units of μ_B calculated within GGA using plane wave basis

	CaCu ₃ Co ₄ O ₁₂	CaCu ₃ Rh ₄ O ₁₂	CaCu ₃ Ir ₄ O ₁₂
B(Co/ Rh/ Ir)	0.70 (0.21)	0.0 (0.0)	0.01 (0.0)
Cu	0.04(0.0)	0.0 (0.0)	0.0 (0.0)
O	0.05 (0.01)	0.0 (0.0)	0.0 (0.0)

Values within parenthesis are corresponding moments calculated using LMTO basis

Table 3 Magnetic moments in units of μ_B calculated within GGA + *U* using plane wave basis

	CaCu ₃ Co ₄ O ₁₂	CaCu ₃ Rh ₄ O ₁₂	CaCu ₃ Ir ₄ O ₁₂
B(Co/ Rh/ Ir)	1.71 (1.68)	0.14 (0.15)	0.67(0.74)
Cu	0.07 (0.05)	-0.05 (-0.01)	0.61 (0.55)
O	-0.02 (0.01)	0.04 (0.03)	0.16 (0.17)

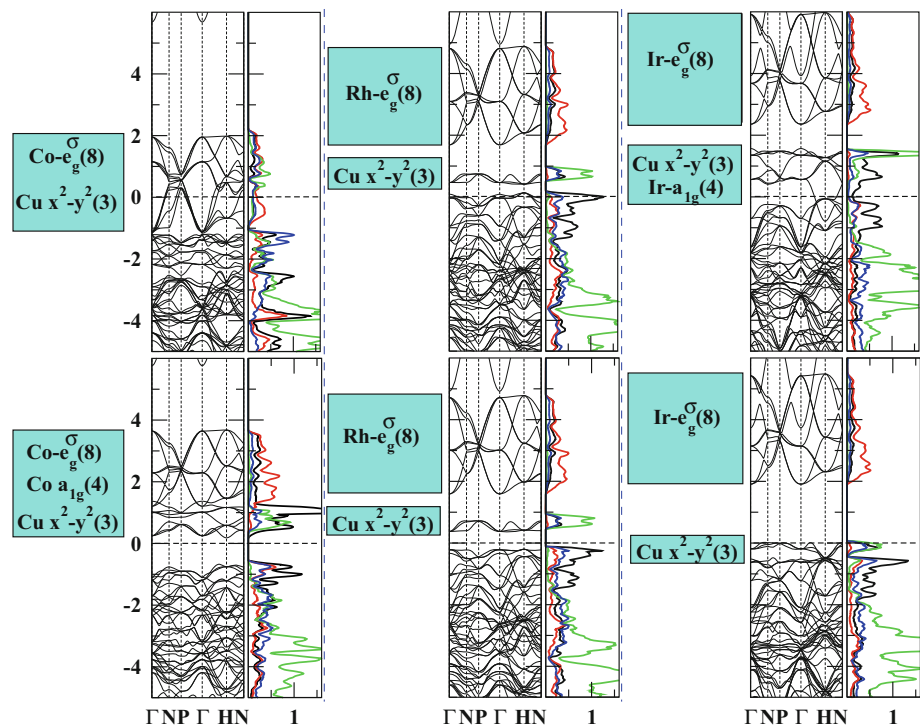
Values within parenthesis are corresponding moments calculated using LMTO basis. *U* values used on Cu and B(= Co, Rh, Ir) ions are 5 and 4 eV, respectively

filled in both spin channel for CaCu₃Co₄O₁₂ as well as CaCu₃Rh₄O₁₂. The small energy level separation between Co *e*_g^σ and Cu *x*² - *y*² make the mixing between the two, stronger for Co compound compared to that in Rh compound. In case of Ir compound, on the other hand the Cu *x*² - *y*² state is occupied in the majority spin channel, and empty in minority spin channel, with rest being occupied in both spin channels. This leads us to conclude that Cu is in (+3) like state in Co and Rh compounds and is in (+2) like state in Ir compound. This is also consistent with negligible magnetic moments of Cu in Co and Rh and an appreciable one in Ir compound. This leaves Co and Rh to be in nominal mixed valence state of *d*^{3.25+} and Ir to be in *d*⁴⁺ state, assuming Ca and O to be in nominal valences of (2+) and (2-), respectively. Focusing on B-*d* states, we find that Co *e*_g^σ and *a*_{1g} are empty in the minority spin channel, Co *e*_g^σ states are partially filled in the majority spin channel, and rest are occupied. This leads to the intermediate spin (IS) state of Co. Moving to Rh, we find Rh *e*_g^σ states become empty in both spin channels, with Rh *a*_{1g} states become partially occupied in majority spin channel, suggesting the low-spin (LS) state of Rh-*d*. For Ir compound, we find while the Ir *e*_g^σ levels are completely empty in both spin channels and *e*_g^π states are filled in both spin channels, Ir *a*_{1g} state is occupied in majority spin channel and partially empty in minority spin channel giving rise to LS state of Ir-*d*.

Discussion and summary

In the present study, we carried out a thorough analysis of the electronic structure of A site ordered perovskites AA'₃B₄O₁₂ with choice of A=Ca, A' = Cu. Keeping this choice fixed, the B site ion is varied between choices of Co, Rh and Ir which belong to the same column of the periodic table and therefore isoelectronic. Our analysis shows that changing the B site cation from a 3*d* element (Co) to 4*d* element (Rh) to 5*d* element (Ir) has interesting and important changes in the Cu valency which in turn effect the valence of B site cation. The nominal valence of Cu is found to be in less known Cu³⁺ state for Co and Rh compounds, while in Cu²⁺ state for Ir compound. Such unusual valence of Cu in square-planar geometry has been reported for LaCu₃Fe₄O₁₂ compound [13] which is found to show interesting temperature driven valence change and large negative thermal expansion at room temperature. Similar effect can also be explored in Co and Rh compound. Preliminary experimental study supports our theoretically predicted Cu³⁺ valence [14]. The change in valence of Cu, causes also the valence at B site to change in moving from Co to Rh to Ir, apart from the spin state changes. The resulting changes in the electronic structure lead to nice half metallic states for Co and Ir compounds

Fig. 4 Spin polarized electronic structure, band structure, and DOS, calculated within GGA + U approach ($U_B = 4$ eV, $U_{Cu} = 5$ eV, $J = 0.8$ eV) of $\text{CaCu}_3\text{Co}_4\text{O}_{12}$ (left panel), $\text{CaCu}_3\text{Rh}_4\text{O}_{12}$ (middle panel) and $\text{CaCu}_3\text{Ir}_4\text{O}_{12}$ (right panel). The top (bottom) panels are for majority (minority) spin channel. Black, red, green, and blue lines in DOS plots represent projections onto $B-t_{2g}$, $B-e_g$, $\text{Cu}-d$, and $O-p$ states respectively. The composition of bands near E_f are shown in boxes, with numbers in brackets indicating the number of bands of the corresponding character (Color figure online)



which may be explored for spintronics applications. Rh compound is found to be at the verge of insulating behavior, a small amount of disorder can lead to a complete insulating solution.

To conclude, using DFT calculations, we investigated the electronic structure, valences and spin states of Cu and B site in $\text{CaCu}_3\text{B}_4\text{O}_{12}$ compounds, with $B=\text{Co}$, Rh , and Ir . Our study shows interesting variation in valences of Cu and B ions upon changing from $3d$ to $4d$ to $5d$ ion at B site. Our theoretically predicted results may be verified experimentally.

Acknowledgements The authors gratefully acknowledge discussions with J. Tchakhalian and M. Greenblatt. The authors also thank J. Tchakhalian for providing the experimental crystal structure data for Ir compound. S.M. and S.S acknowledge the Council of Scientific and Industrial Research, India for financial support.

References

- Zang Z et al (1999) Phys Rev Lett 82:3164
- Ramirez A et al (2000) Solid State Commun 115:217
- Mizokawa T et al (2009) Phys Rev B 80:125105
- Yamada I et al (2010) Chem Mater 22:5328
- Tchakhalian J (private communication)
- Kresse G, Furthmuller J (1996) Phys Rev B 54:11169
- Andersen OK, Jepsen O (1984) Phys Rev Lett 53:2571
- Andersen OK, Saha-Dasgupta T (2000) Phys Rev B 62:R16219
- Perdew JP, Burke K, Ernzerhof M (1996) Phys Rev Lett 77:3865
- Blöchl PE (1994) Phys Rev B 50:17953
- Dudarev SL et al (1998) Phys Rev B 57:1505
- Fujimori A et al (1987) Solid State Commun 63:857
- Long YW et al (2009) Nature 458:60
- Tchakhalian J et al. (unpublished)

A first principles density functional investigation of ligand-protected eight atom gold nanoclusters

Jaita Paul, Swarnakamal Mukherjee, and Tanusri Saha-Dasgupta

Citation: *AIP Advances* **1**, 032150 (2011); doi: 10.1063/1.3638066

View online: <http://dx.doi.org/10.1063/1.3638066>

View Table of Contents: <http://aipadvances.aip.org/resource/1/AAIDBI/v1/i3>

Published by the [American Institute of Physics](#).

Related Articles

Molecular modeling study of agglomeration of [6,6]-phenyl-C61-butyric acid methyl ester in solvents
J. Chem. Phys. **137**, 244308 (2012)

Clustering and mobility of hard rods in a quasicrystalline substrate potential
J. Chem. Phys. **137**, 224705 (2012)

Influence of reactive gas admixture on transition metal cluster nucleation in a gas aggregation cluster source
J. Appl. Phys. **112**, 114321 (2012)

Direct imaging of atomic clusters in an amorphous matrix: A Co-C granular thin film
Appl. Phys. Lett. **101**, 191902 (2012)

Germanium nano-cluster films as humidity and hydrogen sensors
J. Appl. Phys. **112**, 074514 (2012)

Additional information on AIP Advances

Journal Homepage: <http://aipadvances.aip.org>

Journal Information: <http://aipadvances.aip.org/about/journal>

Top downloads: http://aipadvances.aip.org/most_downloaded

Information for Authors: <http://aipadvances.aip.org/authors>

ADVERTISEMENT



AIPAdvances

Now Indexed in Thomson Reuters Databases

Explore AIP's open access journal:

- Rapid publication
- Article-level metrics
- Post-publication rating and commenting

A first principles density functional investigation of ligand-protected eight atom gold nanoclusters

Jaita Paul, Swarnakamal Mukherjee, and Tanusri Saha-Dasgupta
*S. N. Bose National Centre For Basic Sciences, JD-Block, Sector-III, Saltlake City,
 Kolkata-700098, India*

(Received 23 May 2011; accepted 15 August 2011; published online 31 August 2011)

Based on first principles density functional calculations we have studied the effect of ligand attachment on eight atom gold clusters of two-dimensional (2D) and three-dimensional (3D) geometries. Recent experimental synthesis of this magic numbered cluster using glutathione [Muhammed *et al.*, Nano Res. **1**, 333 (2008)] has instigated this investigation. We have chosen ethyl mercaptan ($\text{CH}_3\text{-CH}_2\text{SH}$) as the ligand which is the simplified form of glutathione ($\text{HO}_2\text{CCH}_2\text{NHCOCH}(\text{NH}_2)\text{-CH}_2\text{CH}_2\text{CONHCH}(\text{CO}_2\text{H})\text{-CH}_2\text{SH}$). We have analyzed the energetics, *sd*-hybridization, density of states and charge density distributions of the bare and ligand-capped clusters. Our findings indicate that attachment of ethyl mercaptan ligands on eight atom gold clusters enhances the stability of planar 2D geometries over 3D like structure. Copyright 2011 Author(s). This article is distributed under a Creative Commons Attribution 3.0 Unported License. [doi:10.1063/1.3638066]

I. INTRODUCTION

Nanoclusters are systems of profound research interest since they offer a plethora of applications in various fields such as nanocatalysis, biomedical sciences and in nanotechnology industry in general.^{1,2} Though several investigations have been conducted to understand the properties of these clusters, several challenges still remain. It is well known that at the nanoscale, the properties of clusters not only deviate significantly from their bulk behavior but they also exhibit strong dependence on the size and the atomic arrangement of the cluster. This in turn affects the nature of the bonds formed when these clusters interact with other compounds as often is the case when they are used in e.g., catalysis.³ Detailed understanding of the structural evolution of nano clusters and their electronic properties is thus extremely important.

Among various metallic nanoclusters, Au nanoclusters particularly have received a lot of attention due to a highly promising and reliable utilization owing to their long term stability, easy synthesis and favorable chemical modifications.⁴⁻⁶ They have also gathered a lot of interest as system of choice in nanoscale electronics.⁷ The properties exhibited by the gold clusters are found to be extremely sensitive to the size, structure and dimension of the cluster. This led to extensive research to determine the size *N* at which the 3D geometries become energetically more favorable over the 2D geometries. Several experimental and theoretical studies have predicted this number to fall in a range from 6 to 13.⁸⁻²⁰ For anionic and cationic gold clusters the 2D-3D transitions are observed to occur at *N* = 13 and *N* = 8, respectively. Theoretical calculations for neutral clusters have predicted the transition to occur at six,⁸ seven,^{9,10} eight^{11,12} as well as in the range from 11-15 atom clusters.¹³⁻²⁰ It has been anticipated that the different methods and models adopted to determine the cluster size at which the 2D-3D transition takes place can possibly be one of the reasons for the large spread in the obtained results (from 6-15). Gold clusters are reported to retain their planar structures to cluster sizes larger compared to Ag and Cu clusters which remain planar upto 7 atom cluster sizes only.²¹ This has been anticipated to occur due to the relativistic effect in gold which results in a strong *sd*-hybridization leading to a delocalization of the *d*-electrons over the volume of the cluster which in turn produces a stronger *d-d* interaction of neighboring Au atoms.²¹



However, the clusters observed in experiments are prepared in ligand-resolved solution. This makes the comparison of theoretical models with experimental observations less obvious. In recent years, the consensus is developed that the ligands known as “passivators”, originally employed to check the growth of the clusters which otherwise would grow to large sizes, appear to play a more active role in terms of determining the structure of the cluster primarily by influencing the surface geometry through a change of surface chemistry. This has led to several theoretical studies involving cluster together with ligands. Using first-principles calculations, Häkkinen *et al.*²² explored the electronic structure properties of passivated $\text{Au}_{38}(\text{SCH}_3)_{24}$ and showed a complex spatial charge distribution where mostly charge transfer occurred between the surface gold atoms and the sulfur atoms of the thiols attached to the surface. It was also shown in theoretical studies^{23–27} that different kinds of ligands have different effects on the electronic structure of the clusters and the interaction of the ligand molecules with the clusters give a detailed picture of the nature of the bonds between gold and the ligand molecules. Considering small Au atoms, particularly those falling in the range of crossover transition between 2D-like to 3D-like geometry theoretical studies have been carried out for 11-atom and 13-atom clusters.^{24,25} The studies indicate that the structure of small gold clusters are altered substantially in the presence of ligands, in the sense the planar geometries predicted by calculations for bare clusters were found to be stabilized in 3D-like geometries upon ligation. The rationale for the stabilization of markedly different geometries were traced to Au-ligand covalency.

Recently, 8 atom Au-cluster has been synthesized by the process of ligand etching with glutathione,²⁸ which to the best of our knowledge is the smallest Au cluster that has been synthesized. Eight atom clusters can be termed as so called ‘magic numbered’ clusters since the number ‘eight’ falls among the number of valence electrons i.e., 2, 8, 18, 32... $2(m + 1)^2$, m being an integer, that can complete the electronic shell filling. An experimental structural analysis has not yet been done for 8-atom clusters which have also been predicted by several studies to be a possible case for 2D-3D crossover.

In the present study based on first principles density functional theory (DFT) calculations, we investigate the effect of ligand capping on the results of the earlier studies on the stabilization of 2D and 3D geometries. Note that the nature of ligand capping on the eight atom cluster can not be anticipated based on earlier predicted results on different sized clusters,^{24,25} since the Au-ligand covalency is expected to depend on the details of the considered bare cluster geometry as well as on nature of ligand. For our study we chose as ligand ethyl mercaptan ($\text{CH}_3\text{-CH}_2\text{SH}$) which bears similarity to the sulfur chain of glutathione ($\text{HO}_2\text{CCH}_2\text{NHCOCH}(\text{NH}_2)\text{CH}_2\text{CH}_2\text{CONHCH}(\text{CO}_2\text{H})\text{-CH}_2\text{SH}$) but is much smaller in size. This termination is based on previous studies where they showed that the length of a ligand chain do not alter the properties of the ligand-cluster complex.^{29–31} We have studied the variance of properties of Au_8 clusters in 2D and 3D geometries with and without the presence of the chosen ligand molecule. Properties reported here include density of states (DOS), charge densities of the highest and lowest occupied molecular levels (HOMO and LUMO), ionization potentials, electron affinities, sd -hybridization and bonding charge densities.

II. COMPUTATIONAL METHODS

The *ab initio* DFT calculations reported in this paper were performed using the PWscf (plane wave self consistent field) code of the QUANTUM ESPRESSO distribution.^{32,33} The wavefunctions in this code are expanded in a basis consisting of plane waves. An energy cut-off of 680 eV chosen for the wavefunctions was found to be sufficient to converge the binding energies. Spin-orbit coupling was shown to increase the values of binding energies of all clusters. But the relative stability between different structures was not altered significantly from calculations without spin-orbit coupling. We have thus used scalar relativistic ultrasoft pseudopotentials³⁴ to approximate the interactions between ion cores and valence electrons of individual Au atoms. We have used LDA parametrized by Perdew and Zunger³⁵ to treat exchange and correlation in all our calculations. We checked that using Perdew-Burke-Ernzerhof Generalized Gradient Approximation (PBE-GGA)³⁶ instead of LDA does not affect the trend of results (see results presented in Table I for details). The inter-periodic image distance was maintained at $\sim 8 \text{ \AA}$ for all systems. Thomas-Fermi smearing technique with a smearing factor of 0.04 eV was used for obtaining the density of states (DOS) and projected DOS. The different

TABLE I. Binding energies E_B (in eV/atom) of bare clusters (B) and the interaction energies E_I (in eV/ligand) of the ligand capped clusters (WL). The HOMO-LUMO energy gap E_g (in eV) is also listed. The numbers within the brackets for $E_B(B)/E_I(WL)$ indicate results obtained using PBE-GGA.

Structure	$E_B(B)/E_I(WL)$	E_g
Star(B)	2.78 (2.06)	1.17
Hex(B)	2.77 (2.02)	0.77
3D(B)	2.77 (2.03)	2.01
Star(WL)	0.88 (0.31)	1.41
Hex(WL)	1.16 (0.49)	1.34
3D(WL)	0.98 (0.33)	1.18

structures in 2D and 3D geometries corresponding to the Au_8 isomers were optimized where all the atoms were allowed to relax according to the Hellmann-Feynman forces. For optimization of the structures an energy convergence of 1.36×10^{-7} eV and force convergence of 0.02 eV/Å (on each atom) was used. Since we are dealing with molecular calculations, all results corresponded to Γ point simulations.

The binding energy E_B per atom for the clusters is defined as:

$$E_B = -\left\{ \frac{E_{Au_8} - 8 \times E_{Au}}{8} \right\}, \quad (1)$$

where E_{Au_8} is the total energy of the Au_8 cluster, E_{Au} is the energy of an isolated Au atom, and 8 is the number of atoms. The interaction energy E_I of the ligand molecules with the various isomers of Au_8 clusters is defined as:

$$N_{Lig} \times E_I = E_{(Au_8+N_{Lig})} - E_{Au_8} + N_{Lig} \times E_{Lig}, \quad (2)$$

where $E_{Au_8+N_{Lig}}$ is the total energy of the Au_8 cluster with N_{Lig} number of ligands attached and E_{Lig} is the total energy of the ligand. The ionization potentials (IP) and the electron affinities (EA) have been calculated as:

$$IP = E_{N-1} - E_N, \quad (3)$$

$$EA = E_N - E_{N+1}, \quad (4)$$

where E_{N-1} , E_{N+1} and E_N are the total energies of the anionic, cationic and neutral clusters respectively. For vertical IPs and EAs, the total energies were obtained at the optimized coordinates of the neutral cluster with a difference in the number of electrons and for adiabatic IPs and EAs, the geometries were relaxed. We have calculated the hybridization between the s and d states according to Ref [15]:

$$H_{sd} = \sum_{i=1}^{occ.} \sum_{l=1}^8 w_{i,s}^l w_{i,d}^l, \quad (5)$$

where $w_{i,s}^l$ and $w_{i,d}^l$ are the squares of the projections of the i -th Kohn-Sham orbital onto the s and d spherical harmonics respectively, centred on the i -th atom integrated over a sphere whose radius is equal to half the nearest neighbor bond distances of the cluster.

III. RESULTS

A. Structural stability of bare clusters

We have considered all possible 2D minimum energy configurations of Au_8 atom cluster available in literature (see top panel of Fig. 1). The structures were then optimized and the binding energies E_B 's were calculated and average bond lengths were obtained. In accordance with previously reported results^{13,15-18,37} we find the edge-bridged rhombus (star) structure (left most figure in the top panel of Fig. 1) to be the most stable of the 2D structures ($E_B = 2.78$ eV/atom). The E_B of

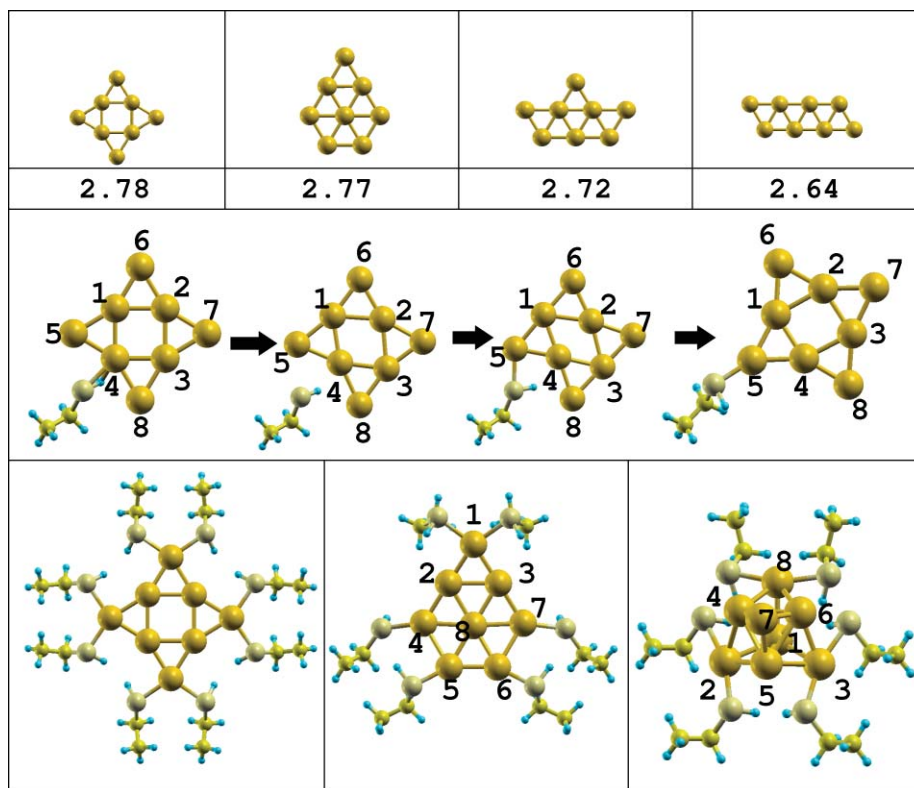


FIG. 1. (Color online) Top panel: 2D structures of Au cluster and their corresponding binding energies in eV/atom. The first and second structures, from left, are referred to as the ‘star’ and ‘hex’ cluster, respectively. Middle panel : The structural optimization of the star cluster with one ligand chain attached to atom 4 (corner atom) at 1st, 10th, 19th and final ionic steps (sequentially ordered from left to right). Bottom panel: Ligand capped cluster configurations. From left to right: four double ligand chains attached to the four top atoms of the star cluster, six ligand chains attached to selective atoms of the hex cluster and the 3D cluster capped by three double ligand chains.

the triangle-capped hexagonal (hex) structure (second figure from left in the top panel of Fig. 1) is 0.01 eV/atom less compared to the star structure making the two structures energetically close. The E_B 's of the structures, shown in third and fourth figures from left in top panel of Fig. 1, are much lower (2.72 and 2.64 eV/atom, respectively) making them lesser stable structures compared to star and hex. Based on the strength of the binding energies we, therefore, find the star and hex structures form the most stable isomers. Most studies have found these two species to be the most stable configurations of the 2D planar Au₈ clusters irrespective of the choice of basis sets, exchange-correlation functionals and pseudopotentials.^{12,16–18} Among the 3D isomers, DFT calculations predict the bicapped distorted octahedron to be most stable.^{8,9,12,16,17} This is the only 3D structure on which we have performed all calculations and the effect of ligand-attachment is investigated for the two 2D structures (star and hex) and this 3D structure. One may argue that upon ligand attachment some other high energy structure may become more stable. While one cannot rule out such possibility, it is beyond the capability of our computational effort to explore all possible excited structures. Our study, in this context, should be considered as specific case study considering only the low energy bare Au structures, and not as a study to predict the most stable capped Au structure.

B. Properties of ligand-capped clusters

1. Selective attachment of ligand chains

In order to study the properties of ligand-capped clusters, one needs to know the amount of coverage by ligands (i.e., the number of ligands to be attached) as well as the sites where the ligands

prefer to be attached. Unfortunately both the above information are not known accurately from experiments. We therefore first report the results of our study on the site selective attachment of the ligand molecules on the chosen isomers.

The star structure has two sets of nonequivalent points, the corners of the square (points marked 1,2,3,4 in figures shown in the middle panel of Fig. 1) and the vertices of the triangles (points marked 5,6,7,8 in figures shown in the middle panel of Fig. 1). The atom seated at position 4 (and similarly for the atoms at points 1,2 and 3) we refer to as the 'corner' site. The 'top' site is referred to an atom seated on position 5 (and similarly for atoms at points 6,7 and 8). We attach a single ligand molecule to an atom seated on position 4. Upon optimizing the structure where a single ligand chain is attached to the corner, it is seen that eventually as the minimum energy configuration is approached the ligand molecule detaches itself from the corner atom and clings to the adjacent top atom (see figures shown in the middle panel of Fig. 1). A single ligand chain was attached to a top atom (in position 6) which has two nearest neighbors (1 and 2) and it had remained attached without breaking away. These two observations indicate that a gold atom in a cluster having four or more number of nearest neighbor (NN) bonds is less likely to attach a ligand. We next check the probability of top Au atom to attach more than one ligand chain. We have chosen the initial Au-S bond length to be 2.38 Å which was obtained by Häkkinen and co-workers²⁶ and lies in the range predicted³⁸ by Jadzinsky *et al.*. The initial S-Au-S angle before optimization is chosen to be 160° which lies in the range 155°-175° suggested in Ref. 38. For the star structure we attach two single chains only to the top atoms since the (corner) atoms with four NNs rule out the possibility of attaching even one ligand. The optimized structure represents a stable configuration with both the chains remaining attached to the top atoms and the structure also does not break off. The angle between S-Au-S becomes 111.02° and the Au-S bond lengths increase to 2.47 Å. This leads to the ligand capped structure displayed in the left most corner of bottom panel of Fig. 1. If we try to attach a third ligand chain to the top atom, then the structure breaks off indicating that a Au atom can attach a maximum of two ligand chains.

The hex structure is less symmetric than the star structure and also has a comparatively lesser number of dangling bonds. Only the atom at the top of the triangle (marked as 1 in the middle figure in the bottom panel of Fig. 1) has two NNs and one can attach a double chain of ligands. The two atoms in the next row (marked as 2 and 3) has four NNs and following the argument from the star structure we do not attach any ligands to these atoms. The other four atoms (marked as 4, 5, 6 and 7) have three NNs and we have attached a single chain of ligand to each of these four atoms. Attaching two ligand chains to these four atoms resulted in an unstable structure possibly due to close spacing of ligands leading to ligand-ligand interaction. The central atom (marked as 8) has five NNs and therefore does not attach any ligand. This leads to the six ligand-capped hex structure, as shown in the central figure in the bottom panel of Fig. 1.

Finally we decide the ligand-capped configuration of the 3D structure shown in the right most corner of the bottom panel of Fig. 1. There are four atoms, corresponding to points 2, 3, 7 and 8 in the figure which have three NNs, and the other four atoms at points 1, 4, 5 and 6 in the figure have more than three NNs. Out of the former four atoms, the position of the 7th atom does not favor attaching any ligand. For the other three atoms (at 2, 3 and 8) we have attached two ligand chains. This structure was found to be stable under optimization. Note that compared to the hex structure this structure allows for three coordinated Au atoms to attach two ligands. This is possibly caused by the specialty of the chosen 3D geometry and the chosen three coordinated atoms which are separated by an average distance of 4.38 Å (compared to hex structure for which separation of 3 coordinated Au atoms is 2.62 Å) leading to much loose packing of ligand chains and hence less ligand-ligand interaction.

We next compare the DOS, HOMO-LUMO charge densities and the IPs and EAs of the bare and ligand protected clusters for the three sets, namely set 1: bare star and ligand-capped star, set 2: bare hex and ligand-capped hex, and set 3: bare 3D and ligand capped 3D.

2. Energetics

The interaction energies of the eight-ligand capped star, six-ligand capped hex and six-ligand capped 3D clusters obtained from Eqn. (2) are listed in Table I. The binding energies corresponding

TABLE II. Adiabatic and vertical ionization potential (AIP, VIP) and electron affinity (AEA, VEA) (in eV) of the bare (B) and ligated (WL) star, hex and 3D clusters.

Structure	VIP	AIP	VEA	AEA
Star(B)	5.67	5.59	3.23	3.29
Star(WL)	2.78	2.65	0.62	0.63
Hex(B)	5.33	5.31	3.37	3.41
Hex(WL)	3.93	3.55	1.28	1.49
3D(B)	5.55	5.54	2.44	2.68
3D(WL)	4.02	3.70	1.60	1.83

to the bare clusters are also listed in Table I. The numbers within the brackets correspond to results obtained with PBE-GGA. The binding energies of the bare 2D hex and the 3D cluster are found to be equal within LDA. Calculating the interaction energies following Eqn. (2) of the 2D hex and 3D structure after attaching six ligands to these two structures shows that E_I of the 2D structure is greater than that of the 3D structure by 0.18 eV per ethyl mercaptan chain. Since both the clusters have equal number of ligands attached to them their interaction energies may be compared. We may therefore conclude that the ligand attachment enhances the stability of the 2D hex structure over the chosen 3D structure. Similar trend is observed in the results obtained using PBE-GGA. We then calculated the first adiabatic and vertical ionization potentials and electron affinities for the bare and ligand protected clusters using Eqns. (3) and (4). The vertical IPs and EAs correspond to the calculations with a difference in electron count keeping the structure same between the two calculations. The adiabatic IPs and EAs on the other hand are obtained by allowing the structures to undergo optimization. This relaxation lowers the IPs and increases the EAs (see Table II) irrespective of bare or ligand-capped clusters. Upon ligand attachment, the IPs and EAs decrease significantly indicating that the ligand protected clusters are more stable compared to their respective bare partners.²² For the 2D star cluster the VIPs (AIPs) decrease by 2.89 eV (2.94 eV). The EAs of both adiabatic as well as vertical star-ligated clusters reduce by 2.61 eV compared to the bare cluster. Ligand-capped hex cluster also shows a decrease in IPs and EAs which though is not as strong as for the star cluster (IPs decrease by ~ 1.4 -1.8 eV and EAs decrease by ~ 2 eV) possibly due to lesser number of ligand attachments. For the 3D cluster the VIP (AIP) and VEA (AEA) decrease by 1.5 (1.8) eV and 0.84 (0.85) eV. The reduction in EA for the 3D cluster is much weaker compared to the 2D clusters indicating that although for all the three cases the ligands passivate the clusters, this passivation is stronger for the 2D clusters compared to the 3D structure.

3. *sd* - hybridization

The relative stability of the respective clusters can be compared calculating the *sd*-hybridization index according to Eqn. (5). The indices obtained for the bare star, hex and the 3D clusters are found to be 1.98, 2.10 and 1.75, respectively. The *sd*-hybridization is found to be stronger in the 2D configurations than 3D cluster considered here, indicating that our calculation shows sustained planarity of bare eight atom Au clusters as a consequence of the relativistic effects of Au.^{21,25} Based on a theoretical study on the effect of phosphine ligand attachment to six-atom octahedral Au-clusters it was suggested that ligands further increase the stability of the clusters by enhancing the hybridization of the valence bands of the Au-atoms.³⁹ However, a contradictory finding was reported from an X-ray photoelectron spectroscopy study on ligated 11 atom Au clusters. Their findings indicated that the magnitude of hybridization between the *s* and *d* orbitals of the Au atoms protected by ligands is weakened when the complex is formed.⁴⁰ We calculated the *sd*-hybridization index for the ligand attached clusters from which we obtained the *sd*-hybridization indices as 1.24, 1.48 and 1.16 for the star, hex and 3D clusters respectively, showing a decrease of the effective hybridization index in agreement with the experimental study.⁴⁰ The values however indicate that

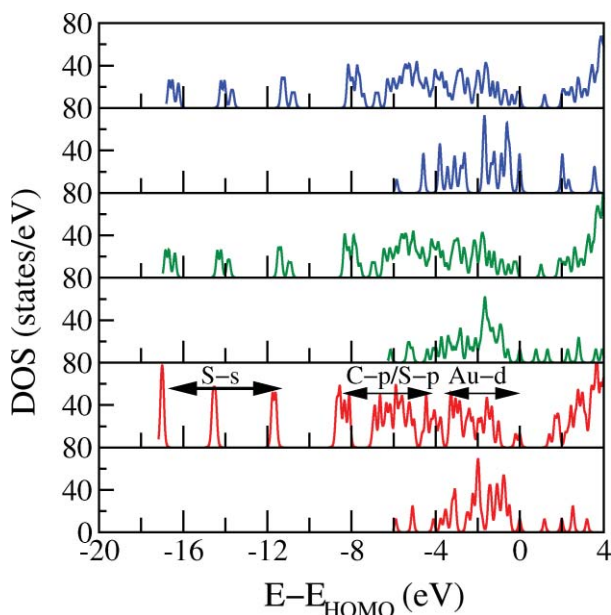


FIG. 2. DOS plotted as a function of $E-E_{HOMO}$ for the systems corresponding to the clusters shown in Fig. 1. From top to bottom, the DOS corresponds to bare 3D, ligated 3D, bare hex, ligated hex, bare star and ligated star, respectively.

even though the sd -hybridization has decreased, the trend remains the same for the bare and ligated clusters.

4. Density of states

The density of states (DOS) of the six systems (three bare and their corresponding ligand capped configurations) shown in Fig. 2 reveal certain important features regarding the stability of the clusters, with and without ligands. Firstly the appearance of extra states in the DOS for the ligand capped clusters contributed by the ligand atoms is evident. $S-s$ states (marked in the fifth panel from top) appear in the ligated clusters at the energy range from -18 eV to -12 eV. This feature finds similarity with the results obtained from theoretical calculations on 38 atom Au-cluster capped by SCH_3 ligands.²² Secondly, the DOS of the ligand capped star, hex and 3D structures show that close to the HOMO energy level, there is a significant mixing of the $S-p$ and $Au-d$ orbitals, which is a very crucial factor in determining the stability of the ligated clusters. The d -orbitals of the Au atoms mix with the p -orbitals of the S atom, the extent of overlap depending on the structure of the cluster and orientation of the ligand chain. $C-p$ orbitals also overlap with $Au-d$ and $S-p$, but it is a comparatively weaker interaction. Finally, the energy gap E_g between the highest occupied and the lowest unoccupied molecular orbitals (HOMO-LUMO) increases (decreases) for the 2D (3D) clusters when ligands are attached. For the star cluster the energy gap increases by 0.23 eV on attaching eight ligand chains to four Au atoms. For the hexagonal cluster, this gap increases by 0.57 eV suggesting that attaching ligands enhances the stability of the gold clusters in the 2D configurations. For the 3D configuration lowering of the gap by 0.84 eV occurs when six ligands are attached to it indicating that attaching ligands does not cater to stabilizing the cluster in a higher dimension. The energy gaps E_g between the HOMO and LUMO levels are quoted in the last column of Table I. The charge density plots presented in the following section accounts for this behavior.

5. HOMO-LUMO charge densities

The HOMO-LUMO charge density plots (Fig. 3) give us some insight into the behavior of the energy gap and stability of the clusters with and without ligands in 2D and 3D geometries. The

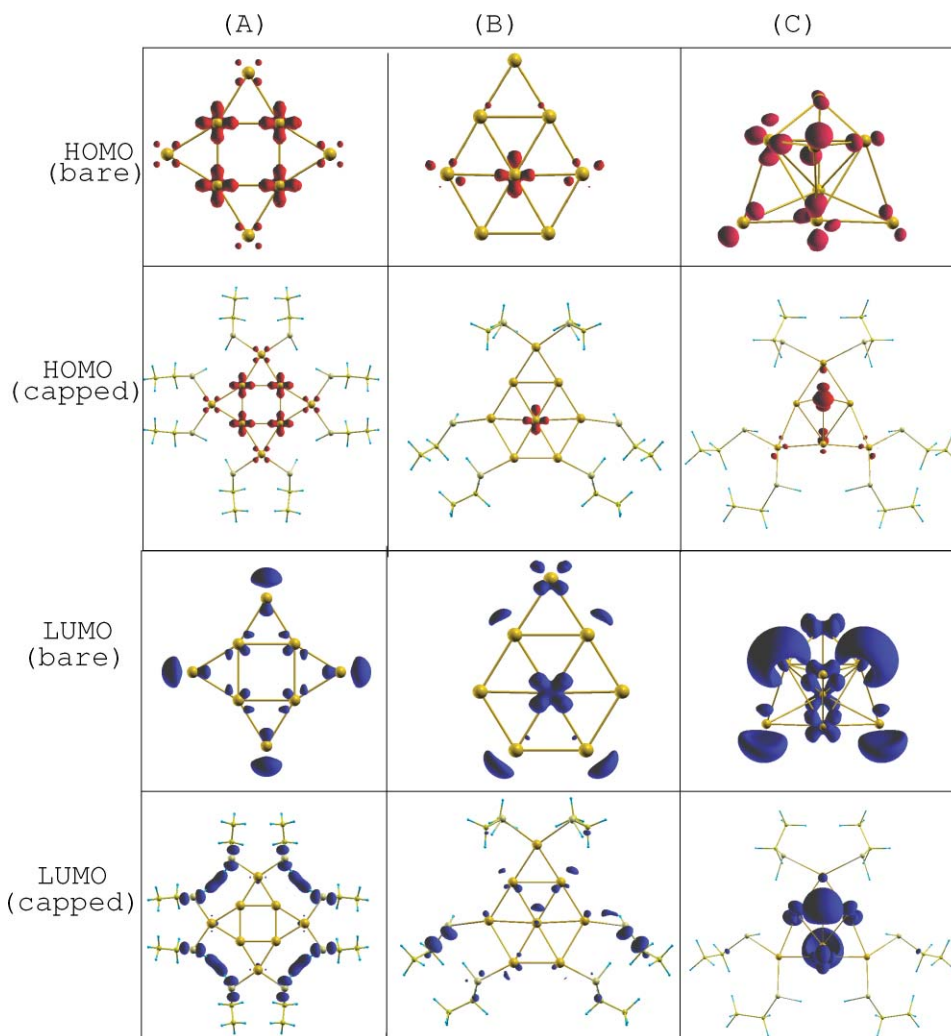


FIG. 3. (Color online) HOMO and LUMO charge density distributions at one-third the maximum of bare and ligand protected star (panels A), hex (panels B) and 3D (panels C) clusters.

HOMO of the bare star cluster shows pronounced d -character ($d_{x^2-y^2}$) on the four atoms at the corners of the square and a faint d -character (d_{xy}) on the top atoms. This nature remains unchanged upon the attachment of ligands. Similar feature is observed for the hex cluster, where only the central atom of the hexagon shows $d_{x^2-y^2}$ -character and the charge density associated with the HOMO remains more or less unaltered when ligands are attached. For the 3D configuration, the HOMO states at the atoms 2, 3 and 8 where ligands are attached disappear; on atom 7 it still remains. The LUMO charge densities show a significant variation upon ligation. The charge density of LUMO of the bare star cluster shows sd -hybridized orbitals at the four top atoms. Upon attachment of ligands, the LUMO-charge densities move from the Au atoms to the ligand chains. The edge atoms of the hex cluster which in bare condition show accumulation of sd -hybridized charge density similarly get rid of the accumulated charge upon ligand attachment by shifting them to the ligand chains. The atoms where ligand is not attached, the sd -hybridization character is retained though weakened a bit. For the bare 3D structure, the LUMO charge density shows sd -hybridized nature on four atoms. A significant difference appears in the LUMO charge density distribution of the ligated 3D cluster. It is interesting to note that in this case the charge density does not move from the Au atoms to the ligand chains. Instead it has moved to the central atoms of the cluster. This explains of the lowering of the energy gap E_g in case of ligand capped 3D clusters as discussed in the previous section.

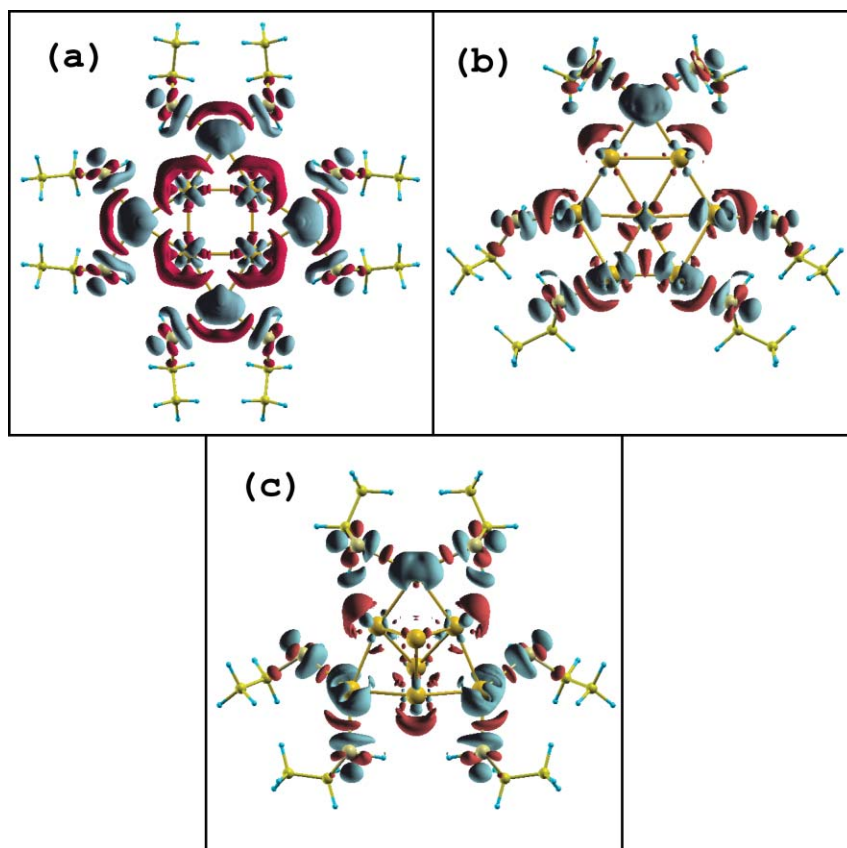


FIG. 4. (Color online) Charge density difference plots at one-third the maximum value of star (a) hex (b) and 3D (c) ligand-protected clusters. Red (dark) and cyan (light) represent charge accumulated and depleted regions.

The energetics of the ligand capped clusters are therefore mostly governed by the LUMO charge densities, the movement of which in the presence of ligands results in an increase (or decrease) of the energy gap (Fig. 2).

6. Bonding charge densities

In order to study the bonding nature of the ligand chains with the Au atoms, we plot the bonding charge densities or the charge density differences. To obtain the charge density difference (ρ_{diff}), we first calculate the charge density of the ligand-cluster complex ($\rho_{complex}$). Then using the same supercell we calculate the charge densities of individual ligands ($\rho_{ligand}(i)$, $i = \text{ligand number}$) and the bare cluster ($\rho_{cluster}$). The charge density difference is then obtained by subtracting these individual ligand charge densities and the bare cluster charge density from the charge density of the ligand-cluster complex:

$$\rho_{diff} = \rho_{complex} - \left(\rho_{cluster} + \sum_{i=1}^{n_{lig}} \rho_{ligand}(i) \right) \quad (6)$$

Fig. 4 shows such charge density plots, in which red (dark shade) and cyan (light shade) regions denote charge accumulated and charge-depleted regions respectively. These plots reveal an important aspect regarding the charge-accumulated regions. Charge transfer from the Au-Au bonds to the Au-S bonds results in a strong covalent bond between the Au and S atoms. The eight ligand protected star cluster shows that there is strong charge accumulation in the Au-S bonds as well as in the S-S bridges. The six-ligand protected hex cluster shows that the charge lost from the Au and S atoms accumulate at the centre of the bond between Au and S atoms. This accumulation is stronger for the

2D hex system than the 3D structure (Fig. 4(b) and 4(c)) supporting the enhanced stability of the 2D systems over the 3D.

IV. SUMMARY

We have carried out first principles DFT calculations on the effect of ligand attachment to 8-atom Au-clusters. We chose to focus on 8-atom clusters since (i) it was a suggested number for a probable 2D-3D transition for bare clusters and (ii) it has been synthesized experimentally.²⁸ We have chosen the ligand molecule to be ethyl mercaptan which is similar to the sulfur tail of glutathione, the ligand which was used for the synthesis of the 8-atom clusters. We have analyzed the site-selective attachment of ligand chains which we show to depend on the coordination as well as the specificities of the geometry giving rise to ligand-ligand interactions. The relative stability of the bare and ligated clusters are studied based on binding and interaction energies, *sd*-hybridization, DOS, HOMO-LUMO charge distributions and charge density differences. Considering the chosen geometries, our studies indicate that for 8 atom clusters, attachment of ethyl mercaptan ligands increases the stability of the 2D like geometries over that of the 3D like geometries. The above obtained trend is rather different from previously reported theoretical studies on ligated 11 and 13 atom clusters which predict stabilization of 3D-like geometry over 2D-like geometry upon ligation. The difference in the predicted trend between ligated 8-atom cluster in the present study and that for ligated 11 and 13 atom clusters corroborates the fact that structure and bonding in small clusters crucially depend on their size. In particular the metal-ligand covalency, which is the primary cause of the difference in geometrical properties between ligated and bare clusters, depends on the nature of the local environment of the Au atom in the bare cluster in which the ligand has been attached or in other words the geometry of the bare cluster and also on the nature of the ligand, as been stressed in several studies.²⁴⁻²⁶ Experimentally it remains to be seen whether eight atom clusters of gold prefer a planar geometry over 3D in the presence of ligands.

Finally, in the actual experimental scenario, the solvent molecules are also present. The solvent molecules, though, interact with the tail part of the ligands leaving the cluster-ligand interaction unperturbed, as the later interaction involves only the head part of the ligand.^{41,42} This also forms the rationale for the present study in terms of considering the simplified form of ligand with shortened tail part. Our study in this respect forms a first step towards a thorough understanding of the experimental realization. Considering our obtained cluster-ligand geometry, in the next step one may construct geometries with the full long tail structure of the ligand, introduce the ligand-solvent molecule interaction, possibly modeled through classical force field, which would control the dispersibility of the ligand-stabilized nanoparticles.

ACKNOWLEDGMENTS

JP would like to thank Prasenjit Ghosh for helpful discussions. SM would like to acknowledge Council of Scientific and Industrial Research (CSIR) for financial support. TSD would like to thank Department of Science and Technology (DST) for support.

- ¹ E. F. Finney, R. Finke, *Jour. Colloid and Interface Science*, **317**, 351 (2008).
- ² J. D. Aiken III, R. Finke, *Jour. Molecular Catalysis A: Chemical* **145**, 1 (1999).
- ³ G. Mills, M. S. Gordon, H. Metiu, *J. Chem. Phys.* **118**, 4198 (2003).
- ⁴ P. Pyykkö, *Angew. Chem. Int. Ed.* **43**, 4412 (2004).
- ⁵ P. Pyykkö, *Nature Nanotechnology* **2**, 273 (2007).
- ⁶ M-C. Daniel, D. Astruc, *Chem. Rev.* **104**, 293 (2004).
- ⁷ S. Creager *et al.*, *J. Am. Chem. Soc.* **121**, 1059 (1999).
- ⁸ Y. Dong, M. Springborg, *Eur. Phys. J. D.* **43**, 15 (2007).
- ⁹ J. Wang, G. Wang, G. Zhao, *J. Phys. Rev. B.* **66**, 035418 (2002).
- ¹⁰ P. K. Jain, *Struc. Chem.* **16**, 421 (2005).
- ¹¹ H. Häkkinen, U. Landman, *Phys. Rev. B(R)*. **62**, 2287 (2000).
- ¹² R. M. Olson, S. Varganov, M. S. Gordon, H. Metiu, S. Chretien, P. Piecuch, K. Kowalski, S. A. Kucharski, M. Musial, *J. Am. Chem. Soc.* **127**, 1049 (2005).
- ¹³ L. Xiao, L. Wang, *Chem. Phys. Lett.* **392**, 452 (2004).

- ¹⁴J. Wang, J. Jellinek, J. Zhao, Z. Chen, R. B. King, P. von R. Schleyer, *J. Phys. Chem. A* **109**, 9265 (2005).
- ¹⁵E. M. Fernandez, J. M. Soler, I. L. Garzon, L. C. Balbas, *Phys. Rev. B* **70**, 165403 (2004).
- ¹⁶H. Häkkinen, B. Yoon, U. Landman, X. Li, H-J. Zhai, L-S Wang, *J. Phys. Chem. A* **107**, 6168 (2003).
- ¹⁷L. Xiao, B. Tollberg, X. Hu, L. Wang, *J. Chem. Phys.* **124**, 114309 (2006).
- ¹⁸X-B Li, H-Y Wang, X-D. Yang, Z-H. Zhu, Y-J. Tang, *J. Chem. Phys.* **126**, 084505 (2007).
- ¹⁹J. C. Idrobo, W. Walkosz, S. F. Yip, S. Ogut, J. Wang, J. Jellinek, *Phys. Rev. B* **76**, 205422 (2007).
- ²⁰B. Assadollahzadeh, P. Schwerdtfeger, *J. Chem. Phys.* **131** (2009).
- ²¹H. Häkkinen, M. Moseler, U. Landman, *Phys. Rev. Lett.* **89**, 033401 (2002).
- ²²H. Häkkinen, R. N. Barnett, U. Landman, *Phys. Rev. Lett.* **82**, 3264 (1999).
- ²³M. Zhu, C. M. Aikens, F. Hollander, G. C. Schatz, R. Jin, *J. Am. Chem. Soc.* **130**,
- ²⁴K. Spivey, J. I. Williams, L. Wang, *Chem. Phys. Lett.* **432**, 163 (2006).
- ²⁵G. Shafai, S. Hong, M. Bertino, T. S. Rahman, *J. Phys. Chem. C* **113**, 12072 (2009).
- ²⁶H. Häkkinen, M. Walter, H. Gronbeck, *J. Phys. Chem. B* **110**, 9927 (2006).
- ²⁷G. S. Shafai, V. Shah, D. G. Kanhere, *J. Chem. Phys.* **126**, 014704 (2007).
- ²⁸M. A. H. Muhammed, S. Ramesh, S. S. Sinha, S. K. Pal, T. Pradeep, *Nano Res.* **1**, 333 (2008).
- ²⁹H. Grönbeck, M. Walter, H. Häkkinen, *J. Am. Chem. Soc.* **128**, 10268 (2006).
- ³⁰J. Akola, M. Walter, R. L. Whetten, H. Häkkinen, H. Gronbeck, *J. Am. Chem. Soc.* **130**, 3756 (2008).
- ³¹H. Fuchs, D. Kruger, R. Rousseau, D. Marx, M. Parrinello, *J. Chem. Phys.* **115**, 4776 (2001).
- ³²<http://www.pwscf.org>
- ³³P. Gianozzi *et al.*, *J. Phys. Cond. Matt.* **21**, 395502 (2009).
- ³⁴D. Vanderbilt, *Phys. Rev. B(R)* **41**, 7892 (1990).
- ³⁵J. P. Perdew, A. Zunger, *Phys. Rev. B* **23**, 5048 (1981).
- ³⁶J. Perdew, K. Burke, M. Ernzerhof, *Phys. Rev. Lett.* **77**, 3865 (1996).
- ³⁷F. Remacle, E. S. Kryachko, *J. Chem. Phys.* **122**, 44304 (2005).
- ³⁸P. D. Jadzinsky, G. Calero, C. J. Ackerson, D. A. Bushnell, R. D. Kornberg, *Science* **318**, 430 (2007).
- ³⁹D. M. P. Mingos, *J. Chem. Soc. Dalton Trans.* 1163 (1976).
- ⁴⁰G. K. Wertheim, J. Kwo, B. K. Teo, K. A. Keating, *Solid. State. Comm.* **55**, 357 (1985).
- ⁴¹M. Anand, M. McLeod, W. Bell, B. Roberts, *J. Phys. Chem. B* **109** 22852 (2005).
- ⁴²M. Schulz-Dobrick, K. Sarathy, M. Jansen, *J. Am. Chem. Soc.* **127** 12816 (2005).

Substantial reduction of Stone-Wales activation barrier in fullerene

Mukul Kabir,^{1,*} Swarnakamal Mukherjee,² and Tanusri Saha-Dasgupta²

¹*Department of Materials Science and Engineering, Massachusetts Institute of Technology, Cambridge, Massachusetts 02139, USA*

²*Advanced Materials Research Unit and Department of Material Sciences, S.N. Bose National Center for Basic Sciences, JD Block, Sector III, Salt Lake City, Kolkata 700 098, India*

(Received 11 May 2011; revised manuscript received 11 October 2011; published 10 November 2011)

Stone-Wales (SW) transformation is a key mechanism responsible for the growth, transformation, and fusion in fullerenes, carbon nanotubes, and other carbon nanostructures. These topological defects also substantially alter the physical and chemical properties of the carbon nanostructures. However, this transformation is thermodynamically limited by very high activation energy (~ 7 eV in fullerenes). Using first-principles density functional calculations, we show that the substitutional boron doping substantially reduces the SW activation barrier (from ~ 7 to 2.54 eV). This reduction is the largest in magnitude among all the mechanisms of barrier reduction reported to date. Analysis of bonding charge density and phonon frequencies suggests that the bond weakening at and around the active SW site in B heterofullerenes is responsible for such a reduction. Therefore, the formation of the SW defect is promoted in such heterofullerenes and is expected to affect their proposed H₂ storage properties. Such substitutional doping also can modify the SW activation barrier in carbon nanotubes and graphene nanostructures and can catalyze isomerization, fusion, and nanowelding processes.

DOI: [10.1103/PhysRevB.84.205404](https://doi.org/10.1103/PhysRevB.84.205404)

PACS number(s): 61.48.-c, 81.05.ub, 34.10.+x

I. INTRODUCTION

Stone-Wales (SW) defects¹ are important topological defects in sp^2 -bonded carbon materials, which play crucial roles in the growth, isomerism, and nanoscale plasticity of carbon nanotubes, fullerenes, and graphitic nanostructures.²⁻⁴ SW transformation involves an in-plane 90°-bond rotation with respect to the bond center. This leads to pentagon-heptagon defects (5-7-7-5 dislocation dipole) in carbon nanotubes and graphene³⁻⁵ and the interchange of a pair of pentagonal and hexagonal rings in fullerenes.¹ Such structural transformation is believed to be the fundamental unit process for the coalescence of fullerenes⁶ and nanotubes,⁷ the formation of molecular junctions for nanoelectronic devices,⁸ and plastic deformation.³ Both chemically modified and unmodified SW defects induce local curvature to the otherwise planar graphitic materials,⁹⁻¹² which may enhance the formation of nanotubes and fullerenes from planar carbon nanostructures.¹³ Also, the coalescence of fullerenes and nanotubes has been proposed to occur through a sequence of such structural transformations.^{6,7} SW defects also alter the electronic properties of carbon nanostructures, and thus, substantially modify chemical reactivity toward adsorbates (reactivity increases compared to the pristine counterpart)¹⁴⁻¹⁷ and transport properties.^{18,19} Also, similar SW defects are observed in boron nitride nanotubes and nanosheets^{5,20} and are found to have important implications in determining the physical and chemical properties.²¹

It is known that 94% of the C₆₀ isomers can be derived by a sequence of SW bond rotations.²² Thus, SW transformation is believed to be the fundamental mechanism for fullerene isomerism or I_h-C₆₀ formation, which is the global minimum on the complex potential energy surface.^{23,24} Interchange of a pair of pentagonal and hexagonal rings in I_h-C₆₀ via a single SW transition leads to C_{2v} symmetry, which does not obey the isolated-pentagon rule.²⁵ This is the first isomer, and it is separated by ~ 1.6 -eV energy from the global I_h minimum.²⁶⁻²⁸ Therefore, C_{2v}-C₆₀ represents the first step toward fullerene isomerism or the last step of the annealing

process before reaching the icosahedral global minimum.²³ Although earlier, the pristine C_{2v} isomer was not observed experimentally, recently, the chlorinated C_{2v} isomer was stabilized experimentally via Krättschmer-Huffman synthesis²⁹ and in the gas phase by subsequent dechlorination.³⁰ However, the SW transition in fullerenes is thermodynamically limited due to a very large activation barrier (~ 7 eV, Fig. 1).^{27,31,32} This energy barrier is reduced in the presence of an extra carbon or hydrogen atom.^{2,33} The extra carbon atom acts as an autocatalyst and reduces the activation energy by ~ 2 eV when preferentially placed in the regions of paired pentagons. In contrast, the endohedral metal doping (K, Ca, and La) is relatively less effective for barrier-height reduction.²⁷

Here, we report the effect of substitutional doping on an SW transition in C₆₀ through first-principles density functional calculations. We find that the activation barrier is reduced substantially by substitutional boron doping at the active SW sites. The quantitative reduction (2.12 and 4.34 eV for single and double B doping, respectively) is much larger compared to the cases with an extra carbon or hydrogen or endohedral metal doping.^{2,27,33} Boron-doped heterofullerenes (C_{60-x}B_x, $x \leq 6$) have been synthesized successfully³⁴ and are believed to be a promising candidate for hydrogen storage.^{35,36} It has been shown that H₂ adsorption energy increases substantially for B heterofullerenes where the B centers act as adsorption centers. The present paper shows that the formation of SW defects is promoted in such B-doped heterofullerenes, which may alter the reversible storage properties as SW defects are known to be more reactive toward adsorbates. Also, the presence of such a substitutional dopant is expected to reduce the activation barrier and to promote SW transition in other carbon nanostructures, and thus, to catalyze isomerism, fusion, and nanowelding processes.

II. METHODOLOGY

Calculations were carried out using density functional theory (DFT) implemented in the Vienna *ab initio*

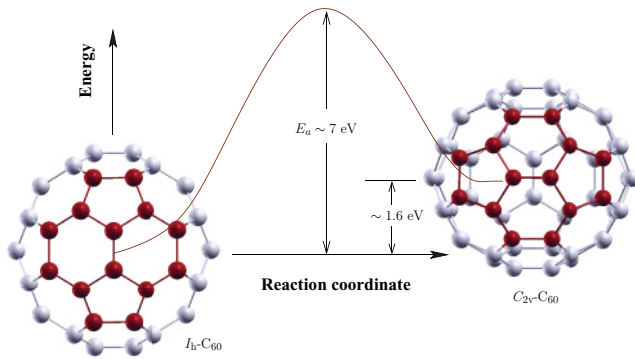


FIG. 1. (Color online) The activation energy barrier E_a for the I_h - $C_{60} \rightarrow C_{2v}$ - C_{60} transition, which represents a single SW transition, is very high. The activation barrier for the reverse transition (C_{2v} - $C_{60} \rightarrow I_h$ - C_{60}) is smaller by ~ 1.6 eV, which is the energy difference between I_h and C_{2v} symmetries. The pyracyclene region is highlighted (red).

simulation package³⁷ with the projector augmented wave pseudopotential.³⁸ If not otherwise stated, we used the Perdew-Burke-Ernzerhof (PBE) exchange-correlation functional,³⁹ and non-spin-polarized calculations were performed. The kinetic-energy cutoff was chosen to be 800 eV. Symmetry unrestricted geometry optimizations were terminated when the force on each atom was less than 0.005 eV/Å. Reciprocal space integrations were carried out at the Γ point. We determined the minimum-energy path for SW transition and the corresponding migration energy barrier E_a using the climbing-image nudged elastic band (NEB) method.⁴⁰ In NEB, a set of intermediate states (images) is distributed along the reaction path connecting optimized initial and final states. To ensure the continuity of the reaction path, the images are coupled with elastic forces, and each intermediate state is fully relaxed in the hyperspace perpendicular to the reaction coordinate.

III. RESULTS AND DISCUSSIONS

Determination of the activation energy necessary for SW transition ($I_h \rightleftharpoons C_{2v}$) via the climbing-image NEB method requires structural information of the initial and final structures within the concerned level of theory. Therefore, before we discuss the effect of B doping on the SW activation barrier, we begin our discussion with the geometric and electronic properties of C_{60} , $C_{59}B$, and $C_{58}B_2$ cages.

A. C_{60} , $C_{59}B$, and $C_{58}B_2$: Structural and electronic properties

There are two types of bonds in I_h - C_{60} : [6,6] bonds (1.399 Å) at the junctions of two hexagons are smaller than [5,6] bonds (1.453 Å) at the junctions of a pentagon and a hexagon. The C_{2v} structure is the first isomer, and in agreement with previous theoretical reports,^{26–28,32} we find that this structure is 1.57 -eV higher in energy compared to the global I_h minimum. The optimized C_{60} geometries for both I_h and C_{2v} symmetries are shown in Fig. 1, and a 14-atom pyracyclene region containing the rotating C_2 dimer is shown in Fig. 2(a). Calculated^{5,6}- and⁶-bond lengths [Fig. 2(a)] are in excellent agreement with previous theoretical calculations^{32,41} and experimental measurements^{42–45} for I_h - C_{60} . The rotating

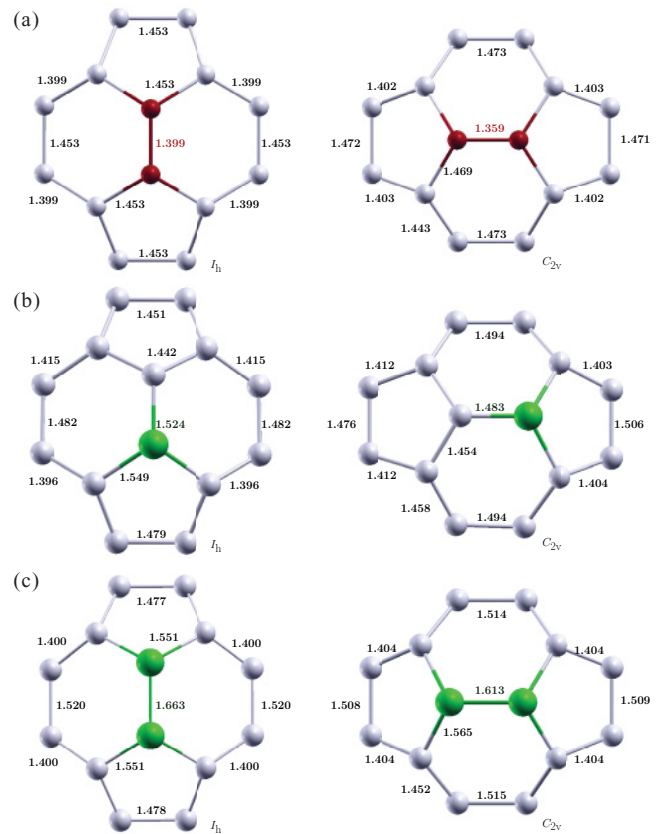


FIG. 2. (Color online) Local pyracyclene region for the optimized (a) C_{60} , (b) $C_{59}B$, and (c) $C_{58}B_2$ in I_h and C_{2v} symmetries. The rotating dimer corresponding to the SW transition is highlighted for C_{60} . The bond lengths are shown in angstroms. The length of the rotating bond decreases substantially in the C_{2v} structure for all the cages. Boron doping induces a significant local strain in $C_{59}B$, and $C_{58}B_2$ compared to pristine C_{60} .

bond in C_{2v} - C_{60} is much smaller (1.359 Å), which is also in agreement with previous theoretical calculations.^{28,32,41} However, no experimental information is available on pristine C_{2v} - C_{60} ; chlorinated C_{2v} structure ($C_{60}Cl_8$) shows a similar bond shortening of the rotating dimer (1.37 Å).²⁹ Such bond shortening introduces a local strain for the C_{2v} structure, and thus, a distribution of the bond length is observed in the pyracyclene region [Fig. 2(a)].

When one of the C atoms in the rotating dimer is replaced by B, three bond lengths involving C and B are increased (two [5,6]-C-B = 1.549 Å and one [6,6]-C-B = 1.524 Å) for I_h - $C_{59}B$ [Fig. 2(b)]. This is responsible for the bond deformation in the pyracyclene region (C-C bond distribution ranges from 1.442 to 1.482 Å). The trend of the structural changes in moving from I_h - $C_{59}B$ to C_{2v} - $C_{59}B$ remains the same as observed for pristine C_{60} . The structural properties of $C_{58}B_2$ show similar qualitative behavior. The pyracyclene region is comparatively more deformed due to the presence of one B-B (1.663 Å) bond and four C-B (1.551 Å) bonds [Fig. 2(c)]. Although, strictly speaking, both I_h and C_{2v} symmetries are broken due to B doping; for simplicity, we will retain the same nomenclature throughout the paper.

Next, we briefly discuss the electronic properties. Pure C_{60} is found to be a closed-shell singlet, whereas, doped B

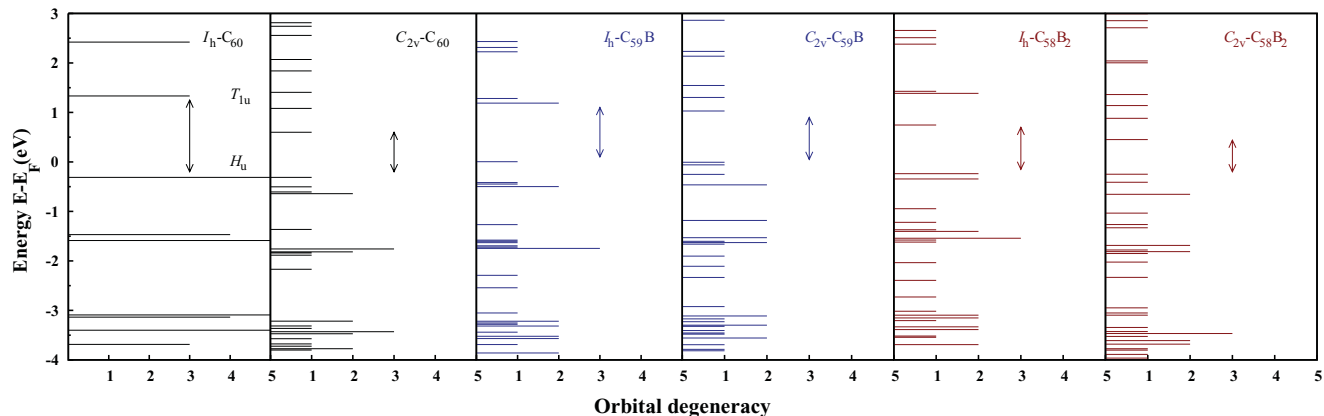


FIG. 3. (Color online) Kohn-Sham orbital degeneracy for pristine and substitutional B-doped fullerenes ($C_{59}B$ and $C_{58}B_2$) for both I_h and C_{2v} symmetries. The HOMO (LUMO) of the icosahedral C_{60} , H_u (T_{1u}) is fivefold (threefold) degenerate. Bottom (top) of the vertical arrow represents HOMO (LUMO). The introduction of defects, both in terms of topological defect and substitutional B, breaks the orbital degeneracy, and thus, reduces the Kohn-Sham energy gap E_g (see Table I).

introduces a hole (one/B doping) into the system. We note that, for $C_{59}B$, spin-polarized calculation lowers the total energy by 80 meV with respect to the non-spin-polarized calculation and yields a doublet state. In contrast, the $C_{58}B_2$ is a singlet, whereas, the triplet state lies significantly higher in energy.

The calculated Kohn-Sham energy gap between the highest occupied molecular level (HOMO) and the lowest unoccupied molecular level (LUMO) is 1.63 eV for I_h-C_{60} . Conventional density functional calculations usually underestimate the HOMO-LUMO gap obtained from the Kohn-Sham eigenvalues, which is much lower than the quasiparticle energy gap.^{46–48} For an N electron molecular system, the quasiparticle energy gap can be defined as the difference between the ionization potential ($IP = E[N - 1] - E[N]$) and the electron affinity ($EA = E[N] - E[N + 1]$). Here, $E[N]$ is the DFT total energy of a neutral system of N electrons. Our DFT-PBE calculations predict the IP and EA to be 7.32 and 2.75 eV, respectively, in agreement with previous DFT calculations.⁴⁹ These results, and thus, the quasiparticle gap (4.57 eV) also agree well with the self-consistent GW calculations ($IP = 7.41$ eV and $EA = 2.51$ eV)⁴⁶ and experimental measurements [$IP = 7.54 \pm 0.04$ eV (Ref. 47) and $EA = 2.65 \pm 0.05$ eV (Ref. 48)]. B heterofullerenes have somewhat smaller IP and bigger EA compared with C_{60} (Table I). These suggest that the formation of both cations and anions is relatively easier for B heterofullerenes, which indicate their enhanced redox characteristics.

Due to icosahedral symmetry, the Kohn-Sham HOMO (H_u) and LUMO (T_{1u}) are five- and threefold degenerate,

TABLE I. Energy difference between the structures in I_h and C_{2v} symmetries, $\Delta E = E(I_h) - E(C_{2v})$, and the Kohn-Sham HOMO-LUMO gap E_g . Calculated ionization potential and electron affinity for I_h symmetry. All the energies are in eV.

	ΔE	$E_g(I_h)$	$E_g(C_{2v})$	$IP(I_h)$	$EA(I_h)$
Pristine- C_{60}	1.57	1.63	0.91	7.32	2.75
$C_{59}B$	1.67	1.18	1.04	7.00	3.71
$C_{58}B_2$	1.75	0.98	0.70	7.21	3.27

respectively, for I_h-C_{60} . These degeneracies are lifted (Fig. 3) due to the presence of (1) a topological defect introduced by the SW transition and (2) substitutional B doping. Both cause a reduction in the HOMO-LUMO gap (Table I). For pristine $C_{2v}-C_{60}$, the degeneracy of both the HOMO and the LUMO is completely broken (Fig. 3), and the HOMO-LUMO gap is reduced by ~ 0.7 eV (Table I).

Substitutional B introduces a significant bond deformation in the pyracyclene region [Figs. 2(b) and 2(c)], and thus, the inherent structural symmetries are broken. This removes the degeneracies of HOMO and LUMO levels (Fig. 3) and reduces the Kohn-Sham HOMO-LUMO energy gap (Table I). With subsequent B doping, the structural deformation increases [Figs. 2(b) and 2(c)], and thus, the energy gap decreases (Table I). Similarly, the presence of the SW defect further lifts the degeneracy (Fig. 3), and the gap is lower in the corresponding C_{2v} structures compared to the I_h heterofullerenes (Table I).

B. Activation barrier: Effect of substitutional B doping

Activation barriers for the SW transition in carbon nanotubes, graphitic nanostructures, and fullerenes are generally very high.^{28,50,51} Our calculated energy barrier for pristine C_{60} is found to be 6.88 eV (Table II), which is in agreement with previous reports obtained within a range of theories.^{2,27,28,32}

TABLE II. Although the activation barrier is underestimated in the PBE functional compared to the hybrid Hyed-Scuseria-Ernzerhof screened hybrid functional (HSE06), they show a similar qualitative trend. $\delta E_a [= E_a(C_{60}) - E_a(X)]$ is the reduction in the activation barrier compared to pristine C_{60} .

	Activation barrier (eV)		δE_a (eV)
	PBE	HSE06	
C_{60}	6.88	7.61	
C_{60}^+	6.40	7.05	0.48 (0.56)
$C_{59}B$	4.76	5.22	2.12 (2.39)
$C_{58}B_2$	2.54	2.80	4.34 (4.81)

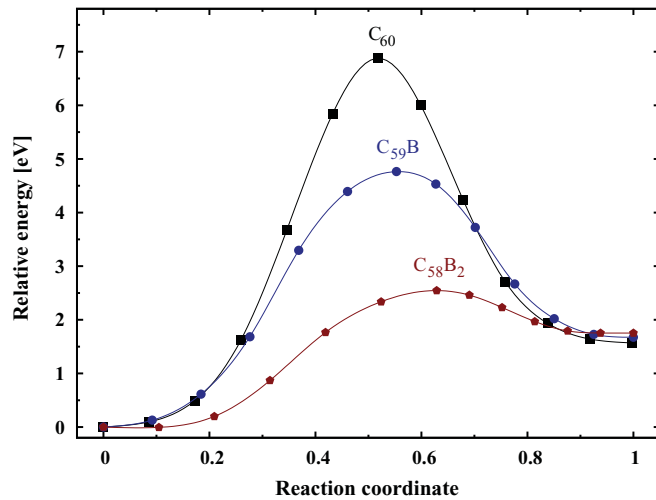


FIG. 4. (Color online) The activation energy barrier for the SW transition ($I_h \rightarrow C_{2v}$) reduces substantially for the B heterofullerenes when B is doped in the active SW sites (rotating dimer). The reverse barrier is smaller by an amount ΔE (Table I), which is similar in magnitude for all cages.

Compared to carbon nanotubes or graphitic nanostructures, the activation barrier in a fullerene is considerably less due to the strain present in the fullerene structure.²⁸ We find that the rotating C_2 unit in the transition state (TS) pops out by ~ 0.21 Å from the C_{60} surface. A similar TS was predicted previously.^{28,32,52} The bond length of the rotating C_2 unit shrinks to 1.248 Å in the TS from the corresponding bond lengths in I_h (1.399 Å) and C_{2v} (1.359 Å) symmetries.

We find that the large SW activation barrier is reduced substantially due to B doping (Table II and Fig. 4) at the active SW site. The barrier is reduced by 2.12 eV when a single C atom is replaced in the rotating dimer by B in the $C_{59}B$ heterofullerene. The reduction is comparable in magnitude with the cases where an extra carbon is strategically placed in the regions of paired pentagons² or is catalyzed by hydrogen.³³ In contrast, the endohedral metal doping has a relatively

smaller effect where the barrier is found to reduce by only 0.80 eV for La doping.²⁷ As we discussed earlier, the fact that $C_{59}B$ develops a (doublet) spin moment, we recalculated the activation barrier including spin polarization. We find that the spin-polarized activation barrier (4.67 eV) is only slightly lower than the non-spin-polarized calculation (4.76 eV).

Similar to $C_{59}B$, the activation barrier becomes lower in the singly charged fullerene C_{60}^+ compared to the neutral C_{60} . Although $C_{59}B$ is isoelectronic with C_{60}^+ , the quantitative reduction in the activation barrier is much higher for $C_{59}B$ (2.12 eV) compared to C_{60}^+ (0.48 eV). The doped B not only introduces a localized hole, but also introduces a substantial local strain. The active C-B bonds are much larger [Fig. 2(b)] and weaker compared to the C-C bonds, and thus, the activation barrier is much lower for the case of B doping.

The activation barrier is further reduced to 2.54 eV (Table II and Fig. 4) when both C atoms in the rotating dimer are replaced with B atoms for the $C_{58}B_2$ heterofullerene. Compared to pristine C_{60} , a total reduction of 4.34 eV is obtained, which is the maximum reported to date.

We find that the structure corresponding to the saddle point for all cages has only one vibrational mode with an imaginary frequency. This confirms that the obtained saddle points are indeed true first-order transition states. Frequency of the imaginary mode decreases with subsequent B doping (962, 377, and 167 cm^{-1} for C_{60} , $C_{59}B$, and $C_{58}B_2$, respectively). Thus, the variation in energy along the reaction path becomes slower, i.e., the NEB curve gets flatter, with the introduction of boron (Fig. 4).

To confirm the trend observed in the activation barrier, we have recalculated the same using an HSE06.⁵³ Although the PBE functional underestimates the activation barrier, the qualitative trend is found to be the same with the HSE06 functional (Table II). HSE06 activation barriers are calculated using the PBE reaction path and performing a single-point calculation on each intermediate image.

The origin of reduction in the SW activation barrier can be explained in terms of changes in bond strength, charge density, and phonon spectra, which point toward bond

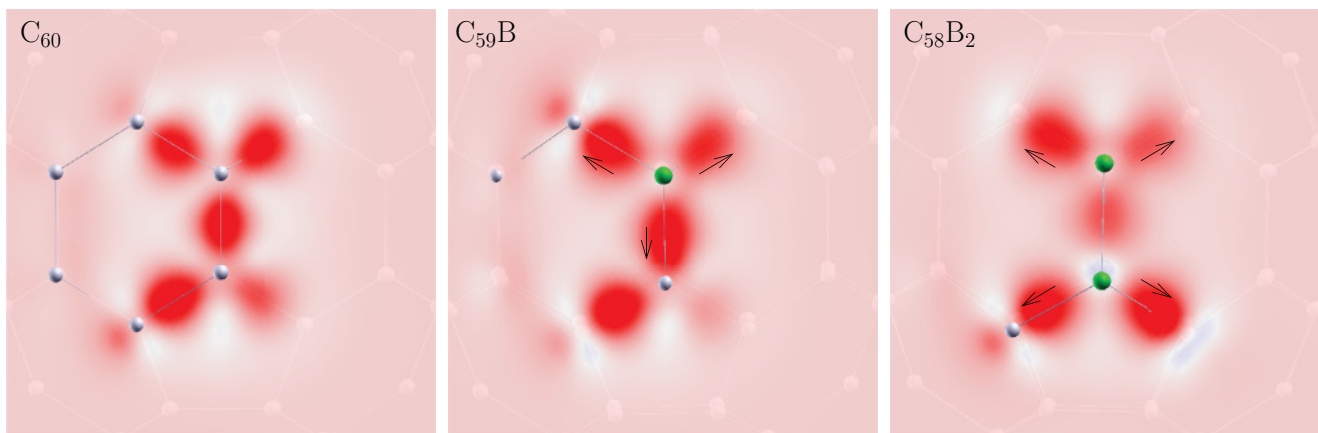


FIG. 5. (Color online) Bonding charge densities $\Delta\rho$ for pristine C_{60} , single, and double B-doped heterofullerenes. The B atoms are shown in green. The $\Delta\rho$ for a particular cage is calculated as $\Delta\rho = \rho^{\text{tot}}(\mathbf{r}) - \rho^{C_{58}}(\mathbf{r}) - \rho^X(\mathbf{r}) - \rho^Y(\mathbf{r})$, where X - Y represents the rotating C-C, C-B, and B-B dimers for C_{60} , $C_{59}B$, and $C_{59}B_2$ structures, respectively. For pristine C_{60} , the charge accumulation centers (red) appear at the middle of the bond, which indicate covalent C-C bonds. In contrast, due to B doping, the charge accumulation centers significantly shift toward the C atoms (shown with the arrows) indicating the ionic C-B character.

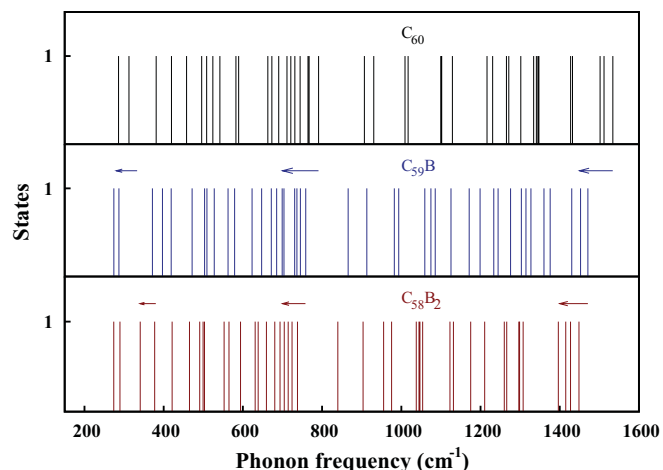


FIG. 6. (Color online) Phonons for the 14-atom pyracyclene around the rotating dimer are shown for I_h symmetry. Due to B-doping, phonons shift toward lower frequencies, which indicate bond weakening.

weakening at and around the rotating dimer. First, we calculate C-C, C-B, and B-B bond strengths in pristine C_{60} , $C_{59}B$, and $C_{58}B_2$, respectively, which can be calculated approximately using the following expressions:

$$\begin{aligned} E_{C-C} &= E_{C_{60}}^{\text{tot}}/90, \\ E_{C-B} &= [E_{C_{59}B}^{\text{tot}} - 87 \times E_{C-C}]/3, \\ E_{B-B} &= [E_{C_{58}B_2}^{\text{tot}} - 85 \times E_{C-C} - 4 \times E_{C-B}], \end{aligned} \quad (1)$$

where E^{tot} represents the total binding energy of the respective structure. We find that E_{C-C} (5.87 eV) $>$ E_{C-B} (4.74 eV) $>$ E_{B-B} (3.75 eV). Due to these weaker C-B bonds around the rotating dimer, the SW rotation becomes easier for the heterofullerenes. We further notice that the amount of reduction is related to the reduction in bond strength as $\delta E_a = n[E_{C-C} - E_{C-B}]$, where n is the number of C-B bonds involved in the SW transition for $C_{59}B$ (two) and $C_{58}B_2$ (four) heterofullerenes.

Bonding charge-density analysis (Fig. 5) also qualitatively points toward softening of the bonds that are involved in the SW process. Figure 5 shows the bonding charge densities for pristine C_{60} and B-doped heterofullerenes. For C_{60} , the C-C bonding is completely covalent i.e., the bonding charge accumulates at the centers of the bond. This picture deviates for B-doped cases, where the charge accumulation centers move toward the C atom for C-B bonds, imparting ionic character to the C-B bonds. Thus, the C-C rotation is increasingly easier for $C_{59}B$ and $C_{58}B_2$ heterofullerenes. Also, the bonding character can be understood quantitatively from Bader charge analysis,⁵⁴ which reveals that each B atom loses an $\sim 1|e|$ charge to the neighboring C atoms, which also indicate the deviation from perfect covalent character.

Next, we turn our attention to the phonon frequencies calculated at the Γ point. It is reasonable to assume that the atoms around the rotating dimer are mostly affected due to B doping and SW rotation. Thus, we considered the 14-atom pyracyclene ring around the rotating bond to calculate the normal vibrational modes. This significantly reduces the size of the Hessian matrix (from 180×180 for the full cluster

to 42×42 for the pyracyclene ring) to calculate phonon frequencies. Due to B doping, phonon frequencies gradually shift to the lower frequencies (Fig. 6). This indicates that the bonds get softer as phonon frequency (ν) is related to bond stiffness (k), $\nu \propto \sqrt{k}$. The observed softening in phonon frequencies arises due to two factors. First, the C-B and B-B bonds are longer and are weaker compared to the C-C bonds, as pointed out earlier. Additionally, the C-C bonds around the rotating unit also get elongated due to the substantial strain introduced by B doping, and thus, get weakened. The rotation of the bond is easier in such a softer environment, which eventually reduces the SW activation barrier.

C. Reaction rate and characteristic time scale

At temperatures well below the melting point, the harmonic approximation to transition state theory (HTST) can be applied to study the reaction rate or characteristic time scale associated with the reaction. The reaction rate can be expressed in terms of energy and normal mode frequencies at the saddle point and initial state,⁵⁵

$$k^{\text{HTST}} = \frac{\prod_i^{3N} \nu_i^I}{\prod_i^{3N-1} \nu_i^{\text{TS}}} e^{-(E_a/k_B T)}, \quad (2)$$

where $E_a = (E^{\text{TS}} - E^I)$ is the activation energy with E^I (E^{TS}) being the energy corresponding to the initial (transition) state and ν_i are the corresponding normal mode frequencies. Within the harmonic approximation, the entropic effect to the reaction rate is included in the prefactor involving phonon frequencies calculated at zero temperature. The first-order transition state is characterized by one imaginary phonon, which is excluded for the transition state. To calculate the prefactor, we have considered only the normal modes corresponding to the 14-atom pyracyclene ring around the rotating dimer. The characteristic time scale associated with a given reaction can be calculated from the knowledge of reaction rate k^{HTST} as $\tau = 1/k^{\text{HTST}}$. Figure 7 shows the characteristic time required for a single $I_h \rightarrow C_{2v}$ SW transition plotted as a function

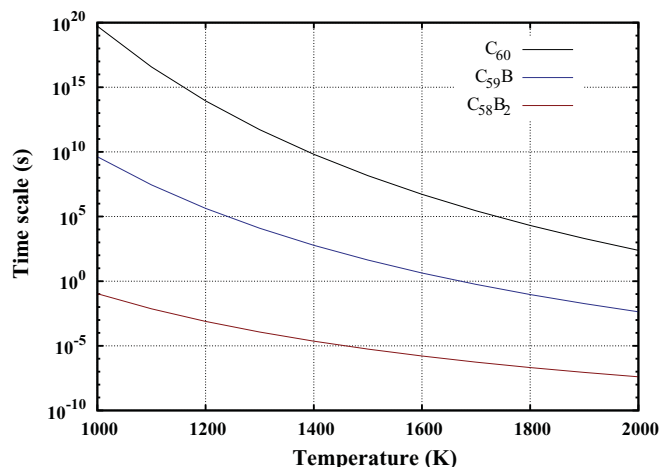


FIG. 7. (Color online) The $I_h \rightarrow C_{2v}$ transition (reaction) rate, and thus, the characteristic time scale for the corresponding transition has Arrhenius dependence on temperature and activation energy. Subsequent B doping in the rotating dimer reduces the characteristic time scale enormously via a decrease in the activation barrier.

of temperature. The characteristic time scale, measured in seconds, differs by 10^{10} – 10^6 due to subsequent B doping in the temperature range of 1000–2000 K. For example, at 1700 K, a single SW bond rotation event takes place in ~ 10 days for pristine C_{60} . In contrast, at the same temperature, the process is enormously accelerated and requires only about a second and a microsecond for $C_{59}B$ and $C_{58}B_2$, respectively. The reverse transition ($C_{2v} \rightarrow I_h$, which is not shown in Fig. 7) is $\exp(\Delta E/k_B T)$ times faster than the forward transition. For example, the reverse transition is 5 orders of magnitude faster for C_{60} at 1700 K.

IV. CONCLUSIONS

The SW activation barrier in pristine fullerenes is very large. It has been reported earlier that this high barrier can be reduced by $\sim 35\%$ due to the presence of an extra carbon or hydrogen.^{2,33} The present calculation shows that the presence of the substitutional boron at the active sites can become more effective in the reduction of the SW activation barrier. We show that it can be reduced substantially by $\sim 30\%$ and 60% via single and double B doping, respectively. Calculated bond strength, charge density, and phonon spectrum indicate that

the C-B bonds are softer compared to the C-C bonds. Thus, the presence of such weaker bonds around the rotating dimer is responsible for the observed reduction in the activation barrier. From a thermodynamic point of view, such a reduction in the barrier ΔE_a enormously reduces the time scale associated with the SW process. The reduction is on the order of $\exp(\Delta E_a/k_B T)$, which is 10^6 -fold (10^{12} -fold) at a temperature of 1700 K for single (double) B doping. SW defects are known to alter the chemical reactivity toward adsorbates,^{14–17} and thus, are expected to affect the proposed reversible H_2 storage properties of B heterofullerenes.^{35,36} Although we have shown the reduction in the SW activation barrier for fullerene here, a similar reduction is expected for carbon nanotubes and graphene nanostructures due to B doping, which could catalyze fusion, and the welding process necessary for nanoelectronic device applications.

ACKNOWLEDGMENTS

M.K. acknowledges the congenial hospitality of the S. N. Bose National Centre for Basic Sciences, Kolkata. S.M. acknowledges the Council of Scientific and Industrial Research, India for financial support.

*Corresponding author: mukulkab@mit.edu

¹A. Stone and D. Wales, *Chem. Phys. Lett.* **128**, 501 (1986); D. J. Wales, M. A. Miller, and T. R. Walsh, *Nature (London)* **394**, 758 (1998).

²B. R. Eggen, M. I. Heggie, G. Jungnickel, C. D. Latham, R. Jones, and P. R. Briddon, *Science* **272**, 87 (1996).

³M. Buongiorno Nardelli, B. I. Yakobson, and J. Bernholc, *Phys. Rev. Lett.* **81**, 4656 (1998); *Phys. Rev. B* **57**, R4277 (1998).

⁴G. G. Samsonidze, G. G. Samsonidze, and B. I. Yakobson, *Phys. Rev. Lett.* **88**, 065501 (2002).

⁵Y. Miyamoto, A. Rubio, S. Berber, M. Yoon, and D. Tománek, *Phys. Rev. B* **69**, 121413 (2004).

⁶Y.-H. Kim, I.-H. Lee, K. J. Chang, and S. Lee, *Phys. Rev. Lett.* **90**, 065501 (2003); Y. Zhao, B. I. Yakobson, and R. E. Smalley, *ibid.* **88**, 185501 (2002).

⁷M. Yoon, S. Han, G. Kim, S. B. Lee, S. Berber, E. Osawa, J. Ihm, M. Terrones, F. Banhart, J.-C. Charlier, N. Grobert, H. Terrones, P. M. Ajayan, and D. Tománek, *Phys. Rev. Lett.* **92**, 075504 (2004).

⁸M. Ouyang, J.-L. Huang, C. L. Cheung, and C. M. Lieber, *Science* **291**, 97 (2001); V. H. Crespi, M. L. Cohen, and A. Rubio, *Phys. Rev. Lett.* **79**, 2093 (1997).

⁹E. J. Duplock, M. Scheffler, and P. J. D. Lindan, *Phys. Rev. Lett.* **92**, 225502 (2004).

¹⁰F. OuYang, B. Huang, Z. Li, J. Xiao, H. Wang, and H. Xu, *J. Phys. Chem. C* **112**, 12003 (2008).

¹¹H. Terrones and A. Mackay, *Carbon* **30**, 1251 (1992).

¹²J. Ma, D. Alfè, A. Michaelides, and E. Wang, *Phys. Rev. B* **80**, 033407 (2009).

¹³D. Ugarte, *Nature (London)* **359**, 707 (1992).

¹⁴Z. Slanina, X. Zhao, F. Uhlík, M. Ozawa, and E. Ōsawa, *J. Organomet. Chem.* **599**, 57 (2000).

¹⁵D. Tasis, N. Tagmatarchis, A. Bianco, and M. Prato, *Chem. Rev.* **106**, 1105 (2006).

¹⁶A. H. Nevidomskyy, G. Csányi, and M. C. Payne, *Phys. Rev. Lett.* **91**, 105502 (2003).

¹⁷H. F. Bettinger, *J. Phys. Chem. B* **109**, 6922 (2005).

¹⁸J. Kang, J. Bang, B. Ryu, and K. J. Chang, *Phys. Rev. B* **77**, 115453 (2008).

¹⁹D. W. Boukhvalov and M. I. Katsnelson, *Nano Lett.* **8**, 4373 (2008).

²⁰H. F. Bettinger, T. Dumitrică, G. E. Scuseria, and B. I. Yakobson, *Phys. Rev. B* **65**, 041406 (2002); W. Chen, Y. Li, G. Yu, Z. Zhou, and Z. Chen, *J. Chem. Theory Comput.* **5**, 3088 (2009).

²¹Y. Lin, T. V. Williams, W. Cao, H. E. Elsayed-Ali, and J. W. Connell, *J. Phys. Chem. C* **114**, 17434 (2010); C. Y. Won and N. R. Aluru, *J. Am. Chem. Soc.* **130**, 13649 (2008); X. Wu, J. Yang, J. G. Hou, and Q. Zhu, *J. Chem. Phys.* **124**, 054706 (2006); Y. Li, Z. Zhou, D. Golberg, Y. Bando, P. von Ragué Schleyer, and Z. Chen, *J. Phys. Chem. C* **112**, 1365 (2008); W. An, X. Wu, J. L. Yang, and X. C. Zeng, *ibid.* **111**, 14105 (2007).

²²S. Austin, P. Fowler, D. Manolopoulos, and F. Zerbetto, *Chem. Phys. Lett.* **235**, 146 (1995).

²³T. R. Walsh and D. J. Wales, *J. Chem. Phys.* **109**, 6691 (1998).

²⁴C. Xu and G. E. Scuseria, *Phys. Rev. Lett.* **72**, 669 (1994).

²⁵H. W. Kroto, *Nature (London)* **329**, 529 (1987).

²⁶S. J. Austin, P. W. Fowler, D. E. Manolopoulos, G. Orlandi, and F. Zerbetto, *J. Phys. Chem.* **99**, 8076 (1995).

²⁷W. I. Choi, G. Kim, S. Han, and J. Ihm, *Phys. Rev. B* **73**, 113406 (2006).

²⁸J.-Y. Yi and J. Bernholc, *J. Chem. Phys.* **96**, 8634 (1992).

²⁹Y.-Z. Tan, Z.-J. Liao, Z.-Z. Qian, R.-T. Chen, X. Wu, H. Liang, X. Han, F. Zhu, S.-J. Zhou, Z. Zheng, X. Lu, S.-Y. Xie, R.-B. Huang, and L.-S. Zheng, *Nature Mater.* **7**, 790 (2008).

³⁰R.-T. Chen, S.-J. Zhou, H. Liang, Z.-Z. Qian, J.-M. Li, Q. He, L. Zhang, Y.-Z. Tan, X. Han, Z.-J. Liao, W.-Z. Weng, S.-Y. Xie, R.-B. Huang, and L.-S. Zheng, *J. Phys. Chem. C* **113**, 16901 (2009).

- ³¹M. S. Dresselhaus, G. Dresselhaus, and P. C. Eklund, *Science of Fullerenes and Carbon Nanotubes* (Academic, San Diego, 1996).
- ³²H. F. Bettinger, B. I. Yakobson, and G. E. Scuseria, *J. Am. Chem. Soc.* **125**, 5572 (2003).
- ³³M. I. Heggie, C. D. Latham, R. Jones, and P. R. Briddon, in *Fullerenes: Chemistry, Physics, and New Directions VII*, edited by K. M. Kadish and R. S. Rudoff (Electrochemical Society, Pennington, NJ, 1995), pp. 1218–1223.
- ³⁴H. J. Muhr, R. Nesper, B. Schnyder, and R. Kötz, *Chem. Phys. Lett.* **249**, 399 (1996); T. Guo, C. Jin, and R. E. Smalley, *J. Phys. Chem.* **95**, 4948 (1991).
- ³⁵Y. Zhao, Y.-H. Kim, A. C. Dillon, M. J. Heben, and S. B. Zhang, *Phys. Rev. Lett.* **94**, 155504 (2005).
- ³⁶Y.-H. Kim, Y. Zhao, A. Williamson, M. J. Heben, and S. B. Zhang, *Phys. Rev. Lett.* **96**, 016102 (2006).
- ³⁷G. Kresse and J. Hafner, *Phys. Rev. B* **47**, 558 (1993); G. Kresse and J. Furthmüller, *ibid.* **54**, 11169 (1996).
- ³⁸P. E. Blöchl, *Phys. Rev. B* **50**, 17953 (1994).
- ³⁹J. P. Perdew, K. Burke, and M. Ernzerhof, *Phys. Rev. Lett.* **77**, 3865 (1996).
- ⁴⁰G. Henkelman, B. P. Uberuaga, and H. Jónsson, *J. Chem. Phys.* **113**, 9901 (2000); G. Henkelman and H. Jónsson, *ibid.* **113**, 9978 (2000).
- ⁴¹M. Hser, J. Almlf, and G. E. Scuseria, *Chem. Phys. Lett.* **181**, 497 (1991).
- ⁴²W. I. F. David, R. M. Ibberson, J. C. Matthewman, K. Prassides, T. J. S. Dennis, J. P. Hare, H. W. Kroto, R. Taylor, and D. R. M. Walton, *Nature (London)* **353**, 147 (1991).
- ⁴³K. Hedberg, L. Hedberg, D. S. Bethune, C. A. Brown, H. C. Dorn, R. D. Johnson, and M. De Vries, *Science* **254**, 410 (1991).
- ⁴⁴S. Liu, Y.-J. Lu, M. M. Kappes, and J. A. Ibrés, *Science* **254**, 408 (1991).
- ⁴⁵C. S. Yannoni, P. P. Bernier, D. S. Bethune, G. Meijer, and J. R. Salem, *J. Am. Chem. Soc.* **113**, 3190 (1991).
- ⁴⁶X. Blase, C. Attaccalite, and V. Olevano, *Phys. Rev. B* **83**, 115103 (2011).
- ⁴⁷I. V. Hertel, H. Steger, J. de Vries, B. Weisser, C. Menzel, B. Kamke, and W. Kamke, *Phys. Rev. Lett.* **68**, 784 (1992).
- ⁴⁸L.-S. Wang, J. Conceicao, C. Jin, and R. Smalley, *Chem. Phys. Lett.* **182**, 5 (1991).
- ⁴⁹J. D. Sau, J. B. Neaton, H. J. Choi, S. G. Louie, and M. L. Cohen, *Phys. Rev. Lett.* **101**, 026804 (2008).
- ⁵⁰E. Kaxiras and K. C. Pandey, *Phys. Rev. Lett.* **61**, 2693 (1988).
- ⁵¹T. Dumitrica and B. I. Yakobson, *Appl. Phys. Lett.* **84**, 2775 (2004).
- ⁵²R. L. Murry, D. L. Strout, G. K. Odom, and G. E. Scuseria, *Nature (London)* **366**, 665 (1993).
- ⁵³J. Heyd, G. E. Scuseria, and M. Ernzerhof, *J. Chem. Phys.* **118**, 8207 (2003); A. F. Izmaylov, G. E. Scuseria, and M. J. Frisch, *ibid.* **125**, 104103 (2006).
- ⁵⁴R. F. W. Bader, *Atoms in Molecules-A Quantum Theory* (Oxford University Press, Oxford, 1990); G. Henkelman, A. Arnaldsson, and H. Jnsson, *Comput. Mater. Sci.* **36**, 354 (2006).
- ⁵⁵G. H. Vineyard, *J. Phys. Chem. Solids* **3**, 121 (1957).